

Thermodynamics and Kinetics of Elementary Surface Reaction Steps in Catalysis by Single
Crystal Adsorption Calorimetry

Trent L. Silbaugh

A dissertation

submitted in partial fulfillment of the
requirements for the degree of

Doctor of Philosophy

University of Washington

2014

Reading Committee:

Prof. Charles T. Campbell, Chair

Prof. Stuart B. Adler

Prof. Eric M. Stuve

Program Authorized to Offer Degree:

Chemical Engineering

©Copyright 2014

Trent L. Silbaugh

University of Washington

Abstract

Thermodynamics and Kinetics of Elementary Surface Reaction Steps in Catalysis by Single
Crystal Adsorption Calorimetry

Trent L. Silbaugh

Chair of the Supervisory Committee:
Professor Charles T. Campbell
Chemical Engineering

Many chemical technologies rely on the interaction of gas phase molecules with solid surfaces. One of the most important application fields among these technologies is heterogeneous catalysis, which includes chemical manufacturing, energy generation, conversion and storage and environmental technology. Many of the related processes include one or more steps catalyzed at solid interfaces or involve adsorption of gaseous molecules. For the rational design of new catalytic and other functional materials, a detailed knowledge of the energetics of the adsorbate-surface interaction and the thermodynamics of surface reaction intermediates is required. Recent results have revealed that state-of-the-art computational methods based on density functional theory have far greater energy errors than originally believed, so they are

insufficient for this task. The data set of experimental benchmarks needed to improve these is also still far too limited. Thus, more measurements of adsorption energies are badly needed.

Because many of these important intermediates exist in metastable states, traditional experimental techniques that rely on reversible desorption of adsorbed species to get adsorption energies (i.e. temperature programmed desorption and equilibrium adsorption isotherms) cannot be used. In this thesis, single crystal adsorption calorimetry (SCAC), which allows for the direct measurement of heat deposition during surface adsorption and reaction processes, is utilized to determine the energetics of several simple adsorbed molecular fragments on Pt(111).

A new data analysis method is introduced here that allows SCAC to be used to simultaneously probe the thermodynamics as well as kinetics of surface reactions. This analysis method is used to provide the rate barriers for elementary steps in the decomposition of formic acid on oxygen precovered Pt(111).

A review of all SCAC studies of molecular adsorption and reaction is also provided, and important recent results from this body of literature is discussed. A correlation of bond enthalpies determined from SCAC data to gas phase bond enthalpies has provided a linear relationship that allows for the prediction of surface bond strengths from gas phase data. Also, using energetics from several SCAC and TPD studies, a complete energy landscape for the oxidation of methanol and formic acid on oxygen precovered Pt(111) has been generated which provides insight into the mechanism of this process. A comparison of experimental bond energies to values obtained from density functional theory (DFT) calculations shows that errors in standard DFT can be quite large, particularly for systems with large van der Waals interactions, and that these errors are *not* systematic.

Table of Contents

Abstract	iii
List of Tables	vii
List of Figures	viii
Acknowledgements	xiii
Chapter 1 Introduction	14
Chapter 2 Experimental	19
2.1 Figures	23
Chapter 3 Adsorption Energy of <i>tert</i>-Butyl on Pt(111) by Dissociation of <i>tert</i>-Butyl Iodide: Calorimetry and DFT	24
3.1 Introduction	24
3.2 Experimental.....	27
3.3 Density Functional Theory Calculations	31
3.4 Results and Discussion	33
3.5 Conclusions	47
3.6 Appendix	49
3.7 Figures	50
Chapter 4 Surface Kinetics and Energetics from Single Crystal Adsorption Calorimetry Lineshape Analysis: Methyl from Methyl Iodide on Pt(111)	59
4.1 Introduction	59
4.2 Pulseshape and heat measurement for fast heat deposition	63
4.3 Pulseshape analysis for multi-step heat deposition processes	66
4.4 Application: Dissociative adsorption of methyl iodide on Pt(111) at 270 K	70
4.5 Conclusions	78
4.6 Figures	79
Chapter 5 Energetics of formic acid conversion to adsorbed formates on Pt(111) by transient calorimetry	87
5.1 Introduction	87

5.2	Experimental.....	89
5.3	Results	94
5.4	Discussion.....	98
5.5	Conclusions	107
5.6	Figures	108
Chapter 6	Energetics of Methanol and Formic Acid Oxidation on Pt(111): Mechanistic Insights from Adsorption Calorimetry	113
6.1	Figures	119
6.2	Supporting Information	121
Chapter 7	Bond energies of molecular fragments to metal surfaces track their bond energies to H atoms.....	125
7.1	Figures	133
Chapter 8	Energetics of Adsorbed Catalytic Intermediates on Transition Metals by Single Crystal Adsorption Calorimetry.....	134
8.1	Introduction	134
8.2	Single Crystal Adsorption Calorimetry: Thermodynamic and Kinetic Information....	135
8.3	From Heats of Adsorption to Enthalpies of Formation and Bond Enthalpies.....	137
8.4	Use of SCAC Experimental Benchmarks as Comparisons to Periodic Density Functional Theory Calculations.....	138
8.5	Summary of Results	140
8.6	Applications.....	153
8.7	Conclusions	159
8.8	Figures	160
Chapter 9	Conclusions and Outlook.....	164
9.1	Figures	170
References	171
Appendix A	181
Curriculum Vitae	200

List of Tables

Table A.3.1: Bond energies (in eV) on Pt(111) calculated with the optB86b vdW-DF using different sets of parameters.	49
Table S.6.1: Experimentally determined standard enthalpies of formation of gas phase and adsorbed molecules and molecular fragments. When possible, we have used enthalpies determined at a consistent coverage of 1/4 ML. Gases are at 1 bar pressure.	124
Table 7.1: Calorimetrically measured standard heats of formation (ΔH_f°) and adsorbate-Pt(111) bond strengths (i.e., adiabatic bond enthalpies) of three oxygen-bound adsorbates on Pt(111) and their corresponding gas-phase H—OR bond strengths. Literature citations are given as superscripts to the known enthalpy values.	127
Table 7.2: Predicted heats of formation and bond enthalpies of several oxygen-bound adsorbates on Pt(111) from the fitted line in Figure I. Literature citations are given as superscripts to the known enthalpy values.	129
Table 8.1: Integral heats of molecular adsorption of CO on low index transition metal surfaces. All measurements performed at room temperature using SCAC. Note the excellent agreement between measurements from three separate groups of CO adsorption on Pt(111). Coverage, in ML, indicates the surface density of metal surface atoms for each surface. Heats marked with an asterisk (*) indicate values that have been corrected for errors in metal reflectivity. For all values that list two references, the actual numerical values are taken from the review by Brown et al., ⁸ which corrected several data sets from the original publications.	141
Table 8.2: Enthalpies of molecular adsorption measured with SCAC. All equations represent differential heats of adsorption valid over the stated coverage range collected at the stated temperature.	144
Table 8.3: Measured enthalpies of reaction from SCAC. All enthalpies are integral values at the stated coverage and temperature, unless otherwise noted. All equations represent differential heats of adsorption. Equations are dif. heat over stated coverage range.	147
Table 8.4: SCAC measured integral enthalpies of reaction for oxygen containing species on O-Pt(111) at the specified coverage and temperature.	149
Table 8.5: Experimentally determined enthalpies of formation of important atomic intermediates on Pt(111) as determined from TPD and nuclear microprobe analysis (NMA).	150
Table 8.6: Activation energies for molecular and atomic desorption from TPD and EAI experiments. Preexponential factors (ν) marked with a # have been calculated using the gas phase entropy of the desorbing species as described by Campbell and Sellers. ⁹⁰ β is the heating rate used in the TPD experiment.	152
Table 8.7: Experimental activation energies for desorption determined from TPD and time resolved electron energy loss spectroscopy (TREEELS). Transition state theory	

(TST) was used to estimate a preexponential factor for desorption from Ni(111) to simulate TPD data.....	152
Table 8.8: Activation barriers for the recombinative desorption of H_{ad} to make $H_{2,g}$. Adsorbate induced surface reconstructions are indicated when observed experimentally. TPD found this to be a second order process on all surfaces where no reconstruction was present. In most cases, the preexponential factor was not provided in original publications.....	153
Table 8.9: Comparison of binding energies of adsorbates on Pt(111) from SCAC and TPD experimental data with DFT calculations.....	158

List of Figures

Figure 2.1: Schematic of a single crystal adsorption calorimetry experiment. A pyroelectric polymer ribbon (actual detector ribbon and housing pictured in upper left corner) is placed in mechanical contact with the back of a single crystal metal sample. A pulsed molecular beam is directed at the front sample surface. Molecules that adsorb/react on the sample surface deposit heat, while molecules that do not stick to the surface are detected by a mass spectrometer without line-of-sight to the sample.....	23
Figure 3.1: XPS spectra of the I 3d peak obtained after adsorption of 0.067 ML of <i>t</i> -BuI on Pt(111) at 100 K (bottom curve) and at 300 K (top curve). Spectra were obtained at the same exposure temperature. The background for the clean Pt(111) sample was subtracted and the peaks were fitted by a Gaussian-Lorentzian curve to obtain the indicated peak maxima. The energy scale has been calibrated using the Pt $4f_{7/2}$ (BE= 70.9 eV) and Cu $2p_{3/2}$ (BE= 932.4 eV) peaks for these pure metals.	50
Figure 3.2: RAIRS spectra for increasing doses of <i>t</i> -BuI on Pt(111) at 100 K. Exposures are given in Langmuirs (L) but these should only be taken as a relative measure of exposure, since they were measured at the ion gauge and not at the Pt surface, where the exposures are expected to be much lower due to pumping by the surrounding cryogenically-cooled surfaces.....	51
Figure 3.3: RAIRS spectra for 5 L of <i>t</i> -BuI dosed on Pt(111) at 100 K, and after heating briefly to the indicated increasing temperatures.	52
Figure 3.4: Top (upper panels) and side (lower panels) snapshots of the DFT (optB86b vdW-DF) calculated minimum energy configurations for the various surface species on Pt(111): (a) <i>t</i> -BuI; (b) <i>t</i> -Bu+I; (c) di- σ <i>i</i> -butene+I+H; (d) <i>t</i> -Bu; (e) di- σ <i>i</i> -butene; (f) transition state for C-I bond scission in <i>t</i> -BuI; (g) transition state for C-H bond scission in <i>t</i> -Bu with coadsorbed I; (h) I; (i) H. Large white, large grey, medium black, and small white spheres correspond to Pt, I, C, and H atoms, respectively. The coverage shown is 1/16 ML except for (a) and (f), for which it is 1/9 ML. The surface unit cell boundaries for 1/16 ML are illustrated in (h). The various labeled bond distances in (f) and (g) are: $d_{C-I}=2.843 \text{ \AA}$; $d_{C-H}=1.146 \text{ \AA}$ (f) and 1.526 \AA (g); $d_{Pt-H}=2.246 \text{ \AA}$ (f) and 1.623 \AA (g).	53

Figure 3.5: DFT (optB86b vdW-DF) calculated IR spectra of possible surface species formed upon the adsorption of <i>t</i> -BuI on Pt(111). The DFT-calculated IR spectrum of gaseous <i>t</i> -BuI is shown for comparison. See text for peak positions.....	54
Figure 3.6: Long-term sticking probability of <i>t</i> -BuI on Pt(111) at 100 and 120 K versus the total <i>t</i> -BuI coverage that irreversibly adsorbed (irrespective of its structure in the adlayer). These measurements were obtained simultaneously with the heat of adsorption data of Fig. 7, which were used to assign the cutoffs between dissociative and molecular adsorption (thin dashed line) and between the first and second layers (heavy dashed line). Completion of the second layer (also shown by a heavy dashed line) was assigned to the point where this 120 K sticking probability has decreased to 0.5. The short-term sticking probability (not shown) was unity at all these conditions.....	55
Figure 3.7: Differential heats of adsorption of <i>t</i> -BuI versus coverage on Pt(111) at 110±10 K (i.e., the average of several runs each at 100 and 120 K). The corresponding coverage ranges for different processes are indicated. “Second Layer” here indicates that this surface already contains the first layer of surface species derived from <i>t</i> -BuI adsorption (both dissociative and then molecular)	56
Figure 3.8: Thermodynamic cycle used to determine the standard enthalpy of formation of adsorbed <i>t</i> -Bu and its bond enthalpy to Pt(111) from the dissociative adsorption of <i>t</i> -buI on Pt(111). The measured integral enthalpy of dissociative adsorption at 0.04 ML coverage at 100-120 K is shown as ΔH_{RXN} on the bottom right. Derived heats for the <i>t</i> -Bu-Pt(111) bond enthalpy and for the enthalpy of formation of adsorbed <i>t</i> -Bu on Pt(111) are boxed. Because the final error in the calculated values (± 20 kJ/mol) is dominated by the error in the I-Pt(111) bond energy (see text), individual errors are not shown in this cycle.	57
Figure 4.1: Typical heat detector response and beam intensity (mass spectrometer signal intensity, which is proportional to the molecular beam flux) for cyclohexene adsorption on Pt(111) at 102 K. Beam pulses are 100 ms in duration (FWHM) and repeated every 2 seconds. (Reprinted with permission from. ¹⁰⁹ Copyright 2008 American Chemical Society.)	79
Figure 4.2: Heat detector response for a pulse of methyl iodide adsorbing on Pt(111) at 100 K (red) and for a laser pulse used to calibrate the signal (blue dashed). Each pulse was 102 ms long (FWHM) and repeated every 5 s (only the first 3 s are shown), and multiple pulses were averaged to improve signal to noise ratio. Also shown are demonstrations of measurements of the heat signal magnitude using either the peak height (from the initial baseline to the peak maximum, as shown) or the slope of the initial fast rise. The slope is obtained from a linear fit to the data between 10% and 90% of the peak maximum, as shown in green. The rise-time is defined as the time for the signal to rise through this 10% to 90% range, as shown.	80
Figure 4.3: Detector responses to single pulses of the laser used for calibration (blue) and of the laser convoluted with a first-order decay with a time constant of 350 ms (green). This latter corresponds to a 2-step kinetic model where the first step (physisorption) is	

instantaneous but has negligible heat, and the heat is all deposited in the second, slow step whose rate constant is $(350 \text{ ms})^{-1}$	81
Figure 4.4: Normalized detector responses for the laser calibration and molecular adsorption of methyl iodide on Pt(111) at 270 K. The response from molecular adsorption is broadened due to slow heat deposition. The inset shows the same pulses on a shorter timescale.....	82
Figure 4.5: Simulated heat pulse (purple dashed) of 212 kJ/mol created using values obtained from the best fit method for the third average methyl iodide pulse (0.037-0.055 ML) on Pt(111) at 270 K (red). This simulated heat pulse is the sum of the fast step 1 heat (blue) of 136 kJ/mol and slow step 2 heat (green) of 76 kJ/mol that is deposited with a τ of 240 ms. Also shown for comparison is the normalized measured signal for pulses of CH ₃ I adsorption at these conditions.	83
Figure 4.6: Calculated total differential heat of adsorption (black triangles), Step 1 heat (red squares) and Step 2 heat (blue circles) for methyl iodide pulses on Pt(111) at 270 K as a function of dissociatively adsorbed methyl iodide coverage, θ , in ML. Lines through the data show the best-fit straight lines.....	84
Figure 4.7: Time constants for the dissociation of adsorbed CH ₃ I on Pt(111) (red squares), in ms, obtained from the best-fit analysis of methyl iodide pulses on Pt(111) at 270 K as a function of total amount of dissociatively adsorbed methyl iodide coverage, θ , in ML. The rate constants (k , blue circles), in s^{-1} , are the inverse of the time constant (τ^{-1}). $k = k_0 (1 - \theta/\theta_{\text{max}})$ with a k_0 of 6.2 sec^{-1} and a θ_{max} of 0.16 ML.....	85
Figure 4.8: Energy lanscape for the reaction of $\text{CH}_3\text{I}_g \rightarrow \text{CH}_3\text{I}_{\text{ad}} + \text{I}_{\text{ad}}$ on Pt(111) at 270 K at the limit of zero coverage. The enthaply of $\text{CH}_3\text{I}_{\text{ad}}$ relative to CH_3I_g was obtained from SCAC at 95 K when only that first step occurs. ²⁰ The total reaction heat of -257 kJ/mol was obtained from the linear fit to the total heat of adsorption versus coverage data (Fig. 6). The activation energy for the second step was estimated using the k_0 value of 6.2 s^{-1} obtained from the linear fit to the experimental k versus coverage data (Fig. 7), assuming a pre-exponential factor of 10^{11} s^{-1} . It corresponds to the slow parts of the surface, with a barrier below $\sim 49 \text{ kJ/mol}$ on $\sim 50\%$ of the surface.....	86
Figure 5.1: (a) Short-term and (b) long-term sticking probabilities of formic acid on clean Pt(111) at 100 K and O-saturated Pt(111) at 150 and 190 K as a function of the total formic acid coverage that adsorbed (irrespective of its final structure after adsorption). Although not shown, the sticking probabilities at 100 K on O-saturated Pt(111) were very similar to those shown here on clean Pt(111) at 100 K.	108
Figure 5.2: Heats of adsorption measured at various temperatures on clean Pt(111) at 100 K (black circles) and O-saturated Pt(111) at 100 K (hollow and solid green circles), 150 K (hollow and solid blue triangles) and 190 K (red squares) as a function of total coverage of adsorbed HCOOH, irrespective of its final structure. Hollow symbols represent fast heat deposition steps while solid symbols represent total heats (i.e., the sum of fast and slow steps). The multilayer heat of adsorption is indicated by a dotted line through the 100 K data in the lower right corner.....	109

Figure 5.3: Experimental and simulated pulses obtained from a best-fit analysis of formic acid on O-sat. Pt(111) at 150 K. The experimental heat-signal pulse (EH) is an average over the coverage range 0.13-0.18 ML. The simulated pulse (SP) fits EH so well that the curves can barely be distinguished. This confirms the accuracy of the parameters (i.e. S1 and S2 heats and the slow step time constant, τ) obtained from this analysis. The species “OH” here is short for the water-OH complex, with the stoichiometry really being that of reaction (4).....	110
Figure 5.4: Thermodynamic cycle used to determine the enthalpy of formation of adsorbed monodentate formate on Pt(111) and its HCOO-Pt(111) bond enthalpy from the integral fast S1 heat of adsorption at 150 K and 3/8 ML, shown as the bottom right-hand step. References for literature values are listed in the text.	111
Figure 5.5: Enthalpy of formation of adsorbed monodentate and bidentate formate species ($\Delta H_f(\text{HCOO}_{\text{ad,mon}})$ and $\Delta H_f(\text{HCOO}_{\text{ad,bi}})$ respectively) as a function of total formic acid coverage. The enthalpies of formation of formate are determined using integral heats of reaction measured at 150 K on O-sat. Pt(111) along with other known enthalpies of formation in a thermodynamic cycle as shown in Fig. 4. The listed coadsorbates (i.e. $(\text{H}_2\text{O-OH})_{\text{ad}}$ and $\text{H}_2\text{O}_{\text{ad}}$) refer to the stoichiometry used in the thermodynamic cycles.	112
Figure 6.1: Energy landscape for methanol and formic acid oxidation to CO_2 and their decomposition to CO plus H_2 . Energy levels and barriers were determined experimentally (Table S.6.1) and represent key intermediates. Enthalpies are referenced to gas phase methanol and adsorbed oxygen atoms on a Pt(111) surface.	119
Figure 6.2: Reaction scheme for the oxidation of methanol and formic acid to carbon dioxide.....	120
Figure 7.1: Calorimetric adiabatic bond dissociation enthalpies of three oxygen-bound adsorbates (deuterated hydroxyl, methoxy, and monodentate formate) to Pt(111) (filled circles) versus their corresponding gas-phase hydrogen-OR adiabatic bond dissociation enthalpies. A line with slope equal to 1.00 fits these three points nearly perfectly. This allows the prediction of the bond strength of other important oxygen-bound adsorbates on Pt(111) that have not been measured (open squares), such as other alkoxy species and hydroperoxy. The error bars on each measurement represent 95% confidence limits.	133
Figure 8.1: A generic thermodynamic cycle used for calculating enthalpies of formation and bond enthalpies (blue text) from measured enthalpies of reaction (red text).....	160
Figure 8.2: Experimentally determined energy landscape for the oxidation of both methanol and formic acid on oxygen precovered Pt(111). The inset in the bottom left corner shows the conversion between monodentate and bidentate formate.	161
Figure 8.3: Surface bond enthalpies of molecular fragments adsorbed on Pt(111) through a single oxygen bond plotted versus their corresponding gas phase hydrogen-OR adiabatic bond enthalpies. A linear relationship with a slope of unity is seen, allowing for the prediction of bond enthalpies of other oxygen bound molecular fragments gas phase data. ²⁶⁵	162

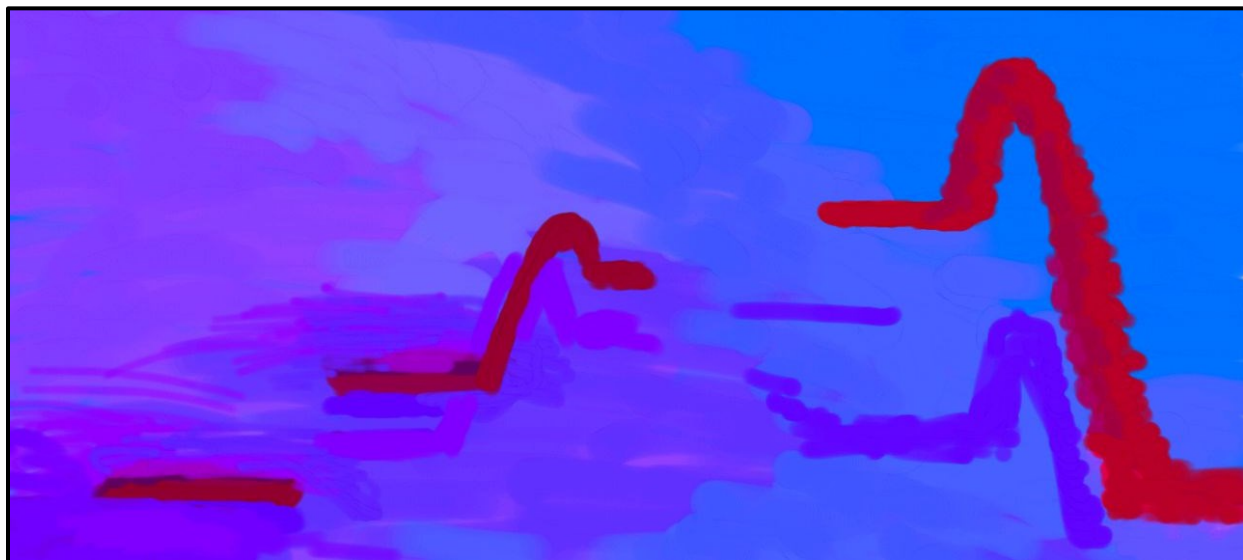
Figure 8.4: Comparison of experimentally determined binding energies to density functional theory calculations.....	163
Figure 9.1: Schematic of high throughput calorimetry sample composition map and ribbon detector electrical contact pattern.....	170

Acknowledgements

First I would like to thank my advisor, Charles T. Campbell, for all of his guidance during my time at the University of Washington; his knowledge and enjoyment of teaching has helped to make me a better scientist. During my time at UW, I have been surrounded by members of the Campbell group who have been fantastic coworkers as well as great friends. I will always look back on this time fondly and hope that we stay in touch professionally and personally. I would like to particularly thank those members of the Campbell group with whom I worked most closely: Eric M. Karp for teaching me all of the ins and outs of the lab and for having great discussions about science, careers, and life in general and Christopher Wolcott for sharing in all of the joys and pains of surface science research.

Members of my committee and staff members of the chemical engineering and chemistry departments have been helpful every step of the way and have made my time in Seattle memorable and enjoyable.

Finally, and most importantly, I would like to thank my wife and best friend for supporting me through it all. I am sure I would never have finished without you.



Chapter 1

Introduction

Many chemical technologies employed presently rely on the interaction of gas phase molecules with surfaces. One of the most important application fields among these technologies is heterogeneous catalysis, which comprises chemical manufacturing, energy generation, conversion and storage¹⁻³ as well as environmental technology.⁴ Many of the related processes include one or more steps catalyzed at solid interfaces or involve adsorption of gaseous molecules. Generally, the performance of any heterogeneous catalyst depends on the ability of the catalytic surface to efficiently bind the reactants, stabilize the desired reaction intermediates and effectively release the products. These properties are determined by the bond strengths of the adsorbed species to the surface and by the relative thermodynamic stabilities of some key reaction intermediates and transition states.

For the controlled molecular design of new catalytic and other functional materials, a detailed knowledge of the energetics of the adsorbate-surface interaction and the thermodynamics of surface reaction intermediates is required, which provide a basis for fundamental understanding of how the surface binds the molecules and guides them through various elementary steps to the products and for predicting the pathway that a reaction will take on a catalyst surface.

Practical catalysts often consist of powders or metallic nanoparticles supported on oxide materials with dimensions on the order of microns. However, gaining a fundamental understanding of molecular and molecular fragment binding on such materials is complicated by the presence of multiple surface facets, defects, and interfaces between particles and their

supports. Calorimetric measurements on such materials provide an ensemble average over all features, making it challenging to tie these measurements to adsorbate structure. This has led to the use in the surface science community of well defined “model catalysts”, which generally consist of single crystal metal samples which expose a single surface facet (e.g. Pt(111)) and have a low density (below ~2%) of defects such as step and kink sites. Molecular adsorption and reaction on such model surfaces has allowed researchers to study the temperature and surface coverage dependent chemistry of adsorbates, leading to a detailed understanding of the intermediates produced and their surface binding configurations. By studying different surface terminations of the same material, the dependence of the chemistry on surface structure can be determined; something that is not possible with practical catalyst materials.

Single Crystal Adsorption Calorimetry (SCAC) allows for the direct measurement of adsorption and reaction enthalpies of gaseous species on these well-defined model surfaces under ultra-high vacuum conditions. A short description of how these experiments are performed is given in Chapter 2. This method was invented by King et al. in the 1990s⁵⁻⁷ and further developed by Campbell et al.⁸⁻¹¹ The results from this method have been discussed in great detail in several review articles.¹²⁻¹⁶ The major advantage of using SCAC is that it *directly* measures the interaction strength of gaseous molecules with the surface of interest. The traditionally used experimental techniques for probing the energetics of adsorption – temperature-programmed desorption (TPD) and equilibrium adsorption isotherm (EAI) measurements – provide reliable results only for systems with fully reversible adsorption. Most of the catalytically-relevant processes, involving dissociation, reaction with co-adsorbates, clustering or diffusion into bulk cannot be probed by these desorption-based methods. Additionally, even for simple reversible adsorption/desorption, a number of assumptions on the details of the desorption process are

sometimes necessary (e.g. the value of the preexponential factor) in order to estimate the binding energy of surface species from kinetics of desorption. These restrictions can be completely overcome by using a direct calorimetric measurement. To date, SCAC has been successfully applied to study the energetics of adsorbate-surface interactions for different molecules and molecular fragments adsorbed on metal single crystals.^{12-14,17-25}

Early SCAC work carried out in the group of Sir David A. King focused on simple molecular adsorption on well-defined metal single crystal surfaces. Initial studies, such as the molecular adsorption of CO on Ni(110),⁶ provided detailed coverage dependent energetics while also serving as a proof of concept for the new technique, as such systems had been widely studied using other surface reaction techniques such as TPD and EAI. This work was followed by molecular adsorption and more complex dissociative adsorption reaction studies (e.g. O₂,^{26,27} C₂H₂ and C₂H₄^{28,29}) on other model catalyst surfaces, such as the low index surfaces of nickel, platinum and palladium and has been covered in great detail elsewhere.^{12,30}

Platinum is used to catalyze many classes of reactions, including hydrocarbon hydrogenation and dehydrogenation, steam reforming, and water-gas-shift. Since Pt(111) is the most stable facet of Pt, it has been a key model catalyst used in surface science studies of prototypical reactions. Studies have provided the energetics of catalytically-interesting, adsorbed molecular fragments (e.g. cyclohexene³¹, methyl (CH₃)^{20,32}, hydroxyl (OH)³³) on the Pt(111) model catalyst surface implicated in countless reaction mechanisms.

In the following chapters, I discuss the results of molecular adsorption and dissociation of *tert*-butyl iodide (Chapter 3), methyl iodide (Chapter 4), and formic acid (Chapter 5) on the clean and oxygen saturated Pt(111) model catalyst surface. These results help highlight the unique

capabilities of SCAC and underscore the key role that this technique plays in gaining a fundamental understanding of surface chemical reactions.

In Chapter 4, I will discuss a recent advance in SCAC data analysis that provides both kinetic and thermodynamic parameters of surface reactions from a detailed analysis of the calorimetry detector signal lineshape.³⁴ Previous SCAC studies required that the intermediates of interest be produced on a timescale much faster than the measurement time (~100 ms) and be stable on a timescale much longer than the measurement, thus greatly limiting the systems that could be studied. This analysis method greatly expands the number of systems whose energetics can be studied using SCAC, including the simultaneous energy measurement of adsorbed intermediates that are only stable for 10–1000 ms, and products that do not appear until 10–1000 ms after the gas strikes the surface.

Complete energy landscapes of a chemical reaction can be constructed by measuring the energetics of multiple intermediates involved. SCAC is often the only suitable technique for determining these energetics, as many intermediates in catalytically relevant reaction pathways exist in metastable states, further decomposing or reacting on a catalyst surface rather than desorbing. Calorimetric measurements of molecules and molecular fragments implicated in the oxidation of methanol and formic acid have provided a nearly complete energy landscape for these processes on Pt(111), as will be discussed in Chapter 6.

It is shown in Chapter 7 that a linear relationship with unit slope holds for experimental bond energies of ligands bound to a late transition metal surface, Pt(111), and their corresponding H-Ligand bond energies. Two of the three measurements that led to the discovery of this trend were made by me and coworkers during my doctoral work. A discussion of this discovery's predictive ability for estimating the bond energies of molecular fragments adsorbed

to transition metal surfaces is provided and a demonstration of how this relationship can be used to gain considerable insight into the thermodynamics of important catalytic reaction mechanisms is given.

In Chapter 8, a review of SCAC data for molecular interactions with single crystal metal surfaces collected to date is presented and several key results of SCAC work is highlighted. A comparison of these results to state-of-the-art computational methods based on density functional theory (DFT) reveal that such DFT calculations have far greater energy errors than originally believed. The data set of experimental benchmarks needed to improve these is also still far too limited. Thus, more measurements of adsorption energies are badly needed.

In Chapter 9, I will discuss the overall conclusions of this work as well as offer an outlook on the future directions that I feel single crystal adsorption calorimetry research may take.

Chapter 2

Experimental

The design of single crystal adsorption calorimetry instrumentation and its implementation has been described in great detail elsewhere.^{5,8,35} This section will briefly describe the principles of the experimental design. For specific details about the experiments reported herein, see the experimental sections within later chapters.

Figure 2.1 shows a schematic of a calorimetry experiment, which are performed in an ultrahigh vacuum chamber (base pressure $< 2 \times 10^{-10}$ mbar). Experiments are performed on a 1 μm thick single crystal sample (i.e. Pt(111)) mounted between two tantalum rings and held in a copper housing. The sample is cleaned by 1.25 kV Ar^+ sputtering, annealing to 1123 K, heating to 773 K in 1×10^{-8} mbar $\text{O}_{2,\text{g}}$ for 1 min, and a final flash to 1123 K. Cleanliness is verified by Auger electron spectroscopy (AES) and surface ordering is verified by low energy electron diffraction (LEED).

Following cleaning, the calorimeter detector is brought into mechanical contact with the back of the sample and allowed to thermally equilibrate (i.e. the detector baseline signal is stable). The detector is then removed from contact, the sample is flashed to 1123 K, and the detector is placed back in contact. As soon as the signal baseline stabilizes, the experiments are begun.

Calorimetry experiments are performed by impinging pulses of gas onto the clean sample surface. Molecular pulses are 102 ms in duration and repeated every 5 s. The molecular beam is created by expanding $\sim 1\text{-}3$ mbar of the target molecule through a microchannel array that is held at a constant temperature (generally 300-360 K) and then collimated through five liquid-nitrogen

cooled orifices. This collimated beam is then mechanically chopped by a spinning disk with a small slit removed. The resulting molecular pulse is 4.36 mm in diameter and contains ~0.5-1% ML ($1-2 \times 10^{12}$ molecules). Throughout this thesis, 1 ML is defined as the atom density of the sample surface (i.e. 1.5×10^{15} Pt atoms/cm² for Pt(111)).

The detector consists of a pyroelectric β -polyvinylidene fluoride (β -PVDF) ribbon that is pressed into mechanical contact with the backside of the single crystal sample. A pulse of molecules deposited onto the sample by the mechanically-chopped, collimated molecular beam leads to a transient heat rise in the sample (for an exothermic process). The resulting temperature change in the sample leads to a transient face-to-face voltage rise in the β -PVDF ribbon that is measured by an external circuit.

To determine how much energy was deposited in a particular detector pulse, a laser of known energy is diverted down the molecular beam, resulting in laser pulses with an identical time profile to the molecular pulses. Each laser pulse leads to the deposition of energy equal to the laser power measured externally by a photodiode times the pulse duration and corrected by the sample reflectivity at the wavelength of the HeNe laser (632.8 nm). This reflectivity has been measured in two independent groups to be 0.76 for the Pt(111) samples used in our experiments. A typical laser pulse deposits 2 μ J per pulse. If the detector response lineshapes from molecular and laser pulses match, as is the case for molecular adsorption and reaction processes where heat is deposited quickly, the ratio of the peak heights or initial slopes (over a ~90 ms window) can be used to determine the amount of total energy deposited in a given molecular pulse. If the lineshapes do not match, due to heat deposition on the 100 ms timescale of the measurement, the analysis method described in Chapter 4 must be employed. The laser

calibration is also only valid if the ribbon remained in contact with the sample between the laser and molecular adsorption experiments.

In order to determine what fraction of molecules in each pulse stick to the surface and therefore contribute to the detector signal, a quadrupole mass spectrometer (QMS) without line-of-sight to the sample (King and Well's method³⁶) is used to determine the molecular sticking probability. The sticking probability (S.P.) is determined by simultaneously monitoring a particular mass during the calorimetry experiment. Any molecules that do not stick to the sample surface will result in an increase in the QMS signal. This signal is then calibrated by placing a room temperature gold flag into the beam path, which provides the QMS signal for full deflection of the molecular pulse. The ratio of the area of the two QMS signals provides the fraction of molecules that do not stick (i.e. 1-S.P.). By multiplying the sticking probability by the molecular flux and beam duration, the amount of molecules that contribute to the detector response as a function of coverage is determined.

The moles of gas deposited per pulse as well as the amount of energy per pulse thus provides the heat of adsorption, in kJ/mol, as a function of surface coverage. The absolute accuracy of these measurements is better than 3% as determined by comparing the multilayer heats of adsorption, obtained at 100 K, to bulk heats of sublimation or multilayer desorption energies from TPD. The coverage resolution is determined by the molecular beam flux and pulse duration, both of which can be varied by the experimentalist. Generally a pulse duration of 50-100 ms is used.

The sample temperature is controlled by passing a stream of nitrogen gas through the large copper, thermal reservoir that supports the sample. The temperature of this nitrogen gas stream is controlled by varying the relative flow rates of two gas streams that are passed through

liquid nitrogen and ice water baths and then mixed. The sample temperature cannot be monitored directly, as it is too thin to mount a thermocouple. The sample temperature is therefore determined as the average reading of thermocouples counted on the thermal reservoir and the calorimetry detector housing. This capability allows for the study of adsorption and reaction process over the temperature range 88-300 K.

To interpret the measured energetics in terms of known surface chemistry, further experimental results are generally required, particularly for systems where surface reactions occur following adsorption. The reactions that occur upon molecular adsorption at a particular surface temperature and coverage are often determined by a combination of surface analysis techniques, such as high resolution electron energy loss spectroscopy (HREELS), reflection absorption infrared spectroscopy (RAIRS), x-ray photoelectron spectroscopy (XPS), and TPD. For many of the systems studied with SCAC, the surface chemistry is well established in the literature (e.g. CO and methyl iodide on Pt(111)). However, in the case of *tert*-butyl iodide on Pt(111) discussed in Chapter 3, the chemistry was not known and therefore required the collection of XPS and RAIRS data as a function of surface temperature and coverage as well as density functional theory calculations to help interpret the SCAC results.

2.1 Figures

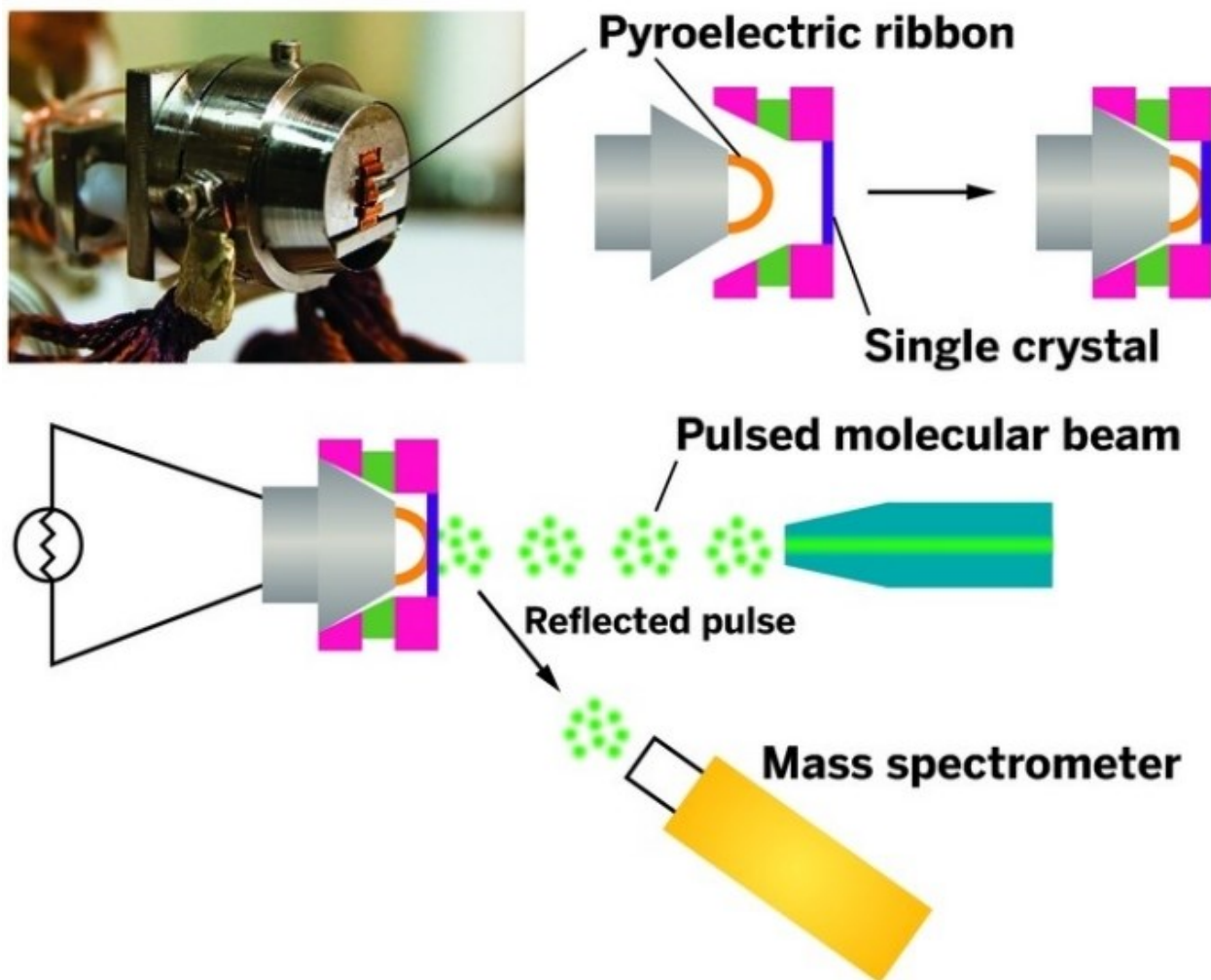


Figure 2.1: Schematic of a single crystal adsorption calorimetry experiment. A pyroelectric polymer ribbon (actual detector ribbon and housing pictured in upper left corner) is placed in mechanical contact with the back of a single crystal metal sample. A pulsed molecular beam is directed at the front sample surface. Molecules that adsorb/react on the sample surface deposit heat, while molecules that do not stick to the surface are detected by a mass spectrometer without line-of-sight to the sample.

Chapter 3

Adsorption Energy of *tert*-Butyl on Pt(111) by Dissociation of *tert*-Butyl

Iodide: Calorimetry and DFT

3.1 Introduction

Hydrocarbon chemistry on transition metal surfaces, particularly Pt(111), has been the subject of numerous studies over the years because of its direct relevance to industrial catalytic processes.^{13,37-40} In the pursuit of ever better, more selective and reactive catalysts, there has been much research aimed at understanding the fundamental details of how the catalyst's surface binds reactants, produces the relevant intermediates via elementary surface reaction steps, and then releases the products. Detailed knowledge of the energetics for the elementary reaction steps involved is essential to understanding reaction mechanisms, why some metals and alloys make better catalysts, and how to design better catalytic materials. One essential challenge is to understand the strength with which late transition metal surfaces bind adsorbed organic fragments at their primary, secondary and tertiary C atoms. We present here the first direct measurement of the enthalpy of formation and metal – surface bond energy for any hydrocarbon fragment bound to any late transition metal single crystal surface via a tertiary C atom, in this case the binding of the *tert*-butyl group ((CH₃)₃C-, referred to throughout as *t*-Bu, to Pt(111). We find a much weaker C-Pt bond than we recently reported for the case of the primary C atom in adsorbed methyl (-CH₃) binding to Pt(111),³² after approximate correction for the additional van der Waals attractions to the three methyl groups on *t*-Bu, estimated using DFT. These data also provide benchmarks for validating the accuracy of theoretical methods used to calculate the energies of adsorbed catalytic intermediates.

Traditional techniques for measuring adsorption energies, such as temperature programmed desorption (TPD) and equilibrium adsorption isotherms, provide reliable results for reversible adsorption processes. However, those techniques are not suitable to determine the thermochemistry of adsorbates or molecular fragments that undergo further decomposition or reaction rather than desorption, as is the case for many catalytically relevant intermediates. To obtain such information, a method called Single Crystal Adsorption Calorimetry (SCAC) was introduced by King et al.,⁴¹ and further developed by Campbell et al..^{8,10,11,42,43} SCAC allows for the direct measurement of heats of adsorption and reaction of gas molecules interacting with a well-defined single-crystal surface. These calorimetric heats, when combined with enthalpies of formation available in the literature, allow for the calculation of enthalpies of formation and bond energies of such adsorbed intermediates.

The chemical bond energy of any given species to a saturated C atom of a hydrocarbon fragment depends strongly upon the number of C nearest neighbors to that C atom (i.e., methyl versus primary, secondary or tertiary).⁴⁴ The bond energy of secondary C atoms to Pt(111) has been measured for the cases of di- σ bound cyclohexene and 2-cyclohexenyl on Pt(111).^{20,31} More recently, the C-Pt bond strength has also been determined for the C in adsorbed methyl (-CH₃) species to Pt(111), produced by the dissociative adsorption of methyl iodide (CH₃I).³² Along this series, the *t*-Bu group is of particular interest as it provides the simplest example of a hydrocarbon bound to a surface through a tertiary carbon, for which no examples exist where the bond energy to Pt(111) or any other surface has been measured. *Tert*-butyl iodide (*t*-BuI) was used here as the parent molecule to produce adsorbed *t*-Bu (*t*-Bu_{ad}), since, as with other alkyl halides,⁴⁵ that molecule is expected to undergo molecular adsorption and facile dissociation to produce *t*-Bu_{ad} and an iodine adatom on the Pt(111) surface. This expectation was based on the

fact that CH_3I readily dissociates on Pt(111) to make adsorbed $-\text{CH}_3$ and an iodine adatom,^{46,47} that the C-I bond in *t*-BuI is even weaker than in CH_3I ⁴⁸, and that *t*-BuI is known to dissociatively adsorb on the Cu(111)⁴⁹ and Ni(100)⁵⁰ surfaces.

In this work, *t*-BuI was dosed onto a clean Pt(111) surface in ultrahigh vacuum (UHV) using a pulsed molecular beam, and its heat of adsorption was measured versus coverage by SCAC at various surface temperatures. The temperature and mechanism of the dissociative adsorption of *t*-BuI on Pt(111) was also studied by photoelectron spectroscopy (XPS), reflection/adsorption infrared spectroscopy (RAIRS) and density functional theory (DFT) calculations, and the surface processes following *t*-BuI adsorption as a function of temperature and surface coverage is proposed based on the combined experimental and theoretical evidence. We found that *t*-Bu_{ad} is produced already at 100 K. To our knowledge, a detailed study of this species on Pt(111) has not been reported. Since the enthalpy of formation of adsorbed iodine adatoms on Pt(111) is already known,⁵¹ these SCAC measurements of the heat of the dissociative adsorption of *t*-BuI provide the enthalpy of formation of adsorbed *t*-Bu and the C-Pt(111) bond energy for this tertiary carbon. We also performed DFT calculations to determine the heats of adsorption of *t*-BuI and the *t*-Bu-Pt bond strength at the corresponding coverages, and found that they agree much better with these SCAC measurements when van der Waals (vdW) interactions are taken into account using the optB86b vdW density functional than when treated at the standard GGA level without vdW corrections. The DFT calculations of these species and other potential reaction products were also used here to help interpret the measured vibrational spectra, and thus help verify the reaction mechanism.

3.2 Experimental

Calorimetry experiments were performed in an ultrahigh vacuum chamber (base pressure $< 2 \times 10^{-10}$ mbar) with capabilities for single crystal adsorption calorimetry and surface analysis, as described previously.^{11,20,31,35} Briefly, the chamber is equipped for SCAC and X-ray photoelectron spectroscopy (XPS), Auger electron spectroscopy (AES), low energy ion scattering spectroscopy (LEIS) and LEED. The sample was a 1 μm thick Pt(111) single crystal foil, supplied by Jacques Chevallier at Aarhus University in Denmark. The sample cleaning procedures that were used in this study are described elsewhere.²⁰ The Pt(111) sample was exposed to a pulsed molecular beam of *t*-BuI; each pulse was 102 ms long and repeated every 5.0 s. After loading *t*-BuI (Alfa Aesar/95%) into a glass reservoir under N_2 atmosphere and subsequent mounting on the vacuum chamber, the liquid was outgassed by five freeze-pump-thaw cycles. Its purity was verified with a mass spectrometer. The *t*-BuI reservoir was surrounded by a stainless steel dewar and aluminum foil at all times to reduce photolysis. The beam was created by expanding ~ 2.0 mbar of *t*-BuI through a microchannel array and then collimated through a series of five liquid nitrogen cooled orifices. Coverages of *t*-BuI are reported here in monolayers (ML) and are defined as the number of *t*-BuI molecules that adsorb onto the surface irreversibly, independent of the actual species they form on the surface following adsorption. We define one monolayer (ML) of adsorbate coverage as being equal to the density of Pt atoms in the Pt(111) surface ($1.50 \times 10^{19} \text{ m}^{-2}$). A typical *t*-BuI pulse is 0.0019 ML ($\sim 4 \times 10^{11}$ molecules). A more detailed description of the experimental principles and implementation of the molecular beam can be found elsewhere.^{31,35} The flux of *t*-BuI from the molecular beam is measured by impinging the beam onto a liquid nitrogen cooled quartz crystal

microbalance (QCM) precovered with multilayers of *t*-BuI. Calibration of the QCM has been described previously.³⁵

The heat released from the adsorption of one *t*-BuI pulse to the sample surface is measured with a pyroelectric polymer ribbon gently pressed against the back of the Pt(111) foil, using the procedures described previously.^{19,20} The sensitivity of the pyroelectric detector was calibrated after each experiment by depositing light pulses of a known amount of energy into the sample using a HeNe (632.8 nm) laser.³⁵ The absolute accuracy of the calorimetric heats, after averaging >5 runs, is estimated to be better than 3% for systems like those studied here, which have sticking probabilities above 0.8, based on comparisons to literature values for standard enthalpies of sublimation of the bulk solid when forming solids with known enthalpies.¹⁹ (This error is due to possible errors in the absolute flux, heat signal calibrations and literature values). Relative measurements (e.g. differences in heat with increasing coverage) are much more accurate, due to the high precision in heat measurements within an experiment.

If the molecular adsorption/reaction process occurs on a time scale of ~10 ms or less, the heat signal lineshapes measured during molecular pulses and laser pulses are identical, allowing for the comparison of the peak heights or slopes of the initial fast rise to extract the deposited energy from a molecular pulse. If some portion of the heat deposition is on the timescale of 10-1000 ms, a noticeable broadening of the detector response line shape occurs and the heat signal must be deconvoluted as described previously³⁴. If some of the heat deposition occurs on a time scale much slower than the beam pulse repeat period, its signal contribution becomes completely demodulated and can be ignored. In the measurements described below of the heat of adsorption of *t*-BuI on Pt(111) at 100 K and 120 K, a secondary heat deposition process led to a slight broadening of the pulse shape, but that occurs with a time constant >400 ms, which is

sufficiently slow compared to the pulse duration of 100 ms to not affect the short-time heat signals or their lineshapes reported and analyzed here. The heats of adsorption presented in this study were calculated using the “slopes method”³¹ and therefore represent only the heat deposited instantaneously upon adsorption.

The calorimeter was mounted on top of a large thermal reservoir cooled by passing a stream of dry nitrogen gas first through coils of Cu tubing immersed in a liquid nitrogen bath (77 K) and then through the reservoir that is in thermal contact with the sample. By controlling the rate of nitrogen gas flow, we were able to obtain the desired sample temperature. We were not able to directly measure the temperature of the thin platinum sample because mounting thermocouples directly to such a thin sample would destroy it. Instead, we measured both the temperatures of the holder of the pyroelectric ribbon (A), which is in thermal contact with the backside of the sample holder, and the directly cooled thermal reservoir (B) in thermal contact with the front side of the sample holder using Type K thermocouples that had been spot welded in place. The average of these two temperatures was used to estimate the sample temperature; typical differences between A and B were ~ 35 K. The sample temperatures used in this study were 100 and 120 K.

The Pt(111) surface was exposed to a chopped molecular beam of *t*-BuI, and the sticking probabilities and the heats of adsorption were measured as a function of *t*-BuI coverage. Sticking probabilities were measured simultaneously with calorimetric measurements using the King and Wells method.³⁶ A mass spectrometer, without line-of-sight to the sample, was used to measure the background pressure increase of *t*-BuI ($m/z = 57$) in the chamber. A room-temperature gold flag was positioned in front of the sample and used to determine the mass spectrometry signal corresponding to full reflection of *t*-BuI. The sticking probability of *t*-BuI

was calculated by comparing the integrated mass spectrometer signals measured from the increase in *t*-BuI partial pressure above background from molecular beam pulses onto the sample surface and onto the inert Au flag. We report two types of sticking probabilities: The long-term sticking probability, which is defined as the probability that molecules in a gas pulse stick on the surface for the time until the next pulse arrives, and the short-term sticking probability, which is defined as the probability that molecules in a gas pulse stick on the surface until the end of the ~140 ms time period used to measure the heat signal.³¹ The long-term sticking probability is used to calculate the coverage at the start of the next pulse, and the short-term sticking probability is used to convert short-term heat signals to adsorption energies per mole adsorbed.³¹

XPS measurements were performed in the same chamber using a standard Al K α source (1486.6 eV, 175 W). Photoelectrons were collected using a hemispherical analyzer (Leybold-Heraeus EA10) with a single channel detector using 50 meV steps and pass energy of 150 eV. Measurements were performed while keeping the Pt(111) temperature at 100 K and 300 K after dosing 0.067 ML of *t*-BuI using the pulsed molecular beam. This coverage falls in the high heat region of the calorimetry experiments where dissociative adsorption occurs (see Results and Discussion). Analysis of the I_{3d} peaks to obtain the corresponding binding energy was performed by first subtracting the portion of the spectrum for the clean Pt(111) sample as background to eliminate the contribution from the Pt_{4p} peak and then fitting to a mixed Gaussian-Lorentzian (70:30) lineshape.

Reflection-absorption infrared spectroscopy (RAIRS) was performed in a separate UHV chamber (base pressure < 2 x 10⁻¹⁰ mbar) described previously^{52,53}. The Pt(111) sample was cleaned in the preparation chamber by sputter-anneal cycles and thermal treatments with O₂ to burn any remaining surface carbon contaminants. The sample was then transferred to the RAIRS

position and dosed with *t*-BuI (Aldrich, >95%) by increasing the background pressure for the required amount of time while maintaining the surface at 100 K. IR spectra were collected in situ under UHV by passing the IR beam through NaCl windows and using a grazing ($\sim 85^\circ$ incidence and reflected angles) geometry. Signal detection was done by using a narrow-band mercury-cadmium-telluride (MCT) detector. All spectra were acquired by averaging the data from 2000 scans taken at a resolution of 4 cm^{-1} and normalized to a spectrum from the clean sample obtained in the same way but before gas dosing. Spectra were taken with both s- and p-polarized light to discriminate between gas-phase and adsorbed species^{54,55}. For annealing/desorption measurements, the sample was heated to the required temperature and IR spectra collected upon returning to the cryogenic temperature.

3.3 Density Functional Theory Calculations

Periodic DFT calculations were performed using the Vienna Ab Initio Simulations Package (VASP)⁵⁶⁻⁵⁸ in the generalized gradient approximation (GGA-PBE)⁵⁹. Core electrons were described by the projector augmented wave (PAW) method^{60,61} (Pt, 230 eV cutoff; I, 176 eV cutoff; C, 400 eV cutoff; and H, 250 eV cutoff) and the Kohn-Sham valence states (including Pt(5d6s); I(5s5p); C(2s2p); and H(1s)) were expanded in a plane wave basis set up to a kinetic energy of 400 eV. The electronic states were smeared using a first-order Methfessel-Paxton scheme with a width of 0.075 eV.⁶² All total energies were extrapolated back to 0 K. Van der Waals (vdW) interactions were treated self-consistently using the optB86b vdW density functional (vdW-DF) developed by Klimeš et al. We chose the optB86b vdW functional because it is based on the self-consistent treatment of the non-local electron correlation that gives rise to dispersion interactions, a scheme originally proposed by Dion et al..³⁹ Other methods that have been proposed recently to remedy DFT include dispersion interactions via the approximate,

pairwise interactions of the form C_6R^{-6} , which is much less rigorous.^{63,64} For comparison, the experimental, PBE, and optB86b bond energy of the tertiary C-H bond in isobutane is 400⁴⁸, 365, and 393 kJ/mol, respectively; and that of the C-I bond in *t*-BuI is 227⁴⁸, 230, and 257 kJ/mol, respectively. The gas-phase species were calculated in a cubic unit cell 20 Å per side.

The calculated lattice constant for Pt is 3.978 Å in PBE and 3.958 Å in optB86b vdW-DF, both in close agreement with experiment (3.92 Å⁶⁵). The Pt(111) surface was modeled using both a (3×3) and a (4×4) surface unit cell, each with four metal layers, corresponding to 1/9 and 1/16 monolayer (ML) of coverage for each adsorbate per unit cell, and the Brillouin zone was sampled on a 5×5×1 and 3×3×1 Monkhorst-Pack *k*-point mesh, respectively. A vacuum space of ~16 Å was included in the *z* direction to minimize interactions of neighboring images, together with electrostatic decoupling in the *z* direction.⁶⁶ The top two layers of metal were fully relaxed, with the bottom two fixed at bulk positions. All geometric optimization was converged to 0.01 eV/Å for each relaxed degree of freedom. Spin polarization was checked and found to be negligible for all of the surface species in this study.

Adsorption energies were calculated as $\Delta E = E_{\text{slab}} + E_{\text{mol}} - E_{\text{total}}$, where E_{slab} , E_{mol} , and E_{total} are the energies of the clean surface without any adsorbate, the adsorbate molecule isolated in the gas phase in a neutral state (closed-shell or radical), and the surface with the adsorbate. A more positive ΔE therefore corresponds to stronger adsorption. The convergence of the adsorption energies with respect to parameters including the valence state cutoff energy, *k*-point sampling density, and number of metal layers in the Pt(111) slab was verified. See Appendix for the results of the convergence tests.

The minimum-energy reaction path for an elementary step and the transition state (TS) associated with it were determined using a combination of the climbing-image nudged elastic

band (CI-NEB) method⁶⁷ and the dimer method.⁶⁸ The activation energy was calculated as $E_a = E_{\text{TS}} - E_{\text{IS}}$, where IS and TS denote the initial state and transition state, respectively. Each TS was verified to possess only one vibrational mode with imaginary frequency in the direction of the bond being broken or formed. The simulated IR spectra of surface adsorbates were calculated using the Atomic Simulation Environment.⁶⁹ The vibrational modes and frequencies were calculated in the harmonic oscillator approximation from a finite difference approximation of the dynamical matrix, and the IR intensities were calculated from a finite difference approximation of the gradient of the dipole moment in the z direction.⁷⁰ The magnitude of the displacement was 0.01 Å in each relaxed degree of freedom. We verified that the choice of the two different functionals makes no material difference in the simulated IR spectra in the range of frequencies of primary interest in this study (1000~1600 cm⁻¹). Simulated IR spectra have been used fruitfully before to identify adsorbate species on a variety of surfaces.⁷¹⁻⁷³ The zero point energies (ZPE) were calculated from the vibrational frequencies (ν_i) of a molecule as

$$E^{\text{ZPE}} = \frac{1}{2} \sum_i h\nu_i$$

3.4 Results and Discussion

3.4.1 XPS and RAIRS: chemistry of adsorbed *t*-butyl iodide on Pt(111)

We present first the XPS and RAIRS spectra obtained following *t*-BuI adsorption on Pt(111) in the submonolayer to multilayer coverage regimes at temperatures between 100 and 300 K as well as the supporting DFT calculations. From these, we find a temperature at which *t*-BuI undergoes dissociative adsorption to form *t*-Bu_{ad} and atomically adsorbed iodine (I_{ad}).

It has been previously shown that the I_{3d} peak's position in XPS can be used to distinguish between intact and dissociated vinyl and alkyl iodide species on Pt(111).^{74,47,75,76}

Figure 3.1 shows XPS spectra of the I_{3d} peak after exposure to *t*-BuI at 100 K and at 300 K for a coverage of 0.067 ML, as determined from the sticking probability measurements discussed in a following section. The two spectra are indistinguishable within our experimental error, demonstrating that the same species exists at both temperatures. As seen in Fig. 3.1, an I_{3d} peak position of 619.4-619.5 eV was observed at both temperatures. For these spectra, the Pt(111) sample was grounded and the binding energy (BE) scale was calibrated using the Pt $4f_{7/2}$ (BE= 70.9 eV⁷⁷) and Cu $2p_{3/2}$ (BE= 932.4 eV⁷⁷) peaks for pure Pt and Cu.

For methyl iodide on Pt(111), the I_{3d} peaks appear at 1.0 eV higher binding energy (BE) for molecularly adsorbed CH_3I than for the C-I dissociated species (i.e, $I_{ad} + CH_{3,ad}$): 620.3 vs. 619.3 eV,⁴⁷ or at 620.8 vs. 619.8 eV,⁷⁵ as measured by different authors. Similarly, Liu et al.⁷⁴ measured the I_{3d} spectra for molecularly adsorbed vinyl iodide and iodine adatoms from this dissociated species on Pt(111) as 619.9 and 619.0 eV BE, respectively, and Zaera et al. reported BE values of 620.2 and 619.3 eV for molecularly adsorbed ethyl iodide and for the dissociated species (i.e., I_{ad} plus surface ethyl groups), respectively.⁷⁸ The *t*-BuI molecule has not been previously measured on Pt(111), but a similar study of *t*-BuI on Cu(111) yielded an I_{3d} peak at 618.8-619.0 eV BE for iodine adatoms, and at 620.5 eV BE for the un-dissociated molecule.⁴⁹ It should be indicated that the Pt and Cu peak positions used for BE scale calibration in these literature sources were the same as those used here (listed above), for the cases where they were reported.⁴⁷ The above literature indicates that I_{ad} on Pt(111) should have a peak position of 619.0-619.8 eV (average of 619.4 eV) BE, with ~1.0 eV higher BE for undissociated alkyl iodides. Clearly, the 619.4 eV BE observed in the spectrum in Fig. 3.1 at 100 K indicates that C-I bond dissociation has already occurred at 100 K for *t*-BuI and that I is in the form of I_{ad} already.

Methyl iodide is known to dissociate readily on Pt(111) above 240 K to form adsorbed methyl and atomically adsorbed iodine.^{46,47} This is consistent with our observation that C-I bond scission in *t*-BuI_{ad} on Pt(111) occurs readily already at 100 K, since the C-I bond in *t*-BuI gas is much weaker than in methyl iodide gas.⁴⁸ Our observation that *t*-BuI dissociates already at 100 K on Pt(111), based on the position of the I_{3d} XPS peak, is consistent with the study of *t*-BuI/Cu(111) where dissociation also occurs below 100 K.⁴⁹ The XPS results therefore indicate that calorimetry experiments performed at 100 K (discussed below) provide the heat of reaction of dissociative adsorption, at least up to a coverage of 0.067 ML.

The appearance of adsorbed species on Pt(111) upon *t*-BuI exposure at varying surface coverages and sample temperatures was independently studied using RAIRS. Figure 3.2 shows the corresponding spectra for increasing doses of *t*-BuI at 100 K for both the C-C stretches of the central carbons (1000-1600 cm⁻¹) and the C-H stretching region (2700-3300 cm⁻¹). The first feature that appears as a function of coverage is a small peak at 1065 cm⁻¹. This peak is visible in the 1 L spectrum and remains present at higher coverages. Upon increasing coverage, another peak at 1113 cm⁻¹ becomes visible at 3 L and saturates by 5 L. Additional peaks (1140, 1232, 1370, and 1455 cm⁻¹) emerge at 3 L and continue to grow with increasing exposure.

With an initial dose of 5 L at 100 K, the Pt(111) sample was heated and the RAIRS signal monitored to observe the species that remain on the surface as desorption occurs (Fig. 3.3). These heating experiments were performed for a dosage where molecular adsorption is present but not large amounts of multilayer material. The small shoulder at 1140 cm⁻¹ disappears between 100 and 120 K. This is followed by a decrease in the peak at 1113 cm⁻¹ between 120 and 150 K and its complete disappearance between 150 and 200 K. Concurrently, the 1065 cm⁻¹ peak intensity increases between 120 and 200 K.

Assignment of the IR absorption bands for all the possible adsorbed species associated with the *t*-BuI/Pt(111) system could not be performed directly since these species have not, to our knowledge, been studied before, although experimental data exists for liquid *t*-BuI⁷⁹ and for the *t*-butyl cation.^{80,81} DFT calculations were therefore performed to generate the IR spectra of the relevant adsorbed species on Pt(111) for comparison to experiments (Figs. 3.2-3). The spectrum for each species was generated using the energy-minimized structure for that species. Molecularly and dissociatively adsorbed *t*-BuI, the latter including *t*-Bu_{ad} + I_{ad} and isobutene (*i*-butene_{ad}) + H_{ad} + I_{ad}, were calculated at 1/9 and 1/16 ML, respectively, following the experimental findings (see below) that molecular adsorption of *t*-BuI occurs above ~0.1 ML, while *t*-BuI adsorbs dissociatively below 0.07 ML. The energy-minimized structures for these three adsorbed states are shown in Fig. 3.4, and the corresponding simulated IR spectra are shown in Fig. 3.5. The *t*-BuI_{ad} produces a major peak at 1084 cm⁻¹ and a smaller peak at 1338 cm⁻¹. Adsorbed *t*-Bu + I gives peaks at 1070 cm⁻¹ and 1430 cm⁻¹. Adsorbed isobutene and hydrogen and iodine adatoms (*i*-butene_{ad} + H_{ad} + I_{ad}) produce peaks at 1019, 1051 and 1424 cm⁻¹. Peak positions were also determined for gas-phase *t*-BuI as an approximation for a weakly adsorbed multilayer, and were found at 1122, 1215, 1351 and 1441 cm⁻¹.

Based on these calculations, the peak observed experimentally by RAIRS at 1065 cm⁻¹ can be assigned to dissociated *t*-BuI molecules yielding either *t*-Bu_{ad} + I_{ad} or *i*-butene_{ad} + H_{ad} + I_{ad}. (The corresponding DFT-calculated C-C stretch mode for *t*-Bu_{ad} is 1070 and for *i*-butene_{ad} are 1019 and 1051 cm⁻¹). The RAIRS spectra for *i*-butene on clean Pt(111) contains a strong peak at a similar position of 1062 cm⁻¹,⁸² which Avery et al. suggested to be due to the di-σ state of *i*-butene.⁸³ However, we choose to assign this peak at 1065 cm⁻¹ to *t*-Bu_{ad} for the following reasons. (1) We do not see a second, lower wavenumber peak in our experimental data. The

IR/VEELS spectra for di- σ bound ethylene on Pt(111) shows two strong peaks at 991/980 and 1048/1040 cm^{-1} ,⁸² and that is consistent with the IR spectrum for di- σ bound *i*-butene calculated here using DFT, which shows two peaks at 1019 and 1051 cm^{-1} (symmetric and asymmetric C-C stretch modes, respectively). (2) To create *i*-butene_{ad}, it is necessary to remove a hydrogen from one of the methyl side groups of *t*-Bu_{ad}. The energy barrier for the breaking of the C-H bond in methyl side groups of adsorbed hydrocarbons on Pt(111) has been shown to be sufficiently high that the rate of this process would be negligible at 100-120 K, the temperature used in these experiments. For instance, RAIRS studies with 1-iodobutane on Pt(111) have shown that in that case the C-I bond breaks at about 200 K, at which point a 1-butyl surface species is formed, and that β -hydride elimination to produce adsorbed butene only occurs at 270 K (although with 2-iodobutane the respective temperatures are much lower, 160 and 170 K respectively).⁸⁴

To further address point (2) above, CI-NEB and dimer calculations were performed to probe the activation energy barriers for the C-I bond scission in *t*-BuI and for the C-H bond scission in *t*-Bu_{ad} (here with co-adsorbed I) on the Pt(111) surface. These calculations showed that the barrier for the C-I bond breaking process is low (optB86b/PBE: 31/26 kJ/mol without ZPE; 24/18 kJ/mol with ZPE; see Fig. 3.4(f) for snapshots of the transition state), consistent with our experiments showing dissociation already at 100 K. The removal of H from a *t*-Bu group adsorbed on Pt(111) was found to have a much larger barrier (102/103 kJ/mol without ZPE; 89/90 kJ/mol with ZPE; see Fig. 3.4(g) for snapshots of the transition state), in agreement with point (2) above. However, our calculations also suggested that immediately following the C-I bond scission in *t*-BuI, two processes can occur with no additional energy barrier. Either the *t*-Bu fragment adsorbs on the Pt(111) surface *or* hydrogen is removed via a β -hydride elimination step to form *i*-butene_{ad} and H_{ad}. The selectivity of these two processes may depend on site

availability and on detailed curve crossing barriers. Based on the RAIRS and DFT calculations alone, therefore, we cannot completely rule out the formation of *i*-butene upon dissociative adsorption of *t*-BuI at 100 K. As noted above, we assign the low coverage dissociative adsorption process here to the formation of $t\text{-Bu}_{\text{ad}} + \text{I}_{\text{ad}}$ when analyzing our calorimetry data for 100 and 120 K below, since C-H bond cleavage has never been observed experimentally at such low temperature on Pt(111) to our knowledge.

At an exposure of 3 L, the peak at 1113 cm^{-1} grows and ultimately saturates by a dose of 5 L. Our calorimetry results (Fig. 3.7, see below) show that molecular adsorption occurs at higher coverages when at and below 120 K. We therefore assign the peak at 1113 cm^{-1} , which remains upon heating to 120 K (Fig. 3.3), to molecularly adsorbed *t*-BuI in the first and second layers. The peak position calculated for adsorbed *t*-BuI by DFT is 1084 cm^{-1} , 29 cm^{-1} lower than the experimental value. Subsequently, the growth of peaks at 1140, 1232, 1370, and 1455 cm^{-1} at exposures of 5 L and higher can be assigned to multilayer, bulk-like growth of *t*-BuI (solid). The disappearance of these multilayer peaks between 100 and 120 K is consistent with the lack of multilayer growth in our calorimetry experiments at 120 K (Fig. 3.6, see below). These peak positions are slightly higher than the DFT calculated peaks for gaseous *t*-BuI (1122 , 1215 , 1351 , and 1442 cm^{-1}), but match well with the main experimentally observed peaks for liquid *t*-BuI (1133 , 1230 , 1367 , and 1452 cm^{-1}),⁷⁹ consistent with the condensed state of the adsorbed molecules.

Heating of the Pt(111) sample to 150 K following an exposure of 5 L of *t*-BuI results in a decrease of the peaks associated with molecularly adsorbed *t*-BuI (e.g. 1113 cm^{-1}) and an increase in the 1063 cm^{-1} peak assigned to adsorbed *t*-Bu fragments. This can be explained by

further dissociation of $t\text{-BuI}_{\text{ad}}$ following the freeing of surface sites upon desorption of $t\text{-BuI}_{\text{ad}}$ and/or surface diffusion of adsorbed species.

3.4.2 Sticking Probability

The sticking probability for $t\text{-BuI}$ molecules on Pt(111) was measured simultaneously with the heats of adsorption. The sticking probability determines the fraction of the molecules from each pulse that adsorb on the sample surface. As described previously,³¹ we measured both the short-term and the long-term sticking probabilities versus coverage. The short-term sticking probability (not shown), observed to be unity at all coverages at 100 and 120 K, was used to calculate heats of adsorption per mole adsorbed. The long-term sticking probability, used to calculate the coverage at the start of the next pulse, is shown in Fig. 3.6. The assignment of the coverage for the completion of the first layer, indicated by a vertical line in Fig. 3.6, was determined using the heat of adsorption data (Fig. 3.7) discussed in the following section, where this transition is quite clear. The high initial sticking probability indicates a precursor-mediated adsorption mechanism. At 100 K, the molecules stick to the surface as well as to the multilayer with unit probability. In contrast, at 120 K, this sticking probability is near unity in the first layer and most of the second layer, but decreases sharply starting at ~ 0.33 ML and reaches zero by 0.43 ML. The completion of the second layer is estimated as the midpoint of this transition, or 0.38 ML, where this sticking probability is 0.5. This observation that the multilayer can be populated at 100 K but not at 120 K agrees with the temperature-dependent RAIRS data that showed the disappearance of the peak due to multilayer adsorption between 100 and 120 K.

3.4.3 Heats of Adsorption

Figure 3.7 shows the heat of adsorption of $t\text{-BuI}$ on Pt(111) at 110 ± 10 K as a function of $t\text{-BuI}$ coverage. The y axis represents the standard enthalpy of adsorption at each temperature

(corrected slightly from the raw heat measurements to adjust for the difference in gas and surface temperatures and to convert from energy to enthalpy, as described previously³¹). The sign convention is, however, reversed so that a positive heat of adsorption here represents an exothermic process. Experiments were performed at sample temperatures of 100 and 120 K (3 and 4 runs, respectively), but we could see no significant difference in heat versus coverage up to 0.34 ML, so we have averaged all seven runs here. The heat of adsorption of *t*-BuI on Pt(111) begins at 247 kJ/mol (first data point) and decreases monotonically to 219 kJ/mol at 0.05 ML. This is followed by a sharp decrease between 0.05 and 0.09 ML, and a slower decrease between 0.09 and 0.15 ML, until reaching a heat of 49 kJ/mol at 0.15 ML. The heat of adsorption thereafter remains nearly constant up to 0.35 ML, with an average value of 44.5 ± 1.9 kJ/mol in this second-layer range from 0.15 to 0.35 ML. The average heat of adsorption observed at 100 K for multilayer coverages (from 0.38 to 0.56 ML) was ~ 38 kJ/mol.

There is no evidence at low coverage of the contribution of defect sites to a higher initial heat. This is consistent with our prior estimates that the defect density of our Pt(111) sample is below 1% ML.³²

Molecular adsorption of methyl iodide on Pt(111) at 95 K has an initial heat of adsorption of 97 kJ/mol.²⁰ Our DFT calculations indicate that *t*-BuI binds to the Pt(111) surface through its iodine atom (Fig. 3.4(a)), as also seen for methyl iodide on Pt(111).⁴⁶ The initial heat measured here of 247 kJ/mol is far too high to be attributed to molecular adsorption (which DFT calculations estimate to require only approx. 140 kJ/mol, see below), but is consistent with the XPS and RAIRS data which show that *t*-BuI initially dissociates to make *t*-Bu_{ad} plus I_{ad}. The heat deposition process at 100-120 K and low coverage (0-0.05 ML) is therefore attributed to the reaction:



As indicated by the RAIRS results, we assign the second region in Fig. 3.7 (0.09-0.15ML) to molecular adsorption in the first layer given by



The decrease in adsorption energy with coverage is consistent with calorimetry experiments of methyl iodide adsorption on Pt(111) at 95 K, where a linear decrease in the molecular heat of adsorption was observed with increasing coverage due to lateral adsorbate-adsorbate repulsions.²⁰

The sharp decrease in heat of adsorption between 0.05-0.09 ML in Fig. 3.7 is attributed to the switch from dissociative to molecular adsorption in the first layer. There is probably a step-function decrease in heat when this occurs, which is broadened here by heterogeneity in the local surface coverage across the surface. We therefore estimate the saturation coverage for the dissociative adsorption process as the steepest part of this curve, which occurs at 0.07 ML (marked by the dotted line in Fig. 3.7). While this seems a low coverage, it should be noted that I_{ad} and $t\text{-Bu}_{\text{ad}}$ are estimated to occupy 3 and 4 Pt atoms, respectively (see below), meaning that 50% of the Pt surface atoms are already covered by adsorbates. Thus between 0.07 and 0.15 ML, additional $t\text{-BuI}$ molecules cannot find enough free sites to dissociate, although they do bond directly to the remaining Pt atoms. The average heat between 0.07 and 0.15 ML is 91 kJ/mol. The constant, smaller heat (45 kJ/mol) above 0.15 ML (dashed line in Fig. 3.7) is assigned to molecular adsorption in the second layer. This nearly constant heat in the second layer suggests island formation. This heat is very similar to the sublimation enthalpy (see below).

The first layer is completed at a coverage of 0.15 ML. DFT calculations show that iodine adatoms preferentially adsorb in fcc sites and *t*-Bu groups preferentially adsorb at atop sites, with each species occupying a minimum of 3 and 4 surface Pt atoms respectively (Fig. 3.4(b)). The occupation of 3 Pt atoms for adsorbed iodine is consistent with the ($\sqrt{3} \times \sqrt{3}$) R30° structure that gives a saturation coverage of I_{ad} of 0.33 ML.⁵¹ The binding geometry of adsorbed, intact *t*-BuI molecules (Fig. 3.4(a)) allow a packing density of 1 molecule per 6 surface Pt atoms, assuming that the distance between iodine atoms in adjacent *t*-BuI adsorbates is equal to or greater than in the ($\sqrt{3} \times \sqrt{3}$) R30° structure for adsorbed atomic iodine and that the methyl groups in *t*-BuI cannot occupy Pt atoms already occupied by iodine atoms in neighboring molecules. We can use these Pt atom occupation numbers ($t\text{-Bu}_{ad} = 4$, $I_{ad} = 3$, $t\text{-Bu}I_{ad} = 6$) along with the respective coverage of each species estimated from Fig. 3.7 at completion of the first layer ($t\text{-Bu}_{ad}$ and $I_{ad} = 0.07$ ML each, and $t\text{-Bu}I_{ad} = 0.08$ ML) to estimate the total number of occupied Pt atoms in the completed first layer. This gives 0.98 as the fractional occupancy of Pt atoms. This explains why the first layer on the Pt(111) surface saturates at a total coverage of 0.15 ML. This is consistent with the saturation coverage of 0.20 reported for molecularly adsorbed n-butane on Pt(111).⁸⁵ The larger coverage in the second layer (0.23 ML) is reasonable, since the molecules are not dissociated and are not required to adsorb with their iodine atoms aligned toward the surface, nor is their packing restricted by the surface Pt atom geometry. Using the density of bulk liquid *t*-BuI (1.571 g/cm³)⁸⁶ and assuming closest packing of spheres gives an effective molecular diameter of 0.650 nm. A closest-packed plane of such spheres has a packing density of 2.73×10^{14} molecules / cm², or 0.18 ML, 22% below that estimated for the second layer (0.23 ML). Denser packing may result from the atomic-scale roughness of the first layer consisting of $t\text{-Bu}_{ad}$, I_{ad} and $t\text{-Bu}I_{ad}$.

The sticking probability data (Fig. 3.6) and heat of adsorption data (Fig. 3.7) have therefore been divided into four coverage regions at 100 K: (1) 0 to 0.07 ML, where *t*-BuI adsorbs dissociatively on Pt(111) to form *t*-Bu_{ad} and I_{ad} species, with an integral heat of reaction of 223 kJ/mol, (2) 0.07-0.15 ML, where *t*-BuI adsorbs molecularly on Pt(111) with an average heat of adsorption of 91 kJ/mol, (3) 0.15-0.43 ML, where *t*-BuI adsorbs molecularly on top of the saturated first layer with an average heat of adsorption of 45 kJ/mol and (4) >0.43 ML, where *t*-BuI adsorbs molecularly in the true multilayer regime (~38 kJ/mol).

The heat of molecular adsorption decreases rapidly with coverage in region (2) between 0.07 and 0.15 ML total coverage (Fig. 3.7). To compare with DFT results below, we use the data of Fig. 3.7 to estimate the heat of adsorption expected if *t*-BuI were to adsorb without any dissociation (e.g., at temperatures well below 100 K). If it is assumed that the heat of adsorption below 0.09 ML stays constant at the same value as at 0.09 ML, an integral heat of adsorption of 101 kJ/mol is estimated at 1/9 ML. If instead it is assumed that the heat of adsorption below 1/9 ML continues to decrease with the same slope as the short, nearly linear region in Fig. 3.7 between 0.09 ML and 0.15 ML, this linear extrapolation leads to an initial heat of adsorption of 187 kJ/mol and gives an integral heat of adsorption at 1/9 ML of 135 kJ/mol. This latter assumption of a linear decrease with coverage is supported by the measured heat of molecular adsorption of methyl iodide on Pt(111), which was found to decrease linearly by 17 kJ/mol over the first 0.15 ML,²⁰ so this larger value is probably a better estimate. If these limits are subtracted from the integral heat of dissociative adsorption at 0.07 ML, an estimate is obtained for the heat for the dissociation of adsorbed *t*-BuI (i.e., $t\text{-BuI}_{\text{ad}} \rightarrow t\text{-Bu}_{\text{ad}} + \text{I}_{\text{ad}}$) of between 69 and 120 kJ/mol, exothermic, averaged over the coverage range up to ~0.07 ML, with the smaller value probably more accurate.

To determine whether our measured heats of adsorption are reasonable, a comparison can be made between our multilayer heat of ~ 38 kJ/mol and the enthalpy of sublimation of 49.8 kJ/mol reported for bulk *t*-BuI solid in the 202-223 K temperature range.⁸⁷ To our knowledge, there is no literature data available for 100 K, and its difference between that at 213 K could be quite large, especially if a more ordered solid is made at the higher temperature. White and Henderson⁸⁸ studied *t*-BuI on rutile TiO₂(110) and showed a second-layer TPD peak maximum at 150 K. A simple Redhead analysis of this, assuming a pre-exponential factor of 10^{16} s⁻¹ based on our entropy correlation⁸⁹ (using the gas-phase entropy for neopentane⁹⁰ to approximate that of *t*-BuI, which was not available in the literature) yields an activation energy of 47 kJ/mol for second layer desorption. This is within <1 kJ/mol of the error range of our enthalpy of adsorption in the second layer of 44.5 ± 1.9 kJ/mol.

3.4.4 Standard enthalpy of formation of adsorbed *t*-butyl and (CH₃)₃C-Pt(111) bond enthalpy

The heats measured in Fig. 3.7 at low coverage (up to 0.07 ML) represent the heat of reaction (1), the dissociative adsorption of *t*-BuI to make *t*-Bu_{ad} plus I_{ad}. Standard enthalpies of formation available in the literature can be used with the simple thermodynamic cycle shown in Fig. 3.8 to convert the measured heat of reaction to the standard enthalpy of formation and C-Pt(111) bond enthalpy for adsorbed *t*-Bu.

Starting from the elements in their standard state, we can follow the bottom path in Fig. 3.8 to first make the gas-phase *t*-BuI molecule and then dissociatively adsorb it on the Pt(111) surface. The first step corresponds to the standard enthalpy of formation for gaseous *t*-BuI, for which there are two reported experimental values: $-72. \pm 1.$ and -68.5 ± 2.6 kJ/mol;^{91,92} the value of $-72. \pm 1$ kJ/mol adopted by NIST³² is used here. The second step corresponds to our measured

integral heat of dissociative adsorption for 0.04 ML of *t*-BuI on the surface (Fig. 3.7) of 240 kJ/mol.

The direct central path from left to right in Fig. 3.8 corresponds to the enthalpy of formation of the adsorbed fragments resulting from the dissociation of *t*-BuI. This direct path is equal to the sum of the two bottom steps (-312 kJ/mol). Subtracting the value for the standard enthalpy of formation of 0.04 ML of atomic iodine adsorbed on Pt(111) of -144 ± 20 kJ/mol (obtained from the integral desorption energy at 0.04 ML of iodine from Pt(111) of 251 ± 20 kJ/mol⁵¹ and the standard enthalpy of formation of the iodine radical in the gas phase of 106.76 ± 0.04 kJ/mol⁹³) gives the standard enthalpy of formation of *t*-Bu_{ad}, $\Delta H_f(t\text{-Bu}_{ad}) = -168 \pm 20$ kJ/mol at 0.04 ML.

To obtain the bond enthalpy between the ternary carbon in *t*-Bu and the Pt(111) surface (D((CH₃)₃C-Pt)), the upper reaction path in Fig. 3.8 must be followed. The standard enthalpy of formation for the gaseous *t*-butyl radical has been previously reported,^{94,95} and the standard enthalpy of formation of adsorbed atomic iodine has been calculated above. Closing the cycle gives $D((\text{CH}_3)_3\text{C-Pt}) = 216 \pm 20$ kJ/mol at 0.04 ML.

Similarly, the standard enthalpy of formation of adsorbed *t*-butyl and the Pt(111)-C(CH₃)₃ bond enthalpy at the limit of zero coverage were determined as -177 ± 9 kJ/mol and 225 ± 9 kJ/mol respectively. These numbers were obtained using the zero-coverage limit heat of adsorption (253 ± 7 kJ/mol) measured here along with the enthalpy of formation of I_{ad} at zero coverage (-148 ± 5 kJ/mol calculated as above but using the desorption energy of I_{ad} extrapolated to zero coverage of 255 ± 5 kJ/mol⁵¹).

Here, it was assumed that, for our measured heats of reaction, the heat capacities of the reactants in the gas phase and the adsorbed products are similar. With this assumption, the

heats of reaction measured here are independent of temperature, and can be used in thermodynamic cycles (Fig. 3.8) with literature values reported at 298 K.

3.4.5 Comparison of Reaction Energies to DFT

The experimental heats of reactions (1) and (2) and the *t*-Bu-Pt bond enthalpy are compared next to values calculated using two different DFT treatments in Table 3.1. For direct comparison of the experimental values to DFT, it is necessary to use the integral heat at the coverage that corresponds to the unit cell size (e.g. 1/16 ML) used in the calculations. The measured heats of reaction and bond enthalpies were converted to reaction energies and bond energies for comparison to DFT here by subtracting RT (i.e. for exothermic processes, the magnitude decreases by RT). Note again that positive values represent an exothermic process. Also included are the reaction energies for *t*-BuI adsorbing to make adsorbed *i*-butene + H + I and the H-Pt and I-Pt bond energies as calculated from DFT. The experimental integral heat of reaction (1) (i.e., dissociative adsorption into *t*-Bu_{ad} and I_{ad}) at 1/16 ML is 230 kJ/mol, equivalent to a reaction energy of 229 kJ/mol, exothermic. Upper and lower bounds for the experimental integral heat of reaction (2) (i.e., molecular adsorption) at 1/9 ML were estimated as described above as 101 to 135 kJ/mol, with the larger value likely to be more accurate.

As Table 3.1 shows, GGA-PBE does well when treating highly localized interactions,⁹⁶ as seen in the good agreement with the experimentally determined bond energies of I_{ad} and H_{ad}.^{51,97} Here the optB86b vdW-DF gives a description of the H-Pt(111) bond energy that is nearly as good as GGA-PBE, but the large atomic number of the I atom may have caused it to significantly overestimate the I-Pt(111) bond energy. On the other hand, the optB86b vdW-DF does far better with adsorbates whose bonding contains large contributions from dispersion interactions, as seen in the close agreement between the calculated and experimental values for

the heat of reaction (1), which makes $t\text{-Bu}_{\text{ad}}$, the heat of reaction (2), which is the heat of molecular adsorption for $t\text{-BuI}$, and the $t\text{-Bu-Pt(111)}$ bond energy. In these cases, GGA-PBE significantly under-predicts the adsorption energies.

However, the GGA-PBE value of the $(\text{CH}_3)_3\text{C-Pt(111)}$ bond energy may offer a useful insight, which accomplishes something that is not possible experimentally: With its nearly complete lack of account for the dispersion interaction, what is captured by GGA-PBE could be regarded as approximately the chemical component of this $(\text{CH}_3)_3\text{C-Pt(111)}$ bond energy, which is 137 kJ/mol (Table 3.1). Indeed, this is 60 kJ/mol weaker than the $\text{H}_3\text{C-Pt(111)}$ bond for methyl adsorbed on Pt(111), which has been both measured and calculated as 197 kJ/mol.^{32,97} This is comparable to the known difference of ~ 40 kJ/mol between the C-H bond energy in methane (439.3 kJ/mol⁴⁸) and at the central carbon of isobutane (400 kJ/mol⁴⁸). This extra van der Waals bonding for $t\text{-Bu}$ explains the puzzling fact that the measured C-Pt bond energy for $t\text{-Bu}$ is somewhat higher than that for methyl, even though its tertiary C bond is expected to bond more weakly than the C in methyl to Pt. Further improvement of vdW-DFs may be beneficial, perhaps allowing researchers to unify the treatment of small and large adsorbates on surfaces with similar accuracy. Incidentally, the close agreement between the calculated and experimental values for the heat of reaction (1) and the much larger difference when comparing the measured heat at this same coverage to the calculated value for the heat of $t\text{-BuI}_{\text{g}} \rightarrow i\text{-butene}_{\text{ad}} + \text{H}_{\text{ad}} + \text{I}_{\text{ad}}$ further confirms that $i\text{-butene}_{\text{ad}}$ is not formed in our SCAC experiments.

3.5 Conclusions

We have determined the following adsorption, dissociation and desorption processes for $t\text{-butyl iodide}$ on Pt(111) in the indicated surface coverage and temperature ranges. Up to 0.07 ML total coverage of $t\text{-BuI}$, $t\text{-BuI}$ dissociatively adsorbs to form $t\text{-Bu}_{\text{ad}}$ plus I_{ad} at 100 K, with an

integral heat of reaction of 230 kJ/mol. This dissociative adsorption process results in the occupation of ~50% of the surface Pt atoms. The remaining surface atoms are occupied by molecularly adsorbed *t*-BuI up to a total coverage of 0.15 ML, with an average heat of adsorption of 101-135 kJ/mol. Following the completion of the first layer, *t*-BuI molecularly adsorbs on top of the saturated Pt(111) surface between 0.15 and 0.38 ML, with a constant heat of adsorption of 44.5 ± 1.9 kJ/mol. This second layer desorbs between 120 and 150 K. Following completion of the second layer, molecular adsorption in the multilayer regime occurs. Desorption of the multilayer occurs between 100 and 120 K, and molecules in this regime bind ~6 kJ/mol more weakly than in the second molecular layer.

Adsorbed *t*-Bu and atomic iodine are formed upon C-I bond cleavage. Although the formation of adsorbed *i*-butene + H rather than *t*-Bu was not completely ruled out by the vibrational spectra, the combination of the IR and SCAC measurements and DFT calculations strongly support the formation of *t*-Bu_{ad}.

SCAC measurements provided the standard enthalpy of formation of adsorbed *t*-butyl and the Pt-*t*-butyl bond strengths at 0.04 ML (1/25 ML) of -168 ± 20 kJ/mol and 216 ± 20 kJ/mol respectively. These values were found to increase in magnitude by 9 kJ/mol in the limit of zero coverage. The integral heats of molecular and dissociative ($t\text{-BuI}_g \rightarrow t\text{-Bu}_{ad} + \text{I}_{ad}$) adsorption were found to be 101-135 kJ/mol at 1/9 ML and 230 kJ/mol at 1/16 ML respectively. DFT calculations were performed using the GGA-PBE and optB86b vdW density functionals to calculate the heats of reaction and the binding energies of relevant adsorbates. Comparison of the calorimetry experiments to these calculations found that the optB86b vdW-DF provides more accurate energies than GGA-PBE for describing the adsorption and bonding of *t*-BuI and *t*-Bu on Pt(111) because these energies contain large contributions from dispersion.

3.6 Appendix

The convergence of adsorption energies with respect to the valence state cutoff energy, the k -point sampling density, and the number of metal layers in the Pt(111) slab was tested using t -bu and atomic iodine as the examples. The results, shown in the table below, suggest that the following sets of parameters are sufficient to converge the adsorption energy to within 0.1 eV: 4-layer Pt(111) slab, 400 eV cutoff energy, $5 \times 5 \times 1$ k -points for the (3×3) surface unit cell, and $3 \times 3 \times 1$ k -points for the (4×4) surface unit cell.

Table A.3.1: Bond energies (in eV) on Pt(111) calculated with the optB86b vdW-DF using different sets of parameters.

	t -butyl	I
<i>(3 × 3) surface unit cell; top 2 metal layers relaxed; 5 × 5 × 1 k-points; 400 eV cutoff energy</i>		
4 metal layers in slab	-2.36	-3.06
5 metal layers in slab	-2.42	-3.19
6 metal layers in slab	-2.36	-3.07
<i>(3 × 3) surface unit cell; 4 metal layers with top 2 layers relaxed</i>		
<i>5 × 5 × 1 k-points; 400 eV cutoff energy; 400 eV cutoff PAW potential for C and 250 eV PAW potential for H</i>	-2.36	-3.06
<i>7 × 7 × 1 k-points; 700 eV cutoff energy; 700 eV cutoff PAW potentials for C and H</i>	-2.35	-3.08
<i>(4 × 4) surface unit cell; 4 metal layers with top 2 layers relaxed; 400 eV cutoff energy</i>		
<i>3 × 3 × 1 k-points</i>	-2.38	-3.08
<i>5 × 5 × 1 k-points</i>	-2.41	-3.18

3.7 Figures

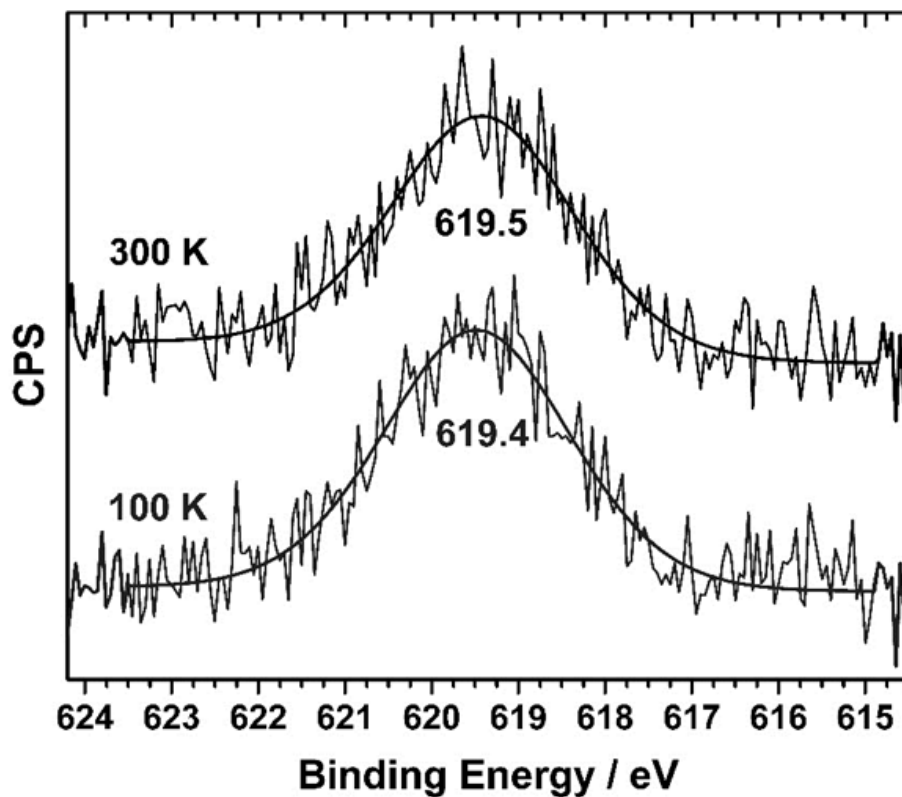


Figure 3.1: XPS spectra of the I 3d peak obtained after adsorption of 0.067 ML of *t*-BuI on Pt(111) at 100 K (bottom curve) and at 300 K (top curve). Spectra were obtained at the same exposure temperature. The background for the clean Pt(111) sample was subtracted and the peaks were fitted by a Gaussian-Lorentzian curve to obtain the indicated peak maxima. The energy scale has been calibrated using the Pt 4f_{7/2} (BE= 70.9 eV) and Cu 2p_{3/2} (BE= 932.4 eV) peaks for these pure metals.

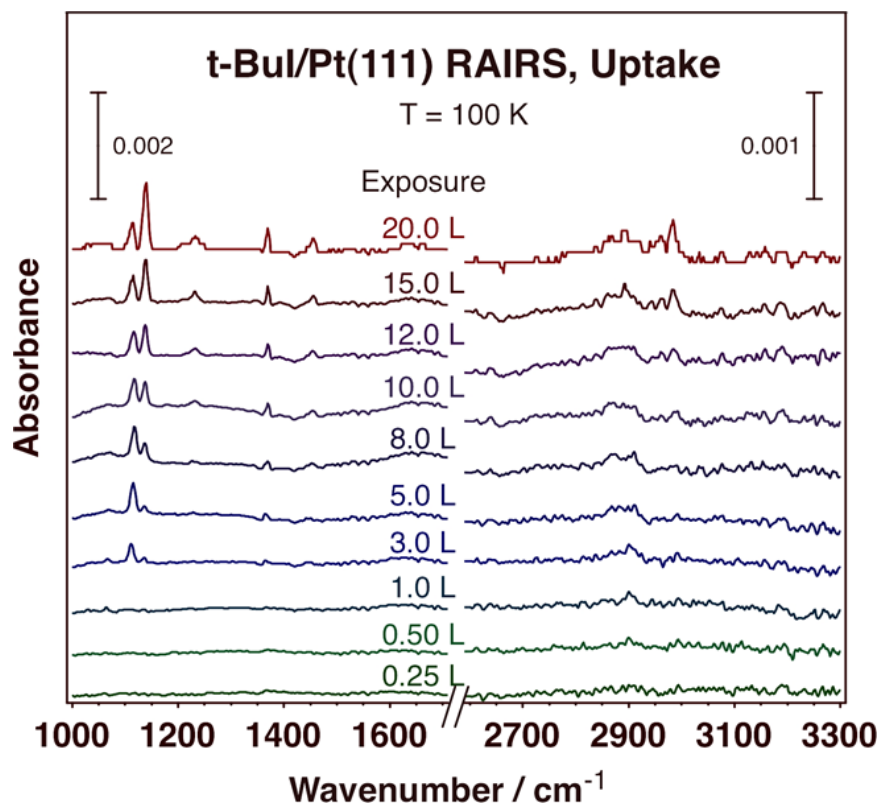


Figure 3.2: RAIRS spectra for increasing doses of *t*-BuI on Pt(111) at 100 K. Exposures are given in Langmuirs (L) but these should only be taken as a relative measure of exposure, since they were measured at the ion gauge and not at the Pt surface, where the exposures are expected to be much lower due to pumping by the surrounding cryogenically-cooled surfaces.

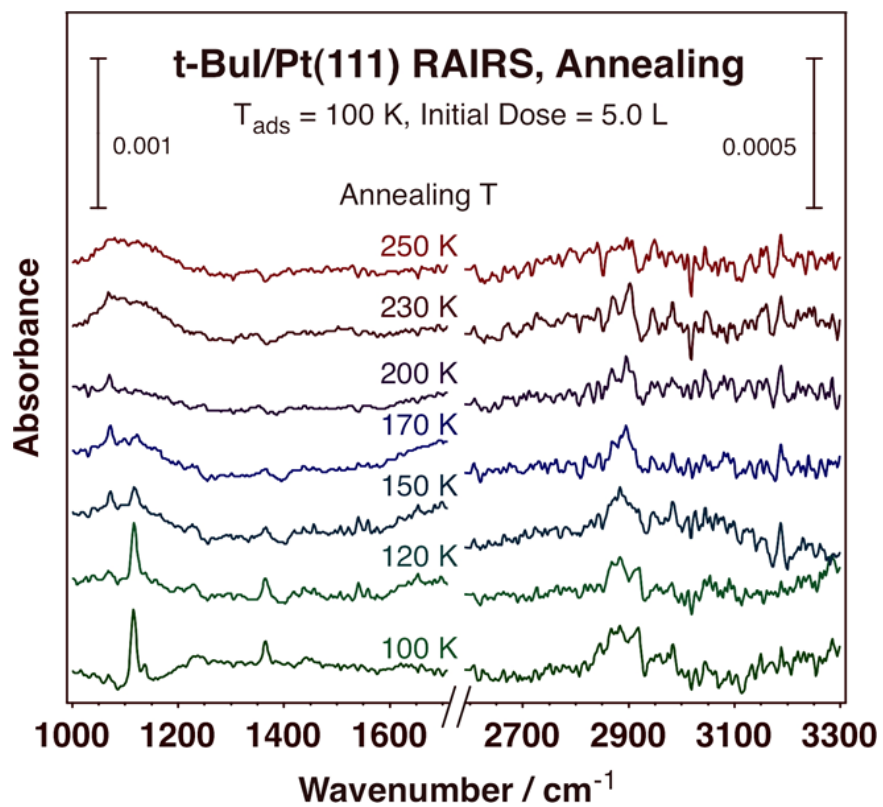


Figure 3.3: RAIRS spectra for 5 L of t-BuI dosed on Pt(111) at 100 K, and after heating briefly to the indicated increasing temperatures.

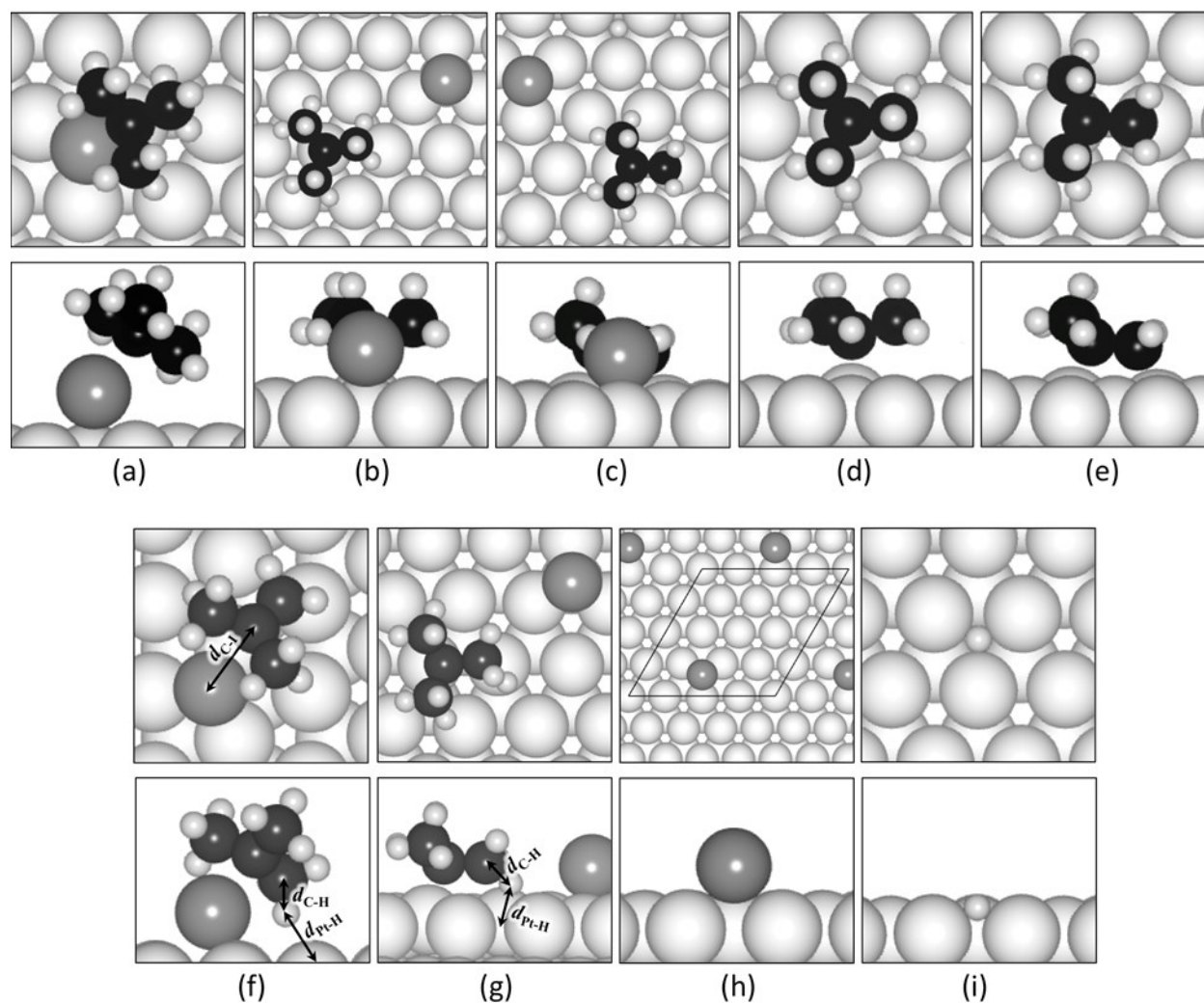


Figure 3.4: Top (upper panels) and side (lower panels) snapshots of the DFT (optB86b vdW-DF) calculated minimum energy configurations for the various surface species on Pt(111): (a) *t*-BuI; (b) *t*-Bu+I; (c) di- σ *i*-butene+I+H; (d) *t*-Bu; (e) di- σ *i*-butene; (f) transition state for C-I bond scission in *t*-BuI; (g) transition state for C-H bond scission in *t*-Bu with coadsorbed I; (h) I; (i) H. Large white, large grey, medium black, and small white spheres correspond to Pt, I, C, and H atoms, respectively. The coverage shown is 1/16 ML except for (a) and (f), for which it is 1/9 ML. The surface unit cell boundaries for 1/16 ML are illustrated in (h). The various labeled bond distances in (f) and (g) are: $d_{C-I}=2.843$ Å; $d_{C-H}=1.146$ Å (f) and 1.526 Å (g); $d_{Pt-H}=2.246$ Å (f) and 1.623 Å (g).

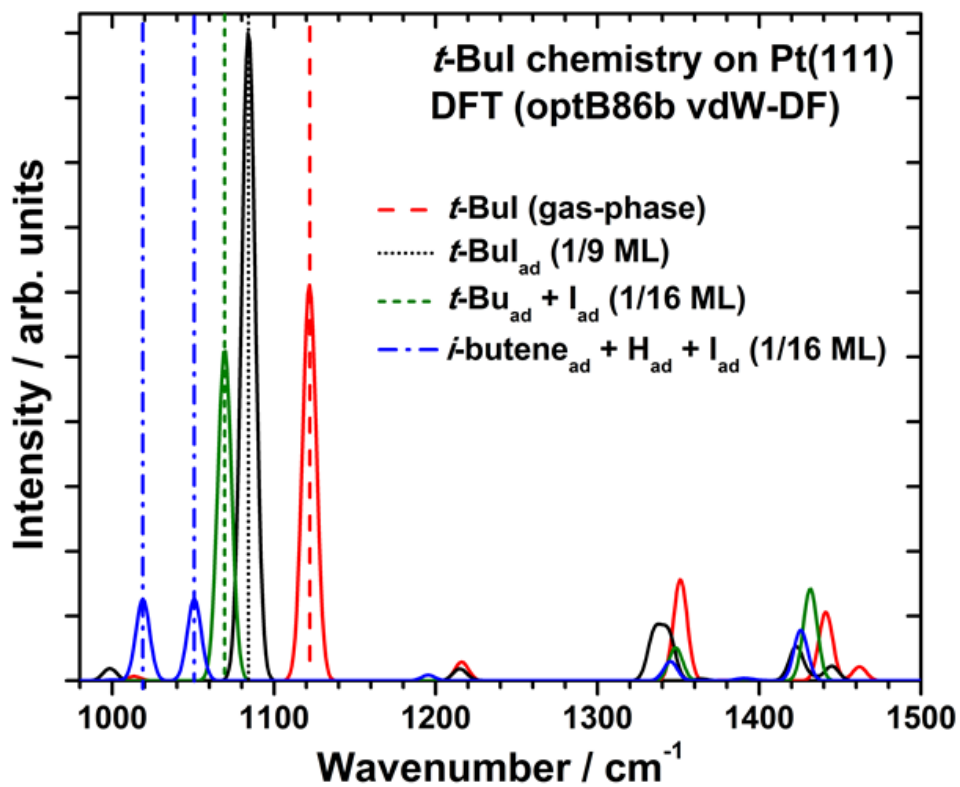


Figure 3.5: DFT (optB86b vdW-DF) calculated IR spectra of possible surface species formed upon the adsorption of *t*-BuI on Pt(111). The DFT-calculated IR spectrum of gaseous *t*-BuI is shown for comparison. See text for peak positions.

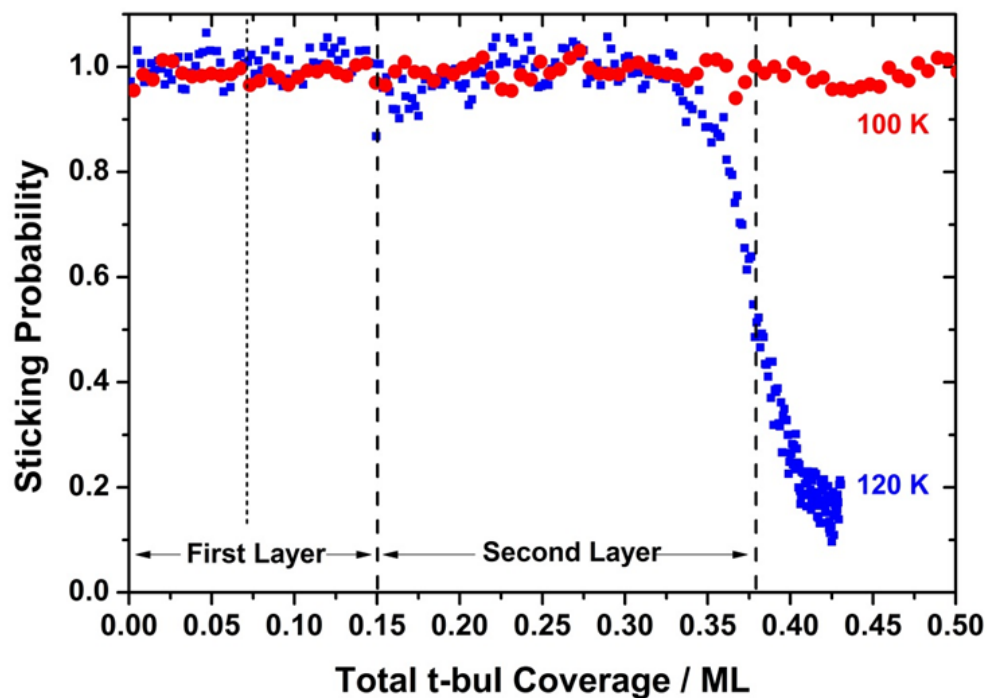


Figure 3.6: Long-term sticking probability of *t*-BuI on Pt(111) at 100 and 120 K versus the total *t*-BuI coverage that irreversibly adsorbed (irrespective of its structure in the adlayer). These measurements were obtained simultaneously with the heat of adsorption data of Fig. 7, which were used to assign the cutoffs between dissociative and molecular adsorption (thin dashed line) and between the first and second layers (heavy dashed line). Completion of the second layer (also shown by a heavy dashed line) was assigned to the point where this 120 K sticking probability has decreased to 0.5. The short-term sticking probability (not shown) was unity at all these conditions.

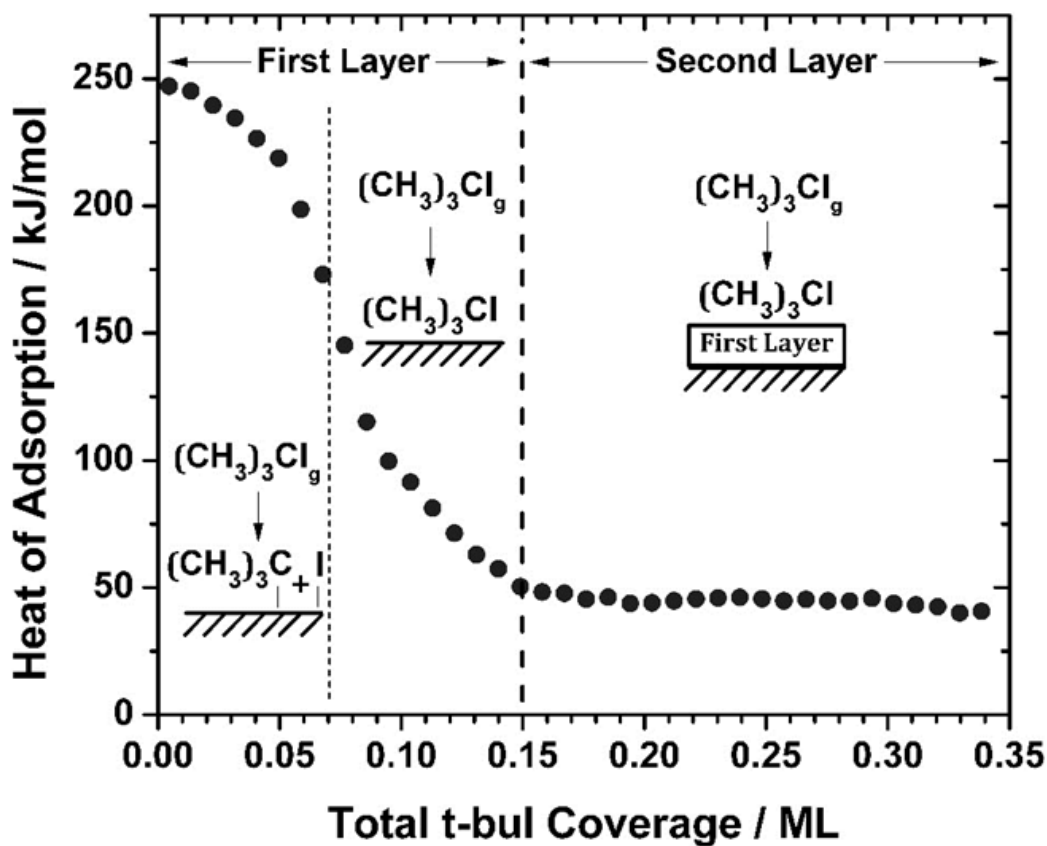


Figure 3.7: Differential heats of adsorption of *t*-BuI versus coverage on Pt(111) at 110 ± 10 K (i.e., the average of several runs each at 100 and 120 K). The corresponding coverage ranges for different processes are indicated. “Second Layer” here indicates that this surface already contains the first layer of surface species derived from *t*-BuI adsorption (both dissociative and then molecular)

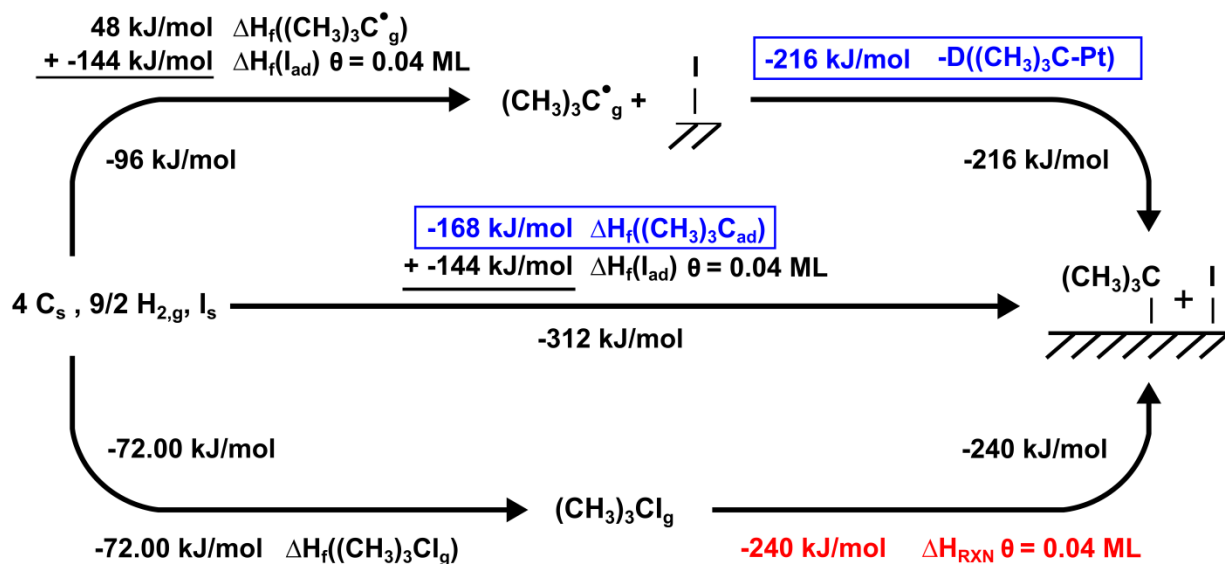


Figure 3.8: Thermodynamic cycle used to determine the standard enthalpy of formation of adsorbed *t*-Bu and its bond enthalpy to Pt(111) from the dissociative adsorption of *t*-BuI on Pt(111). The measured integral enthalpy of dissociative adsorption at 0.04 ML coverage at 100-120 K is shown as ΔH_{RXN} on the bottom right. Derived heats for the *t*-Bu-Pt(111) bond enthalpy and for the enthalpy of formation of adsorbed *t*-Bu on Pt(111) are boxed. Because the final error in the calculated values ($\pm 20 \text{ kJ/mol}$) is dominated by the error in the I-Pt(111) bond energy (see text), individual errors are not shown in this cycle.

Table 3.1: Comparison of measured and calculated adsorption energies (all in kJ/mol) for several key surface intermediates on Pt(111). Calculated values are from periodic DFT at the GGA-PBE and optB86b vdW-DF levels. Corresponding experimental values are included for comparison where available. Positive values represent exothermic processes. All experimental enthalpies have been converted to reaction energies and bond energies by subtracting RT.

Adsorbate		<i>t</i> -BuI ^a	<i>t</i> -Bu+I ^a	i-butene+I+H ^a	<i>t</i> -Bu ^b	i-butene ^b	I ^b	H ^b
Configuration		tilted	atop+fcc	atop+fcc+hcp	atop	di-σ	fcc	fcc
		kJ/mol	kJ/mol	kJ/mol	kJ/mol	kJ/mol	kJ/mol	kJ/mol
GGA-PBE (ZPE-corrected)	0 ML ^c	-	151	189	-	-	-	-
	1/16 ML	55	128	171	128	69	254	251
	1/9 ML	52	103	129	125	66	250	251
optB86b vdW-DF	0 ML	-	268	300	-	-	-	-
	1/16 ML	136	248	288	232	165	306	286
	1/9 ML	140	220	236	228	158	295	284
optB86b vdW-DF (ZPE-corrected)	0 ML	-	272	318	-	-	-	-
	1/16 ML	140	252	306	225	163	305	272
	1/9 ML	143	223	252	220	156	294	270
Experiment	0 ML	-	252	-	224±9	-	255±5	258
	1/16 ML	-	229 ^d	-	207±20 ^d	-	249±20	258
	1/9 ML	100-134 ^e	-	-	-	-	244±20	258
Experimental Ref.		this work	this work	-	this work	-	⁵¹	⁹⁹

^a With respect to energy of gas-phase molecular *t*-BuI.

^b With respect to energy of this same adsorbate in the gas phase, as calculated by the same DFT method or, for experiments, as determined from literature values as described in text.

^c As can be seen, the adsorption energy for a *single adsorbate* per unit cell generally changes by 10 kJ/mol or less from 1/9 ML to 1/16 ML, suggesting that the latter is already approaching the zero-coverage, no-interaction limit. Therefore, these DFT values for *coadsorbates* at the zero-coverage limit (0 ML) were estimated based on the energies of each individual adsorbate at 1/16 ML in separate unit cells.

^d Experimental integral heat at 0.0625 ML calculated using extrapolation of linear fit to data in the coverage range 0-0.05 ML.

^e Estimated range for the energy of molecular adsorption as described in the text.

Chapter 4

Surface Kinetics and Energetics from Single Crystal Adsorption Calorimetry

Lineshape Analysis: Methyl from Methyl Iodide on Pt(111)

4.1 Introduction

Measuring the kinetics of elementary steps occurring on solid surfaces is crucial for fundamental understanding in heterogeneous catalysis and many other technologies. Yet few techniques allow one to measure the rate constants for processes where the product is adsorbed and the reaction's time constant is faster than 1 s. When the reactant begins as a gas, this can be done with sticking probability measurements by monitoring the depletion of the gas (for example, using the King and Wells method³⁶). However, this fails when most of the gas reacts. In that case, one must monitor the appearance of some surface species using a surface analysis technique that measures surface concentrations faster than 1 s. There are few such techniques and the ones that exist tend to be very expensive, require very special situations to apply and/or use probe techniques that do surface damage during the measurements. Here we show that analysis of the heat signal lineshape in single crystal adsorption calorimetry (SCAC) can provide the rate constant for the conversion of one surface species to another when that process has a characteristic time constant between 10 and 1000 ms. Specifically, we address here the very common situation that occurs in catalysis studies where a molecule adsorbs molecularly with almost unit sticking probability and then has a slower second step that leads to adsorbed product(s). For example, the initial molecular adsorbate dissociates to adsorbed fragments or reacts with another pre-adsorbed species to make an adsorbed adduct. We show that the rate constant for this slower second step can be determined from detailed fitting of the SCAC heat

signal lineshape with a convolution of the instrument response function with a kinetic model for the deposition of heat by the two elementary reaction steps (one fast and one slow). This simultaneously provides the enthalpies for each of these two elementary steps, so that the information content is very rich, providing a powerful approach for analyzing fundamental aspects of surface reactions. Importantly, this can all be done on single crystal surfaces, so that the nature of the adsorbed species involved can be fully characterized using the array of surface analysis techniques that work so much better on single crystals, and which can be fully modeled using computational techniques that require periodic boundary conditions (as is used for most density functional theory (DFT) studies of surface reactions).

Knowledge of the relative stabilities of chemical species adsorbed on surfaces is important to the advancement of the field of heterogeneous catalysis. Thus, a large body of work exists that use techniques such as temperature programmed desorption (TPD) or adsorption isotherms to extract heats of adsorption of well-defined adsorbates on single crystal surfaces. The limitation of these techniques is that they require the species of interest to be reversibly adsorbed. Because many catalytically interesting intermediates may exist in metastable states or undergo decomposition or reaction with coadsorbed species rather than desorbing, a direct measurement technique is required.

These limitations in existing surface science techniques has led to the development over the past several decades of a calorimetric technique^{12,15,16} that now has sufficient sensitivity to measure the temperature change of single crystal samples that arises from the adsorption of molecular pulses containing only 1% monolayer with a detection limit of only 3 kJ/mol^{20,32}. This technique, known as single crystal adsorption calorimetry (SCAC), was first developed in the group of David A. King at Cambridge University^{7,41,100} and then further improved in our

group^{10,101,102} and others^{42,103}. SCAC utilizes well-defined single crystal surfaces on which the chemical structures and bonding configurations of adsorbates can be determined using other surface science characterization techniques, thus allowing for measurements to be easily converted to heats of formation or bond energies of adsorbed species. These direct calorimetric measurements have led to the determination of the heat of formation of a wide range of catalytically relevant oxygenates (e.g. water¹⁷ and hydroxyl^{104,105}, methanol and methoxy¹⁹), hydrocarbon fragments (e.g. CH²⁰, CH₃³², C₂H₂, C₂H₃, CHCH₃ and C₂H₄^{29,106}, di- σ cyclohexene¹⁰⁷, benzene¹⁰⁸ and naphthalene¹⁰⁹) and other small molecules (e.g. NO, CO, and atomic oxygen¹²) on metal single crystal surfaces.

In parallel with the development of experimental methods, theoretical methods such as density functional theory (DFT) calculations have been implemented to determine bond strengths of catalytic intermediates and the activation barriers of elementary chemical reactions. This allows for the theoretical identification of complex reaction mechanisms using microkinetic modeling as well as the development of trends that link catalytic performance to bond strengths of key adsorbed intermediates. However, without experimental data, the accuracy of theoretically determined bond strengths is not known. A recent perspective by Klimes and Michaelides¹¹⁰ highlights the efforts over the past decade to greatly improve the accuracy of calculations for molecular adsorption processes that involve a large dispersion component. The experimental determination of these values can therefore provide benchmarks for the continued improvement in the accuracy of theoretical calculations.

To date, SCAC studies have investigated systems in which heat deposition from molecular adsorption/reaction is extremely fast in comparison to the timescale of the heat measurement. Under these conditions, the heat detector's response signal from the molecular

beam pulse exhibits a nearly identical intensity-normalized lineshape to that seen from the laser pulses used to calibrate the heat signal. In this case, any kinetic information for the process of interest is completely lost. However, the important potential for the determination of dynamical information from SCAC data was emphasized by King when he first started talking about his results from SCAC, and can be inferred from the early discussion by Stuck et al.¹¹¹ of the change in detector signal lineshape that results from a change in the molecular or laser pulse duration. There are a few examples in the literature where SCAC lineshapes have already been used to obtain some qualitative kinetic information, including work by Lytken et al. where mass spectrometer measurements of the short-term and long-term sticking probabilities were introduced to allow a proper accounting for a contribution to the heat signal lineshape that arises from slower molecular desorption after the initial fast heat deposition from adsorption¹⁰⁷, and by Lew et al., where a slow surface reorganization of adsorbates led to a slight broadening of the detector response, for which the signal intensity was corrected to obtain accurate heats¹⁷. However, no attempt was made to use the detector response as a probe of the reaction kinetics.

Here, we show for the first time that it is possible to extend quantitative measurements of adsorption heats to cases where all or some portion of the heat is deposited on a timescale similar to the heat measurements (i.e. 10-1000 ms, compared to the molecular beam pulse width of 50-100 ms). Previous SCAC studies required that the intermediates of interest be produced on a timescale much faster than the measurement time (~100 ms) *and* be stable on a timescale much longer than the measurement, thus greatly limiting the systems that could be studied. The analysis method presented here greatly expands the number of systems whose energetics can be studied using SCAC, including the *simultaneous* energy measurement of adsorbed intermediates

that are only stable for 10-1000 ms, and products that do not appear until 10-1000 ms after the gas strikes the surface.

We also show how this analysis provides important kinetic rate constants for the studied systems, thus demonstrating for the first time the extraction of quantitative dynamical information from the heat pulse lineshape in SCAC. Specifically, we study the dissociative adsorption of methyl iodide on Pt(111) at 270 K by SCAC, and determine from pulse shape analysis three kinetic/thermodynamic properties of the adsorbates involved: the rate constant for the dissociation of adsorbed methyl iodide into adsorbed methyl plus iodine on Pt(111), plus the heats of reaction for both the slow and the fast reactions. At low coverage, the mechanism is simple: $\text{CH}_3\text{I}_{\text{ad}} \rightarrow \text{CH}_{3,\text{ad}} + \text{I}_{\text{ad}}$, but this is followed by $\text{CH}_{3,\text{ad}} \rightarrow \text{CH}_{\text{ad}} + 2\text{H}_{\text{ad}}$ and $\text{CH}_{3,\text{ad}} + \text{H}_{\text{ad}} \rightarrow \text{CH}_{4,\text{g}}$ when the total coverage of $\text{CH}_{3,\text{ad}}$ plus I_{ad} exceeds 0.08 ML. The heat signal analysis provides the rate constant for the dissociation of $\text{CH}_3\text{I}_{\text{ad}}$ and the heat of formation of both $\text{CH}_{3,\text{ad}}$ and CH_{ad} . These two heats agree with values determined by SCAC at 320 K where the rates are so fast that lineshape analysis is not needed.^{20,32} This agreement proves the validity of the lineshape deconvolution method introduced here for analyzing SCAC pulse shapes when the pulse shape changes from that seen in heat calibration (i.e., where the heat is provided by laser pulses that deposit heat instantaneously).

4.2 Pulseshape and heat measurement for fast heat deposition

If the heat deposition from a molecular pulse is fast in comparison to the calorimetric measurement, the heat detector signal's lineshape will match that seen from the laser pulses used in heat signal calibration. The laser pulses used for calibration must have the same temporal and spatial distribution on the sample as the molecular beam pulse. This is accomplished in our experiments by directing a laser into the beam path and allowing it to pass through the same

series of apertures and mechanical chopper as the molecular beam.¹⁰ If the response lineshapes match, the total heat from the molecular pulse can be determined from the ratio of the intensity of the heat signal upon adsorption to that from the laser pulse that deposits a known amount of heat. This heat signal intensity ratio has been measured using various methods (e.g. comparison of peak heights^{41,101} or slopes on the rising side of the peaks¹⁰⁷).

The detector response signal to an instantaneous pulse at time t' of a unit amount of heat onto the single crystal sample (i.e. a delta function input of a unit amount of heat) is by definition the instrument response function, $R(t-t')$. It has been shown⁹ that the lineshape of $R(t-t')$ in SCAC using our type of heat detector (a pyroelectric polymer ribbon pressed against the back of the single crystal) is dictated by system parameters such as the time constants of heat transfer between the sample and detector ribbon and within the sample holder assembly, thermal conductivities, sample emissivity, etc., as well as the design and settings of the signal preamplifier and remote amplifier. Note that R depends on the detector ribbon and sample mounting and the contact between the two. However, there is usually no noticeable change in R provided the detector ribbon remains pressed in contact with the sample, meaning that R is constant over the course of a single heat-versus-coverage measurement involving hundreds of molecular beam pulses striking the single crystal surface⁹. This is tested by measuring R with laser pulses before and after each such multi-pulse molecular beam experiment.

In such experiments, the heat deposited into the sample versus time for a given molecular beam pulse, $H(t')$, may extend over a broader time period than the laser pulse and may vary in its total amount from pulse to pulse. In this case, the measured heat signal for that pulse, $S(t)$, is a convolution of $H(t')$ with the instrument response function $R(t-t')$:

$$S(t) = \int_{-\infty}^{\infty} H(t')R(t - t') dt' , \quad (1)$$

or using a shorthand notation for convolution, $S = H * R$.

In many cases of interest here, the surface processes that occur upon adsorption are very fast compared to the duration of the gas pulse from the molecular beam. In this case, it is convenient to express $H(t')$ as:

$$H(t') = x C(t'), \quad (2)$$

where x is a scaling factor proportional to the total amount of heat input and $C(t')$ is the heat input for a unit amount of heat with the same time profile as the molecular beam pulse's flux (identical for each pulse). A typical example of a real molecular beam pulse lineshape, which in this case has the same shape as $H(t')$ and $C(t')$, is shown in Fig. 4.1. The function $C(t')$ is entirely dictated by the rotational velocity and geometric design of the molecular beam chopper and is approximately described by a trapezoidal pulse with a full width at half maximum (FWHM) of typically 50-100 ms repeated every 1-5 seconds. Since the laser used for heat calibration also deposits heat from photon adsorption rapidly, its heat input can also be described by $H(t') = x C(t')$. For these cases,

$$S = x (C * R). \quad (3)$$

The limitations of the laser calibration method described earlier can be envisioned by looking at the equations that describe the detector's response signal to a laser pulse with total heat x_{laser} :

$$S_{\text{laser}} = x_{\text{laser}} (C * R), \quad (4)$$

and to a molecular pulse of total heat x_{mol} :

$$S_{\text{mol}} = x_{\text{mol}} (C' * R), \quad (5)$$

where C' is the heat deposition profile for molecular pulses. Because the laser calibration is performed during each experiment without breaking the ribbon/sample contact, R is the same for

Equations 4 and 5. For fast heat deposition upon molecular adsorption, $C' = C$. In this case, one can easily see that

$$x_{\text{mol}} = x_{\text{laser}} (S_{\text{mol}}/S_{\text{laser}}), \quad (6)$$

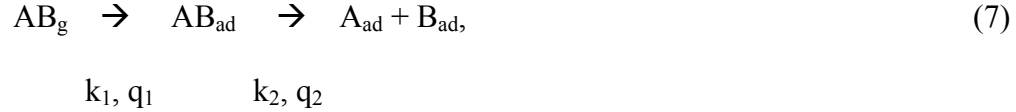
where x_{laser} can easily be calculated from the measured laser power and $(S_{\text{mol}}/S_{\text{laser}})$ can be determined from the ratio of peak heights or slopes during the initial rise-time of the respective pulses. An example experiment where this was the case is shown in Fig. 4.2, which also shows how peak height and rise-time are defined and measured. The lineshape for the detector response to a laser pulse is different in this more recent heat detector design than in the old result of Fig. 4.1 due to improvements in the thermal contact to the sample and changes in detector capacitance and electronics.¹⁰² The agreement between the laser and molecular pulse lineshapes in Fig. 4.2, where heat deposition is fast, indicate that differences between C and C' due to the difference in photon and molecular velocities is negligible compared to the time resolution of our experiments, as expected for the short beam path used here (~30 cm).

This type of analysis is valid for most simple molecular adsorption processes because the activation barrier for molecular adsorption on surfaces is usually negligible. The chemisorption process is therefore very fast compared to the heat pulse duration and indeed $C' = C$, as seen in Fig. 4.2. However this only works when $C' = C$. We next describe the effects that arise when the surface chemical reactions are slower and C' is broadened compared to C .

4.3 Pulseshape analysis for multi-step heat deposition processes

Now let us consider the case where there is some time delay in deposition of some of the heat from the molecular pulse, but where all of the heat is still deposited on a time scale that is comparable to the length of the molecular beam pulse, which is typically 50 to 100 ms,²⁰ but

could be 10 ms or even below. A very common example is a simple two-step dissociative adsorption process:



with reaction rate constants (k_1 and k_2) and enthalpies (q_1 and q_2) and step 1 is fast but step 2 is slow (i.e. $1/k_2 = \sim 10-1000$ ms for a pulse width of ~ 100 ms).

In this example, the heat deposition profile for the molecular pulse (C') is no longer a rectangular pulse, and therefore cannot be analyzed directly with the laser calibration method described earlier. However, if q_1 is negligible (i.e., $q_1 \ll q_2$) one can model C' using a method described in a previous publication,¹⁷ by convoluting the laser pulse with an exponential decay for a first-order reaction:

$$D = (1/\tau) \text{Exp}(-t/\tau), \quad (8)$$

where τ is the inverse of the rate constant of the slow reaction step (i.e., $\tau = 1/k_2$). This gives a new approach similar to Equations 4-7, but where the laser heat deposition, C , is instead replaced with what it would be if it were also broadened by this same rate constant, $C*D$, and S_{laser} is replaced with S_{conv} given by:

$$S_{\text{conv}} = S_{\text{laser}}*D = x_{\text{laser}}(C*D)*R. \quad (9)$$

Figure 4.3 shows an example of this convolution for the case where τ equals 350 ms, using a real experimental laser calibration signal for S_{laser} .

The value of τ can then be adjusted until the normalized lineshape from the convoluted laser (S_{conv}) matches that from the molecular pulse (i.e. $C*D = C'$). This value of τ then gives the kinetic rate constant k_2 for the reaction. The integral of Equation 8 is unity, meaning that convolution with the laser calibration lineshape does not change the integral of the pulse. The

heat from the molecular pulse, x_{mol} , can then be calculated using S_{conv} in place of S_{laser} in Equation 6: $x_{\text{mol}} = x_{\text{laser}} (S_{\text{mol}}/S_{\text{conv}})$.

As the convolution (i.e. pulse broadening) does not change the integral of the pulse over the entire pulse duration, the ratio of the integrals of the molecular (broadened) and laser signals could also be used to calculate the total heat, in principle. However, because the signal contains both positive and negative components, the integral is generally small and greatly affected by low-frequency noise (e.g. baseline shifts), making this approach impractical.

Now let us consider the same two-step dissociative adsorption mechanism, reaction (7), but now where q_1 and q_2 are of similar magnitudes. In this more complex but much more common case, the detector response is made up of two steps: heat deposited instantaneously during adsorption ($C' = C$) and heat deposition from dissociation which occurs with a first-order time constant on the order of the time of the heat measurement. In this case, the heat signal is:

$$S_{\text{mol}} = x_{S1}'(C * R) + x_{S2}'(C' * R) = (x_{S1}'C + x_{S2}'C') * R, \quad (10)$$

where x_{S1}' and x_{S2}' are the amounts of heat deposited in the fast and slow steps, 1 and 2, respectively. Substitution of expressions like those in Equations 4 and 9 as the first and second terms of Equation 10, respectively, shows that S_{mol} can be described using scaled laser and convoluted laser pulses:

$$S_{\text{mol}} = (x_{S1}'C + x_{S2}'(C * D)) * R = (x_{S1}'/x_{\text{laser}}) S_{\text{laser}} + (x_{S2}'/x_{\text{laser}}) S_{\text{conv}}. \quad (11)$$

In this form, it is easy to see that one can create a simulated pulse,

$$S_{\text{sim}} = (x_{S1}C + x_{S2}(C * D)) * R = (x_{S1}/x_{\text{laser}}) S_{\text{laser}} + (x_{S2}/x_{\text{laser}}) S_{\text{conv}}, \quad (12)$$

by guessing $(x_{S1}/x_{\text{laser}})$, $(x_{S2}/x_{\text{laser}})$ and τ . Note that we have replaced x_{Si}' with x_{Si} for the simulated signal, to emphasize that these are fitting parameters. This simulation will fit the data, S_{mol} , (i.e., $S_{\text{sim}} = S_{\text{mol}}$) if and only if all three parameters match the real physical situation.

We can further simplify Equations 10 and 12 by factoring out x_{S1}' and x_{S1} , respectively, to give:

$$S_{mol} = x_{S1}'(C + (x_{S2}'/x_{S1}')(C'))*R \quad (13)$$

and

$$S_{sim} = x_{S1}(C + (x_{S2}/x_{S1})(C*D))*R \quad (14)$$

In this form, it is clear that by normalizing the two functions (S_{sim} and S_{mol}), just two-parameters (x_{S2}/x_{S1} and τ) are needed to match the lineshape of S_{sim} to S_{mol} . Once a match is obtained the scaling factor used to normalize gives x_{S1}'/x_{S1} and thus the total heat deposited in each step, x_{S1}' and x_{S2}' .

It is immediately clear that simulating the heat lineshape is not as straight-forward as the previous example when $q_1 \ll q_2$. This is because creating a simulated pulse that matches the lineshape, following normalization, of a molecular pulse requires knowledge of both τ and the ratio of the amount of heat deposited in the two steps (x_{S2}'/x_{S1}'), both of which are generally not known.

Although we described Equations 13 and 14 in the context of a simple dissociative adsorption process, these equations can be used to describe any sequential heat deposition process with many fast steps but only one slow intermediate step. Equation 13 is therefore the general form for the detector response to heat deposition from a molecular pulse that undergoes a sequential set of reactions with a single slow intermediate step. The heats for the steps before the slow step are simply added together and treated as a single fast step, and those for the slow and subsequent steps are added together and treated as a single slow step. Analogously, Equation 14 is the general form that can be used to generate a simulated pulse of a multi-step sequential reaction with a single slow step. It is constructed using detector responses from the laser

calibration and the laser calibration convoluted with an exponential decay for a first order reaction.

Although we have not yet done so, one could use this same approach to analyze cases where the net reaction starting from the slow step is endothermic. The most obvious case of this type is the simple two-step reaction sequence where the second, slow step is simple desorption of the adsorbate produced in step 1. As pointed out and observed by Lytken et al., when slower, endothermic desorption occurs, it removes heat signal at long times, and thus leads to an apparent narrowing of the peak width of the heat signal.¹⁰⁷

In a future paper, we will discuss the implementation of two efficient computational methods we developed for determining the values of x_{S1}' , x_{S2}' , and τ . We used these methods to determine these three parameters in the example application we describe next.

4.4 Application: Dissociative adsorption of methyl iodide on Pt(111) at 270 K

We will now describe the first determination of kinetic parameters of a surface chemical reaction from SCAC measurements using data from a recent study of methyl iodide adsorption on Pt(111) at 270 K. Details of the experimental methodology can be found elsewhere.^{10,20,102,107} Briefly, experiments were performed in an ultrahigh vacuum chamber with base pressure $<2 \times 10^{-10}$ mbar. Methyl iodide pulses of 102 ms duration containing 0.0046 ML were repeated every 5 seconds. Here ML is defined as the surface density of Pt atoms in the (111) plane (1.5×10^{19} /m²). The sticking probability of methyl iodide is unity up to 0.11 ML coverage at this temperature. We can therefore convert x_{S1}' and x_{S2}' from J/pulse to kJ/mol using the measured flux and sticking probabilities. To improve the signal to noise ratio, the detector signals from four pulses were summed together, so that each summed methyl iodide pulse effectively contains 0.0184 ML.

A representative heat signal from such a (summed) molecular pulse for this experiment is shown in Fig. 4.4, in the coverage range 0.037-0.055 ML at 270 K, along with the average heat signal from the laser calibration pulses. Broadening of the molecular pulse with respect to the laser pulse is clearly seen. Figure 4.5 shows a comparison of the signal lineshape for this molecular pulse with a simulated pulse created using Equation 13. The signal contributions from the two steps that make up the simulated pulse are also included. It is clear that the simulated pulse reproduces the experimental pulse extremely well, meaning that parameters used in this simulation (i.e. the differential heat deposited in each of the two steps ($x_{S1}' = 136$ kJ/mol and $x_{S2}' = 76$ kJ/mol) and the τ of the slow reaction step (240 ms)) are accurate.

The heat signal lineshape for each molecular beam pulse, measured as the surface coverage was built up from clean Pt(111) to saturation coverage at 270 K was similarly analyzed to determine the differential heats of reaction for both step 1 and step 2 as well as the time constant τ of the slow reaction as a detailed function of surface coverage. The resulting heats for step 1 and step 2, and the total differential heat of adsorption of methyl iodide (all in kJ/mol) are shown in Fig. 4.6 as a function of the methyl iodide surface coverage (i.e., the total amount of methyl iodide that permanently stuck to the surface, irrespective of its final dissociated products). The corresponding time constants are shown in Fig. 4.7.

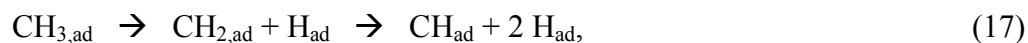
We will interpret these results in terms of the mechanisms we determined from studies of the adsorption of methyl iodide on Pt(111) over a broad temperature range (95-320 K) using SCAC and molecular beam / surface scattering reported elsewhere,²⁰ and our corresponding analysis of the relevant spectroscopic literature which is summarized in that report. We now summarize those mechanistic results as they pertain here. At low coverage (0 – 0.04 ML), the following two elementary steps occur:



and



At coverages above 0.04 ML, adsorbed methyl begins to dehydrogenate and hydrogenate according to the following reactions:



and



Since hydrogen desorption is negligibly slow at 270 K, reactions (15)-(18) eventually proceed to completion, giving the net reaction:



We showed that the absence of methyl dehydrogenation at coverages below 0.04 ML is not due to slow kinetics, since the mass spectrometer shows no methane there even at long times. We showed that its absence is instead due to the very small equilibrium constant for net reaction (17) resulting from its endothermicity (+23 kJ/mol).²⁰ At high coverages however, the removal of H_{ad} via reaction (18) drives production of CH_{ad} in spite of the thermodynamic preference for $\text{CH}_{3,ad}$.

Below 0.04 ML, where only reactions (15) and (16) occur, it is tempting to interpret step 1 as reaction (15) and step 2 as reaction (16). However, we know that the heat for reaction (15) is only ~95 kJ/mol (at least when measured at 95 K),²⁰ whereas the fast reaction in Fig. 4.6 has a much larger heat of 185 to 150 kJ/mol. Thus, we propose that both reactions (15) plus (16) are occurring quickly over part of the surface at 270 K and contribute to ‘step 1’, and that the slow step 2 (which contributes only ~1/3 of the total heat) is due to reaction (16) occurring more slowly on other parts of the surface (either at step edges or where the local surface coverage is

higher). In any case, the sum of the heats for steps 1+2 averaged over this coverage range gives a value of 230 kJ/mol for the net conversion of reactions (15) + (16) at 270 K. This is very close to the value of 212 kJ/mol measured at 320 K where this deconvolution analysis is not needed since both steps are nearly instantaneous relative the heat measurement time.²⁰ This good agreement proves the validity of this new data analysis method. The value of 230 kJ/mol gives an enthalpy of formation for CH_{3,ad} of -71 kJ/mol using the enthalpies of formation for the other species involved (CH_{3I_g} = 14.6 kJ/mol,¹¹² I_{ad} = 144 kJ/mol⁵¹).

We can estimate the fraction, x , of the methyl iodide below 0.04 ML that reacts quickly in both reactions (15) and (16) at 270 K by assuming that reaction (15) has the same heat as measured for it at 95 K over this same coverage range (0 to 0.04 ML), 96 kJ/mol.²⁰ Thus, the integral heat for step 1 up to 0.04 ML (163 kJ/mol) equals 96 kJ/mol plus x times ΔH_{16} , where ΔH_{16} is the heat of reaction (16). Similarly, the integral heat for step 2 (75 kJ/mol) equals $(1-x)$ times ΔH_{16} . Solving these two equations gives $x = 0.47$ and $\Delta H_{16} = 142$ kJ/mol, for the coverage range 0 to 0.04 ML. We also determined a time constant detection limit of 30 ms for the fraction x that reacts quickly in reaction (16) by simulating this exact same situation, only now adding a longer and longer time constant to the heat deposition of reaction (16) for that fraction x . We could not see any significant difference in the quality of the fit to the experimental lineshape until this time constant reached 30 ms, at which value the fit was noticeably worse. This detection limit of 30 ms is longer than the detection limit of 10 ms we determined for the simpler case where all the heat is deposited in a single slow step.

For coverages above 0.04 ML, reactions (17) and (18) also contribute to the net products, but mass spectroscopy showed that the methane product of reaction (18) is mainly produced on a time scale too slow to be seen by these heat measurements at 270 K.²⁰ Thus, the net reaction

measured calorimetrically is the sum of reactions (15) thru (17): $\text{CH}_3\text{I}_g \rightarrow \text{CH}_{\text{ad}} + 2 \text{H}_{\text{ad}} + \text{I}_{\text{ad}}$. At 0.07 ML, this heat (i.e., the sum of heats for steps 1+2) equals 189 kJ/mol (Fig. 4.6). This value gives an enthalpy of formation for CH_{ad} of +32 kJ/mol using the enthalpies of formation for the other species involved ($\text{CH}_3\text{I}_g = 14.6 \text{ kJ/mol}$,¹¹² I_{ad} at a coverage of 0.07 ML = 134 kJ/mol⁵¹, and $\text{H}_{\text{ad}} = -36 \text{ kJ/mol}$ ¹⁰⁷). This compares well to the range of values of +23 to +42 kJ/mol estimated from our measurements at 320 K where the reactions are fast and this deconvolution is not needed²⁰. Small differences are expected due to the effect of different coverages on the heats.

Using the above enthalpies of formation for $\text{CH}_{3,\text{ad}}$ at lower coverage (-71 kJ/mol) and CH_{ad} at higher coverage (+32 kJ/mol), together with the enthalpy of formation for H_{ad} at low coverage (-36 kJ/mol [21]) gives an enthalpy of +31 kJ/mol for net reaction (17).

The rate of reaction (16) must get slower due to site blocking at higher coverages. Thus, the fraction of reaction (16) that is fast (i.e., included in this analysis as ‘step 1’) should get smaller with increasing coverage. Consistent with this, the ‘fast’ heat in Fig. 4.6 decreases with coverage to a minimum value of ~100 kJ/mol at 0.1 ML, very close to the known heat for reaction (15) alone of 87 kJ/mol at 0.1 ML of $\text{CH}_3\text{I}_{\text{ad}}$ ²⁰. The slow heat is now dominated by reaction (16) but decreased by endothermic contributions from reactions (17). The quality of fits obtained in this coverage range are good (i.e., comparable to that shown in Fig. 4.5), indicating that, in spite of this mechanistic complexity, the net reaction may be approximated at each coverage by the simple two-step model of reaction (7) using pseudo-first-order kinetics in its rate-limiting step 2.

Note that the coverage shown in Figs. 4.6 and 4.7 is the total amount of CH_3I which reacts in any way with the surface to prevent it reappearing in the gas phase as CH_3I . Relating

this to the actual surface coverage of adsorbed species is complicated by these further dehydrogenation and hydrogenation products seen above 0.04 ML.²⁰

Similar heats of adsorption from SCAC at 320 K where deconvolution is not needed were used to estimate the standard enthalpies of formation (ΔH_f^0) and Pt—C bond energies for $\text{CH}_{3,\text{ad}}$ and CH_{ad} on Pt(111)²⁰, giving $\Delta H_f^0(\text{CH}_{3,\text{ad}}) = -53 \text{ kJ/mol}$, $\text{Pt—CH}_3 = 200 \text{ kJ/mol}$, $\Delta H_f^0(\text{CH}_{\text{ad}}) = 23\text{-}42 \text{ kJ/mol}$ and $\text{Pt—CH} = 552\text{-}571 \text{ kJ/mol}$.

The time constants for the slow step 2, τ , presented in Fig. 4.7 have each been converted into a pseudo-first-order rate constant, $k = \tau^{-1}$, (also shown in Fig. 4.7) as a function of coverage, all at 270 K. We can see that τ increases (k decreases) with coverage, indicating that the reaction proceeds more slowly as surface coverage increases. This is consistent with the mechanism proposed above for the slow step (and how it changes with coverage), since the proposed slow step (mainly reaction (16)) produces more adsorbed fragments and thus requires free sites. The linear decrease of k , extrapolating to zero at 0.16 ML, is consistent with a simple site-blocking model where the reaction stops when the total methyl iodide coverage is 0.16 ML (which gives a total adsorbate coverage of 0.33 ML or higher).

French and Harrison⁴⁶ reported an activation energy (E_{act}) for $\text{H}_3\text{C-I}$ bond cleavage in adsorbed CH_3I on Pt(111) (i.e., reaction (16)) of $48 \pm 3 \text{ kJ/mol}$ and a pre-exponential factor of $8 \times 10^{10 \pm 1.3} \text{ s}^{-1}$ at a coverage of 0.080 ML. These values give a rate constant at 270 K of 41 s^{-1} , but with an error range of a factor of 75 up or down. This agrees with the value of $\sim 3 \text{ s}^{-1}$ at 0.08 ML for step 2 here (Fig. 4.7). However, as noted above, reaction (16) occurs over about half of the surface with a rate constant that is faster than our detection limit ($\sim 30 \text{ ms}$ or $\sim 30 \text{ s}^{-1}$), also consistent with the rate measurements of French and Harrison.

The rate constants presented in Fig. 4.7 are very close to that measured for reaction (16) in a previous study by Hugenschmidt et al.,¹¹³ where the authors used bismuth postdosing thermal desorption mass spectroscopy (BPTDS) to determine an E_{act} of 53.6 kJ/mol for the scission of the C-I bond in $\text{CH}_{3,\text{ad}}$ on Pt(111) assuming a first order reaction and a pre-exponential factor of 10^{11} s^{-1} . This yields k equal to 4.3 s^{-1} at 270 K; identical to the average k value in Fig. 4.7 over the cover range 0 - 0.10 ML. We think this level of agreement is fortuitous for two reasons:

(1) The value by Hugenschmidt et al. was measured starting at saturation coverage of $\text{CH}_{3,\text{ad}}$ at 100 K and heating the surface. In that case, reaction (16) was surely rate limited by the desorption of $\text{CH}_{3,\text{ad}}$ to create free sites needed for dissociation, and therefore much slower than its true rate.

(2) We argued above that approximately half of reaction (16) measured here occurs faster than that part which gives the k value in Fig. 4.7, at least below 0.04 ML.

Note that the rate constants in Fig. 4.7 decrease with coverage. This finding is consistent with the BPTDS study, where the broadening of the TDS curve in comparison to a curve simulated using the calculated E_{act} was explained by either product inhibition of the dissociation reaction (thus decreasing the pseudo-first-order rate constant k) or lateral adsorbate-adsorbate interactions that cause the activation energy to increase with coverage.

If the decrease in k with increasing coverage is due to product inhibition, the true rate constant would occur at the zero-coverage limit. A linear fit to the k data yields the equation $k = 6.2(1 - \theta / 0.16)$ (shown in Fig. 4.7). Here θ is the coverage of dissociatively adsorbed methyl iodide. From this equation, we obtain the initial (true) rate constant, k_0 , of 6.2 s^{-1} and the coverage maximum, θ_{max} , of 0.16 ML. The k_0 of 6.2 s^{-1} was used to calculate an E_{act} of 53

kJ/mol for this process assuming a pre-exponential factor of 10^{11} s^{-1} .¹¹³ Note that the use of k values obtained at non-zero coverages, such as those from the BPTDS study discussed earlier, result in a larger calculated E_{act} energy.

As discussed previously, the observed decrease in k with coverage could instead be dominated by lateral adsorbate-adsorbate interactions that lead to an activation energy that decreases with coverage. To quantify this, we again assume a pre-exponential factor of 10^{11} s^{-1} to calculate E_{act} for $\text{H}_3\text{C-I}$ bond cleavage in adsorbed methyl iodide as a function of coverage. This gives $E_{\text{act}} = (53 \pm 22 \text{ kJ/mol})$, with an average value of 54 kJ/mol for the 0.1 ML coverage range studied. If we use instead the pre-exponential factor of 8×10^{10} estimated by French and Harrison,⁴⁶ the activation barriers are lowered uniformly by 0.5 kJ/mol.

From the heat of adsorption data shown in Fig. 4.6 and the activation energy of 53 kJ/mol, we can create an energy landscape for the complete reaction $\text{CH}_3\text{I}_g \rightarrow \text{CH}_3\text{ad} + \text{Iad}$, as seen in Fig. 4.8. All enthalpies used are in the limit of zero coverage, obtained from linear fits to the heat of adsorption data. We have used here the initial heat of molecular adsorption of CH_3I_g of 98 kJ/mol measured at 95 K where there is no competition with dissociation.²⁰ Formation of the final products $\text{CH}_3\text{ad} + \text{Iad}$ is downhill in energy by $179 \text{ kJ/mol} + 78 \text{ kJ/mol} = 257 \text{ kJ/mol}$, from Fig. 4.6. However, for the second step to occur, a barrier must be overcome. As noted above, this barrier is 53 kJ/mol on some “slow” parts of the surface, perhaps defects or where surface crowding has occurred even at the lowest coverage used to determine this value (0.01 ML). On ~50% of the surface, this step occurs with a time constant below the detection limit (~30 ms) and thus corresponds to a barrier below ~49 kJ/mol assuming a pre-exponential factor of 10^{11} s^{-1} . The barrier shown in Fig. 4.8 represents a maximum barrier, since it is only for the ‘slow’ parts of the surface. On the rest of the surface, it is below 49 kJ/mol.

4.5 Conclusions

It is demonstrated for the first time that kinetic information can be extracted from adsorption calorimetry measurements on single crystals. Traditional analysis of SCAC data required that the molecular process of interest occur much faster than the time scale of the experiment. This meant that for the study of a particular intermediate species, experimental conditions have to be found where the following two statements are true: (1) the intermediate of interest is produced on a time scale much faster than the measurement *and* (2) has a lifetime on a timescale much longer than the measurement. The new analysis method presented here which allows the separation of the detector response into two distinct heat deposition processes, one fast and one slow, now only requires that the intermediate be stable on a timescale similar to the heat measurement. This greatly expands the number of systems that can be studied using SCAC, and provides additional rate constant information. This new lineshape analysis method has been applied to study the dissociative adsorption of methyl iodide on Pt(111), providing the coverage-dependent heats and rate constants for this quasi-two-step reaction process at 270 K. The heats agree with values measured at 320 K where the rates are so fast that lineshape analysis is not needed, thus verifying the deconvolution analysis method presented here. The pseudo-first-order rate constant for the slow second step, k , obtained from this analysis decreases with surface coverage due to product inhibition. These data provide a complete energy diagram for the reaction $\text{CH}_3\text{I}_g \rightarrow \text{CH}_{3,\text{ad}} + \text{I}_{\text{ad}}$, and the formation energies of $\text{CH}_{3,\text{ad}}$ and CH_{ad} .

4.6 Figures

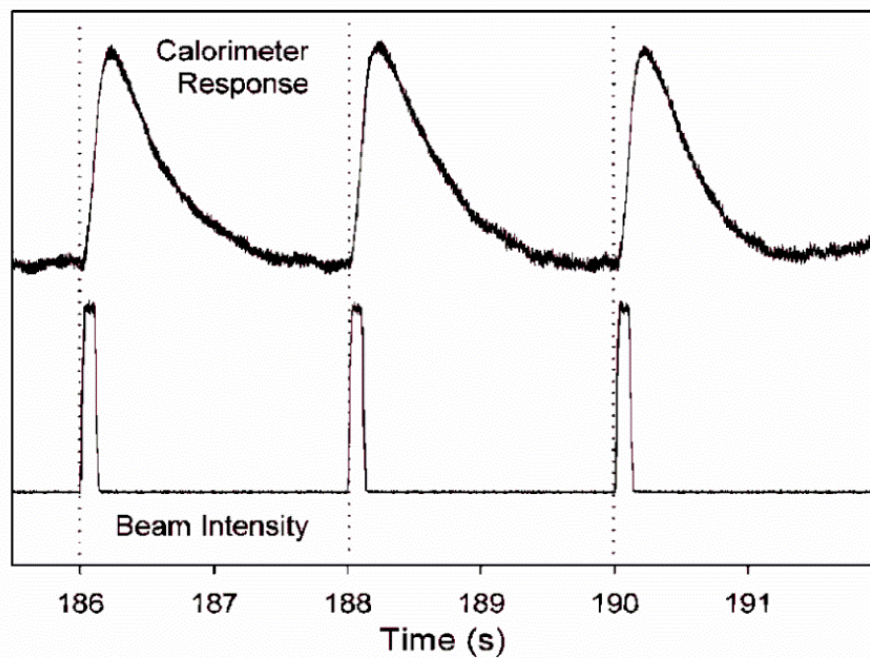


Figure 4.1: Typical heat detector response and beam intensity (mass spectrometer signal intensity, which is proportional to the molecular beam flux) for cyclohexene adsorption on Pt(111) at 102 K. Beam pulses are 100 ms in duration (FWHM) and repeated every 2 seconds. (Reprinted with permission from.¹⁰⁷ Copyright 2008 American Chemical Society.)

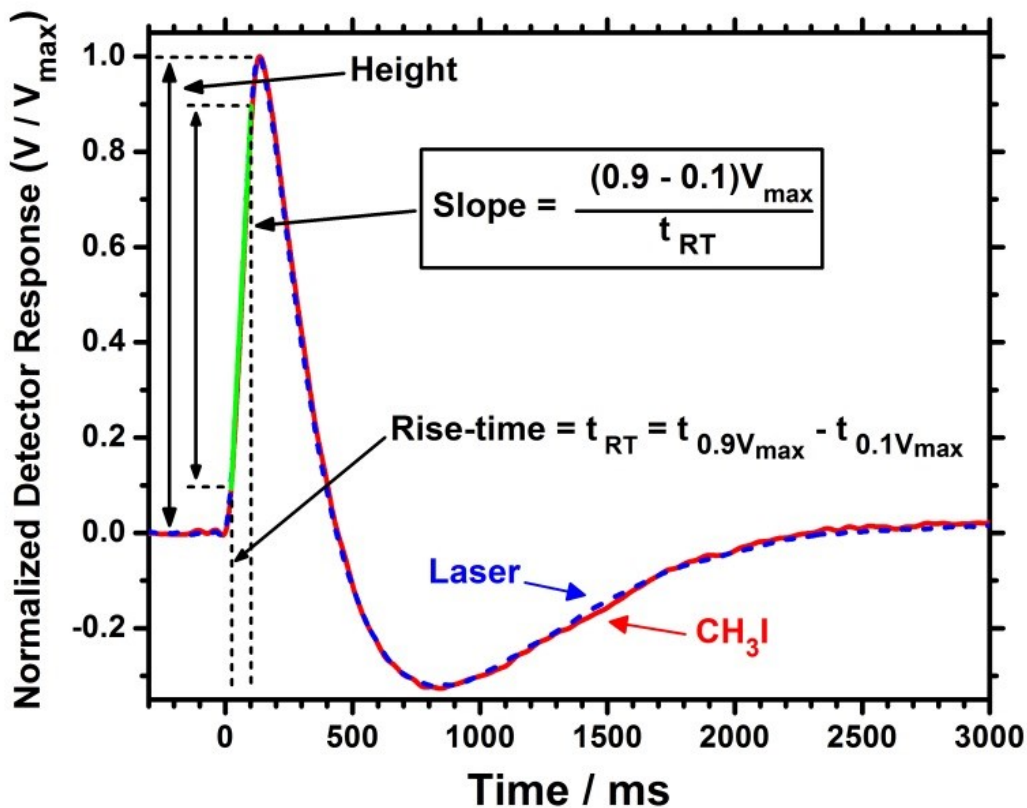


Figure 4.2: Heat detector response for a pulse of methyl iodide adsorbing on Pt(111) at 100 K (red) and for a laser pulse used to calibrate the signal (blue dashed). Each pulse was 102 ms long (FWHM) and repeated every 5 s (only the first 3 s are shown), and multiple pulses were averaged to improve signal to noise ratio. Also shown are demonstrations of measurements of the heat signal magnitude using either the peak height (from the initial baseline to the peak maximum, as shown) or the slope of the initial fast rise. The slope is obtained from a linear fit to the data between 10% and 90% of the peak maximum, as shown in green. The rise-time is defined as the time for the signal to rise through this 10% to 90% range, as shown.

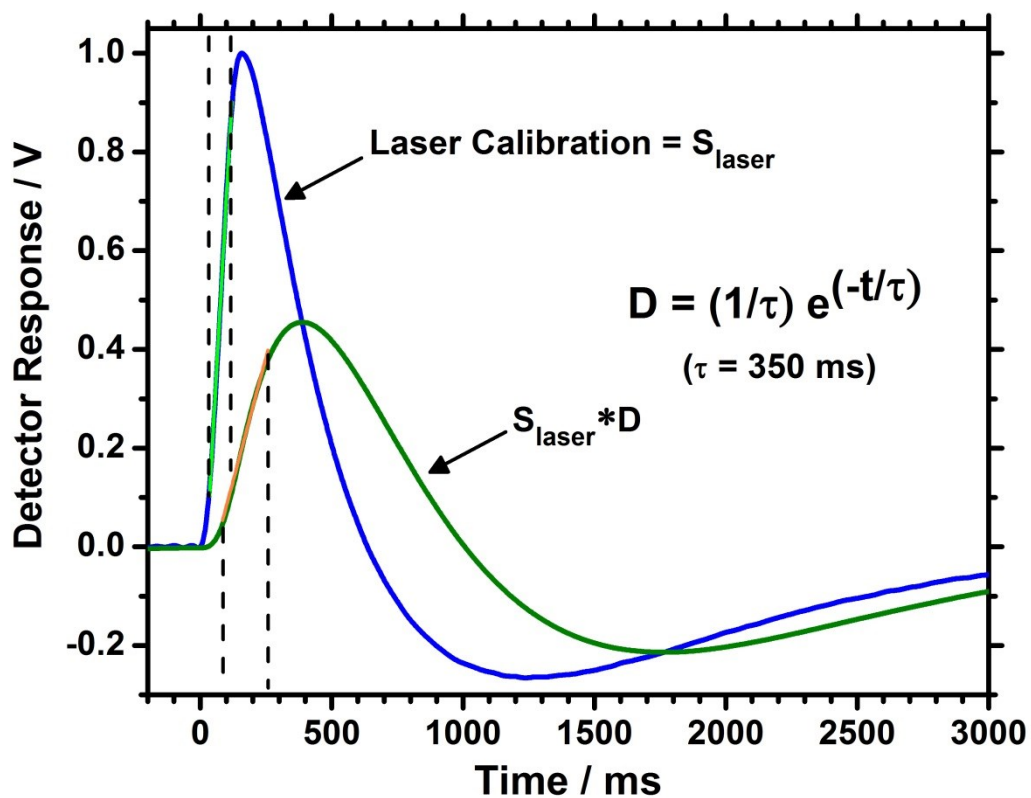


Figure 4.3: Detector responses to single pulses of the laser used for calibration (blue) and of the laser convoluted with a first-order decay with a time constant of 350 ms (green). This latter corresponds to a 2-step kinetic model where the first step (physisorption) is instantaneous but has negligible heat, and the heat is all deposited in the second, slow step whose rate constant is $(350 \text{ ms})^{-1}$.

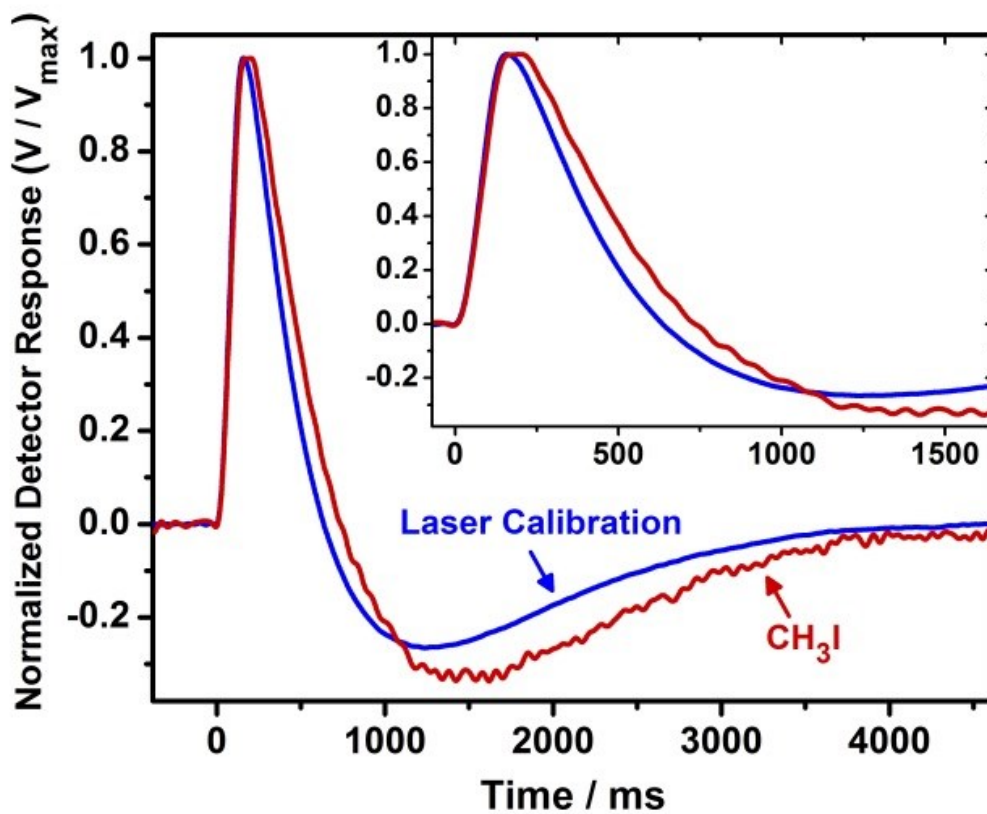


Figure 4.4: Normalized detector responses for the laser calibration and molecular adsorption of methyl iodide on Pt(111) at 270 K. The response from molecular adsorption is broadened due to slow heat deposition. The inset shows the same pulses on a shorter timescale.

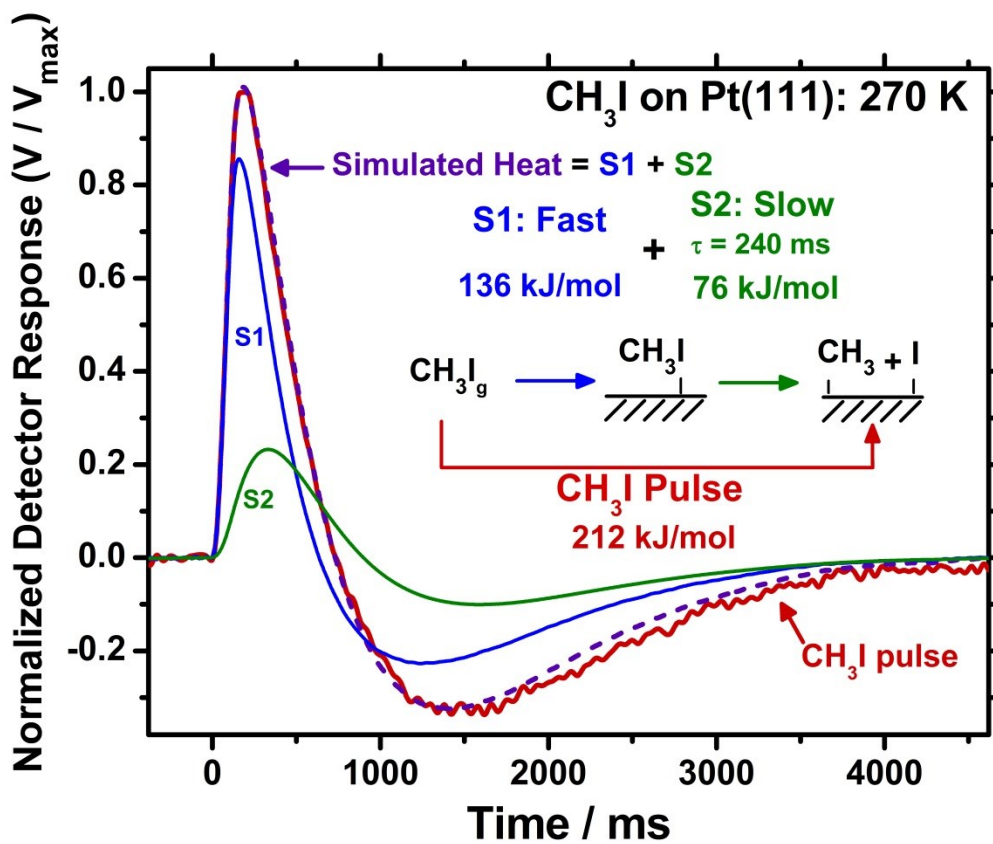


Figure 4.5: Simulated heat pulse (purple dashed) of 212 kJ/mol created using values obtained from the best fit method for the third average methyl iodide pulse (0.037-0.055 ML) on Pt(111) at 270 K (red). This simulated heat pulse is the sum of the fast step 1 heat (blue) of 136 kJ/mol and slow step 2 heat (green) of 76 kJ/mol that is deposited with a τ of 240 ms. Also shown for comparison is the normalized measured signal for pulses of CH₃I adsorption at these conditions.

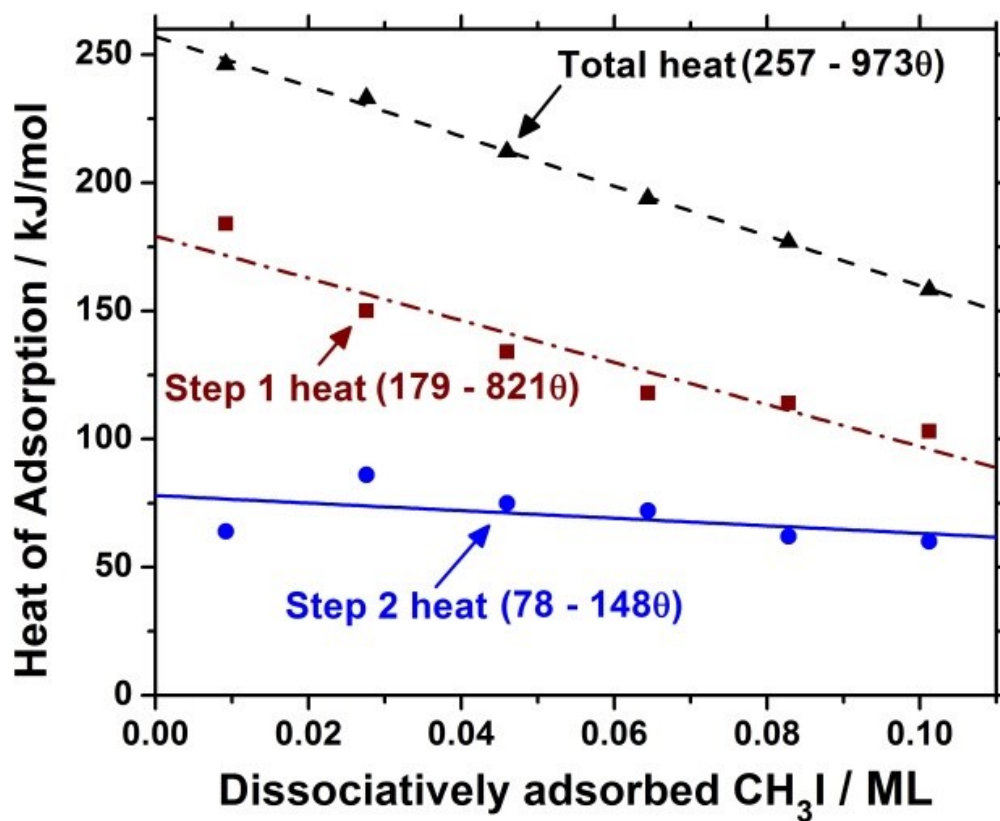


Figure 4.6: Calculated total differential heat of adsorption (black triangles), Step 1 heat (red squares) and Step 2 heat (blue circles) for methyl iodide pulses on Pt(111) at 270 K as a function of dissociatively adsorbed methyl iodide coverage, θ , in ML. Lines through the data show the best-fit straight lines.

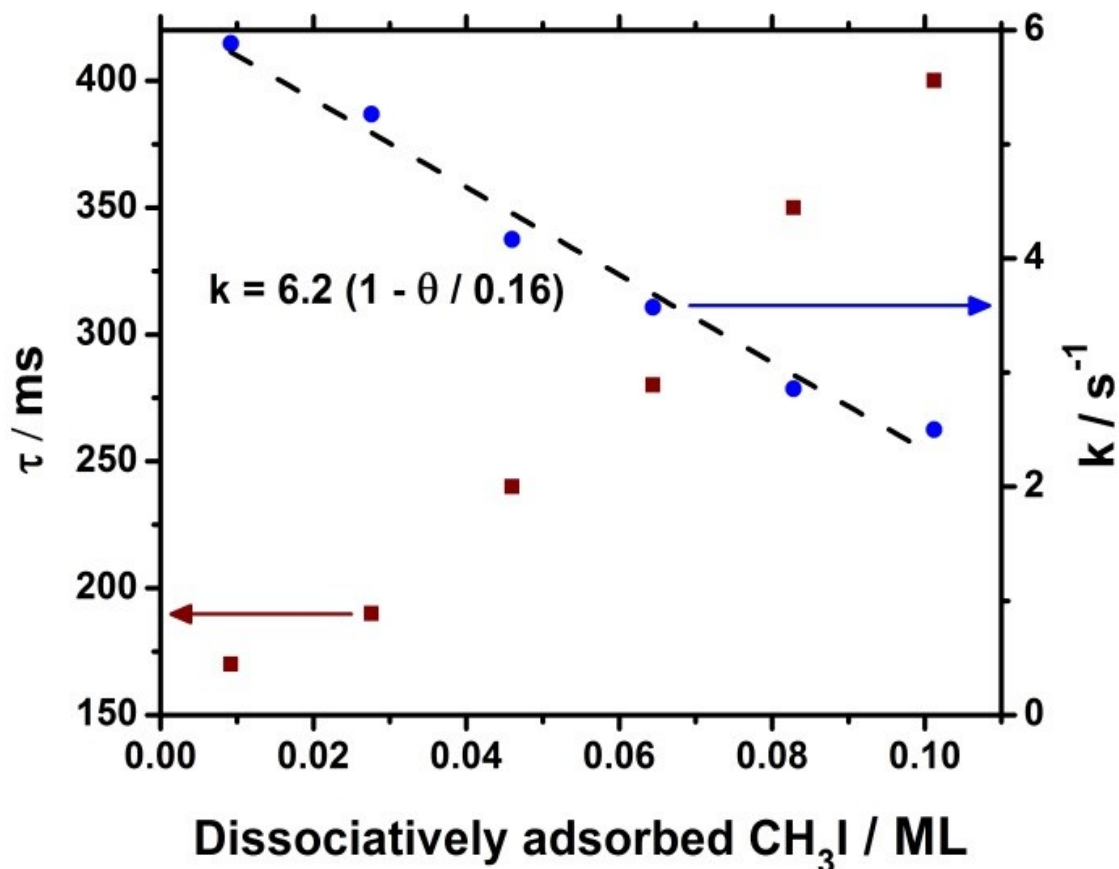


Figure 4.7: Time constants for the dissociation of adsorbed CH₃I on Pt(111) (red squares), in ms, obtained from the best-fit analysis of methyl iodide pulses on Pt(111) at 270 K as a function of total amount of dissociatively adsorbed methyl iodide coverage, θ , in ML. The rate constants (k , blue circles), in s⁻¹, are the inverse of the time constant (τ^{-1}). $k = k_0 (1 - \theta/\theta_{\max})$ with a k_0 of 6.2 sec⁻¹ and a θ_{\max} of 0.16 ML.

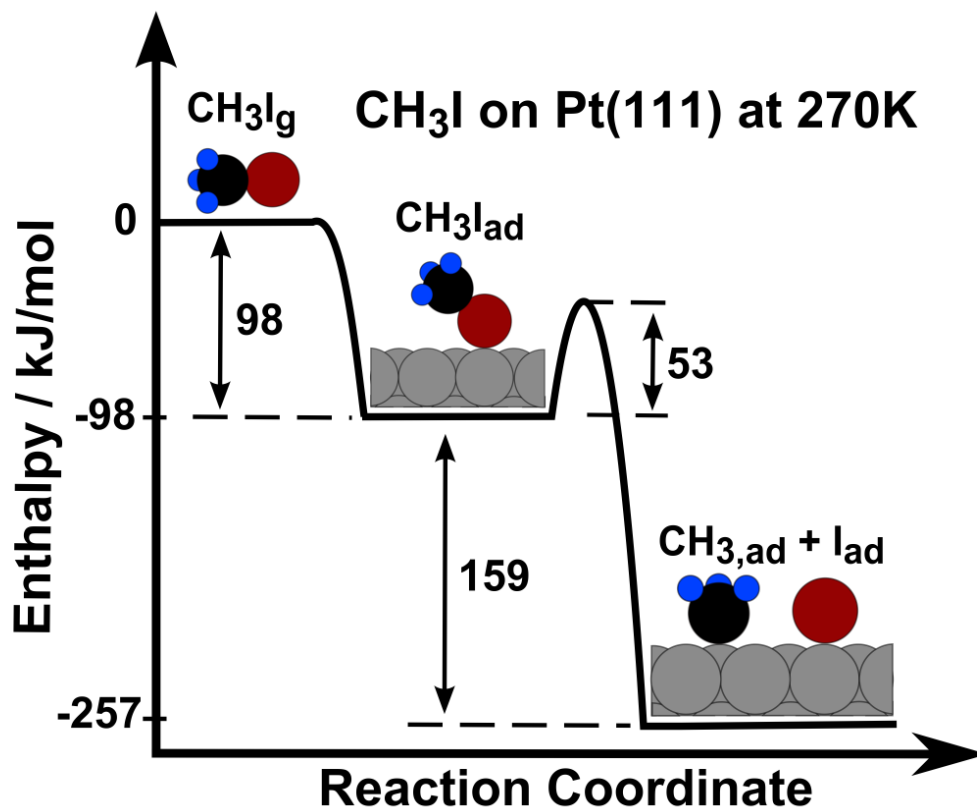


Figure 4.8: Energy landscape for the reaction of $\text{CH}_3\text{I}_g \rightarrow \text{CH}_{3,\text{ad}} + \text{I}_{\text{ad}}$ on Pt(111) at 270 K at the limit of zero coverage. The enthalpy of $\text{CH}_3\text{I}_{\text{ad}}$ relative to CH_3I_g was obtained from SCAC at 95 K when only that first step occurs.²⁰ The total reaction heat of -257 kJ/mol was obtained from the linear fit to the total heat of adsorption versus coverage data (Fig. 6). The activation energy for the second step was estimated using the k_0 value of 6.2 s^{-1} obtained from the linear fit to the experimental k versus coverage data (Fig. 7), assuming a pre-exponential factor of 10^{11} s^{-1} . It corresponds to the slow parts of the surface, with a barrier below $\sim 49 \text{ kJ/mol}$ on $\sim 50\%$ of the surface.

Chapter 5

Energetics of formic acid conversion to adsorbed formates on Pt(111) by transient calorimetry

5.1 Introduction

Surface carboxylates, of which formate is the simplest, are common species in many catalytic reactions and are used as linkers for attaching alkyl chains and other organic functional groups to surfaces. Adsorbed formate has been investigated as a potential catalytic intermediate in many catalytic reactions on Pt, including the water-gas shift reaction,^{114,115} methanol oxidation and direct methanol fuel cells,¹¹⁶⁻¹²⁰ and is probably present in many oxidation and steam reforming reactions as well. The surface interactions of organic molecules containing -COO⁻ and -COOH groups, including amino acid residues, peptides, and proteins, are also important for the organo-functionalization of surfaces,¹²¹ the synthesis of size- and shape-controlled inorganic nanoparticles^{121,122} and their use in medical applications,¹²³ medical implants,¹²⁴ chemical sensors and many other areas. However the heat of formation has not been measured for *any* well-defined surface formate nor for *any* other carboxylate on *any* surface. Here we report experimental measurements of the enthalpies of formation and bond strengths of adsorbed formate in both monodentate and bridge-bonded bidentate bonding configurations on Pt(111), produced by the dissociative adsorption of formic acid. This surface is the most thermodynamically stable face of platinum and therefore the most studied as a model catalyst. The surface interactions of formic acid (HCOOH) itself have been studied due to its potential as a hydrogen storage material¹²⁵ and a fuel for direct formic acid fuel cells.¹²⁶

Surface science studies of HCOOH adsorption on Pt(111) have found that, when the surface is pre-dosed with oxygen adatoms, formic acid deprotonates to form adsorbed formate (HCOO_{ad}), OH_{ad} and/or $\text{H}_2\text{O}_{\text{ad}}$.¹²⁷⁻¹²⁹ The OH_{ad} product in those studies was assigned based on comparison to vibrational spectra for OH_{ad} produced by dosing water to oxygen-dosed Pt(111), which was later proven to actually be a $(\text{H}_2\text{O}-\text{OH})_{\text{ad}}$ complex^{104,130}, so this $(\text{H}_2\text{O}-\text{OH})_{\text{ad}}$ complex is the most likely product, rather than OH_{ad} alone as originally proposed. Adsorbed formate has been observed in the monodentate structure on Pt(111), that then converts to the more stable bridge-bonded bidentate formate at higher temperature.¹²⁷ Carboxyl ($-\text{COOH}$) has been suggested by DFT calculations to be an important but unstable intermediate on Pt in many reactions, most notably water-gas shift.^{114,115} However, it has never been observed experimentally, probably because it quickly converts to other species. So, while it might be produced in very small concentrations after dosing HCOOH to O / Pt(111), formates are the dominant products of that stoichiometry. This is consistent with the relative instability of carboxyl compared to formates on Pt(111) predicted by DFT.^{114,115}

Knowledge of fundamental thermodynamic information, especially the enthalpies of formation of adsorbed species on metal surfaces, allows us to better understand complex reaction mechanisms occurring on catalytic surfaces. The difficulty of obtaining this information experimentally is that the usual techniques (e.g. temperature programmed desorption (TPD) and equilibrium adsorption isotherms) require adsorbates to desorb reversibly. However, many adsorbates further react or decompose prior to desorption, thus limiting the utility of those techniques. As a result, experimentally determined enthalpies of formation of adsorbed molecular fragments and their adsorbate-surface bond enthalpies are still rarely available. An ultrahigh vacuum technique that can directly measure the heat released upon adsorption, known

as single crystal adsorption calorimetry (SCAC), was developed in King's group at Cambridge to overcome this problem^{5,7} and has been further improved by our group^{8,10}. This technique has been shown to be useful for determining the heat of many types of adsorption reactions, whether molecular, dissociative, reversible or irreversible.^{19,20,23,32,104,131} It has also been shown recently that an analysis of the heat detector's signal lineshape in SCAC can provide kinetic information for reactions occurring on the same timescale as the measurements (10-1000 ms).³⁴

In this study we investigated the adsorption of formic acid on clean and O-presaturated Pt(111) using SCAC between 100 and 190 K. From these heat measurements, we were able to extract the enthalpies of formation and bond strengths of adsorbed formate in both monodentate and bidentate bonding configurations on Pt(111), as well as that for molecularly adsorbed formic acid.

5.2 Experimental

Experiments were performed in an ultrahigh vacuum (UHV) chamber (base pressure $< 2 \times 10^{-10}$ mbar) with capabilities for single crystal adsorption microcalorimetry and surface analysis, as described previously.^{10,102} Briefly, the chamber is equipped for X-ray photoelectron spectroscopy (XPS), Auger electron spectroscopy (AES), low energy ion scattering spectroscopy (LEIS) and LEED. The sample was a 1 μm thick Pt(111) single crystal foil, supplied by Jacques Chevallier at Aarhus University in Denmark. The sample cleaning procedures that were used in this study are described elsewhere.¹⁰⁷ A detailed description of the experimental principles and implementation of the molecular beam flux, sticking probability and heat measurements can be found elsewhere.^{10,102,107} Briefly, the Pt(111) sample was exposed to a pulsed molecular beam of formic acid. Each pulse was 102 ms long and repeated every 2.0 s at 100 K and every 5.0 s at 150 and 190 K. After loading formic acid (Fisher Chemical, Optima LC/MS $\geq 99.5\%$) into a

glass reservoir under N₂ atmosphere and subsequent mounting on the vacuum chamber, the liquid was outgassed by five freeze-pump-thaw cycles. Its purity was verified with a mass spectrometer in the UHV chamber and compared with spectra obtained with gas chromatography – mass spectrometry. Also, water was proven to be below the detection limit of 1% in the starting HCOOH using NMR, consistent with the manufacturer’s claim. The beam was created by expanding ~2 mbar of formic acid through a microchannel array and then collimated through a series of five liquid nitrogen cooled orifices. The microchannel array was heated to 360 K to reduce gas phase dimerization to <1%.¹³² This was verified by mass spectrometry by monitoring the ratio of the *m/e* 46 and 47 signals¹³³ as a function of microchannel temperature. Pulses were created by mechanically chopping the beam using a spinning plate that has had a small slit removed.

Surface coverages are reported here in monolayers (ML) and are defined as the number of formic acid molecules which adsorb onto the surface irreversibly, independent of the actual species they form on the surface following adsorption. We define one monolayer (ML) of adsorbate coverage as being equal to the density of Pt atoms in the Pt(111) surface ($1.50 \times 10^{19} \text{ m}^{-2}$). A typical formic pulse is 0.0095 ML ($\sim 2 \times 10^{12}$ molecules).

The flux of formic acid from the molecular beam is measured by impinging the beam onto a liquid nitrogen cooled quartz crystal microbalance (QCM). A unity sticking probability of formic acid onto the QCM was ensured by precovering the QCM with multilayers of formic acid. Calibration of the QCM has been described previously.¹⁰ The heat released from the adsorption of one formic acid pulse to the sample surface is measured with a pyroelectric polymer ribbon gently pressed against the back side of the platinum sample, as described previously.¹⁰² The

indicated references provide a more in-depth discussion of heat transfer between sample and ribbon.⁹

The sensitivity of the pyroelectric detector was calibrated after each experiment by depositing pulses of a known amount of energy into the sample using a HeNe (632.8 nm) laser, as described previously.¹⁰² The error in absolute accuracy of the calorimetric heats (after averaging >5 runs) is estimated to be less than 3% for systems like those studied here which have sticking probabilities above 0.8, based on comparisons of our measurements to literature values when forming multilayers with known energies for four different molecules.¹⁹ (This error is due to possible errors in the absolute flux, heat signal calibrations and in the literature values.) Relative measurements (e.g. differences in heat with increasing coverage) are much more accurate, due to the high precision in heat measurements within a run. The sample temperature was controlled during calorimetry as described previously.¹⁰⁵

The time scale of our heat measurement is comparable to the beam-pulse duration (~100 ms). If the molecular adsorption/reaction process occurs on a time scale of ~10 ms or less, the heat signal line shapes measured during molecular and laser pulses are identical, allowing for the comparison of the peak heights or instantaneous slopes to extract the deposited energy from a molecular pulse.^{8,107} Heat deposited on a timescale of ~10 ms or longer results in broadening of the detector response line shape. The detector response of formic acid pulses on clean Pt(111) at 100 K were not broadened with respect to the laser calibration. At 100 and 150 K on O-saturated Pt(111), a secondary heat deposition process occurred with a time constant of ~170 and ~130 ms respectively at all times, requiring a more complex data analysis method as described previously.³⁴ At 190 K on O-saturated Pt(111), a slight pulse sharpening occurred due to water

desorption with a time constant of ~ 600 ms, which was sufficiently slow to not affect the initial slope of the pulse shape.

The Pt(111) surface was exposed to a chopped molecular beam of formic acid, and the sticking probabilities and the heats of adsorption were measured as a function of formic acid coverage. A mass spectrometer was used to monitor the background pressure increase of formic acid ($m/e = 46$) in the chamber. A room temperature gold flag was positioned in front of the sample and used to determine the mass spectrometry signal corresponding to full reflection of formic acid. The sticking probability is calculated by comparing the time-integrated mass spectrometer signals measured from the increase in formic acid partial pressure above background from molecular beam pulses onto the sample surface and onto the inert gold flag. We report two types of sticking probabilities: the long-term sticking probability, which is defined as the probability that molecules in a gas pulse stick during the full duration of the pulse repeat period (5 s), and the short-term sticking probability, which is defined as the probability that molecules in a gas pulse stick on the surface until the end of the ~ 140 ms time period used to measure the heat signal, measured as described previously.¹⁰⁷ The long-term sticking probability is used to calculate the coverage at the start of the next pulse, and the short-term sticking probability is used to calculate adsorption energies per mole adsorbed.

Due to the transient sticking of a small amount of formic acid on the vacuum chamber walls, a slightly different procedure from that described in the paper cited above was required to measure these sticking probabilities. These sticking probabilities were measured using both the true King and Wells method with non-line-of-site (NLOS) detection³⁶ and a modified King and Wells method which uses line-of-sight (LOS) detection⁸. For the modified King and Wells

method, the flag blocking LOS to the mass spectrometer was removed, giving direct line-of-sight to the sample.

The results from these two types of sticking probability measurements showed two minor but significant differences:

(1) When the sticking probabilities were constant and not changing with time, the value determined from the LOS measurements were found to differ slightly in absolute magnitude from the NLOS measurements due to the different temperatures of the sample and gold flag and their different positions relative to the mass spectrometer ion source, which lead to errors in the non-sticking reference signal in the LOS measurements, not present in the NLOS measurements. Since the NLOS measurements give the true value for the non-sticking fraction, the LOS measurements of this fraction can be scaled to the true NLOS value.

(2) When the surface saturates, there is often a sharp decrease in the sticking probability, or an increase in the non-sticking fraction measured. This increase in mass spectrometer signal was always observed to occur several pulses sooner using LOS than the NLOS measurements. This delay in the NLOS signal is attributed to the transient consumption of a small amount of formic acid by the chamber walls. The result is a higher apparent saturation coverage in the NLOS measurements. This does not occur in LOS measurements since the majority of detected molecules do not contact the chamber walls.

Thus, neither sticking probability measurement is completely accurate except when $S = 1$, since both the LOS and NLOS measurements would lead to one type error or the other. The NLOS measurements are accurate in absolute value when S is constant (i.e., at both low and high coverages), but not when S is rapidly decreasing. We therefore use the LOS values here, but

scale their magnitude so that they agree with the sticking probabilities from the NLOS data at coverages where S is constant.

5.3 Results

5.3.1 Sticking Probability

The short- and long-term sticking probabilities of formic acid on clean and O-saturated Pt(111) were measured at several temperatures, as shown in Fig. 5.1. Here, O-saturated (or O-sat.) Pt(111) refers to a Pt(111) surface covered with 0.25 ML of oxygen adatoms. The sticking probabilities at 100 K were obtained using NLOS data only, while those for 150 and 190 K were measured using the LOS data but scaled using the NLOS data as described above. The initial sticking probabilities are high (> 0.9) at all temperatures, and their constant or even increasing values with coverage indicate a precursor-mediated adsorption mechanism.¹⁹ The increase in sticking probability over the first 0.25 ML is due to mass matching between adsorbates and incoming molecules and has been observed previously for both H_2O ^{17,104} and methanol¹⁹ on O-sat. Pt(111). A clear temperature dependence of the saturation coverage of formic acid on Pt(111) can be seen in Figure 5.1. At 100 K, formic acid continues to populate a multilayer state upon saturating the surface. However at 150 K, the sticking probability decreased rapidly above 0.4 ML and dropped to zero at 0.52 ML. This lack of multilayer growth at 150 K is consistent with TPD results that report a multilayer desorption peak beginning at ~ 130 K and peaking at 160-170 K.¹²⁸ The sticking probability at 190 K begins decreasing sharply at 0.25 ML and reaches zero at a saturation coverage of 0.31 ML.

5.3.2 Heat of Adsorption

From the literature, it is known that formic acid adsorbs molecularly on clean Pt(111) at 100 K.^{129,133} Our measurements at 100 K (Fig. 5.2) show that the initial heat of formic acid

molecular adsorption is 65 kJ/mol and drops slowly to 60 kJ/mol at 0.25 ML. From 0.25 ML to 0.5 ML, the heat of adsorption decreases more quickly, falling to 52.8 ± 2.5 kJ/mol at 0.5 ML. This coverage of 0.5 ML (7.5×10^{18} molecules/m²) is similar to the saturation coverages of both the α -phase and β -phase of formic acid adsorbed on graphitized Ni(110), where molecule-surface interactions are minimal, of 7.0 and 6.2×10^{18} molecules/m² respectively.¹³⁴ The slightly higher packing density seen here may be due to the stronger binding to, and the packing density and geometry of sites on, the Pt(111) surface. The heat above 0.5 ML remains level at 52.8 ± 2.5 kJ/mol as subsequent layers are populated.

We can compare this multilayer heat to multilayer desorption of formic acid from TPD data available in the literature.¹³³ We estimate an activation energy for desorption of 50 kJ/mol from the reported peak temperature of 170 K¹³³ using simple first-order Redhead analysis.⁸⁹ For this, we estimated a prefactor of $10^{15.4}$ s⁻¹ following the entropy method developed by Sellers and Campbell^{89,135} using the gas-phase entropy of formic acid at 170 K of 248.7 J/(mol K)¹³⁶. To compare this TPD value to our results, we must also add to it $\frac{1}{2} RT$, giving 50.7 kJ/mol. The agreement is quite good, with this TPD value falling within the error of our measurements. This confirms the absolute accuracy of our calorimetric heats.

Below 143 K, adsorption of formic acid at high coverage results in the formation of an amorphous multilayer rather than the more stable crystalline α -phase.^{137,138} Our measured heat of adsorption at 100 K therefore corresponds to the binding of formic acid in an amorphous multilayer and is consequently lower than the heat of sublimation of ~ 60.5 kJ/mol¹³⁹ obtained above 200 K for the crystalline α -phase.

In order to describe the calorimetry results obtained at 100 and 150 K on O-saturated Pt(111), we must first describe a new heat detector signal-lineshape analysis method developed

in our lab.³⁴ The necessity for this new method comes from the observation that if all, or some fraction, of heat deposition from molecular adsorption occurs on a timescale of 10-1000 ms for a pulse length of ~102 ms, a visible broadening of the detector response pulse for molecular adsorption is seen relative to the laser calibration response.³⁴

The following is a brief description of this analysis method, which is described in detail elsewhere.³⁴ This method involves fitting the detector response using a two-step reaction sequence with a single rate-limiting step. The first step is fast and its heat is deposited on a timescale much faster than the pulse duration, as is common, for example, in simple molecular adsorption. Since it is fast, its heat signal pulse lineshape is well represented by the lineshape obtained from the laser heat calibration experiment. The second step is slower, and deposits heat on the same timescale of the heat measurement. This can be due to activated dissociation of an adsorbed molecule, or some activated conversion of some quickly-adsorbed molecular fragment (for example, the conversion of mono-dentate formate to bi-dentate formate). It is responsible for the observed pulse broadening and is fit using the laser calibration lineshape convoluted with an exponential decay for a first-order reaction. The time constant of this exponential decay is a fitting parameter, and is equal to the inverse of the reaction rate constant for this process. The fraction of heat in each of these two steps and the time constant are adjusted until the simulated pulse (SP) (sum of the two pulse lineshapes) best fits the experimental heat pulse (EH). From this analysis method, we are able to obtain heats of adsorption for the first step (labeled “Fast” in Fig. 5.2) and the sum of the first and second steps (labeled “Total” in Fig. 5.2) as well as the reaction time constant, τ , for the slow second step.

A representative broadened detector lineshape is shown in Fig. 5.3 along with the best-fit simulated pulse obtained from the sum of pulse lineshapes representing a fast (S1) and a slow

(S2) heat deposition process. This particular pulse was obtained for formic acid adsorption on O-sat. Pt(111) at 150 K, and was well fitted with a S1 heat of 79 kJ/mol, S2 = 36 kJ/mol and $\tau = 100$ ms ($k = 10$ s⁻¹). For this analysis method, groups of five consecutive pulses were averaged to improve signal to noise. As a consequence, the heat data points reported for the 100 and 150 K experiments represent doses of 0.0475 ML. The negative voltage region in these signals is due to the detector preamplifier (which has both integrating and differentiating components), and is seen with laser pulses as well. It does not indicate an endothermic process.

As was observed for methyl iodide adsorption on Pt(111) at 270 K^{20,34}, dosing of formic acid on O-sat. Pt(111) at 100 and 150 K resulted in noticeably broadened pulse lineshapes. Pulseshape analysis therefore provides two heats of adsorption (“fast” and “total”) for each pulse.

Dosing of formic acid on O-sat. Pt(111) at 100 K results in fast heats of adsorption that are similar to those seen on the clean Pt(111) surface, Fig. 5.2. This is consistent with calorimetry experiments of H₂O adsorption on clean and O-sat. Pt(111) at 100 K, where the heats of molecular adsorption of H₂O were nearly unaffected by the presence of adsorbed oxygen atoms (increasing by only 3.7 kJ/mol).¹⁷ The initial fast heat of adsorption (i.e. at the zero coverage limit) is 65 kJ/mol and decreases linearly with increasing coverage. However, unlike the H₂O experiments, a second, slower reaction (with a τ of 170 ± 19 ms) deposits additional heat here, of magnitude almost 30 kJ/mol initially but decreasing with coverage. The initial total heat of adsorption of formic acid on O-sat. Pt(111) at 100 K is the sum of the heats for these two steps, or ~ 90 kJ/mol initially followed by a linear decrease with coverage. The data shown in Fig. 5.2 at 100 K on O-sat. Pt(111) is the average of 3 experiments.

Dosing of formic acid on O-sat. Pt(111) at 150 K results in fast heats of adsorption that are similar to the total heats measured on the O-sat. Pt(111) surface at 100 K. This makes sense since any chemical step with a τ of 170 ms at 100 K should be much faster than the timescale of the experiment (i.e., <10 ms) already at 150 K. The heat of adsorption, initially 91 kJ/mol, decreases linearly with increasing coverage and eventually falls to 60 kJ/mol at a coverage of 0.4 ML (Fig. 5.2). The heat remains constant at 60 kJ/mol up to 0.5 ML. As seen at 100 K on O-sat. Pt(111), this fast heat deposition is followed by a second slow process, this time with a τ of 130 ± 13 ms. The total heat of adsorption in the limit of zero coverage is 131 kJ/mol and decreases linearly to 100 kJ/mol at 0.25 ML. This is followed by a slightly sharper drop between 0.25 and 0.3 ML (100 to 84 kJ/mol) and then a slow linear decrease between 0.3 and 0.5 ML, eventually ending at 60 kJ/mol. The data shown in Fig. 5.2 at 150 K on O-sat. Pt(111) are the average of five experiments.

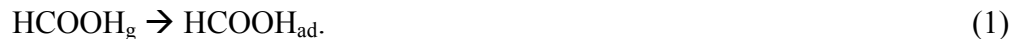
Formic acid dosed on O-sat. Pt(111) at 190 K exhibits a linearly decreasing heat of adsorption up to 0.25 ML. A linear fit to this data gives the equation $(110-45.8\theta)$ kJ/mol, where θ is the total HCOOH coverage in ML. Between 0.25 and 0.31 ML, a much sharper linear decrease is seen, falling from a heat of adsorption of 99 kJ/mol at 0.25 ML to 60 kJ/mol at 0.31 ML.

5.4 Discussion

5.4.1 Formic acid chemistry on clean and O-saturated Pt(111)

To interpret the above results, we must first discuss the temperature-dependent chemistry of formic acid on O-sat. Pt(111). The reactions posed in the following paragraphs are drawn from the existing body of literature as well as observations from the current report.

As already discussed, formic acid molecularly adsorbs on clean Pt(111) at 100 K¹³³ as given by the reaction:



However on the O-sat. Pt(111) surface, high resolution electron energy loss spectroscopy (HREELS) was used to show that formic acid deprotonates at 100 K.¹²⁸ This promotion of deprotonation by adsorbed atomic oxygen has been observed previously for formic acid, alcohols and other acids (e.g. methanol, acetic acid) on several metal surfaces (e.g. Pt(111)^{128,129,140}, Cu(110)¹⁴¹, Rh(111)¹⁴², Ag(110)¹⁴³).

This loss of the acid proton of HCOOH was reported to lead to the formation of *both* monodentate and bidentate formate adsorbed to Pt(111) at 100 K.¹²⁸ However, in that study, the authors assigned the dual peaks at 1330 and 1630 cm⁻¹ (the two peaks were of nearly equal magnitude) to the presence of bidentate and monodentate formate, respectively, citing earlier work by Avery¹²⁷. These assignments are inconsistent with the cited report by Avery,¹²⁷ which assigned two peaks of equal magnitude at 1290 and 1620 cm⁻¹ to the presence of *only* monodentate formate. It is also important to note that these experiments that initially observed the monodentate formate species, performed at 130 K, found that the monodentate species was stable on the order of minutes, converting to a bidentate formate species in the time it took to run a second HREELS scan (~10 minutes). It seems unlikely that a monodentate species would convert to a bidentate configuration at 100 K if the conversion was observed to be so slow at 130 K. We therefore conclude that formic acid deprotonates to form *only* monodentate formate at 100 K.

The presence of hydroxyl groups was observed for low and high submonolayer coverages of formic acid at 170 K and 130 K respectively, consistent with the observed low-coverage water

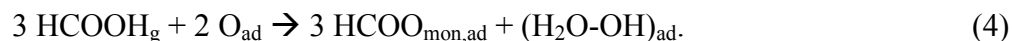
desorption peak at 205 K in TPD arising from the recombination of adsorbed –OH groups.¹²⁸ This TPD peak broadened to lower temperatures with increasing formic acid coverage, eventually exhibiting a peak maximum characteristic of the desorption of pure adsorbed H₂O at 170-175 K. This explains why only this low temperature TPD peak (180 K) was observed by Avery, as his experiments were performed at much higher formic acid coverages.¹²⁹ We therefore adopt the reaction scheme below, whereby adsorbed oxygen and then hydroxyl are sequentially protonated by the acid H of HCOOH. At low coverage, formic acid first adsorbs molecularly:



and then donates its acid proton to adsorbed oxygen to form adsorbed monodentate formate and hydroxyl:



However, it is well known that OH_{ad} on Pt(111) quickly converts to a (H₂O-OH)_{ad} complex at 150 K and above,¹⁰⁴ so that the net reaction observed at low coverages and 150 or 190 K is then the more complex reaction:



Although this (H₂O-OH)_{ad} complex is quickly formed by dosing water to O_{ad} on Pt(111) at 150 K, it is not yet formed at 100 K.^{17,104} However, it might be formed by dosing HCOOH to O_{ad} at 100 K, and our heat results suggest it does, as discussed below. The production of co-adsorbed water has already been proposed for the reaction of adsorbed formic acid with atomic oxygen on Pt(111)¹²⁸, Ag(110)¹⁴³, and Rh(111)¹⁴².

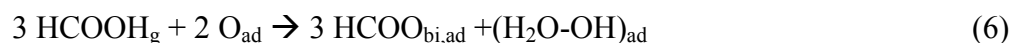
Given that the saturation coverage of O_{ad} on Pt(111) is 0.25 ML, reaction (4) can proceed to a coverage of 0.375 ML of adsorbed formate. This is consistent with the coverage where the

heats drop to that characteristic of molecular adsorption at 150 and 190 K in Fig. 5.2, given that this drop may be broadened by heterogeneity in local surface coverage.

As noted previously, a slow transition to bridge-bonded bidentate formate was observed at 130 K by HREELS,¹²⁷ as given by



At 150 K and above, reaction (4) will therefore be followed by reaction (5), ultimately giving the net reaction:



at saturation.

Mass spectrometry measurements of the water signal (not shown) revealed the desorption of a water pulse following each formic acid pulse at 190 K on O-sat. Pt(111) at low coverages. This water pulse had a tail that was reasonably well fit by an exponential decay with a time constant of ~100 ms. This is consistent with the report that water is stable in the water-OH complex on Pt(111) at 150 K, but shows significant desorption within 2 s at higher temperatures.¹⁰⁴ Similarly, HREELS experiments after dosing HCOOH to O_{ad} on Pt(111) observed the disappearance of H₂O_{ad} upon heating to 190 K.^{127,128} Therefore, at 190 K, some water desorption must also be considered in analyzing the heat data.

We can now discuss our calorimetry results in the context of known formic acid chemistry on Pt(111), by assigning particular reactions to each heat of adsorption curve (Fig. 5.2). As discussed earlier, both the total heat on clean Pt(111) at 100 K and the fast heat on O-sat. Pt(111) at 100 K can be assigned to molecular adsorption, as given by either reaction (1) on clean Pt(111) or reaction (2) on O-sat. Pt(111), respectively. On the O-sat. surface, a second,

slow heat deposition is also seen, and can be assigned to the deprotonation of formic acid via reaction (3) at low coverage and 100 K.

At 150 K, the deprotonation of HCOOH_{ad} to form OH_{ad} is much faster than the timescale of our measurement. As noted above, the water-OH complex is also quickly formed at this temperature. Thus, we assign the fast heat at 150 K to reaction (4) up to 0.375 ML. The agreement between the fast heats at 150 K and the total heats at 100 K on O-sat. Pt(111) indicate that we can also assign the total heats at 100 K to reactions (4) up to 0.375 ML. As expected from HREELS, a second, slower step is observed at 150 K that we can assign to the subsequent conversion of monodentate to bidentate formate, reaction (5). The total heats at 150 K therefore correspond to the sum of reactions (4) and (5), i.e., net reaction (6), up to 0.375 ML.

At 190 K, the net reaction should also be reaction (6). However, because the desorption of H_2O during each pulse occurs with a time constant (~ 100 ms) comparable to the time used for heat measurement (140 ms), some fraction of H_2O desorbs during heat detection, and the rest remains adsorbed. This means that the total heats of adsorption instead represent a combination of reaction (6) but with some fraction of the $(\text{H}_2\text{O-OH})_{\text{ad}}$ complex decomposing to release water vapor. This is clear in the initial (low coverage) total heats of adsorption that are $\sim 15\text{-}20$ kJ/mol lower at 190 K than at 150 K. We attribute this to the fact that some of the water desorb at 190 K from the water-OH complex (which has a heat of adsorption of ~ 60 kJ per mole of water when formed from water vapor plus $\text{O}_{\text{ad}}^{104}$). Because the stoichiometry of reaction (6) requires three formic acid molecules to make one $(\text{H}_2\text{O-OH})_{\text{ad}}$, and each $(\text{H}_2\text{O-OH})_{\text{ad}}$ produces $3/2$ $\text{H}_2\text{O}_{\text{g}}$ molecules upon thermal decomposition, only half of this 60 kJ/mol (i.e., 30 kJ/mol) is consumed by water desorption per formic acid molecule adsorbed. The measured initial heat at 190 K is only 15-20 kJ/mol lower than at 150 K, implying that only about 50-65% of the $(\text{H}_2\text{O-OH})_{\text{ad}}$

complex decomposes in the time of the heat measurement at 190 K. Note also that the difference between the heats at 190 K versus 150 K decreases with increasing formic acid coverage until it drops to zero at a coverage of 0.25 ML.

5.4.2 Enthalpies of Formation of Monodentate and Bidentate Formate on Pt(111)

As discussed above, our measurements represent the heats of reaction upon formic acid adsorption. Using available literature values for the heats of formation of various gas phase and adsorbed molecules, we can use these measured heats of reaction to determine the enthalpies of formation of adsorbed formate (both monodentate and bidentate) and the HCOO-Pt(111) bond enthalpies.

Based on the above discussion, the integral heat of fast adsorption at 3/8 ML and 150 K (76 kJ/mol from integrating the curve in Fig. 5.2) corresponds to the complete consumption of adsorbed oxygen to form adsorbed monodentate formate and the water-hydroxyl complex (reaction (4)). Figure 5.4 shows how to combine this heat in a thermodynamic cycle with other known literature values to calculate the enthalpy of formation of monodentate formate ($\Delta H_f(\text{HCOO}_{\text{mon,ad}})$). The bottom path starts with elements in their standard state. The bottom left arrow uses the enthalpies of formation of gas phase formic acid (-379.2 ± 0.6 kJ/mol)¹⁴⁴ and adsorbed atomic oxygen.¹⁴⁵ The enthalpy of formation of atomic oxygen used here is calculated using the integral heat of dissociative O₂ adsorption at 0.25 ML coverage (-99 ± 8 kJ/mol O).¹⁴⁵

Note that all positive heats of adsorption in Fig. 5.2 represent exothermic processes. In this section, all positive heats of adsorption have been converted to negative enthalpies of reaction for use in thermodynamic cycles. The bottom right-hand arrow in Fig. 5.4 represents our measurement, with an integral enthalpy of reaction of -76 kJ/mol (the fast reaction only at 150 K and 3/8 ML).

The central path in Fig. 5.4 takes elements from their standard states directly to the adsorbed products. The central path must equal the sum of the two steps in the bottom path, thus allowing us to calculate the standard enthalpy of formation of monodentate formate, $\Delta H_f(\text{HCOO}_{\text{mon,ad}})$, to be -354 kJ/mol, using the known enthalpy of formation of adsorbed water-hydroxyl complex ($\Delta H_f((\text{H}_2\text{O}-\text{OH})_{\text{ad}})$), -503 kJ/mol.¹⁴⁵

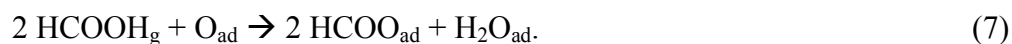
Similarly, we can use this thermodynamic cycle to calculate the Pt-O bond enthalpy for adsorbed monodentate formate. The upper left arrow in Fig. 5.4 proceeds from elements in their standard state to the gas phase formate radical and $(\text{H}_2\text{O}-\text{OH})_{\text{ad}}$ using the enthalpies of formation of the formate radical (-129.7 ± 12.6 kJ/mol)⁴⁸ and $\Delta H_f((\text{H}_2\text{O}-\text{OH})_{\text{ad}})$ (-503 ± 7 kJ/mol). The only unknown in the complete upper path is the arrow representing the negative of the $\text{HCOO}-\text{Pt}(111)$ adiabatic bond dissociation enthalpy ($D(\text{Pt}-\text{OOCH})$), which is then calculated as 224 kJ/mol.

Using the integral total heat up to 3/8 ML at 150 K (-106 kJ/mol) rather than the fast S1 heat as in Fig. 5.4 (-76 kJ/mol), we can use the same methodology to calculate $\Delta H_f(\text{HCOO}_{\text{bi,ad}})$ and the $\text{HCOO}_{\text{bi}}-\text{Pt}(111)$ bond enthalpy for bidentate formate, where the only difference to Fig. 5.4 is the number of O-Pt bonds created (2 rather than 1) and the measured heat. This gives the enthalpy of formation of bidentate formate ($\Delta H_f(\text{HCOO}_{\text{bi,ad}})$) to be -384 kJ/mol and the net bond enthalpy of $\text{HCOO}_{\text{bi,ad}}$ to the Pt(111) surface to be 254 kJ/mol, or 127 kJ/mol for each of the two Pt-O bonds. Note that this is almost 100 kJ/mol less than the single Pt-O bond enthalpy for monodentate formate above.

Similarly, we can calculate the enthalpy of formation and $\text{HCOO}-\text{Pt}(111)$ bond enthalpy for monodentate and bidentate formate at intermediate coverages using the integral heat between 0 and 0.375 ML total HCOOH coverage, where some fraction of the 0.25 ML of adsorbed

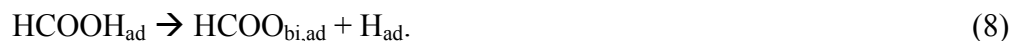
oxygen has been consumed via reaction (4)). As seen in Fig. 5.5, this allows us to calculate the coverage dependent enthalpy of formation of monodentate and bidentate formate. If we calculate these enthalpies assuming either reaction (4) or (6) for the fast or total heat at 150 K respectively, we obtain values indicated by blue square symbols in Fig. 5.5. Linear fits to this data provide equations for the coverage dependent enthalpy of formation of monodentate formate, $\Delta H_f(\text{HCOO}_{\text{mon,ad}}) = -(367 - 41 \theta)$ kJ/mol, and bidentate formate, $\Delta H_f(\text{HCOO}_{\text{bi,ad}}) = -(410 - 74 \theta)$ kJ/mol, where θ is the total number of HCOOH molecules adsorbed per Pt(111) surface atom. As discussed above, this reaction stoichiometry is best supported by spectroscopic data available in the literature.

We have also calculated these same enthalpies of formation assuming the formation of adsorbed water instead of the adsorbed water-hydroxyl complex, as given by



The enthalpies of formation calculated with the stoichiometry from reaction (7) (red triangles in Fig. 5.5) give enthalpies of formation that are more exothermic by ~ 5 kJ/mol, showing that the enthalpies of formate formation are quite insensitive to our proposal that the final structure of the H atom abstracted from the formic acid is as the water-OH complex instead of as simply adsorbed water. Nevertheless, we believe the literature is most consistent with the products represented by the upper curves (blue points) in Fig. 5.5.

We can use these enthalpies of formation determined here to predict the energetics of important elementary reactions such as the deprotonation of formic acid on clean Pt(111) to form adsorbed bidentate formate and a hydrogen adatom (H_{ad}), given by



Using the enthalpies of formation of bidentate formate at 0.375 ML (-382 kJ/mol), H_{ad} at zero coverage (-36 kJ/mol)¹⁰⁷, and formic acid gas (-379.2 kJ/mol) and the enthalpy of molecular adsorption of formic acid (-62.5 kJ/mol), the enthalpy of reaction (8) is found to 24 kJ/mol *uphill* in energy (i.e. $-382 + -36 - (-379.2 + -62.5) = 24$ kJ/mol). However this reaction is *exothermic* by 4 kJ/mol using instead the enthalpy of formation of formate at the zero coverage limit. The shift from exothermic to endothermic occurs when the enthalpy of formation of formate is -406 kJ/mol at a coverage of 0.06 ML. Since monodentate formate is 30-40 kJ/mol less stable than bidentate formate (Fig. 5.5), dehydrogenation of adsorbed formic acid to make monodentate formate plus H_{ad} is always endothermic, by ~40-50 kJ/mol depending on coverage.

The above enthalpies indicates that a much lower final coverage of formate can be expected on a clean Pt(111) surface than on a surface precovered with atomic oxygen. This is consistent with previous experiments that observed ~6-7 times lower coverages of adsorbed formate on the clean Pt(111) than on O-sat. Pt(111).¹²⁹ These energetics show that the presence of a proton acceptor (e.g. O_{ad} or OH_{ad}) cause this deprotonation reaction to become a much more thermodynamically favorable process at low coverage and allow the deprotonation process to be remain exothermic at higher coverages.

As noted above, the lower initial total heat of adsorption at 190 K relative to the total heat at 150 K is due to the desorption of H_2O formed during reaction (6). As mentioned earlier, this difference, initially 15-20 kJ/mol at zero coverage, decreases with increasing formic acid coverage until a coverage of 0.25 ML where the difference falls to zero. Above 0.25 ML, the heat of adsorption at 190 K falls sharply until the sticking probability reaches zero at ~0.31 ML. The decrease in the difference in the heats between the two temperatures coincides with a decrease in the intensity of the water desorption pulse seen in the mass spectrometer. This may

indicate that adsorbed formate stabilizes the water hydroxyl complex, making decomposition of the complex slower at higher formate coverage. The sharp decrease in heat and lower saturation coverage at 190 K (0.31 ML) than at 150 K is likely due to competition between desorption and deprotonation of formic acid at 190 K. After $\frac{1}{4}$ of surface sites are occupied, a formic acid molecule becomes increasingly more likely to desorb rather than deprotonate, consistent with the sticking data shown in Fig. 5.1.

5.5 Conclusions

The enthalpies of formation of monodentate and bidentate formate on Pt(111) are -354 ± 5 and -384 ± 5 kJ/mol respectively at $\frac{3}{8}$ ML coverage. The total formate-Pt(111) bond enthalpy in adsorbed monodentate formate is 224 ± 13 kJ/mol. The total bond enthalpy of bidentate formate to Pt(111) (two Pt-O bonds) is 254 ± 13 kJ/mol. The integral heat of adsorption of molecularly adsorbed formic acid on clean Pt(111) at 100 K is 62.5 kJ/mol at 0.25 ML. These enthalpies give the enthalpy of the reaction $\text{HCOOH}_{\text{ad}} \rightarrow \text{HCOO}_{\text{bi,ad}} + \text{H}_{\text{ad}}$ to be -4 kJ/mol at zero coverage and +24 kJ/mol at 0.375 ML. The first layer of molecularly adsorbed HCOOH saturates at a coverage of 0.5 ML at 100 K. Saturation coverages of bidentate formate on O-saturated Pt(111) at 150 and 190 K are 0.5 and 0.31 ML respectively.

Chapter reprinted with permission from ¹⁴⁶. Copyright 2014 American Chemical Society.

5.6 Figures

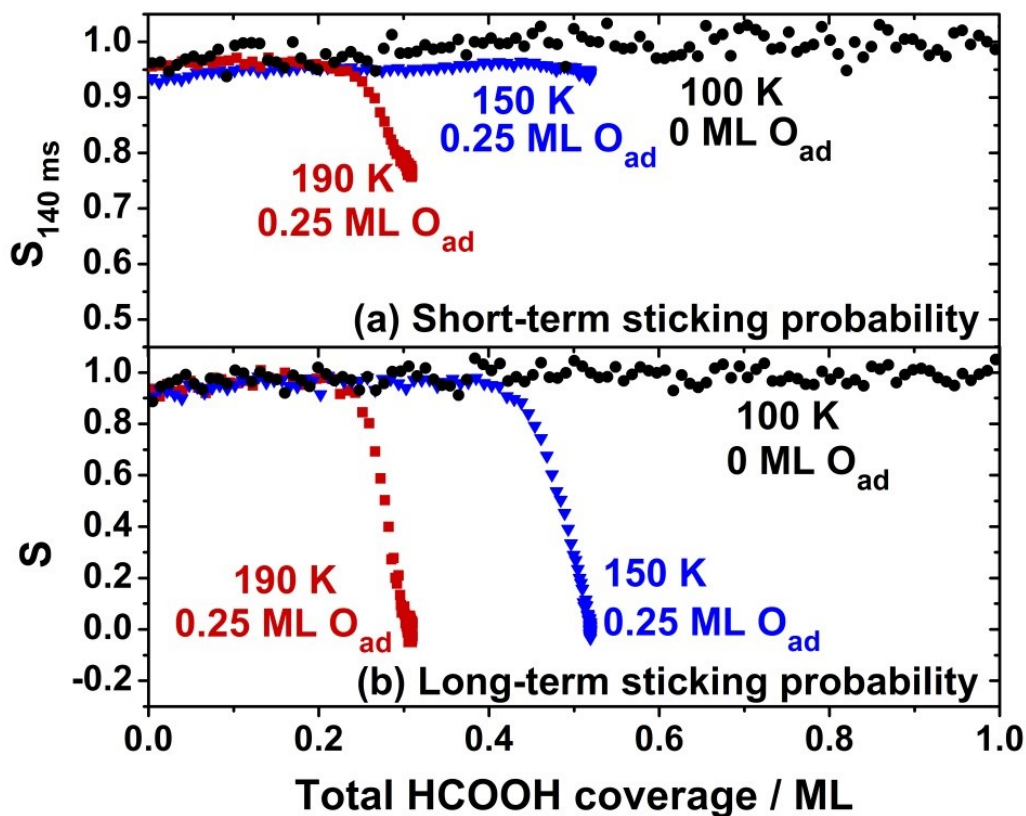


Figure 5.1: (a) Short-term and (b) long-term sticking probabilities of formic acid on clean Pt(111) at 100 K and O-saturated Pt(111) at 150 and 190 K as a function of the total formic acid coverage that adsorbed (irrespective of its final structure after adsorption). Although not shown, the sticking probabilities at 100 K on O-saturated Pt(111) were very similar to those shown here on clean Pt(111) at 100 K.

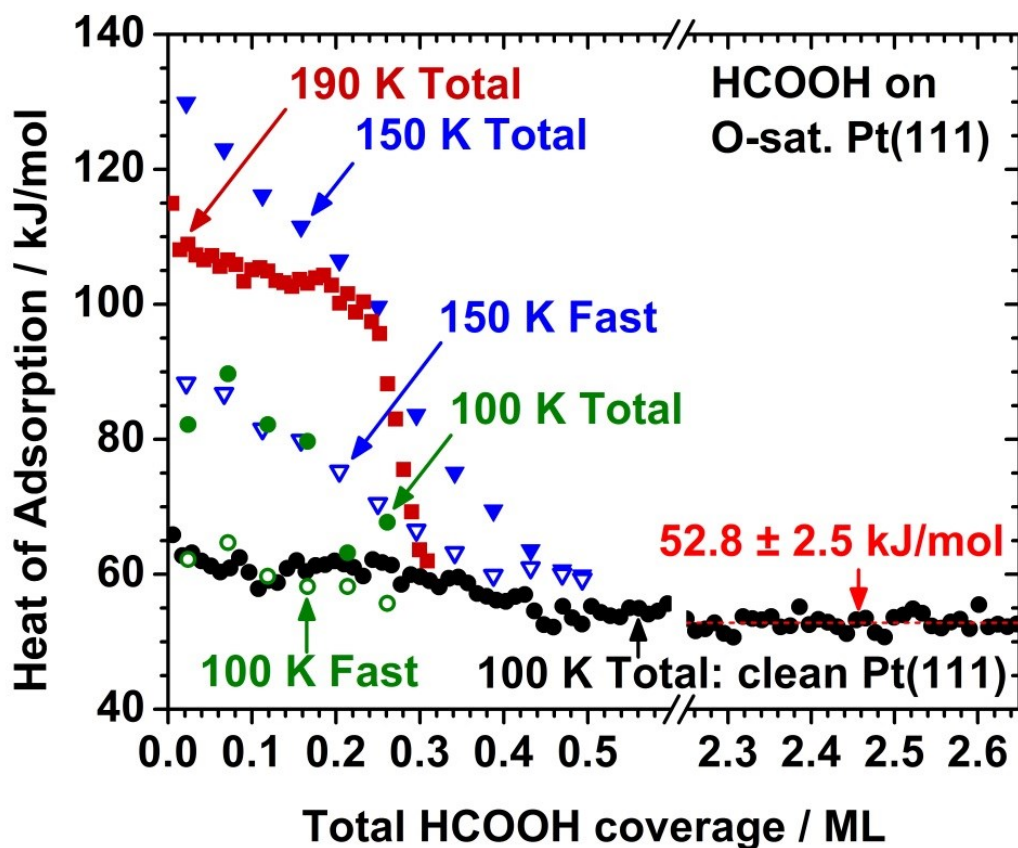


Figure 5.2: Heats of adsorption measured at various temperatures on clean Pt(111) at 100 K (black circles) and O-saturated Pt(111) at 100 K (hollow and solid green circles), 150 K (hollow and solid blue triangles) and 190 K (red squares) as a function of total coverage of adsorbed HCOOH, irrespective of its final structure. Hollow symbols represent fast heat deposition steps while solid symbols represent total heats (i.e., the sum of fast and slow steps). The multilayer heat of adsorption is indicated by a dotted line through the 100 K data in the lower right corner.

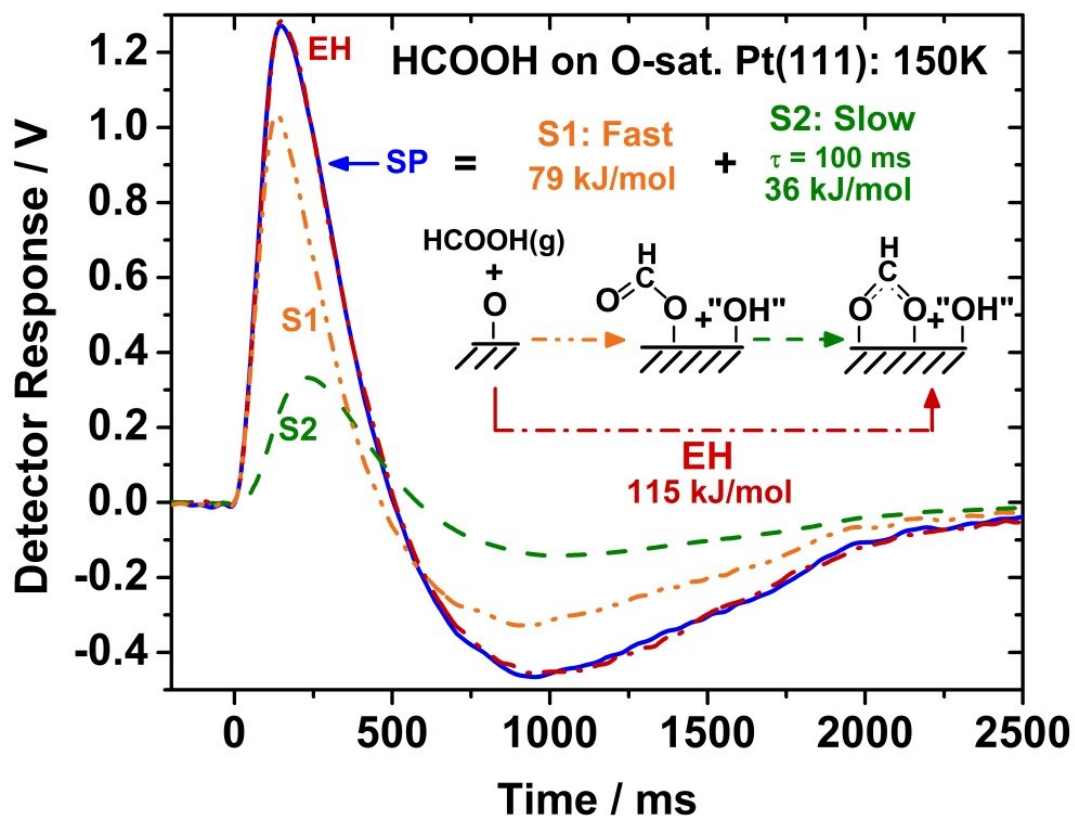


Figure 5.3: Experimental and simulated pulses obtained from a best-fit analysis of formic acid on O-sat. Pt(111) at 150 K. The experimental heat-signal pulse (EH) is an average over the coverage range 0.13-0.18 ML. The simulated pulse (SP) fits EH so well that the curves can barely be distinguished. This confirms the accuracy of the parameters (i.e. S1 and S2 heats and the slow step time constant, τ) obtained from this analysis. The species "OH" here is short for the water-OH complex, with the stoichiometry really being that of reaction (4).

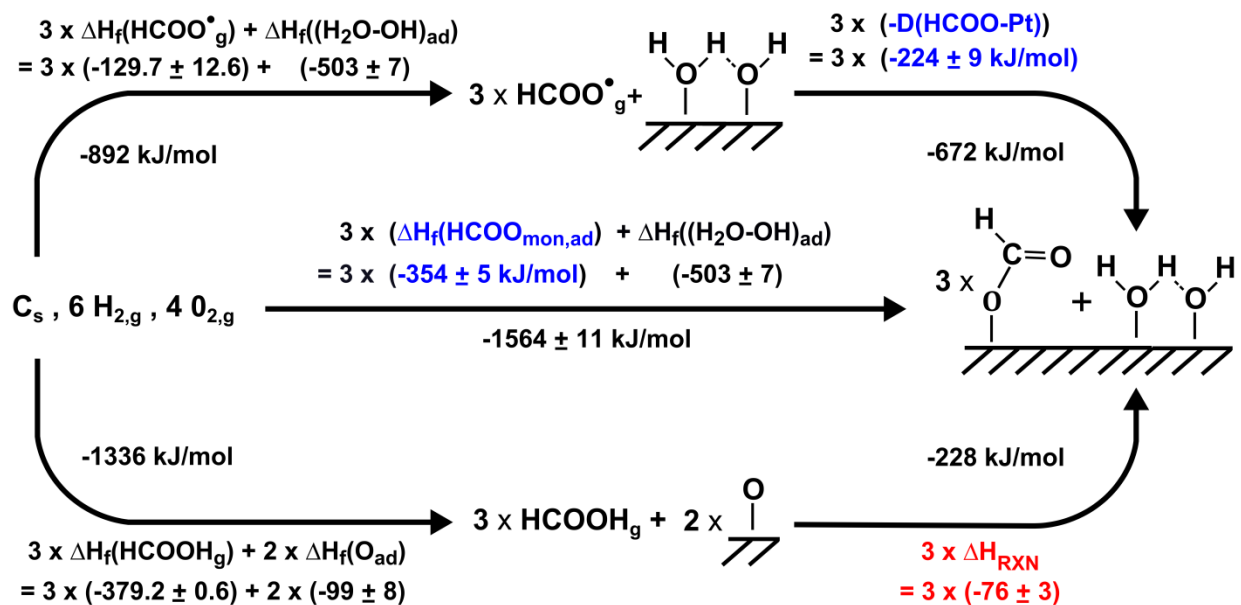


Figure 5.4: Thermodynamic cycle used to determine the enthalpy of formation of adsorbed monodentate formate on Pt(111) and its HCOO-Pt(111) bond enthalpy from the integral fast S1 heat of adsorption at 150 K and 3/8 ML, shown as the bottom right-hand step. References for literature values are listed in the text.

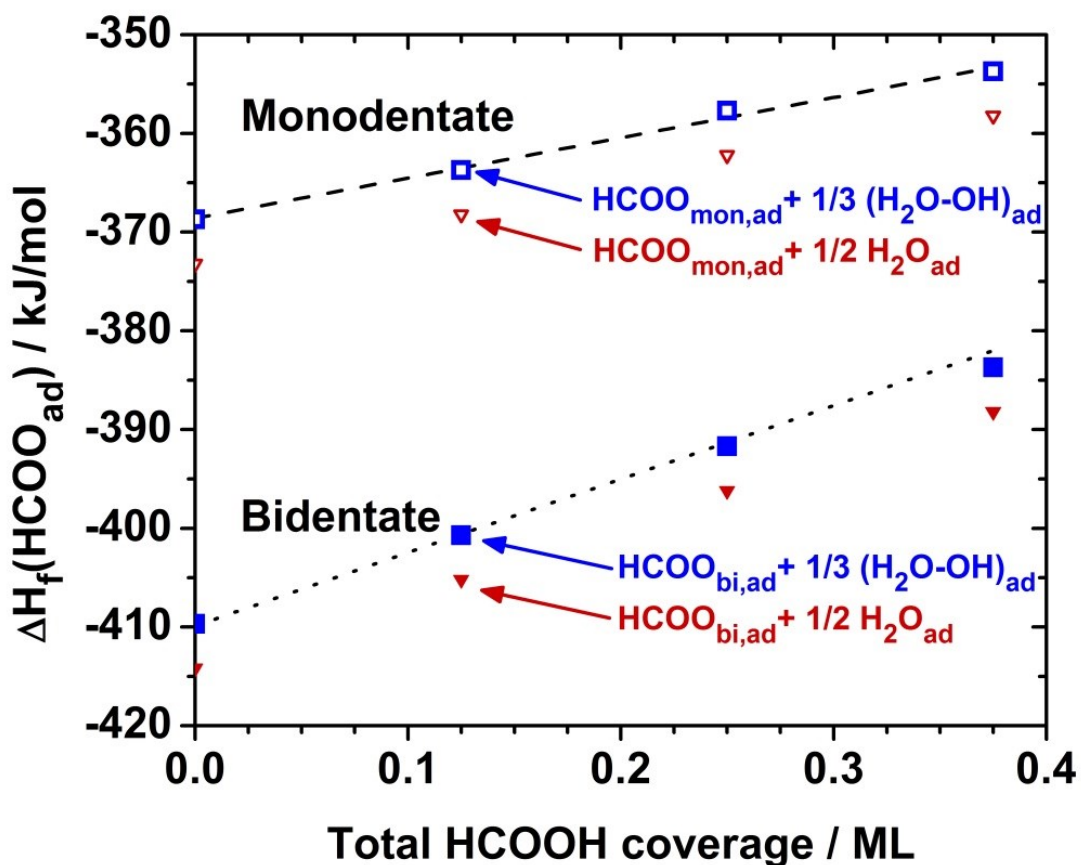


Figure 5.5: Enthalpy of formation of adsorbed monodentate and bidentate formate species ($\Delta H_f(\text{HCOO}_{\text{ad,mon}})$ and $\Delta H_f(\text{HCOO}_{\text{ad,bi}})$ respectively) as a function of total formic acid coverage. The enthalpies of formation of formate are determined using integral heats of reaction measured at 150 K on O-sat. Pt(111) along with other known enthalpies of formation in a thermodynamic cycle as shown in Fig. 4. The listed coadsorbates (i.e. $(\text{H}_2\text{O-OH})_{\text{ad}}$ and $\text{H}_2\text{O}_{\text{ad}}$) refer to the stoichiometry used in the thermodynamic cycles.

Chapter 6

Energetics of Methanol and Formic Acid Oxidation on Pt(111): Mechanistic Insights from Adsorption Calorimetry

The catalytic and electrocatalytic oxidation and reforming of methanol and formic acid have received intense interest due to potential use in direct fuel cells and as prototype models for understanding electrocatalysis. Consequently, the energetics of the adsorbed intermediates and elementary steps have been estimated on Pt(111) by density functional theory (DFT) in many studies. However, no experimental measurements of these energetics have been reported, nor is there a consensus on the mechanisms. Here, we use energies of key intermediates on Pt(111) from single crystal adsorption calorimetry (SCAC) and temperature programmed desorption (TPD) to build an energy diagram for these reactions. It suggests a new pathway involving monodentate formate as a key intermediate, with bidentate formate only being a spectator species that slows the rate. This helps reconcile conflicting proposed mechanisms.

Methanol in excess oxygen has been shown to produce bridge-bound formate species on Pt surfaces and ultimately CO₂ gas.^{117,119} Evidence supports a parallel reaction scheme for the electrooxidation of methanol to either CO or directly to CO₂,^{147,148} with a bidentate formate observed during reaction and proposed as the active intermediate in direct methanol combustion on Pt electrodes.¹⁴⁹ The mechanism of the oxidation and electrooxidation of formic acid and surface bound formate on Pt are thus also critical for understanding methanol oxidation and reforming.

In formic acid and methanol electrooxidation on Pt, it is accepted that the mechanism involving adsorbed CO is a minor pathway to CO₂,^{128,150} but the pathway for the dominant

mechanism is contested. Some propose that bidentate formate is the active intermediate,¹⁵¹⁻¹⁵³ while other experimental^{154,155} and DFT¹⁵⁰ studies suggest that bidentate formate contributes minimally to overall CO₂ production and inhibits catalyst activity by occupying active sites. This led to the proposal of three parallel pathways to CO₂: one primary path plus minor routes via formate and CO. ¹⁵⁵ DFT on Pt(111) suggested that the active intermediate in the main path is adsorbed carboxyl (-COOH).¹⁵⁰ Other DFT calculations show that the oxidation of bidentate formate to CO₂ through a monodentate formate intermediate may be facile in the presence of adsorbed water.¹⁵⁶ Recently, Joo et al. concluded that “weakly bound formate” is the key intermediate in the direct pathway.¹⁵⁷

Figure 1 shows the reaction enthalpy diagram for methanol and formic acid oxidation and decomposition based on experimental measurements on Pt(111) (in the absence of solvent, as for most DFT studies^{71,158}). All enthalpies of formation (ΔH_f) used here were determined from SCAC and TPD studies under ultrahigh vacuum conditions and are listed in the supporting information in Table S1, along with gas-phase literature values. Details about the specific reactions measured in SCAC experiments and literature references are also provided in the supporting information.

The conversion of methoxy to CO_{ad} or HCOOH_{ad}/HCOO_{ad} (either mono. or bi.) is highly exothermic (> 250 kJ/mol *downhill*) and therefore thermodynamically favorable, consistent with the observation that oxygen availability drives the reaction down this pathway. The kinetic barrier for methoxy decomposition to give CO_{ad} + 3 H_{ad} of 47.7 +/- 2.9 kJ/mol (A=5.3 x 10^{13±1} s⁻¹) has been estimated from TP-SIMS.¹⁵⁹ Several DFT studies have looked at the decomposition of single methanol molecules on clean Pt(111), which produce only adsorbed CO and hydrogen due to the lack of excess oxygen to make formate.^{71,160}

The activation barriers for the steps associated with formic acid decomposition have been estimated using a new SCAC data analysis method, described elsewhere,³⁴ which provided the reaction rate constants for the removal of the acid hydrogen of 5.88 s^{-1} and the conversion of monodentate to bidentate formate of 7.69 s^{-1} . Using an Arrhenius form and a preexponential factor of 10^{11} s^{-1} for both reactions (typical for adsorbate dissociation¹⁶¹), these rate constants correspond to activation barriers of 20 and 29 kJ/mol respectively. We use the same prefactor for the bonding configuration conversion as the transition state should be similar to those seen in adsorbate dissociation.

It is known from UHV work that HCOOH first loses its acid hydrogen to form $\text{HCOO}_{\text{mono,ad}}$ which then converts to $\text{HCOO}_{\text{bi,ad}}$.¹²⁷ TPD experiments show that formic acid decomposes to exclusively CO_2 ^{127,128} with a peak position of 320 K at low coverage and 280 K at high coverage, with no CO_2 desorption at temperatures below 280 K. The intermediate peak temperature of 300 K yields an E_{act} of 64-66 kJ/mol for the decomposition process assuming $A=(1.87-4.02) \times 10^{11} \text{ s}^{-1}$ from Cu(111).¹⁶² This is nearly identical to the barrier for the conversion of bidentate to monodentate formate of 64 kJ/mol from SCAC. Note that the errors on the intermediate stabilities from SCAC are ~ 3 kJ/mol and the exact coverages from TPD are not known here.

Let us now consider how such a TPD experiment is performed. Formic acid is adsorbed on an O-Pt(111) surface at low temperature (100 K) where little to no reaction occurs and then the temperature is ramped slowly (e.g. 10 K/s). The decomposition of formic acid in this case is described by the sequence of reactions: (i) HCOOH oxidizes to $\text{HCOO}_{\text{mono,ad}}$ (ii) $\text{HCOO}_{\text{mono,ad}}$ converts mostly to $\text{HCOO}_{\text{bi,ad}}$, with some low equilibrium concentration of $\text{HCOO}_{\text{mono,ad}}$ (iii) $\text{HCOO}_{\text{mono,ad}}$ decomposes to CO_2 , (iv) bidentate formate converts to monodentate formate to

reestablish equilibrium, and steps (iii) and (iv) are repeated until all formate is removed. From this, we can conclude that the activation barrier for the decomposition of $\text{HCOO}_{\text{mon,ad}}$ must be higher, or the prefactor must be lower, than the barrier or prefactor for its conversion to $\text{HCOO}_{\text{bi,ad}}$, or CO_2 would be observed in TPD at a much lower temperature. This description also suggests that bidentate formate is not an active intermediate in the overall formic acid oxidation pathway, but rather acts as a spectator in the net reaction whose existence slows down the net rate.

The rate limiting step in $\text{HCOO}_{\text{bi,ad}}$ decomposition is thus the breaking of this surface oxygen bond, as the barrier from SCAC is similar to the overall decomposition barrier from TPD. Indeed the 280 K TPD peak¹²⁸ could be well fit using the SCAC measured high coverage barrier of 60 kJ/mol for the conversion of bidentate formate to monodentate (29 kJ/mol for the reverse barrier) and a barrier for the decomposition of monodentate formate to CO_2 and H_{ad} of 38 kJ/mol and a prefactor of 10^{13} s^{-1} . If the barrier or prefactor for this step were increased or decreased by a few kJ/mol or an order of magnitude respectively, a simulated low temperature peak (~100-150 K) would appear or the peak maximum would shift to a much higher temperature.

This is consistent with DFT studies on Pt(111)^{114,158} and Cu¹⁶³ surfaces, indicating that the decomposition of $\text{HCOO}_{\text{bi,ad}}$ proceeds through a monodentate configuration.¹¹⁴ In the Cu work, the reaction of $\text{CO}_{2,\text{g}}$ with H_{ad} led to the formation of $\text{HCOO}_{\text{mono,ad}}$, which then converts to $\text{HCOO}_{\text{bi,ad}}$. The structure insensitivity of this formate synthesis reaction seen experimentally is due to similar transition states and $\text{HCOO}_{\text{mono,ad}}$ binding energies for all Cu surfaces. However, the binding strength of $\text{HCOO}_{\text{bi,ad}}$, and consequently the conversion from bidentate to monodentate, was found to vary between Cu surfaces, explaining the experimentally observed

structure sensitivity of formate decomposition and showing that this step is rate determining in formate decomposition.¹⁶⁴

DFT calculations of the oxidation of formic acid on clean Pt(111)¹⁵⁸ and Pt(111) preadsorbed with water molecules¹⁵⁶ (i.e. 1, 2, or 4 H₂O_{ad} per unit cell), to simulate the presence of solvent, qualitatively match the energetics in Figure 1. Referencing all energies to gas phase formic acid, we find that DFT on clean Pt(111) predicts both adsorbed formic acid and bidentate formate to be ~20 kJ/mol less stable than SCAC, while it predicts monodentate formate to be 66 kJ/mol less stable, with a large barrier of 123 kJ/mol for the conversion of HCOO_{bi,ad} to HCOO_{mono,ad}. However in the presence of 2 adsorbed water molecules these intermediates, including monodentate formate, are all found to be ~20 kJ/mol less stable than experiment with the barrier for the conversion of HCOO_{bi,ad} to HCOO_{mono,ad} now falling to 63 kJ/mol. Although, unlike DFT, our SCAC experiments show that monodentate should be stable in the absence of solvent, DFT indicates that in the presence of solvent, monodentate formate is further stabilized, making it a possible intermediate in CO₂ production. It should also be noted that while water is found to be less stable by DFT by 21 kJ/mol, CO_{ad} is more stable than in experiments by ~40 kJ/mol (i.e. adsorption enthalpy of 160 kJ/mol by DFT¹⁵⁸ versus 120 kJ/mol by SCAC^{103,165}).

At elevated temperatures and pressures, or in an electrochemical environment where surface-bound formate is in equilibrium with formate in solution, a short-lived monodentate formate species, perhaps unable to convert to bidentate due to site availability or stabilized by surrounding water molecules, may serve as the active intermediate in the primary pathway, rather than the COOH species commonly cited (which has yet to be observed experimentally). Monodentate formate has been discussed as a possible intermediate from DFT, but always in the context of a conversion from HCOO_{bi,ad}.¹⁵⁶ It is often overlooked that formic acid has already

been shown experimentally to react first to monodentate rather than bidentate formate.¹²⁷ The reaction scheme in Figure 2 modifies the triple pathway commonly presented in the literature to show that the “formate path” acts as a dead end for the active monodentate formate primary path. It is unknown whether the conversion of methoxy to formate proceeds directly to bidentate formate, monodentate formate, or first to formic acid.

A route to minimizing the buildup of unwanted bidentate formate may be to utilize a bimetallic surface consisting of Pt and a metal that binds oxygen species more weakly, resulting in fewer adjacent Pt sites and therefore a potentially larger equilibrium constant for the conversion of bidentate to monodentate formate.

In conclusion, we have presented for the first time an experimentally determined energy landscape for the oxidation of methanol and formic acid on Pt(111). From the insights gained, we propose a new reaction scheme with monodentate formate as the key intermediate in the primary oxidation pathway.

6.1 Figures

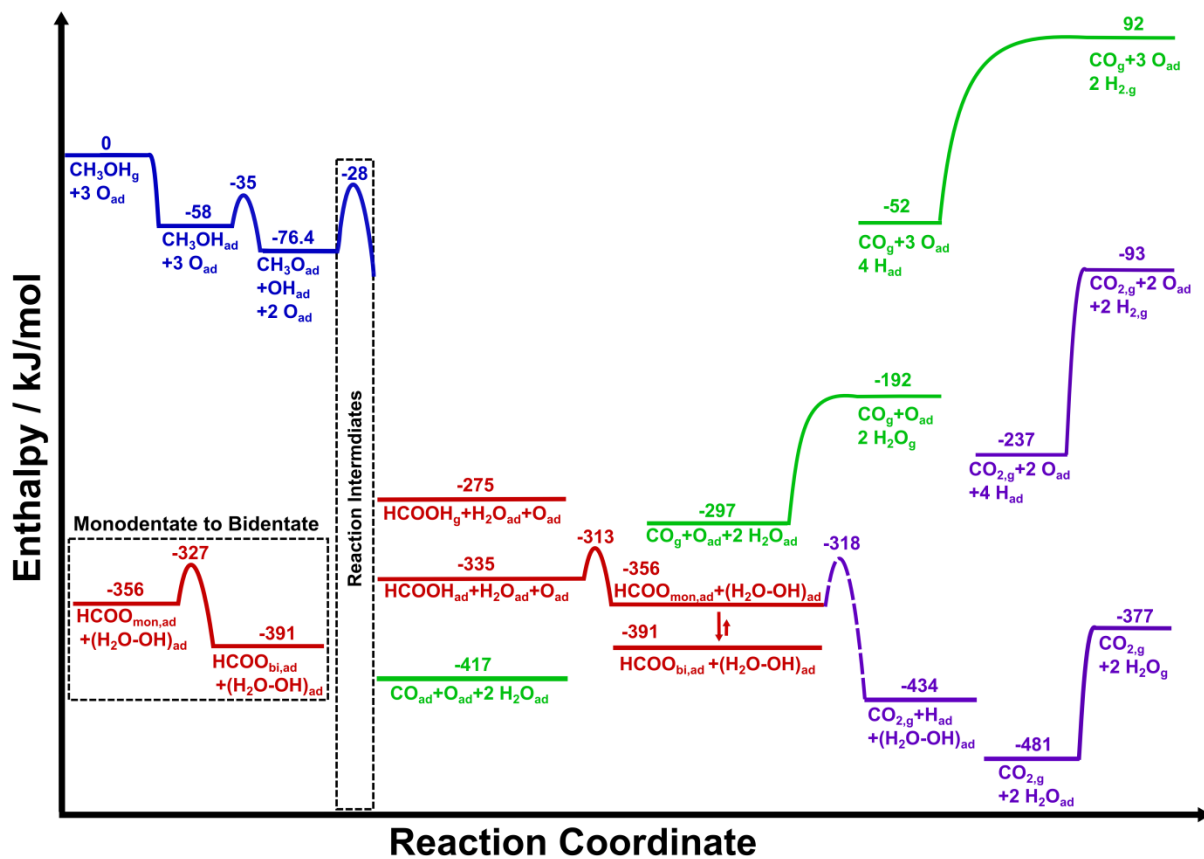


Figure 6.1: Energy landscape for methanol and formic acid oxidation to CO_2 and their decomposition to CO plus H_2 . Energy levels and barriers were determined experimentally (Table S.6.1) and represent key intermediates. Enthalpies are referenced to gas phase methanol and adsorbed oxygen atoms on a Pt(111) surface.

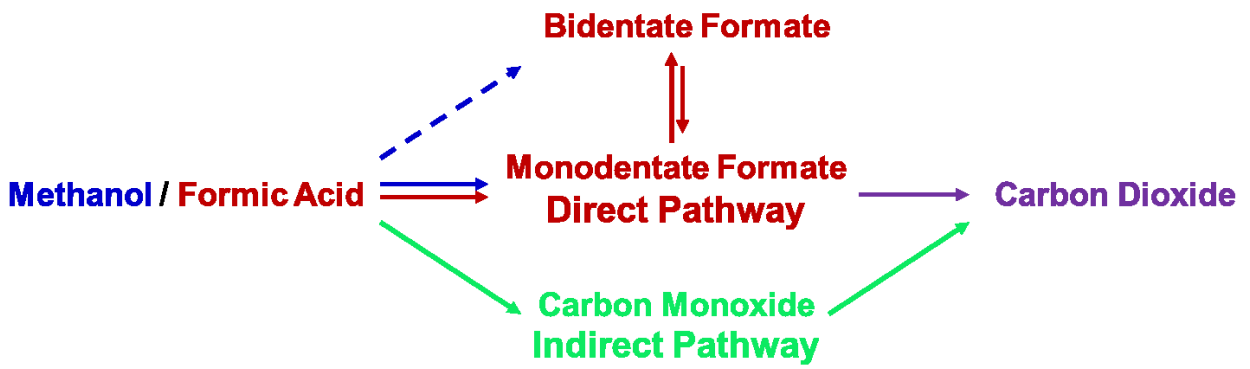


Figure 6.2: Reaction scheme for the oxidation of methanol and formic acid to carbon dioxide.

6.2 Supporting Information

Table S.6.1 lists enthalpies of formation of both adsorbed and gas phase species used in Figure 6.1. Below, we discuss these energetics in more detail. For a greater level of detail, we redirect the reader to the original publications.

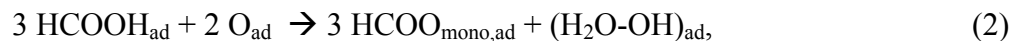
It is known that methanol loses its acid hydrogen in the presence of adsorbed atomic oxygen on Pt(111) to form adsorbed methoxy and hydroxyl,¹⁴⁰ as given by the reaction:



The enthalpy of formation of gas phase methanol has been previously measured as -202 kJ/mol. The enthalpy of adsorption of methanol on O-sat. Pt(111) (defined as 0.25 ML oxygen) has been measured with SCAC as 58 kJ/mol exothermic at 100 K and a coverage of 0.25 ML, giving $\Delta H_f(\text{CH}_3\text{OH}_{\text{ad}}) = -260$ kJ/mol.¹⁹ Similarly, SCAC measurements performed at 150 K on O-sat. Pt(111) provide an enthalpy of reaction (1) of -76.4 kJ/mol.¹⁹ The barrier for this reaction has been estimated to be 23 ± 3 kJ/mol from temperature programmed secondary ion mass spectrometry (TP-SIMS).¹⁵⁹ As the enthalpy of formation of adsorbed hydroxyl has also been determined from SCAC (-207 kJ/mol¹⁴⁵), a $\Delta H_f(\text{CH}_3\text{O}_{\text{ad}})$ of -170 kJ/mol is obtained. The relative energies (referenced to gas phase methanol) are shown in Figure 6.1 in blue. This surface bound methoxy species on Pt(111) is known to decompose above 170 K, with no other stable intermediates, to form CO.¹⁵⁹ However, in an excess of oxygen, methoxy instead forms a surface-bound formate which then decomposes to CO₂.

Formic acid is known to lose its acid hydrogen on both clean and oxygen precovered Pt(111) to ultimately form bidentate formate below 200 K.^{128,129,133} On oxygen precovered Pt(111), formic acid has been observed experimentally to first form monodentate formate.^{127,128} At 130 K, this monodentate formate is stable on the order of minutes before converting to a

bidentate configuration.¹²⁷ The oxidation of formic acid by surface oxygen can therefore be represented by the reactions



followed by



The enthalpies of reactions (2) and (3) have been previously determined from SCAC experiments to be 81 kJ/mol and 35 kJ/mol respectively at 0.25 ML.

Using a new data analysis method for the SCAC heat detector lineshape, described elsewhere,³⁴ we are also able to determine the rate constants for reactions (2) and (3).¹⁴⁶ This is accomplished by performing experiments at temperature conditions where the reaction of interest (e.g. reaction (2)) occurs on a timescale similar to the molecular pulse length of 104 ms. Briefly, this is accomplished by fitting the measured detector lineshape from molecular pulses with a combination of two separate pulses. The first pulse, representing instantaneous heat deposition, is created using the laser calibration detector lineshape that has been multiplied by a scaling factor. The second pulse, representing heat deposition on a similar timescale to the measurement, is created by convoluting the laser calibration lineshape with an exponential decay representing a first order reaction (with a time constant, τ) and multiplying by a scaling factor. The sum of these two pulses creates a simulated pulse whose lineshape is dependent on the ratio of the two scaling factors and τ . These two parameters can therefore be adjusted to obtain a simulated pulse that best fits the measured molecular pulse lineshape (i.e. the residual between the simulated and measured pulses is minimized), providing the total amounts of heat in each reaction step and the time.

The experimentally determined k of 7.69 s^{-1} (from $\tau = 170 \text{ ms}$) at 100 K for reaction (2) to calculate its Arrhenius activation barrier (E_{act}) from equation (4) below:

$$k = Ae^{-(E_{\text{act}}/RT)} \quad (4)$$

Assuming a prefactor factor, A , of 10^{11} s^{-1} (typical for adsorbate dissociation¹⁶¹), E_{act} for the breaking of the O-H bond in HCOOH_{ad} is 20 kJ/mol . Similarly, the τ of 130 ms measured at 150 K gives an activation barrier for reaction (3) of 29 kJ/mol assuming $A=10^{11} \text{ s}^{-1}$ (assuming the transition state for this conversion is similar to adsorbate dissociation¹⁶¹). The barrier for the reverse reaction (i.e. the conversion of bidentate to monodentate formate) is 64 kJ/mol . As this forward barrier was found to be independent of coverage, we can also estimate the low and high coverage activation barriers for the reverse of reaction 3 using SCAC heat data.¹⁴⁶ Near the saturation coverage of bidentate formate of 0.375 ML , this barrier is calculated as 59 kJ/mol using the difference of 30 kJ/mol between $\Delta H_{\text{f}}(\text{HCOO}_{\text{ad,mon}})$ (-352 kJ/mol) and $\Delta H_{\text{f}}(\text{HCOO}_{\text{ad,bi}})$ (-382 kJ/mol). Similarly, the barrier at the zero-coverage limit is estimated as 72 kJ/mol .¹⁴⁶

The energetics of adsorbed CO are already known from temperature programmed desorption (TPD)¹⁶⁶⁻¹⁶⁹ and SCAC^{103,165} experiments. The integral heat of adsorption at 0.25 ML is 120 kJ/mol , giving an enthalpy of formation for CO adsorbed on Pt(111) of -231 kJ/mol (using $\Delta H_{\text{f}}(\text{CO}_{\text{g}}) = -110.5 \text{ kJ/mol}$ ⁹³). Note that CO_{ad} formation from $\text{formate}_{\text{ad}}$ is exothermic by 26 (from bidentate) or 61 kJ/mol (from monodentate).

Table S.6.1: Experimentally determined standard enthalpies of formation of gas phase and adsorbed molecules and molecular fragments. When possible, we have used enthalpies determined at a consistent coverage of 1/4 ML. Gases are at 1 bar pressure.

Species	Enthalpy of Formation (kJ/mol)	Adsorbate Coverage (and co-adsorbate present)	Temperature
CH ₃ OH _g	-202 ¹⁷⁰	-	298 K
CH ₃ OH _{ad}	-260 ¹⁹	1/4 ML	100 K
CH ₃ O _{ad}	-170 ¹⁹	1/4 ML (with 1/12 ML (H ₂ O-OH) _{ad})	150 K
HCOOH _g	-379.2 ¹⁴⁴	-	298 K
HCOOH _{ad}	-440 ¹⁴⁶	1/4 ML	100 K
HCOO _{mon,ad}	-352 ¹⁴⁶	1/4 ML (with 1/12 ML (H ₂ O-OH) _{ad})	150 K
HCOO _{bi,ad}	-387 ¹⁴⁶	1/4 ML (with 1/12 ML (H ₂ O-OH) _{ad})	150 K
O _{ad}	-99 ¹⁴⁵	1/4 ML	300 K
OH _{ad}	-207 ¹⁴⁵	1/3 ML (with 1/3 ML H ₂ O _{ad})	150 K
H ₂ O _g	-242 ⁹³		298 K
H ₂ O _{ad}	-293 ^{17,145}	~2/3 ML	100 K
(H ₂ O-OH) _{ad}	-503 ¹⁴⁵	1/3 ML	150 K
CO _g	-110.5 ⁹³	-	298 K
CO _{ad}	-231 ^{103,165}	1/4 ML	300 K
H _{ad}	-36 ³¹		300 K
CO _{2,g}	-393.5 ⁹³	-	298 K

Chapter 7

Bond energies of molecular fragments to metal surfaces track their bond energies to H atoms

Understanding the energetics of chemical reactions on transition metal surfaces is important to many technologies, including efforts to develop better catalysts for the production of clean fuels, the combustion of fuels and the production of chemicals with improved energy efficiency and less pollution, and in developing better fuel cells and batteries. Thus, one would like to be able to estimate the bond energies of adsorbed molecular fragments to transition metal surfaces. We show here a simple trend with powerful predictive ability in that respect.

With organometallic complexes in liquid solutions, equilibrium measurements have yielded the sigma bond energies of many ligands to metal centers; and these bond strengths have been shown to correlate strongly with the corresponding gas-phase ligand to hydrogen bond strength.¹⁷¹⁻¹⁷³ Specifically, Bryndza and coworkers showed that when the gas-phase hydrogen-to-ligand bond strength is plotted versus the ligand bond strength to a given metal center, the data fall approximately on a straight line with a slope equal to 1.00. This relationship allows the bond strengths of many other ligands to metal centers to be estimated simply from the corresponding hydrogen-to-ligand bond strengths in gas-phase molecules, which are very well known.^{44,174} It has been suggested that this trend should also hold for adsorbates bound to metal surfaces¹⁷⁵ based on an earlier qualitative observation.¹⁷⁶ A similar linear relationship between metal-C bond energies for adsorbed alkyls and H-C bond energies in the corresponding gaseous alkanes was predicted based on density functional theory (DFT) to hold on several late transition metal surfaces, albeit with a different slope.^{177,178} We show here, for the first time, that such a

relationship does indeed hold with unit slope for experimental bond energies of ligands bound to a late transition metal surface, Pt(111). We further discuss this discovery's predictive ability for estimating the bond energies of molecular fragments adsorbed to transition metal surfaces and demonstrate how this relationship can be used to gain considerable insight into the thermodynamics of important catalytic reaction mechanisms.

Table 7.1 lists the adiabatic Pt-OR bond dissociation enthalpies for three oxygen-bound molecular fragments to the Pt(111) surface: deuterated hydroxyl (OD)¹⁸, monodentate formate (O(O)CH)¹⁴⁶, and methoxy (OCH₃)¹⁷⁹, recently measured by Single Crystal Adsorption Calorimetry (SCAC). Also listed are these adsorbates' corresponding gas-phase hydrogen-to-ligand bond enthalpies: H-OD for deuterated hydroxyl, H-OOCH for monodentate formate, and H-OCH₃ for methoxy. In Fig. 7.1, the measured bond enthalpies for these adsorbates to Pt(111) are plotted versus their corresponding hydrogen-to-ligand adiabatic bond dissociation enthalpies. Similar to the work of Bryndza et. al.¹⁷¹ for organometallic complexes, we find that a straight line with a slope of 1.00 ($y = x - 249$ kJ/mol) fits these data very well with a standard deviation = 3.6 kJ/mol. The best-fit line is $y = -234 + 0.97x$, but its standard deviation is 3.5 kJ/mol, not significantly better.

These three adsorbates are each thought to bind to the Pt(111) surface through a single sigma bond to a single Pt atom (i.e. on an atop site)^{18,71,160,180}, which is a similar bonding picture to a ligand bound with a single sigma bond to the metal center in the organometallic complexes of the correlation reported by Bryndza and coworkers.^{146,171,181} Thus, the reason this trend in Fig. 7.1 holds must be the same reason why this trend also holds for organometallic complexes¹⁷¹⁻¹⁷³. To our knowledge, no physical explanation has been published to explain that trend.

Table 7.1: Calorimetrically measured standard heats of formation (ΔH_f°) and adsorbate-Pt(111) bond strengths (i.e., adiabatic bond enthalpies) of three oxygen-bound adsorbates on Pt(111) and their corresponding gas-phase H—OR bond strengths. Literature citations are given as superscripts to the known enthalpy values.

Adsorbate	ΔH_f° (kJ/mol)	Known RO-H Bond Enthalpy (kJ/mol)	Measured RO-Pt(111) Bond Enthalpy (kJ/mol)
-OD	-210 ± 7 ¹⁸²	500. ⁴⁴	248 ± 7 ^{18,182}
-O(O)CH	-353 ± 10 ¹⁴⁶	469 ± 13 ¹⁸³	224 ± 13 ¹⁴⁶
-OCH ₃	-170 ± 10 ¹⁷⁹	437 ¹⁸¹	187 ± 11 ¹⁷⁹

We offer the following simple explanation for Fig. 7.1. To a first approximation, the orbitals involved in the O-Pt bond are identical in local character for all three adsorbates, at least with respect to their average nuclear-nuclear and electron-nuclear and electron-electron Coulomb potential energies and quantum-mechanical electron kinetic energies. These are only mildly affected by the next neighbor to the O atom. The main difference in adiabatic bond dissociation energies is therefore due to final-state effects (i.e., differences in the way this orbital rearranges in the dissociated products). Since the fragment-free Pt surface is one product, but the same in all three cases, the only difference between these fragments is their ability to stabilize the gaseous radical that is produced upon homolytic bond cleavage. For example, methoxy stabilizes this radical much better than hydroxyl, since it has more atoms and greater structural and orbital flexibility to stabilize the radical's electron. This is the very same reason the CH₃O-H bond is weaker than the HO-H bond in the corresponding gas-phase molecules. This is why the RO-Pt(111) bond energy tracks the corresponding RO-H bond energy with a slope of unity: The differences in these dissociated final states between these three different –OR species are the same whether cleaving the RO-H or RO-Pt(111) bond. This trend highlights the local character of the sigma bond of molecular fragments to metal surface atoms, even on extended metal

surfaces. The local nature of bonds to metal surfaces is apparent in the reasonable success of the Bond Order Conservation method in predicting adsorbate energies^{184,185}

The fitted line in Figure 7.1 allows the bond enthalpy of several other oxygen-bound adsorbates to be predicted (approximately). In Table 7.2, the predicted bond enthalpy of several alkoxy fragments and the hydroperoxy species to the Pt(111) surface are listed along with their corresponding known gas-phase hydrogen-ligand bond strengths. Also listed are the adsorbates' predicted heats of formation, which are found by summing the heat of formation of the gas phase radical with the negative of the predicted bond enthalpy. To calculate the heat of formation of the alkoxy radicals, the known bond dissociation enthalpy (Table 7.2 column 3) was used with the known heats of formation of the gaseous alcohols (also listed)^{174,186} and with the known heat of formation of gas-phase H atoms (218 kJ/mol¹⁷⁴).

From these predicted values, insight can be gained into the thermodynamics of a wide variety of chemical pathways on Pt(111). As an example, let us focus on the hydroperoxy species (OOH_{ad}) whose standard enthalpy of formation ($\Delta H_{\text{f}}^0(\text{OOH}_{\text{ad}})$) can be predicted from this trend (Table 7.2 column 5), as described above. Note that the predicted bond enthalpy of OOH_{ad} to Pt(111) is 107 kJ/mol, close to what has been calculated by density functional theory (99.7 kJ/mol)¹⁸⁰. This adsorbate has relevance in polymer electrolyte membrane (PEM) fuel cells where the oxygen reduction reaction occurs over a Pt-based catalyst, but during this reaction hydrogen peroxide is formed as an unwanted byproduct that degrades the membrane. Two chemical pathways have been proposed to form the hydroperoxy intermediate (reactions (1) and (2) below) whose reaction enthalpies can be calculated on Pt(111) from the empirical heats of formation of OH_{ad} ^{18,182} O_{ad} ¹⁸² and the predicted OOH energetics in Table 7.2. Using this

predicted $\Delta H_f^0(\text{OOH}_{\text{ad}})$ of -105 kJ/mol with the standard heats of formation of OH_{ad} , O_{ad} and H_{ad} measured on Pt(111)^{17,18,31,182} allows the following reaction enthalpies to be estimated:



and



From the reaction enthalpies associated with reactions (1) and (2) it is clear that the most energetically favorable route to form OOH_{ad} is through reaction (2), which is the insertion of O_2 into an adsorbed hydrogen adatom to form the OOH_{ad} species (with the O_2 probably weakly adsorbed first).

Table 7.2: Predicted heats of formation and bond enthalpies of several oxygen-bound adsorbates on Pt(111) from the fitted line in Figure I. Literature citations are given as superscripts to the known enthalpy values.

Adsorbate	Known RO-H Bond Enthalpy (kJ/mol)	Predicted RO-Pt(111) Bond Enthalpy (kJ/mol)	Known ΔH_f^0 of Gaseous Alcohol (kJ/mol)	Predicted ΔH_f^0 of Adsorbate (kJ/mol)
<i>t</i> -butoxy	445 ¹⁸⁷	196	-313 ¹⁸⁶	-282
ethoxy	436 ⁴⁴	187	-234 ¹⁷⁴	-203
propoxy	433 ⁴⁴	184	-256 ¹⁷⁴	-225
butoxy	431 ⁴⁴	182	-277 ¹⁷⁴	-246
OOH (hydroperoxy)	356 ¹⁷⁴	107	-136 ¹⁷⁴	-105

A spectroscopic study by MacNaughton et. al.¹⁸⁸ seems to be consistent with the thermodynamics of the above reactions, finding that H_{ad} promotes the formation of the OOH_{ad} species on Pt(111). This O_2 insertion into the metal-H bond is also the same mechanism observed for making the $-\text{OOH}$ ligand on a Pd organometallic complex.¹⁸⁹

Another interesting insight from these reaction enthalpies comes from the reverse of reaction (1), or the decomposition of an OOH_{ad} to OH_{ad} and O_{ad} , shown as reaction (3) below:



The sum of reactions (2) and (3) provides a stepwise-exothermic route to form O_{ad} and OH_{ad} from O_2 on H-covered surfaces which are key intermediates for many reactions, although kinetics may prevent this path.

Based on the reason for the slope of 1.00 in Fig. 1 offered above, it is very likely that this trend also holds for adsorbate species that are bound to the surface through other elements like carbon, as also suggested by DFT but with different slope^{177,178}. However, because Pt(111) could tend to bond to carbon more strongly than oxygen, or vice versa, it may be that the corresponding line for C still retains a slope equal to 1.00 but is shifted to higher or lower ligand-metal bond strengths (i.e. larger or smaller y-intercept) than the line for these oxygen-bound species. Surprisingly, our measured value for the C-Pt(111) bond enthalpy for adsorbed methyl ($-\text{CH}_3$) of 197 kJ/mol locates it at the point (440 kJ/mol, 197 kJ/mol)^{174,190,191}, which is only 6 kJ/mol above the line in Fig. 1 for O-bound species. We have no explanation for the proximity of this C-bound species to the line for O-bound species on Pt(111), but we expect this to depend on the metal. For example, Cu probably bonds to $-\text{OR}$ groups more strongly and to $-\text{CR}_3$ groups more weakly than Pt. Interestingly, C-bound ligands in organometallic complexes lie nearly on top of the line for O-bound species.^{171,172} We found that CO_{ad} does not fall near the line in Fig. 1, but this was expected since the adsorbates in Fig. 1 bond to the metal surface through a simple sigma bond like their bond to H, whereas CO bonding to Pt involves pi back-bonding not possible with an H atom.

This same line in Fig. 1 for Pt(111) adsorbates is not expected to apply to other metal surfaces, since other metals can be more oxophilic, like copper, or less, like gold. It is expected that the line may shift up or down significantly, but keep the same slope of 1.00. Indeed, for organometallic complexes it was found that different metals could be fit to the same line if simply corrected for the differences in their bond energies to the –OH “reference” ligand^{171,192}, so we predict a similar result for metal surfaces as well. Methods for adjusting such a trend to other metal surfaces and other sites have been suggested¹⁷⁸ based on scaling relationships derived from DFT¹⁹³.

Unfortunately, there are some important limitations to the predictive ability of this trend. For adsorbates that form multiple bonds to the surface (like bidentate formate¹⁴⁶ or methylidyne¹⁹⁰) this trend may not hold, because of the influence of one bond on the other. Additionally, it is unlikely that this relationship can predict the energetics of large molecules that have a strong van der Waals attraction with the surface or steric repulsion, since this trend is only good for predicting the chemical bond strength between a single atom in the adsorbate and the surface. However, van der Waals corrections should be easy to estimate.

The excellent correlation found here between bond strengths to a metal surface and the corresponding bond strengths to a H atom for oxygen-bound species on Pt(111) yields insight into the bonding mechanism and energetics of many adsorbates and surface reactions. This trend suggests that a combined theoretical / experimental approach could provide a fast way of estimating bond energies for adsorbates on surfaces. Since bond energies to H within gas-phase molecules are already known or easy to calculate with high accuracy, these could be used to estimate the bond energies of the corresponding molecular fragment to metal surfaces by recognizing the slope of 1.00 and knowing only one experimental point on a plot like Fig. 1 for

that metal surface site. This estimate would need to be corrected for larger molecular fragments with significant van der Waals attractions or steric repulsions, but estimating these corrections theoretically may prove to be more accurate and is surely far faster than quantum mechanical calculations of the full adsorbate / substrate system.

In conclusion, the strength of sigma bonds of oxygen-bound molecular fragments (-OH, -OCH₃, -O(O)CH) to Pt(111) varies linearly with the strength of binding of those same fragments to H atoms in gas-phase molecules with a slope of 1.00, but offset by -249 kJ/mol (weaker to Pt than H). This implies that the bonds to the surface are highly local in character, and suggests semi-empirical methods for estimating the heats of formation of adsorbates on metal surfaces that rely on this trend.

Chapter reprinted with permission from ¹⁹⁴. Copyright 2014 American Chemical Society.

7.1 Figures

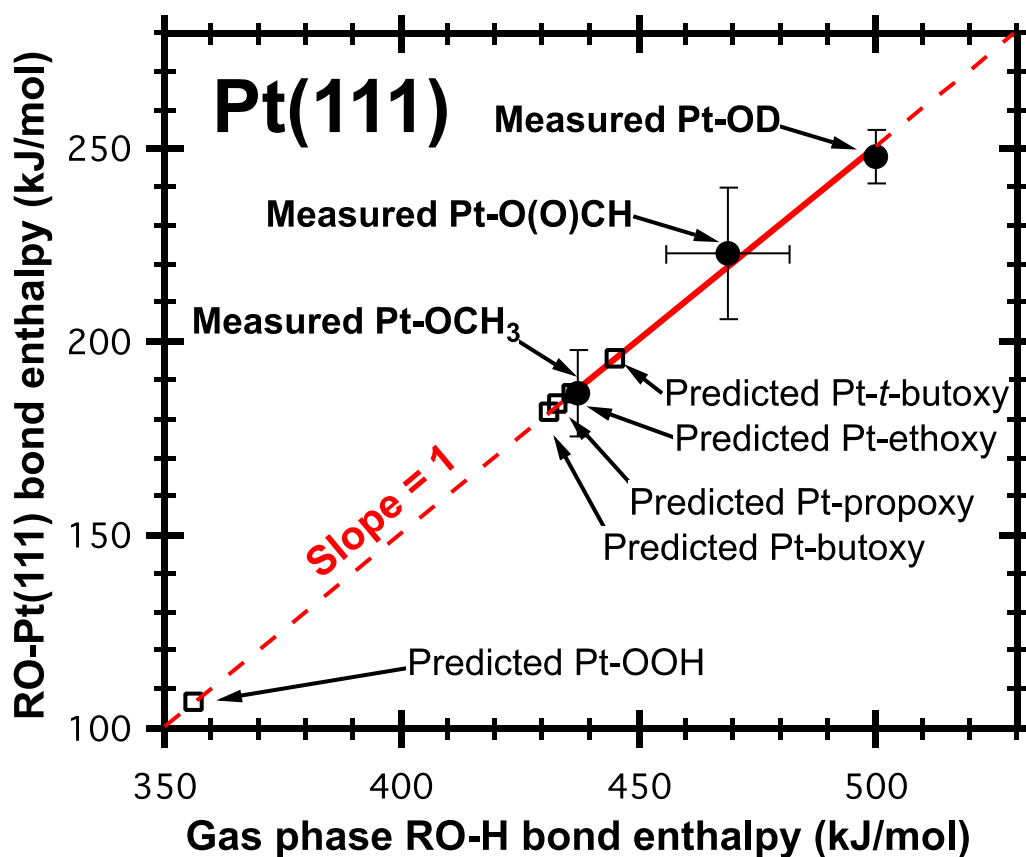


Figure 7.1: Calorimetric adiabatic bond dissociation enthalpies of three oxygen-bound adsorbates (deuterated hydroxyl, methoxy, and monodentate formate) to Pt(111) (filled circles) versus their corresponding gas-phase hydrogen-OR adiabatic bond dissociation enthalpies. A line with slope equal to 1.00 fits these three points nearly perfectly. This allows the prediction of the bond strength of other important oxygen-bound adsorbates on Pt(111) that have not been measured (open squares), such as other alkoxy species and hydroperoxy. The error bars on each measurement represent 95% confidence limits.

Chapter 8

Energetics of Adsorbed Catalytic Intermediates on Transition Metals by Single Crystal Adsorption Calorimetry

8.1 Introduction

The rational design of new catalytic materials requires a fundamental understanding of how catalyst surfaces bind molecules and molecular fragments and guide them through various elementary reaction steps. A detailed knowledge of the thermodynamic stability of surface adsorbates as well as the kinetic barriers (i.e. thermodynamic stability of transition states between stable or metastable adsorbates) of elementary reaction steps is critical for predicting reaction pathways on a catalyst surface. However, such fundamental information is generally not known for molecular fragments adsorbed on catalytically interesting materials, which are often late transition metals. The lack of available data is primarily due to the limitations of the traditionally used experimental techniques of temperature-programmed desorption (TPD) and equilibrium adsorption isotherms (EAI), which provide *indirect* measurements that rely on the intact desorption of the species of interest. As most catalytically-relevant adsorbates decompose or react with co-adsorbates rather than desorbing, desorption-based methods cannot be used.

Due to such limitations, a *direct* measurement technique, known as single crystal adsorption calorimetry (SCAC), was developed in the group of Sir David King⁵⁻⁷ and further improved by Campbell et al.^{9-11,101}. This technique has been successfully applied to study the energetics of molecular adsorption and surface reactions. Because these experiments are carried out on well-defined single crystal substrates under ultrahigh vacuum (UHV) conditions, the measured energetics can be correlated to well characterized, reproducible adsorption and reaction

processes. Early SCAC work has been summarized previously in several excellent reviews that also outline the fundamentals of the experimental technique, including operating principles and instrumentation.¹²⁻¹⁶ To date, SCAC has been successfully applied to study the energetics of adsorbate-surface interactions for different molecular adsorbates on several metal single crystal surfaces, including low index faces of Pt, Ni, Pd, and Fe.^{12-14,17-25}

8.2 Single Crystal Adsorption Calorimetry: Thermodynamic and Kinetic Information

Although the instrumentation and experimental design used in SCAC has been described in detail in previous publications,^{5,6,10,11,111} a brief summary is provided below so that the discussion of recent results can be easily followed by the reader.

In an SCAC experiment, a single crystal metal sample is placed in the path of a pulsed, collimated molecular beam. A fraction of molecules in each pulse adsorb/react on the single crystal surface, releasing energy into the surface which results in a transient temperature rise in the thin single crystal sample (~1 μm thickness). This temperature rise is detected as a transient change in the face-to-face voltage of a pyroelectric polymer ribbon in mechanical contact with the back of the sample. The detection method has no effect on the overall experimental procedure, and other approaches, such as measurement of infrared radiation from the sample or the direct mounting of the sample on a pyroelectric crystal, have been implemented successfully. For details on these detection methods, we refer the reader to previous studies in the King group.⁵ As The fraction of molecules that stick to the surface is determined using a quadrupole mass spectrometer and the King and Wells method³⁶ and the absolute molecular flux is calibrated using a liquid nitrogen cooled quartz crystal microbalance. The final step in the experiment - calibrating the detector signal to convert the measured response to deposited energy - is accomplished by passing a HeNe laser of known energy (measured using a calibrated

photodiode) down the molecular beam path to provide pulses with an identical time profile. To determine the amount of energy deposited into the sample from a laser pulse, the optical reflectivity of the sample must also be known. If heat is deposited during molecular adsorption/reaction on a timescale much faster (<10 ms) than the timescale of the pulse duration (50-100 ms), the lineshape of the detector response will be identical to the detector lineshape during the laser calibration experiment, allowing for a simple ratio of the peak maximums or the slope of the initial fast rise (\sim first 100-150 ms) of the pulse. This sequence of experiments therefore provides the coverage dependent differential heat of adsorption (kJ/mol) with better than 1% ML coverage resolution, where ML is defined as the atom density of the single crystal metal surface (e.g. $1.5 \times 10^{15} \text{ cm}^{-2}$ for Pt(111)). The sign convention is that positive heats of adsorption represent exothermic processes. As has been outlined in a previous review by Brown et al., calorimetric data can be compared to isosteric heat measurements and Arrhenius desorption energies directly by adding $1/2RT$ to the measured heats of adsorption.¹² However, one should be aware of the simplifying assumptions used when making such comparisons, as they may not be valid for particular systems.¹²

It has recently been demonstrated through a new data analysis method that SCAC experiments can be used to make quantitative thermodynamic and kinetic measurements simultaneously. The following is a brief description of the analysis method, which is described in detail elsewhere.^{34,146} If all or some portion of heat deposition upon molecular adsorption/reaction occurs on timescale similar (\sim 10-1000 ms) to the molecular pulse duration, a noticeable broadening of the detector lineshape is observed. The new data analysis method developed in our group involves fitting the broadened detector response using a two-step reaction sequence with a single rate-limiting step. The first step is fast and its heat is deposited

on a timescale much faster than the pulse duration, as is common in simple molecular adsorption. This heat signal pulse lineshape is well represented by the lineshape obtained from the laser heat calibration experiment. The second step is slower, perhaps due to activated dissociation of an adsorbed molecule or activated conversion of some quickly-adsorbed molecular fragment (i.e. the conversion of monodentate formate to bidentate formate) and is responsible for the observed pulse broadening. This broadening is fit using the laser calibration lineshape convoluted with an exponential decay for a first-order reaction. The time constant of this exponential decay is a fitting parameter, and represents the inverse of the reaction rate constant of the process. The proportion of heat in each of these two steps and the time constant are adjusted until the simulated pulse (SP) best fits the experimental heat pulse (EH). A representative broadened detector lineshape, shown in Fig. 7.1, along with the best-fit simulated pulse obtained from the sum of pulse lineshapes representing a fast (S1) and a slow (S2) heat deposition process. The pulse (Fig. 7.1) was obtained for formic acid adsorption on oxygen saturated Pt(111) at 150 K¹⁴⁶ and the nearly perfect fit between SP and EH confirm the accuracy of both the obtained heats and reaction time constant.

8.3 From Heats of Adsorption to Enthalpies of Formation and Bond Enthalpies

Enthalpies of formation and bond enthalpies are commonly used in thermochemistry to predict reactions in solution or the gas phase. To extend such predictive capabilities to heterogeneous catalysis, it is necessary to obtain these fundamental values for adsorbed molecules and molecular fragments. The enthalpy of formation for a species of interest can easily be determined from SCAC data using known enthalpies of formation in a thermodynamic cycle as shown for a generic dissociative adsorption process in Figure 8.2. The bottom path represents the enthalpies of formation of the reactants and the reaction measured in the

calorimetry experiment. The central path must equal this bottom path, thus providing the enthalpy of formation of the adsorbed molecular fragment, A, produced during the measured reaction shown in blue assuming the enthalpy of formation of adsorbed fragment B is known.

Similarly, the bond enthalpies of the adsorbed species, D(A-Pt), can be determined, as shown in the upper path of Fig. 7.2 in blue, by using the enthalpy of formation for the gas phase radical, A^*_g , corresponding to the adsorbed fragment. As the most commonly available data for gas phase species represent molecules in their lowest energy electronic state, the calculated bond enthalpies obtained from the calculations in Fig. 7.2 represent adiabatic bond dissociation energies. This is similar to the quasi-empirical valence bond (QVB) method^{195,196} which uses the lowest energy electronic state and the excitation energy necessary to put the species in the electronic state that most closely matches the species when it is bound to the surface, providing the diabatic bond dissociation energy. Another method, the additivity of bond enthalpies (ABE),⁴⁴ uses known bond dissociation energies (e.g. for C-C or C=O) to determine the metal-ligand bond enthalpy for the adsorbed species. The application of the ABE method to calorimetry data has been described in detail elsewhere.¹⁹⁷ All of the bond enthalpies discussed here are adiabatic bond enthalpies calculated using a thermodynamic cycle as shown in Fig. 7.2 or the ABE method.

8.4 Use of SCAC Experimental Benchmarks as Comparisons to Periodic Density Functional Theory Calculations

It is often useful to use experimentally measured heats of reaction, or bond enthalpies determined from these measurements, to verify the accuracy of theoretical calculations (e.g. density functional theory with periodic boundary conditions). In this section we will comment on

how calorimetry data should be treated when making such a comparison to ensure that conditions match those in the calculations.

It is important to note that SCAC data is often presented as a differential heat of adsorption or reaction, meaning that each heat of adsorption data point represents a finite pulse of molecules (e.g. 1% ML) being adsorbed on a surface already populated with some surface coverage. As DFT with periodic boundary conditions determines energetics on a set unit cell size (i.e. 2x2 or 4x4) representing a particular surface coverage (1/4 ML or 1/16 ML), these calculations are effectively depositing that coverage of molecules all at once. In order to fairly compare to theory, SCAC data must first be converted to *integral* heats of adsorption, which, if all data points are evenly spaced with coverage, is simply the average heat between 0 ML and the coverage of interest. If a best fit equation for the differential heat is available (see Table 8.2 below), the integral heat can be easily determined. This can be critical if the differential heat of adsorption is highly coverage dependent, as is the case for benzene adsorbed on Pt(111).^{103,108} In those experiments, the differential heat drops from ~200 kJ/mol at 0 ML to below 70 kJ/mol at saturation (~0.15 ML). To this end, we provide below integral heats of adsorption at coverages corresponding to common unit cell sizes. For coverages not listed, we refer the reader to the original publications where complete coverage dependent heats are available. In some cases, we opt to provide equations of differential heats that are valid over the listed coverage range, as these allow for easy calculation of integral heat at any coverage.

When using a thermodynamic cycle (Fig. 7.1) to determine the strength of the surface-ligand bond from SCAC data, keep in mind that this yields a bond enthalpy. This can be converted to bond energy by subtracting RT (ideal gas assumption), resulting in a slightly weaker bond. As this correction is on the order of a few kJ/mol or less, for strongly bound

species, such as methoxy that has a binding enthalpy of 187 kJ/mol, the correction is often smaller than the uncertainty of the experiment.

It has also been seen that DFT calculations of reaction energies (e.g. $3 \text{D}_2\text{O}_g + \text{O}_{\text{ad}} \rightarrow 2 (\text{D}_2\text{O-OD})_{\text{ad}}$) are often more accurate than calculated binding energies of individual adsorbates.¹⁸² This is can be due to the accuracy problems associated with calculations of radicals in the gas phase; a situation that is avoided by looking at full reactions. For this reason, we present the enthalpies of reaction measured by SCAC here as well as the enthalpies of formation and bond enthalpies obtained from these measurements.

8.5 Summary of Results

8.5.1 Molecular Adsorption

a) CO and NO

The results of CO and NO adsorption on the low index surfaces of the transition metals Pt, Ni, and Pd have been covered in great detail previously in a review by Brown et al.¹² We return to these results for two reasons. The first is to present the data as integral heats of adsorption that can be easily corrected for temperature and compared to DFT.

The second is to compare the results of CO adsorption on Pt(111) with two new SCAC studies performed in different laboratories. It had previously been noted by Fischer-Wolfarth et al.,¹⁶⁵ when comparing their SCAC numbers to existing SCAC numbers as well as those obtained from EAI, that the original SCAC heats of adsorption were high by ~30%. This discrepancy arose from the use of a Pt sample reflectivity of 0.66 (taken from Weaver¹⁹⁸) rather than the value of 0.76 as measured independently in separate laboratories for the particular samples used in calorimetry experiments.^{108,165} It was noted that a simple correction for reflectivity could be applied to the original data. This correction was also discussed further in regards to the

Table 8.1: Integral heats of molecular adsorption of CO on low index transition metal surfaces. All measurements performed at room temperature using SCAC. Note the excellent agreement between measurements from three separate groups of CO adsorption on Pt(111). Coverage, in ML, indicates the surface density of metal surface atoms for each surface. Heats marked with an asterisk (*) indicate values that have been corrected for errors in metal reflectivity. For all values that list two references, the actual numerical values are taken from the review by Brown et al.,⁸ which corrected several data sets from the original publications.

a Adsorption is dissociative on this surface, as evidenced by the much higher heat of adsorption than seen on other metal surfaces

system	ref	q^0_{cal} (kJ/mol)		
		1/16 ML	1/4 ML	1/2 ML
CO/Ni(111)	12,199	130	127	125
CO/Ni(110)	12,199	131	127	123
CO/Ni(100)	12,199	128	125	120
CO/Pt(111)	12,131	132*	120*	118*
	165	128	118	104
	103	130	118	102
CO/Pt(110)	12,200	136*	128*	122*
CO/Pt(100)-hex	12,201	134*	129*	126*
CO/Pt(100)-(1x1)	12,201	152*	148*	141*
CO/Pd(100)	12,202	163	153	140
NO/Ni(100) ^a	12,203	370	226	175.0
NO/Pt(111)	12,23	124*	109*	-
NO/Pt(110)	12,27	113*	113*	106*
NO/Pt(100)-hex	12,201	133*	120*	114*
NO/Pt(100)-(1x1)	12,201	131*	127*	113*
NO/Pt(211)	23	136 (134)*	134 (116)*	131 (99)*
NO/Pt(411)	23	152 (148)*	148 (141)*	141 (137)*
NO/Pd(100)	12,202	150	135	121

measurements of the dissociative adsorption of O₂ on Pt(111), where a similar discrepancy between SCAC^{23,131} and TPD^{167,204} results were noted, and the same correction was applied to obtain much better agreement.¹⁴⁵ After correction for the Pt sample reflectivity (the correction factor is (1-0.76)/(1-0.66) = 0.71), the integral heats of adsorption, marked with

asterisks in Table 8.1, are obtained. It can be seen that the independent SCAC measurements of CO adsorption on Pt(111) agree incredibly well with one another, and all three studies compare well with the isosteric desorption energy measurement of 135 kJ/mol.¹⁶⁶

b) Water (D₂O)/Pt(111)

The heat of molecular adsorption of D₂O on Pt(111) was measured calorimetrically to be 51.3 ± 1.6 kJ/mol over the coverage range 0-0.5 ML.¹⁷ As water adsorbed on Pt(111) at this temperature is known to form amorphous layers,²⁰⁵⁻²⁰⁷ the near constant heats over this range suggest molecular interactions (i.e. hydrogen bonding) present even at the lowest measured coverages. The multilayer heat of adsorption at 120 K of 47.2 ± 1.4 kJ/mol compares well with the desorption activation energy of amorphous D₂O multilayers from TPD of $49.7 \pm 2\%$ kJ/mol²⁰⁸ (corrected by adding $\frac{1}{2} RT$).

c) Methanol/Pt(111)

Methanol is known to adsorb molecularly on Pt(111) at 100 K.¹⁴⁰ SCAC measurements provided a heat of adsorption that decreased linearly with increasing coverage ($60.5 - 19.3 \cdot \theta$ kJ/mol) up to $\frac{1}{3}$ ML. The initial linear decrease was attributed to repulsive interactions between neighboring molecules. However STM studies on Cu(111) and Au(111) show that methanol forms hydrogen-bonded hexamers or chains²⁰⁹⁻²¹¹ and that the repulsive interactions may therefore be due to repulsions between neighboring clusters or chains.

This initial decrease was followed by a sharper linear decrease over the coverage range 0.33-0.5 ML followed by a leveling off to the multilayer heat of sublimation of 43.8 kJ/mol. The measured multilayer heat of adsorption compared well with the heat of sublimation of 45.3 kJ/mol from bulk thermodynamic data^{19,212,213} and 42.1-44.6 kJ/mol from TPD.²¹⁴

d) Formic Acid/Pt(111)

On clean Pt(111), formic acid molecularly adsorbs at 100 K.^{83,128,133} Below 143 K, continued dosing of formic acid forms an amorphous multilayer phase.^{136,137} Measured heats of adsorption at 100 K showed a best fit line of $61-2\theta$ kJ/mol up to 0.25 ML. By 2 ML, the heat of adsorption reached a constant value of 52.8 ± 2.5 kJ/mol which compared well with the desorption energy of 51 kJ/mol derived from TPD data.^{133,146}

e) Methyl Iodide/Pt(111)

At 100 K, methyl iodide adsorbs molecularly on Pt(111). The measured heat of adsorption was found to decrease linearly with coverage until the surface becomes saturated at 0.25 ML. The best linear fit to these data gives the equation $98.2-110\theta$ kJ/mol (Table 8.3). The linear decrease of adsorption energy was used to estimate the pairwise repulsion between MeI molecules adsorbed at next-nearest-neighbor sites^{20,215} of 4.5 kJ/mol. The multilayer heat of adsorption was found to asymptotically approach 37.9 ± 2.0 kJ/mol above 0.65 ML, in agreement with the heat of sublimation of bulk MeI of 38.0 kJ/mol.

f) Benzene/Pt(111)

Benzene adsorbs molecularly on Pt(111) at 300 K and lies flat on the surface.^{216,217} The saturation coverage was found to be either 2.3 or 2.4×10^{14} molecules/cm² (defined as 1 ML in the original papers^{31,103}) and corresponds to each benzene molecule occupying just over 6 surface sites. To remain consistent with the rest of the data discussed in this review, we have redefined 1 ML to be the surface density of Pt atoms on the (111) surface (i.e. 1.5×10^{15} cm⁻¹). This gives new equations for the heat of adsorption of benzene on Pt(111) of $197-313\theta-3530\theta^2$ and $199-502\theta-2170\theta^2$, as measured by two separate groups. The excellent agreement between the two data sets again confirms the accuracy of the measurements.

The zero coverage limit heat of 197 kJ/mol was used to estimate the average C-Pt(111) bond enthalpy of 33 kJ/mol per bond.¹⁰⁸ This bond enthalpy is ~6 times weaker than the C-Pt σ bonds of adsorbed methyl³² or cyclohexene³¹ on Pt(111) of 200 kJ/mol.

g) Naphthalene/Pt(111)

Similar to benzene, naphthalene adsorbs molecularly on Pt(111) at 300 K and lies flat on the surface. The saturation coverage was found to be 1.55×10^{14} molecules/cm² (defined as 1 ML in the original paper¹⁰⁹) which indicates that each molecule occupies ~10 surface sites. We have again redefined 1 ML here to be the surface density of Pt atoms on the (111) surface (i.e. 1.5×10^{15} cm⁻¹). This gives the equation for the heat of adsorption of naphthalene on Pt(111) of $317-313*\theta-3530*\theta^2$. Using the low coverage limit here of 300 kJ/mol, the average C-Pt(111) bond enthalpy of 30 kJ/mol was determined, in excellent agreement with that seen for benzene.¹⁰⁹

Table 8.2: Enthalpies of molecular adsorption measured with SCAC. All equations represent differential heats of adsorption valid over the stated coverage range collected at the stated temperature.

Reaction	surface	ref	q_{cal} [kJ/mol]	Coverage [ML]	Temp.
$D_2O_g \rightarrow D_2O_{ad}$	Pt(111)	17	51.3 (int. heat)	~0.66	120 K
$MeOH_g \rightarrow MeOH_{ad}$	Pt(111)	19	$60.5-19.3*\theta$	0-0.33	100 K
$HCOOH_g \rightarrow HCOOH_{ad}$	Pt(111)	146	$61-2*\theta$	0-0.25	100 K
$CH_3I_g \rightarrow CH_3I_{ad}$	Pt(111)	20	$98.2-110*\theta$	0-0.25	95 K
$Benz_g \rightarrow Benz_{ad}$	Pt(111)	108	$197-313*\theta-3530*\theta^2$	0-0.153	300 K
	Pt(111)	103	$199-502*\theta-2170*\theta^2$	0-0.153	300 K
$Naphth_g \rightarrow Naphth_{ad}$	Pt(111)	109	$300-329*\theta-18640*\theta^2$	0-0.083	300 K

8.5.2 Dissociative Adsorption and Surface Reactions: Adsorbed Molecular Fragments and Reaction Intermediates

h) Hydrocarbon fragments on transition metal surfaces.

Cyclohexene has been studied due to its key role as an intermediate in the dehydrogenation of cyclohexane to benzene, which has been discussed in two previous reviews from our group.^{13,14}

Alkyl halides (e.g. CH₃I and *t*-BuI) are known to undergo facile dissociation of the carbon-halide bond on metal single crystal surfaces, and have therefore been used in numerous studies to investigate the binding of adsorbed hydrocarbon fragments.^{40,45}

(i) Cyclohexene

Cyclohexene adsorbs molecularly on Pt(111) below 150 K to form di- σ -bonded cyclohexene.²¹⁸⁻²²⁴ At ~200–250 K adsorbed cyclohexene loses an allylic H to form H_{ad} plus adsorbed *c*-C₆H₉.^{220,223,224} Listed in Table 8.4 are equations for the differential heats of adsorption for the reactions: *c*-C₆H_{10,g} → di- σ *c*-C₆H_{10,ad} and *c*-C₆H_{10,g} → π -allyl-*c*-C₆H₉ + H_{ad}. For comparison to theory calculations, these equations can be integrated up to the coverage of interest.

(ii) CH₃ and CH: CH₃I/Pt(111)

The dissociative adsorption of methyl iodide (CH₃I) on Pt(111) to form adsorbed methyl moieties has been studied with a variety of surface analysis techniques (e.g. HREELS, RAIRS, TPD), leading to a clear understanding of its coverage and temperature dependent chemistry.^{46,47,113,225,226} Heating between 170 and 230 K leads to some molecular desorption as well as decomposition to CH_{3,ad} + I_{ad} that is complete by 270 K. Surface methyl groups begin decomposing almost immediately to produce adsorbed hydrogen and methylene (CH_{2,ad}), which

promptly decomposes to form CH_{ad} plus H_{ad} .²⁰ However, the equilibrium constant for this reaction lies to the left, so that methyl remains the dominant product at low coverage. As coverage increases, the probability that a methyl reacts with a hydrogen adatom to form methane rather than decomposing increases, so that at saturation coverage in the 270-310 K range, the only C-containing product that remains on the surface is CH_{ad} .²⁰

SCAC measurements of the adsorption of CH_3I on Pt(111) between 270-320K^{20,32} have provided heats of the reaction allowing for the calculation of the enthalpies of formation of adsorbed methyl (CH_3) and methyldyne (CH); both species are key intermediates in the decomposition of methane on Pt. By using heats of reaction at low surface coverage (<0.04 ML) ($\text{CH}_3\text{I}_{\text{g}} \rightarrow \text{CH}_3(\text{ad}) + \text{I}(\text{ad}) = 212$ kJ/mol). before methane desorption begins, the enthalpy of formation for $\text{CH}_{3,\text{ad}}$ of -53 kJ/mol was obtained. The enthalpy of formation of CH_{ad} of 33 +/- 10 kJ/mol was determined using reaction stoichiometries at saturation coverage ($\text{CH}_3\text{I}_{\text{g}} \rightarrow 0.44 \text{CH}_4(\text{g}) + 0.56 \text{CH}(\text{ad}) + 0.68 \text{H}(\text{ad}) + \text{I}(\text{ad}) = 171$ kJ/mol).

(iii) *t*-Bu: *t*-BuI/Pt(111)

Tert-butyl iodide adsorbs dissociatively on Pt(111) up to a total coverage of 0.07 ML at 100 K to form $t\text{-Bu}_{\text{ad}}$ plus I_{ad} , with an integral heat of reaction of 223 kJ/mol. The chemistry upon adsorption was confirmed with XPS, RAIRS, and DFT calculations.⁹⁸

(iv) C_2H_2 and C_2H_4

These measurements represented the first SCAC measurements that produced adsorbed molecular fragments. Again, all values marked with an asterisk in Table 8.4 have been corrected for sample reflectivity and differ from those reported in the original publications. Also, note that the heats of C_2H_2 and C_2H_4 reactions listed in Table 8.4 are differential values, as the surface

chemistry changes with surface coverage. Therefore, it is not possible to obtain an integral heat of adsorption that represents only a single reaction.

Table 8.3: Measured enthalpies of reaction from SCAC. All enthalpies are integral values at the stated coverage and temperature, unless otherwise noted. All equations represent differential heats of adsorption. Equations are dif. heat over stated coverage range

Reaction	surface	Ref	Int. ΔH_{rxn} [kJ/mol]	Coverage [ML]	Temp.
$CH_3I_g \rightarrow CH_{3,ad} + I_{ad}$	Pt(111)	³²	212	0.04 ML	320 K
$CH_3I_g \rightarrow 0.44 CH_{4,g} + 0.56 CH_{ad} + 0.68 H_{ad} + I_{ad}$	Pt(111)	²⁰	171	0.18 ML	320 K
$t-BuI_g \rightarrow t-Bu_{ad} + I_{ad}$	Pt(111)	⁹⁸	240	0.04 ML	100-120 K
$c-C_6H_{10,g} \rightarrow di-\sigma c-C_6H_{10,ad}$	Pt(111)	³¹	$130-47*\theta-1250*\theta^2$	0-0.24 ML	100 K
$c-C_6H_{10}(g) \rightarrow \pi\text{-allyl-}c-C_6H_9 + H_{ad}$	Pt(111)	³¹	$174-700*\theta-761*\theta^2$	0-0.12 ML	263 - 281 K
$C_2H_4 \rightarrow \equiv C-CH_3 + 1/2H_{2,g}$	Pt(111)	²⁸	98 (dif. Heat)*	0.17 ML	300 K
$C_2H_4 \rightarrow =CH-CH= + 2H_{ad}$	Pt(100)-hex	²⁹	150 (dif. Heat)*	Init	300 K
$C_2H_4 \rightarrow \equiv C-CH_3 + -H_{ad}$	Pt(100)-hex	²⁹	118 (dif. Heat)*	0.06 ML	300 K
$C_2H_4 \rightarrow -CH_2-CH_2-$	Pt(100)-hex	²⁹	106 (dif. Heat)*	0.3 ML	300 K
$C_2H_4 \rightarrow 2 \equiv C-H + 2H_{ad}$	Ni(100)	¹⁰⁶	203	Init.	300K
$C_2H_4 \rightarrow -C=CH (\sigma/\pi) + 3 H_{ad}$	Ni(110)	²²⁷	120	Init.	300 K
$C_2H_2 \rightarrow 2 \equiv C-H$	Ni(100)	¹⁰⁶	264	Init.	300 K
$C_2H_2 \rightarrow -C=CH (\sigma/\pi) + H_{ad}$	Ni(110)	²²⁷	180	Init.	300 K
$C_2H_2 \rightarrow -C=CH \sigma + H_{ad}$	Rh(100)	²²⁸	175	Init.	300 K

i) Oxygen bound reaction intermediates on Pt(111)

Hydroxyl is a key catalytic intermediate in numerous reactions, including the combustion and oxidation of organic molecules, steam reforming reactions, fuel cell applications, etc. Methoxy and formate represent the simplest examples of classes of molecular fragments (i.e. alkoxies and carboxylates) that are present in many of these reactions as well. Because platinum

is known to be active for many of these reactions, the energetics of each of these adsorbed molecular fragments on the Pt(111) surface were determined using SCAC.

Due to their catalytic importance, each of these species has been extensively studied in the literature, leading to a clear understanding of their temperature and coverage dependent surface chemistry. The oxygen bound hydrogen is only removed (significantly) from these species in the presence of atomic oxygen adsorbed on Pt(111) (O-Pt(111)).

(i) Hydroxyl: D₂O/O-Pt(111)

Adsorption of water on O-Pt(111) between 130 and 185 K leads to the formation of a stable water-hydroxyl complex, with stoichiometry (H₂O-OH)_{ad}.²²⁹⁻²³¹ Calorimetric measurements of the reaction of 0.5 ML of D₂O with 0.18 ML O_{ad} on Pt(111) at 150 K therefore leads to the complete consumption of O_{ad} to make 0.33 ML of (D₂O-OD)_{ad}. Table 8.5 shows the measured heat of the reaction $3 \text{ D}_2\text{O}_g + \text{O}_{ad} \rightarrow 2 (\text{D}_2\text{O--OD})_{ad}$ of 172 ± 8.7 kJ/mol. The differential heat of reaction over the coverage range 0-0.5 ML varied by less than 1 kJ/mol. This indicates that, even at low coverage, clustering of the water hydroxyl complex into islands occurs, consistent with low energy electron diffraction (LEED) and scanning tunneling microscopy (STM) experiments that observed ordering with either a ($\sqrt{3} \times \sqrt{3}$)R30° or (3x3) structure.

(ii) Methoxy: CH₃O/O-Pt(111)

Methanol is known to react on O-Pt(111) above 130 K to form adsorbed methoxy (CH₃O_{ad}) and OH_{ad} up to a coverage of 0.25 ML when all O_{ad} is consumed.¹⁴⁰ Calorimetric measurements performed at 150 K provided an integral enthalpy of reaction of 76.4 ± 2.9 kJ/mol at 0.25 ML coverage for the reaction $\text{CH}_3\text{OH}_g + \text{O}_{ad} \rightarrow \text{CH}_3\text{O}_{ad} + \text{OH}_{ad}$.¹⁹ This heat was found to

vary linearly with coverage, with a zero coverage limit of 85.5 kJ/mol. This linear decrease was attributed to repulsions between molecular fragments.

(iii) Formate: HCOOH/O-Pt(111)

Formic acid adsorbed on O-Pt(111) at 150 K results in the formation of adsorbed formate.^{128,129} The abstracted hydrogens from three formic acid molecules react with two O_{ad} to make a water-hydroxyl complex. At 130 K, formate first binds in a monodentate configuration, making a single O-Pt bond, followed by a slow conversion to doubly bound bidentate formate.¹²⁷ Using a new pulshape analysis method,³⁴ calorimetric measurements performed at 150 K provided the heats of reaction for the creation of monodentate formate ($3\text{HCOOH}_g + 2\text{O}_{ad} \rightarrow 3\text{HCOO}_{\text{mon,ad}} + (\text{H}_2\text{O}-\text{OH})_{ad} = 243 \text{ kJ/mol}$) and bidentate formate ($3\text{HCOOH}_g + 2\text{O}_{ad} \rightarrow 3\text{HCOO}_{\text{bi,ad}} + (\text{H}_2\text{O}-\text{OH})_{ad}$). These measured heats were found to linearly decrease with increasing surface coverage.

Table 8.4: SCAC measured integral enthalpies of reaction for oxygen containing species on O-Pt(111) at the specified coverage and temperature.

Reaction	Ref	Int. ΔH _{rxn} [kJ/mol]	Coverage [ML]	Temp.
$3\text{D}_2\text{O}_g + \text{O}_{ad} \rightarrow 2(\text{D}_2\text{O}-\text{OD})_{ad}$	33,145	172 _± 8.7	0.33 ML	150 K
$\text{CH}_3\text{OH}_g + \text{O}_{ad} \rightarrow \text{CH}_3\text{O}_{ad} + \text{OH}_{ad}$	19	76.4 _± 2.9	0.25 ML	150 K
$3\text{HCOOH}_g + 2\text{O}_{ad} \rightarrow 3\text{HCOO}_{\text{mon,ad}} + (\text{H}_2\text{O}-\text{OH})_{ad}$	146	243	0.25 ML	150 K
$3\text{HCOOH}_g + 2\text{O}_{ad} \rightarrow 3\text{HCOO}_{\text{bi,ad}} + (\text{H}_2\text{O}-\text{OH})_{ad}$	146	348	0.25 ML	150 K

8.5.3 Energetics of atomically adsorbed species from experiment

In order to calculate enthalpies of formation, as shown in Figure 8.1, it is often necessary to know the enthalpy of formation of other adsorbed species. Three common species involved in SCAC experiments (as reactants or products) are adsorbed oxygen, hydrogen and iodine. In

many of the studies involving oxygen containing species, such as methanol or water adsorption, preadsorbed oxygen led to deprotonation of the adsorbing species. Obtaining the enthalpy of formation of methoxy therefore required the enthalpy of formation of O_{ad} . Similarly, for many catalytic reactions involving hydrocarbons, H_{ad} is often a reactant or product, as was the case for cyclohexene dehydrogenation, where a cyclohexene reacts on Pt(111) to form π -allyl-c- $C_6H_{9,ad}$ and H_{ad} .

For the production of surface bound hydrocarbon fragments, the use of alkyl halides is common due to the facile breaking of the C-Halogen bond.⁴⁰ On Pt(111), such molecules have been used in SCAC experiments to produce adsorbed CH_3 , CH , and *t*-butyl. In order to obtain the enthalpies of formation of fragments produced from the dissociation of these alkyl iodide species, we also provide the desorption barrier for I_{ad} determined from careful TPD experiments as a function of surface coverage over the range 0-0.33 ML.

As $H_{2,g}$ and $O_{2,g}$ are both standard states for these elements, the enthalpies of reaction (ΔH_{rxn}) from TPD are equal to the enthalpies of formation shown in Table 8.5. However I_g^* has an enthalpy of formation of 106.7 kJ/mol,⁹³ which must be subtracted from the equation for I_{ad} desorption⁵¹ to provide the differential enthalpy of formation in Table 8.5. These values can be used in thermodynamic cycles to determine enthalpies of formation from SCAC experiments.

Table 8.5: Experimentally determined enthalpies of formation of important atomic intermediates on Pt(111) as determined from TPD and nuclear microprobe analysis (NMA).

Reaction	Ref	ΔH_f [kJ/mol]	Coverage [ML]	Technique
H_{ad}	³¹	-36	Ind.	TPD, NMA
O_{ad}	¹⁴⁵	-99	0.25	TPD
I_{ad}	⁵¹	-(148-199 θ)	0-0.33	TPD

8.5.4 Selected adsorbate energetics from other experimental techniques on transition metal surfaces

Tables 8.6-8.8 provide tabulation of selected experimentally determined activation energies for desorption of catalytically relevant molecules and atoms from techniques other than SCAC (i.e. TPD, EAI, time resolved electron energy loss spectroscopy (TREEELS)). Although these data will be discussed in greater detail in a future publication, a few observations will be discussed below.

The barrier for water desorption on Ni(111) (Table 8.6) is nearly identical to that measured on Pt(111) using SCAC (Table 8.2), while the activation barrier for recombinative desorption of H_{ad} is 24 kJ/mol larger than on Pt(111), underlining the observation that strength of binding of adsorbates on metal surfaces does not scale uniformly with metal (e.g. Ni does not bind all species 10 kJ/mol more strongly than Pt)

It is also interesting to note that although the H-ligand bond energies for the halogens F, Cl and I vary by a large amount (i.e. $D(H-F) = 565$ kJ/mol, $D(H-Cl) = 427$ kJ/mol, $D(H-I) = 293$ kJ/mol), the Pt(111)-ligand bond energies determined from TPD are nearly identical. This observation does not fit the linear trend both described in Chapter 7 and observed for halogens bound to organometallics with a Zr metal center.²³²

Table 8.7 shows the activation energy for ammonia desorption from low index faces of several transition metal surfaces. It can be seen that ammonia binds more strongly to Cu and Ni faces than to the Fe surface, which is known to be active in the Haber-Bosch process. The stronger binding of ammonia to the Fe(110) face than the Fe(111) face is an example of the dependence of binding strength on surface structure observed with many molecular fragments.

Table 8.6: Activation energies for molecular and atomic desorption from TPD and EAI experiments. Preexponential factors (ν) marked with a # have been calculated using the gas phase entropy of the desorbing species as described by Campbell and Sellers.⁸⁹ β is the heating rate used in the TPD experiment.

Reaction	surface	ref	E_{act} [kJ/mol]	$\log_{10}[\nu \text{ (s}^{-1}\text{)}]$	Peak Temp. [K]	β [K/s]
$\text{H}_2\text{O}_{ad} \rightarrow \text{H}_2\text{O}_g$	Ni(111)	²³³	52 ± 3	16 ± 1		
$\text{I}_{ad} \rightarrow \text{I}_g^\bullet$	Pt(111)	⁵¹	255-232	$14.2^\#$	890-820 (0.06-0.15 ML)	6
$\text{Cl}_{ad} \rightarrow \text{Cl}_g^\bullet$	Pt(111)	²³⁴	252-244	$14.2^\#$	920-890 (~0.03-.2 ML)	20
$\text{F}_{ad} \rightarrow \text{F}_g^\bullet$	Pt(111)		235	$14.2^\#$	890 (0.17 ML)	70
$\text{CH}_{4,ad} \rightarrow \text{CH}_{4,g}$	Pt(111)	²³⁵	15.2	12.1	63	0.6
$\text{C}_2\text{H}_{6,ad} \rightarrow \text{C}_2\text{H}_{6,g}$	Pt(111)	²³⁵	28.9	13.6	106	0.6
$\text{C}_3\text{H}_{8,ad} \rightarrow \text{C}_3\text{H}_{8,g}$	Pt(111)	²³⁵	41.5	14.8	139	0.6
	Cu(111)	²³⁶	34.2	14.8	119	2
$\text{C}_4\text{H}_{10,ad} \rightarrow \text{C}_4\text{H}_{10,g}$	Pt(111)	²³⁵	50.9	14.7	171	0.6
$\text{C}_6\text{H}_{14,ad} \rightarrow \text{C}_6\text{H}_{14,g}$	Pt(111)	²³⁵	79.8	17.2	229	0.6
	Cu(111)	²³⁶	64.7	17.2	192	2
$\text{Benz}_{ad} \rightarrow \text{Benz}_g$	Cu(111)	²³⁷	67.9-63.2	$15.6^\#$	225-210	4
	Ag(111)	²³⁸	68.9-65.0	$15.6^\#$	220-208*	1

Table 8.7: Experimental activation energies for desorption determined from TPD and time resolved electron energy loss spectroscopy (TREELS). Transition state theory (TST) was used to estimate a preexponential factor for desorption from Ni(111) to simulate TPD data.

Reaction	surface	ref	Tech.	Peak Temp [K] (β [K/s])	E_{act} [kJ/mol]	ν [s^{-1}]	rev $\log(\nu)$	rev E_{act} [kJ/mol]
$\text{NH}_{3,ad} \rightarrow \text{NH}_{3,g}$	Cu(111)	²³⁹	TPD [TREELS]	275 (8)	69 [57]	10^{13} ($10^{13.4 \pm 0.4}$)	14.7	77.3
	Cu(100)	²⁴⁰	TREELS		57	$10^{13.4 \pm 0.4}$		
	Fe(111)	²⁴¹	TPD	210 (20)	52	10^{13}	14.7	56.9
	Fe(110)	²⁴²	TPD	255 (9)	77	10^{13}	14.7	71.3
	Ni(111)	²⁴³ [²⁴⁴]	TPD [TST sim]	290 (10)	[88-15.5*0]	$[9.5 * 10^{17}]$	14.7	81.2
	Ni(110)	²⁴⁵	TPD	330 (2)	86	10^{13}	14.7	97.2

Table 8.8: Activation barriers for the recombinative desorption of H_{ad} to make $H_{2,g}$. Adsorbate induced surface reconstructions are indicated when observed experimentally. TPD found this to be a second order process on all surfaces where no reconstruction was present. In most cases, the preexponential factor was not provided in original publications.

Reaction	surface	ref	Technique	Eact [kJ/mol]	v [order]	Surface Reconstruction
$2H_{ad} \rightarrow H_{2,g}$	Cu(111)	²⁴⁶	TPD (TTPD(King)) [avg]	79 (88) [84-20*0]	$3 \cdot 10^{-4}$ $cm^2 s^{-1}$ [2nd]	-
	Cu(110)	²⁴⁷	H.P. titration of O_{ad}	60 ± 5.9		Missing row (1x2) ^{248,249}
	Cu(100)	²⁵⁰	T depend sticking	48 ± 6		(2x2)p4g: above 0.5 ML and 450 K ^{251,252}
	Fe(111)	²⁵³	TPD	88	[2nd]	-
	Fe(110)	²⁵³	TPD	109	[2nd]	-
	Fe(100)	^{254,255}	TPD	96	[2nd]	-
	Fe(100)	²⁵³	TPD	100	[2nd]	-
	Ni(111)	²⁵⁶	Isosteric Heat	96		-
	Ni(100)	²⁵⁶	Isosteric Heat	96		-
Pt(111)	³¹	TPD, NMA	72		-	

8.6 Applications

8.6.1 Reaction Pathways

A catalyst serves to create a lower energy pathway to move reacts to desired products. Gaining a fundamental understanding of the thermodynamic stability of key intermediates and the reaction barriers for their conversion is critical in the design of new materials or the prediction of novel reactions on existing materials. Because many intermediates of interest exist in metastable states, SCAC is often the only experimental technique available for obtaining this information. By measuring a series of intermediates with SCAC on a particular surface known,

it is possible to build detailed energy landscapes of a complete reaction pathway. From these energy landscapes, rate determining steps or key intermediates can be identified. This has been done previously for cyclohexane and cyclohexene dehydrogenation to benzene on Pt(111),¹³ leading to a fundamental understanding of why the dehydrogenation of cyclohexane does not stop at the cyclohexene product and why benzene desorption becomes competitive with its surface decomposition only at high surface coverage.

a) Methanol and Formic Acid Oxidation

Methanol and formic acid have garnered a great deal of attention for their potential use in direct fuel cells²⁵⁷⁻²⁵⁹ and hydrogen storage¹²⁵ applications. Platinum has been shown to be an active catalyst for the oxidation and reforming of both of these molecules to CO₂,²⁵⁹ however, particularly in the case of methanol, the formation of surface bound CO can lead to poisoning of the catalyst and a loss in activity. And, although these reactions have been studied in great detail, a consensus on the dominant pathways and relevant intermediates involved has not been reached. Gaining a fundamental understanding of the energetics of the intermediates identified in these reactions on Pt(111) (the most thermodynamically stable face of this metal) has led to insights into the potential mechanisms.

It is known that methanol oxidation can proceed to either adsorbed CO or formate (or possibly first formic acid) on Pt(111), depending on the availability of oxygen. However the active intermediate in the oxidation of formic acid on Pt(111) is still under discussion. In the surface science literature, the oxidation of formic acid on O-Pt(111) is known to proceed through a bidentate formate species which decomposes exclusively to CO₂ with an activation barrier of 60-67 kJ/mol (depending on coverage).^{127,128} From our energy landscape, shown in Fig. 7.2, it is clear that this activation barrier matches very closely the barrier necessary for converting

bidentate formate to the more weakly bound monodentate formate. This suggests that the rate determining step in formic acid oxidation is the activation of this binding configuration change.

This observation is consistent with DFT calculations and kinetic measurements of formate decomposition and synthesis on low index Cu surfaces,¹⁶³ which observed that the rate of decomposition was structure sensitive but the synthesis of formate was not. It was found from DFT that the reaction proceeds through a monodentate formate intermediate on all Cu surfaces (i.e. Cu(110), Cu(111), Cu(100)). This monodentate species had similar binding energies on all surfaces, while the binding strength of bidentate species varied with surface structure. The structure sensitivity in the decomposition reaction rate was due to variability in the activation barrier for breaking a single O-Cu to make monodentate formate. Based on the energetics in Figure 8.2, it was proposed that this same rate limiting step

8.6.2 Trends of Adsorbate Binding

By comparing our recent calorimetry measurements of the adiabatic bond dissociation enthalpies of three oxygen-bound molecular fragments (-OD,^{18,145} -OCH₃,¹⁹ and -O(O)CH¹⁴⁶) to the Pt(111) surface, as seen in Table 8.5, to gas phase thermodynamic data, it was found that these RO-Pt(111) bond enthalpies vary linearly with the RO-H bond enthalpies in the corresponding gas-phase molecules (water, methanol and formic acid), with a slope of unity¹⁹⁴ (Fig. 8.3). Such a correlation had been shown for ligand binding to organometallic complexes,^{172,173,260} where the sigma bond energies of many ligands to metal centers have been determined from equilibrium measurements. The data obtained from SCAC measurements discussed here confirmed for the first time that such a relationship holds for the binding of molecular fragments to an extended surface of a late transition metal (Pt(111)).

This correlation allows for the prediction of binding strength other surface species on the Pt(111) surface, as indicated by open square symbols in Figure 8.3, that are not produced in large enough concentrations or are not stable on a measurable timescale. For example, the hydroperoxy (-OOH) species is a possible intermediate in the activation of molecular oxygen on metal surfaces in the presence of adsorbed hydrogen.^{188,261} Using the predicted binding energy of -OOH of 107 kJ/mol, the stepwise reaction:



was shown to be stepwise exothermic (i.e. -69 kJ/mol for step one and -211 kJ/mol for step 2), although it may not be kinetically favored. See the report by Karp et al. for more details.¹⁹⁴

8.6.3 Comparison of experimental data to DFT calculations

It is common to see binding energies used to comparing DFT calculations and experimental data for adsorbates on metal surfaces. Because of the lack of experimental numbers for many catalytic intermediates, such comparisons can generally only be made on a few intermediates out of many for a particular reaction pathway, leaving the overall accuracy of a reaction pathway open to skepticism. Now that we have a more substantial database of adsorbates, both molecular and molecular fragments, on a single surface (Pt(111)), we can compare experimental numbers for binding energies to a commonly used generalized gradient approximation (GGA) functionals (i.e. PBE, RPBE and PW91). The numbers reported in Table 8.5 have all been previously published (see Table for references), with the exception of the PBE numbers lacking citations that have been provided by Ye Xu in a private communication. Also included are calculations performed with newer functionals that include van der Waals interactions (vdW-DF, PBE+vdW^{surf}).

One clear observation from these data is that PBE, RPBE, and PW-91 functionals predict the binding energies of weakly bound hydrocarbon species, such as methane, propane, and benzene to be much lower than experiment. This is because these functionals do not incorporate van der Waals (vdW) dispersion forces which are the dominant binding forces in these adsorbate systems. However, functionals that incorporate vdW interactions, such as those reported here, have already led to improvements in absolute accuracy.^{96,110,262}

By plotting the absolute errors of each of these DFT numbers (by subtracting the respective experimental binding energy) versus experimental binding energy (Figure 8.4), we see that there is no clear trend in accuracy. Many of the species are more weakly bound according to DFT, with the exception of CO_{ad} and O_{ad}; both of which are consistently overbound. However, even when reported within the same study, the errors differ greatly from species to species. For example, a binding energy of 160 kJ/mol was reported for CO (44 kJ/mol larger than experiment), while monodentate and bidentate formate errors are -78 and -23 kJ/mol respectively.¹⁵⁸ When a reaction diagram is developed using energetics with such errors, it is difficult to know whether the favored pathways indicated are accurate. Rather than comparing binding energies, comparing energetics of full reactions, as reported in Tables 8.1-4, may be more straightforward.

Table 8.9: Comparison of binding energies of adsorbates on Pt(111) from SCAC and TPD experimental data with DFT calculations.

Adsorbates on Pt(111)	Experiment	GGA-PBE	GGA-RPBE	GGA-PW91	vdW-DF/PBE+vdW ^{surf}
	ΔE (kJ/mol)	ΔE (kJ/mol)	ΔE (kJ/mol)	ΔE (kJ/mol)	ΔE (kJ/mol)
methyl	200 ^{32†}	174, 192 ²⁶³	163 ^{97 a}	197 ⁹⁷	
tert-butyl	207 ^{98†}	128 ⁹⁸			225 ⁹⁸
methane	15.2 ^{235*}	1.2	-3 ²⁶⁴	3.8 ^{265 a}	20
propane	41.5 ^{235*}	6.3, 6 ²⁶³	0 ^{266 b}		33 ^{b 266}
propane	41.5 ^{235*}	6.3 ^a	-9 ^{266 a}		41 ^{a 267}
benzene	166 ¹⁰⁸	78.6, 78 ²⁶²		67.5 ²⁶⁸ , 86.8 ²⁶⁹ , 117 ²⁷⁰	189 ²⁶²
methylidyne	561.5 ²⁰	630, 643 ²⁶³	569 ^{97 a}	620 ⁹⁷	
OH within (H ₂ O-OH)complex	248 ^{145 d}	262	217 ^{145 d}		
Methanol	59.4 ^{19 e}	24 ^{271 e §}			
Methanol	59 ^{19 a}	72.4 ^{272 a}		31.8 ^{71,160} , 20 ²⁷³	
Methoxy	186 ^{19 a}	204 ²⁷²	95	161 ^{274 a}	
Water hexagonal network	51.3 ^{145 f}	38.7	30 ^{145 f}		
HCOO _{mon.ad} (w/ H ₂ O-OH _{ad})	229 ^{146 a}	151 ^{158 a}			
HCOO _{bi.ad} (w/ H ₂ O-OH _{ad})	264 ^{146 a}	241 ^{158 a}	159 ^{114 a}	223 ¹¹⁴	
O	348 ^{145 a*}	384	352 ^{145 a}	360 ¹¹⁴ , 389 ²⁷⁵	
CO	116 ^{42,103 a}	160 ^{158 a}	129 ^{276 a}	176 ¹¹⁴	

All coverages are 1/9 ML unless otherwise noted. All experimental data from SCAC unless otherwise noted. * Temperature programmed desorption data. † coverage of 1/20 ML coadsorbed with 1/20 ML atomic iodine. § adsorbed on H₂O-sat. Pt(111). ^a coverage of 1/4 ML. ^b coverage of 1/8 ML. ^c coverage of 1/16 ML. ^d coverage of 1/3 ML. ^e coverage of 1/37 ML. ^f coverage of 2/3 ML.

8.7 Conclusions

Here we provide experimentally determined energetics of reactions determined from SCAC. These numbers have been used to build reaction landscapes for important catalytic reactions, such as cyclohexane dehydrogenation and methanol and formic acid oxidation. From these landscapes, previous experimental observations about these systems have been explained by the energetics of individual reaction steps, leading to a fundamental understanding of how reaction rates or product distributions may be affected by developing a material that changes the energetics of a particular intermediate. For example, the barrier for desorption of cyclohexene is much larger than the barrier for further dehydrogenation to benzene. The rate limiting step in formic acid oxidation on Pt(111) is the breaking of a single Pt-O bond, converting bidentate to monodentate formate. By destabilizing cyclohexene or creating a surface with an ensemble of sites that causes bidentate formate to have one strong and one weak Pt-O bond, catalysts could be identified developed that greatly improve desired product yields and operating conditions.

The correlation of three adsorbed molecular fragments bound through an oxygen to the Pt(111) surface to gas phase data for H-ligand bond strengths shows a linear relationship with a slope of unity. This correlation allows for the empirical prediction of other surface bound species from well-known gas phase data, greatly expanding the utility of SCAC.

These numbers can also be used as experimental benchmarks for comparison to DFT calculations. We have shown that for commonly used functionals, such as GGA-PBE, GGA-RPBE, and GGA-PW91, the calculated binding energies of molecular fragments contain large errors, particularly when vdWs interactions are present.

8.8 Figures

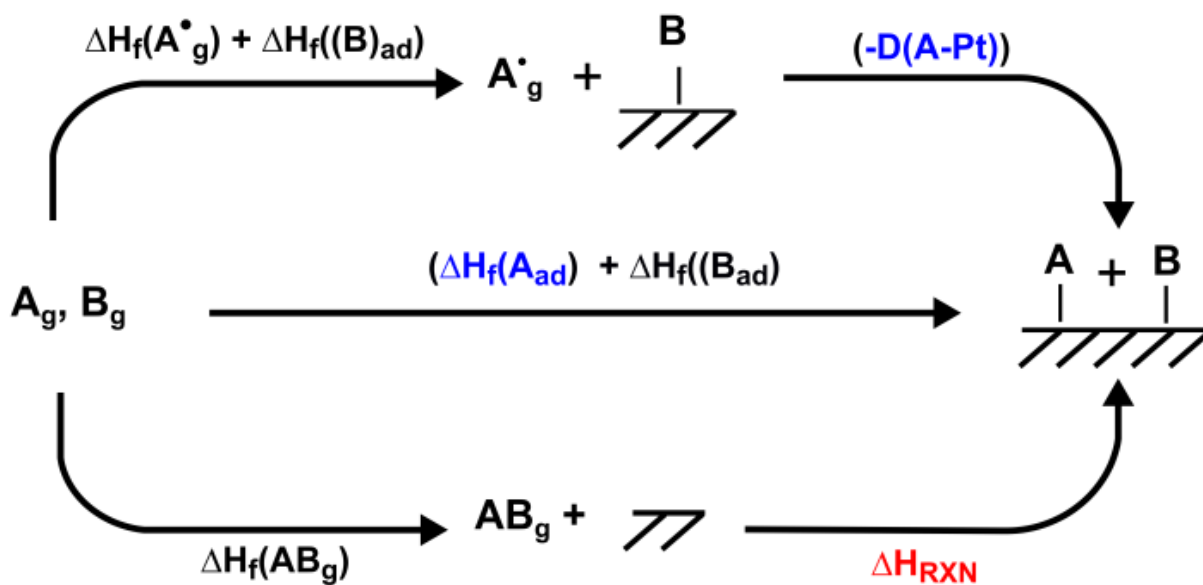


Figure 8.1: A generic thermodynamic cycle used for calculating enthalpies of formation and bond enthalpies (blue text) from measured enthalpies of reaction (red text).

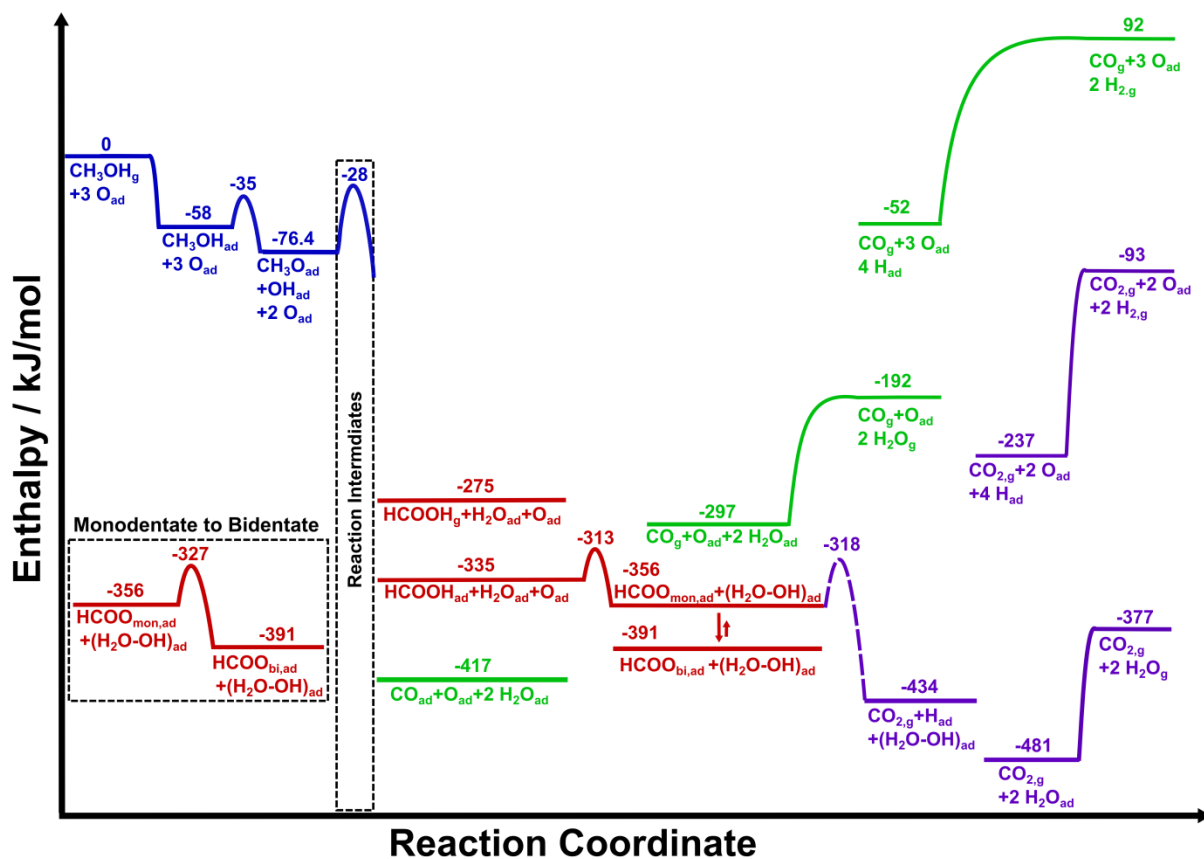


Figure 8.2: Experimentally determined energy landscape for the oxidation of both methanol and formic acid on oxygen precovered Pt(111). The inset in the bottom left corner shows the conversion between monodentate and bidentate formate.

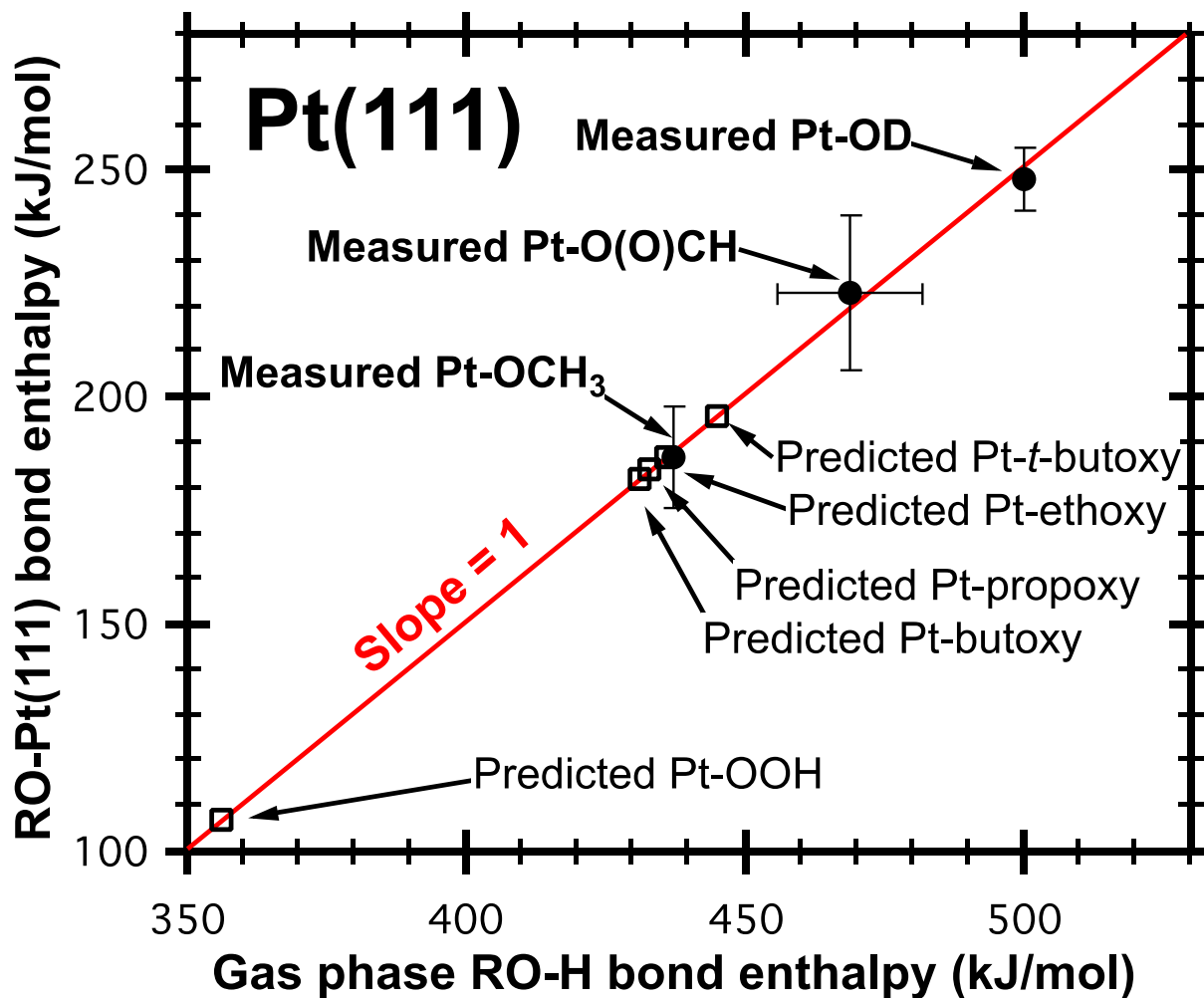


Figure 8.3: Surface bond enthalpies of molecular fragments adsorbed on Pt(111) through a single oxygen bond plotted versus their corresponding gas phase hydrogen-OR adiabatic bond enthalpies. A linear relationship with a slope of unity is seen, allowing for the prediction of bond enthalpies of other oxygen bound molecular fragments gas phase data.¹⁹⁴

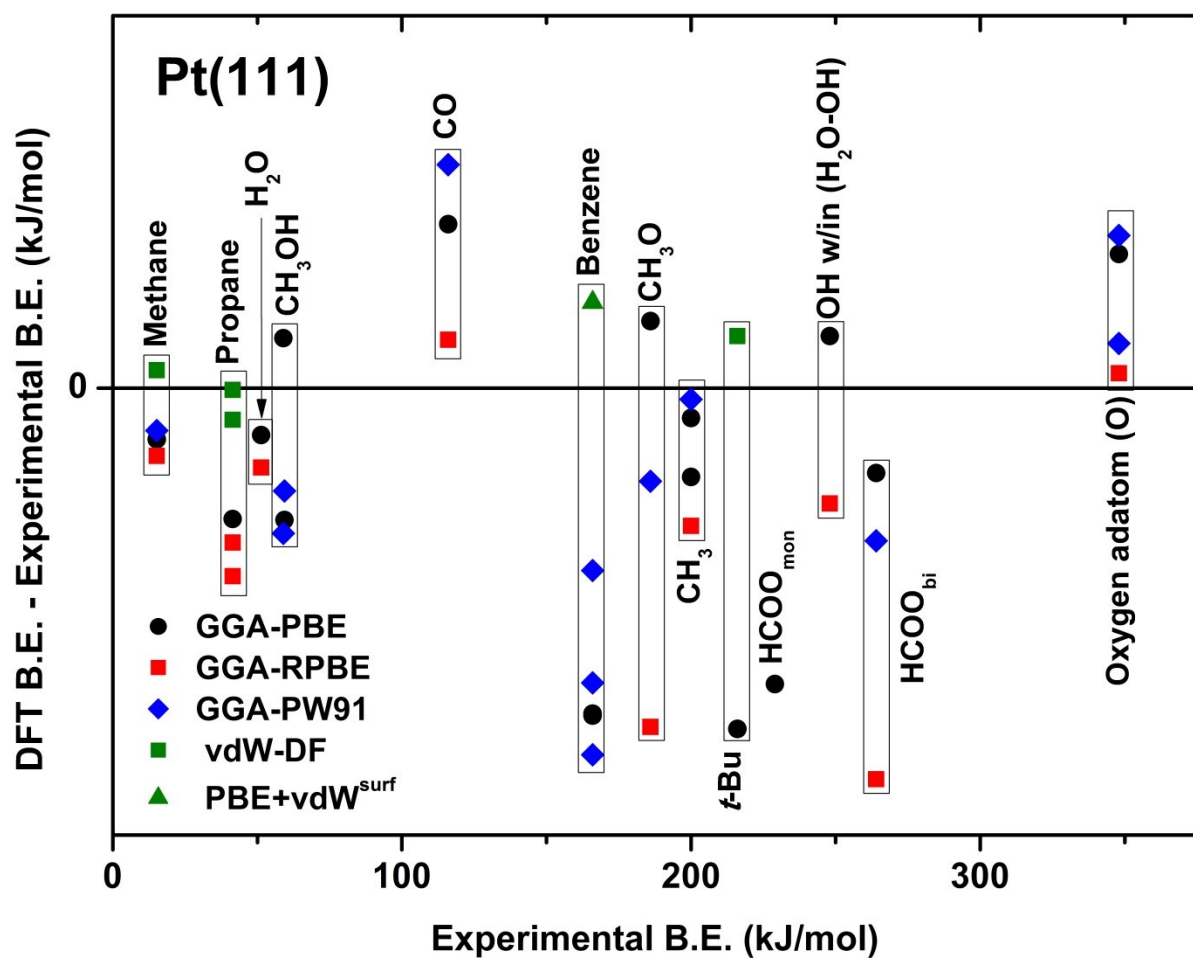


Figure 8.4: Comparison of experimentally determined binding energies to density functional theory calculations.

Chapter 9

Conclusions and Outlook

In this thesis, I have presented the results of SCAC studies of molecular adsorption and reaction on Pt(111). From this work the database of reliable, experimentally determined binding energies and enthalpies of formation of adsorbed species has been greatly increased. I have also demonstrated that SCAC can be used to obtain kinetic information from surface chemical reactions.

First, we have determined the following adsorption, dissociation and desorption processes for *t*-butyl iodide on Pt(111) in the indicated surface coverage and temperature ranges. Up to 0.07 ML total coverage of *t*-BuI, *t*-BuI dissociatively adsorbs to form *t*-Bu_{ad} plus I_{ad} at 100 K, with an integral heat of reaction of 230 kJ/mol. This dissociative adsorption process results in the occupation of ~50% of the surface Pt atoms. The remaining surface atoms are occupied by molecularly adsorbed *t*-BuI up to a total coverage of 0.15 ML, with an average heat of adsorption of 101-135 kJ/mol. Following the completion of the first layer, *t*-BuI molecularly adsorbs on top of the saturated Pt(111) surface between 0.15 and 0.38 ML, with a constant heat of adsorption of 44.5 ± 1.9 kJ/mol. This second layer desorbs between 120 and 150 K. Following completion of the second layer, molecular adsorption in the multilayer regime occurs. Desorption of the multilayer occurs between 100 and 120 K, and molecules in this regime bind ~6 kJ/mol more weakly than in the second molecular layer.

SCAC measurements provided the standard enthalpy of formation of adsorbed *t*-butyl and the Pt-*t*-butyl bond strengths at 0.04 ML (1/25 ML) of -168 ± 20 kJ/mol and 216 ± 20 kJ/mol respectively. These values were found to increase in magnitude by 9 kJ/mol in the limit of zero

coverage. The integral heats of molecular and dissociative ($t\text{-BuI}_g \rightarrow t\text{-Bu}_{\text{ad}} + \text{I}_{\text{ad}}$) adsorption were found to be 101-135 kJ/mol at 1/9 ML and 230 kJ/mol at 1/16 ML respectively. DFT calculations were performed using the GGA-PBE and optB86b vdW density functionals to calculate the heats of reaction and the binding energies of relevant adsorbates. Comparison of the calorimetry experiments to these calculations found that the optB86b vdW-DF provides more accurate energies than GGA-PBE for describing the adsorption and bonding of $t\text{-BuI}$ and $t\text{-Bu}$ on Pt(111) because these energies contain large contributions from dispersion.

It has also been demonstrated for the first time that kinetic information can be extracted from adsorption calorimetry measurements on single crystals. This capability arose from the need to analyze data from CH_3I and formic acid adsorption on Pt(111) that exhibited changes in detector pulse lineshape. Traditional analysis of SCAC data required that the molecular process of interest occur much faster than the time scale of the experiment. This meant that for the study of a particular intermediate species, experimental conditions have to be found where the following two statements are true: (1) the intermediate of interest is produced on a time scale much faster than the measurement *and* (2) has a lifetime on a timescale much longer than the measurement. The new analysis method presented here which allows the separation of the detector response into two distinct heat deposition processes, one fast and one slow, now only requires that the intermediate be stable on a timescale similar to the heat measurement. This greatly expands the number of systems that can be studied using SCAC, and provides additional rate constant information. This new lineshape analysis method has been applied to study the dissociative adsorption of methyl iodide on Pt(111), providing the coverage-dependent heats and rate constants for this quasi-two-step reaction process at 270 K. The heats agree with values measured at 320 K where the rates are so fast that lineshape analysis is not needed, thus verifying

the deconvolution analysis method presented here. The pseudo-first-order rate constant for the slow second step, k , obtained from this analysis decreases with surface coverage due to product inhibition. These data provide a complete energy diagram for the reaction $\text{CH}_3\text{I}_g \rightarrow \text{CH}_{3,\text{ad}} + \text{I}_{\text{ad}}$, and the formation energies of $\text{CH}_{3,\text{ad}}$ and CH_{ad} .

We have utilized this new analysis in the study of formic acid adsorption and reaction on clean and oxygen precovered Pt(111). From this work, the enthalpies of formation of monodentate and bidentate formate on Pt(111) are -354 ± 5 and -384 ± 5 kJ/mol respectively at $3/8$ ML coverage. The total formate-Pt(111) bond enthalpy in adsorbed monodentate formate is 224 ± 13 kJ/mol. The total bond enthalpy of bidentate formate to Pt(111) (two Pt-O bonds) is 254 ± 13 kJ/mol. The integral heat of adsorption of molecularly adsorbed formic acid on clean Pt(111) at 100 K is 62.5 kJ/mol at 0.25 ML. These enthalpies give the enthalpy of the reaction $\text{HCOOH}_{\text{ad}} \rightarrow \text{HCOO}_{\text{bi,ad}} + \text{H}_{\text{ad}}$ to be -4 kJ/mol at zero coverage and +24 kJ/mol at 0.375 ML. The first layer of molecularly adsorbed HCOOH saturates at a coverage of 0.5 ML at 100 K. Saturation coverages of bidentate formate on O-saturated Pt(111) at 150 and 190 K are 0.5 and 0.31 ML respectively.

A complete energy landscape for the oxidation of methanol and formic acid on Pt(111) was developed entirely from experimental data. From this, the conversion of bidentate formate to monodentate formate was identified as the rate determining step for the decomposition of bidentate formate, which has been observed in numerous experimental studies of methanol and formic acid oxidation and electrooxidation. This suggested that monodentate formate, rather than the more stable bidentate formate, is an active intermediate in the production of CO_2 . A route to minimizing bidentate formate buildup may be to minimize Pt ensemble size by using a bimetallic material.

The correlation of three adsorbed molecular fragments bound through an oxygen to the Pt(111) surface to gas phase data for H-ligand bond strengths shows a linear relationship with a slope of unity. This correlation allows for the empirical prediction of other surface bound species from well-known gas phase data, greatly expanding the utility of SCAC.

I have also presented a review of SCAC measurements for molecular adsorption and reaction made to date. Also included are experimental results utilizing TPD and EAI for a few important catalytic intermediates. A subset of the results from this review was compared to DFT calculations, showing that for the commonly used functionals GGA-PBE, GGA-RPBE, and GGA-PW91, the calculated binding energies of molecular fragments contain large, non-systematic errors, particularly when vdW interactions are present.

I believe there are many directions that future SCAC work can take. The most obvious is to make similar measurement to those above (i.e. molecular adsorption and reaction) on a wide range of material surfaces, adding to the existing body of experimental benchmarks. Below, I will briefly discuss two additional directions that I believe adsorption calorimetry can take.

Until now, measurements of simple molecular adsorption and reaction have been performed on single crystal surfaces with uniform composition. However, it is known for example that many catalytic processes can be improved by utilizing a bimetallic material in order to tune the binding strengths of intermediate species as well as the type and density of active catalytic sites. From an experimental standpoint, this poses a problem, as the combination of materials and their relative composition can lead to an enormous number of potential material compositions. This has led to the development of high throughput techniques for the studying catalytic processes.

Work in the Gellman group at Carnegie Mellon has utilized composition spread surfaces, which have been studied for many decades, to perform high throughput studies of catalyst activity and selectivity.²⁷⁷ The preparation method used in the Gellman lab involves simultaneously depositing up to four metals on a single crystal sample from sources that are physically offset from the sample center in combination with several rotating masks. This leads to a continuously changing metal composition over the sample surface that can be tuned by the user.²⁷⁸

This preparation technique could easily be applied to the 1 μm thick metal single crystal samples used in our SCAC experiments to produce a bimetallic surface that varies in composition over the width of the sample. In order to perform high throughput style calorimetry measurements of molecular adsorption and reaction on this composition spread surface, it would also be necessary to modify the pyroelectric ribbon detectors that are currently used in our lab. The detectors used now have a single metallic lead, roughly 4 mm in width,¹¹ on either side of the ribbon that is connected to an external circuit. Lithography techniques could be used to create thin leads on either side, perhaps on the order of hundreds of microns, spaced along the width of the ribbon. By pressing this ribbon against the back of a composition spread sample, where the length of each lead sees only one bimetallic composition, a single pulse of molecules over the entire sample would yield a detector signal for each surface composition. A schematic of the sample composition and detector design is shown in Figure 8.1.

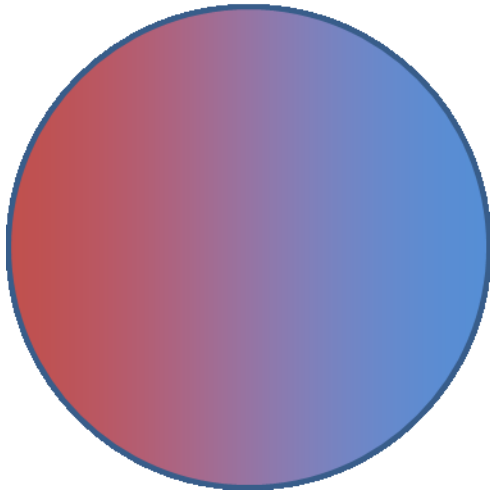
In order to do these experiments, it would also be necessary to measure the sticking probability of molecules on the surface. As the sticking probability would potentially vary with surface composition, a position sensitive mass spectrometry technique would be necessary. One such technique, known as Pixel Imaging Mass Spectrometry (PIImMS),²⁷⁹ has been developed

recently to allow for the monitoring of multiple masses during an experiment and to determine the spatial origin of the measured signal. This would allow this high throughput calorimetry technique to measure both sticking probabilities, as well as to monitor potential gas phase products, on a composition spread sample as a function of position.

A second development, that could be used independently or in conjunction with the high throughput setup, is the use of pulsed UV lasers to excite adsorbed molecular fragments following each molecular pulse. This would potentially allow one to obtain the energetics, and possibly kinetics through signal shape analysis, of multiple reaction steps during a single experiment. For example, performing an experiment at 100K might lead to molecular adsorption only. However if the molecular pulse is succeeded with a laser pulse (or sequence of laser pulses of varying intensity), you would obtain the detector signal for the adsorption and then a second (or sequence of) detector signal(s) that would be a combination of the laser pulse heating the sample (which can be calibrated for) as well as additional heat deposition (or extraction) for the reaction or desorption process. The addition of the pulsed laser would also allow for the controlled study of the effect of coadsorbates on the adsorption and reaction energetics. It would allow for the running of a calorimetry experiment at the same temperature condition but with different adsorbed fragments at controlled, variable coverages.

9.1 Figures

Composition spread
sample orientation



PVDF Detector ribbon and lead
design schematic

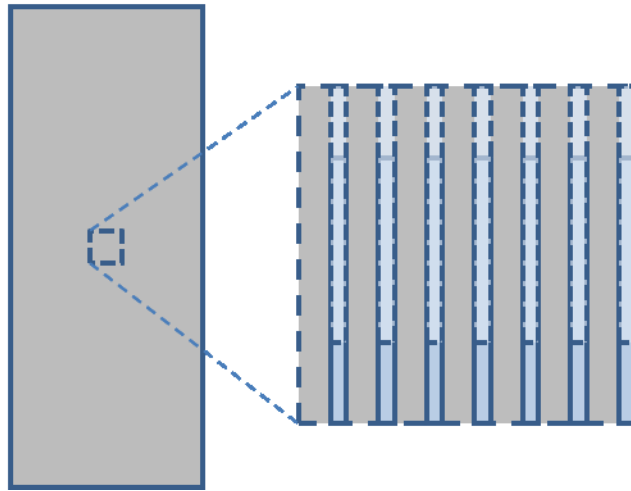


Figure 9.1: Schematic of high throughput calorimetry sample composition map and ribbon detector electrical contact pattern.

References

- (1) Ertl, G.; Knözinger, H.; Weitkamp, J. *Handbook of Heterogeneous Catalysis*; VCH: Weinheim, 1997.
- (2) Thomas, J. M.; Thomas, W. J. *Principles and Practice of Heterogeneous Catalysis*; Wiley, 1997.
- (3) Boudart, M. In *Advances in Catalysis*; D.D. Eley, H. P., Paul, B. W., Eds.; Academic Press: 1969; Vol. Volume 20, p 153.
- (4) Ertl, G.; Knözinger, H.; Weitkamp, J. *Environmental catalysis*; Wiley-VCH, 1999.
- (5) Borronibird, C. E.; King, D. A. *Review of Scientific Instruments* **1991**, *62*, 2177.
- (6) Borroni-Bird, C. E.; Al-Sarraf, N.; Andersson, S.; King, D. A. *Chem. Phys. Lett.* **1991**, *183*, 516.
- (7) Dixonwarren, S. J.; Kovar, M.; Wartnaby, C. E.; King, D. A. *Surface Science* **1994**, *307*, 16.
- (8) Stuckless, J. T.; Frei, N. A.; Campbell, C. T. *Review of Scientific Instruments* **1998**, *69*, 2427.
- (9) Stuckless, J. T.; Frei, N. A.; Campbell, C. T. *Sensors and Actuators B-Chemical* **2000**, *62*, 13.
- (10) Ajo, H. M.; Ihm, H.; Moilanen, D. E.; Campbell, C. T. *Rev. Sci. Instrum.* **2004**, *75*, 4471.
- (11) Lew, W.; Lytken, O.; Farmer, J. A.; Crowe, M. C.; Campbell, C. T. *Review of Scientific Instruments* **2010**, *81*, 9.
- (12) Brown, W. A.; Kose, R.; King, D. A. *Chemical Reviews* **1998**, *98*, 797.
- (13) Lytken, O.; Lew, W.; Campbell, C. T. *Chemical Society Reviews* **2008**, *37*, 2172.
- (14) Campbell, C. T.; Lytken, O. *Surf. Sci.* **2009**, *603*, 1365.
- (15) Crowe, M. C.; Campbell, C. T. In *Annual Review of Analytical Chemistry, Vol 4*; Cooks, R. G., Yeung, E. S., Eds.; Annual Reviews: Palo Alto, 2011; Vol. 4, p 41.
- (16) Freund, H. J.; Nilius, N.; Risse, T.; Schauermaun, S.; Schmidt, T. *Chemphyschem* **2011**, *12*, 79.
- (17) Lew, W. D.; Crowe, M. C.; Karp, E.; Campbell, C. T. *J. Phys. Chem. C* **2011**, *115*, 9164.
- (18) Lew, W.; Crowe, M. C.; Karp, E.; Lytken, O.; Farmer, J. A.; Arnadottir, L.; Schoenbaum, C.; Campbell, C. T. *J. Phys. Chem. C* **2011**, *115*, 11586.
- (19) Karp, E. M.; Silbaugh, T. L.; Crowe, M. C.; Campbell, C. T. *J. Am. Chem. Soc.* **2012**, *134*, 20388.
- (20) Karp, E. M.; Silbaugh, T. L.; Campbell, C. T. *Journal of Physical Chemistry C* **2013**, *117*, 6325.
- (21) Karmazyn, A. D.; Fiorin, V.; King, D. A. *Surf. Sci.* **2003**, *547*, 184.
- (22) Borthwick, D.; Fiorin, V.; Jenkins, S. J.; King, D. A. *Surface Science* **2008**, *602*, 2325.
- (23) Fiorin, V.; Borthwick, D.; King, D. A. *Surface Science* **2009**, *603*, 1360.
- (24) Liao, K.; Fiorin, V.; Jenkins, S. J.; King, D. A. *Physical Chemistry Chemical Physics* **2012**, *14*, 7528.

- (25) Liao, K.; Fiorin, V.; Gunn, D. S. D.; Jenkins, S. J.; King, D. A. *Physical Chemistry Chemical Physics* **2013**, *15*, 4059.
- (26) Stuckless, J. T.; Wartnaby, C. E.; AlSarraf, N.; DixonWarren, S. J. B.; Kovar, M.; King, D. A. *Journal of Chemical Physics* **1997**, *106*, 2012.
- (27) Wartnaby, C. E.; Stuck, A.; Yee, Y. Y.; King, D. A. *Journal of Physical Chemistry* **1996**, *100*, 12483.
- (28) Yeo, Y. Y.; Stuck, A.; Wartnaby, C. E.; King, D. A. *Chemical Physics Letters* **1996**, *259*, 28.
- (29) Yeo, Y. Y.; Stuck, A.; Wartnaby, C. E.; Kose, R.; King, D. A. *Journal of Molecular Catalysis a-Chemical* **1998**, *131*, 31.
- (30) Ge, Q. F.; Kose, R.; King, D. A. *Advances in Catalysis, Vol 45: Impact of Surface Science on Catalysis* **2000**, *45*, 207.
- (31) Lytken, O.; Lew, W.; Harris, J. J. W.; Vestergaard, E. K.; Gottfried, J. M.; Campbell, C. T. *Journal of the American Chemical Society* **2008**, *130*, 10247.
- (32) Karp, E. M.; Silbaugh, T. L.; Campbell, C. T. *Journal of the American Chemical Society* **2013**, *135*, 5208.
- (33) Lew, W.; Crowe, M. C.; Lytken, O.; Karp, E.; Farmer, J. A.; Schoenbaum, C.; Campbell, C. T. *Abstracts of Papers of the American Chemical Society* **2010**, 239.
- (34) Silbaugh, T. L.; Karp, E. M.; Campbell, C. T. *Journal of Catalysis* **2013**, *308*, 114.
- (35) Ajo, H. M.; Ihm, H.; Moilanen, D. E.; Campbell, C. T. *Review of Scientific Instruments* **2004**, *75*, 4471.
- (36) King, D. A.; Wells, M. G. *Surface Science* **1972**, *29*, 454.
- (37) Bond, G. C. *Metal catalysed reactions of hydrocarbons*; Springer: New York, 2005.
- (38) Weaver, J. F.; Carlsson, A. F.; Madix, R. J. *Surf. Sci. Rep.* **2003**, *50*, 107.
- (39) Zaera, F. *Chemical Reviews* **1995**, *95*, 2651.
- (40) Bent, B. E. *Chem. Rev.* **1996**, *96*, 1361.
- (41) Borroni-Bird, C. E.; King, D. A. *Rev. Sci. Instrum.* **1991**, *62*, 2177.
- (42) Fischer-Wolfarth, J.-H.; Hartmann, J.; Farmer, J. A.; Flores-Camacho, J. M.; Campbell, C. T.; Schauermaun, S.; Freund, H.-J. *Rev. Sci. Instrum.* **2011**, *82*, 024102.
- (43) Campbell, C. T.; Lytken, O. *Surf. Sci.* **2009**, *603*, 1365.
- (44) McMillen, D. F.; Golden, D. M. *Annu. Rev. Phys. Chem.* **1982**, *33*, 493.
- (45) Zaera, F. *Acc. Chem. Res.* **1992**, *25*, 260.
- (46) French, C.; Harrison, I. *Surface Science* **1995**, *342*, 85.
- (47) Zaera, F.; Hoffmann, H. *Journal of Physical Chemistry* **1991**, *95*, 6297.
- (48) Luo, Y.-R. *Comprehensive Handbook of Chemical Bond Energies*; CRC Press, 2007.
- (49) Sohn, Y.; Wei, W.; White, J. M. *Surface Science* **2008**, *602*, 2706.
- (50) Tjandra, S.; Zaera, F. *Journal of the American Chemical Society* **1995**, *117*, 9749.
- (51) Labayen, M.; Furman, S. A.; Harrington, D. A. *Surf. Sci.* **2003**, *525*, 149.
- (52) Hoffmann, H.; Griffiths, P. R.; Zaera, F. *Surface Science* **1992**, *262*, 141.
- (53) Tilekaratne, A.; Simonovis, J. P.; Fagundez, M. F. L.; Ebrahimi, M.; Zaera, F. *Acs Catalysis* **2012**, *2*, 2259.
- (54) Hoffmann, F. M. *Surface Science Reports* **1983**, *3*, 107.

- (55) Zaera, F. *International Reviews in Physical Chemistry* **2002**, *21*, 433.
- (56) Kresse, G.; Hafner, J. *Physical Review B* **1994**, *49*, 14251.
- (57) Kresse, G.; Furthmuller, J. *Computational Materials Science* **1996**, *6*, 15.
- (58) Kresse, G.; Furthmuller, J. *Physical Review B* **1996**, *54*, 11169.
- (59) Perdew, J. P.; Burke, K.; Ernzerhof, M. *Physical Review Letters* **1996**, *77*, 3865.
- (60) Blochl, P. E. *Physical Review B* **1994**, *50*, 17953.
- (61) Kresse, G.; Joubert, D. *Physical Review B* **1999**, *59*, 1758.
- (62) Methfessel, M.; Paxton, A. T. *Physical Review B* **1989**, *40*, 3616.
- (63) Klimes, J.; Bowler, D. R.; Michaelides, A. *Journal of Physics-Condensed Matter* **2010**, *22*, 5.
- (64) Klimes, J.; Bowler, D. R.; Michaelides, A. *Physical Review B* **2011**, *83*, 13.
- (65) Ashcroft, N. W. M. N. D. *Solid state physics*; Holt, Rinehart and Winston: New York, 1976.
- (66) Neugebauer, J.; Scheffler, M. *Physical Review B* **1992**, *46*, 16067.
- (67) Henkelman, G.; Uberuaga, B. P.; Jonsson, H. *Journal of Chemical Physics* **2000**, *113*, 9901.
- (68) Henkelman, G.; Jonsson, H. *Journal of Chemical Physics* **1999**, *111*, 7010.
- (69) Bahn, S. R.; Jacobsen, K. W. *Computing in Science & Engineering* **2002**, *4*, 56.
- (70) Porezag, D.; Pederson, M. R. *Physical Review B* **1996**, *54*, 7830.
- (71) Greeley, J.; Mavrikakis, M. *Journal of the American Chemical Society* **2004**, *126*, 3910.
- (72) Calaza, F. C.; Xu, Y.; Mullins, D. R.; Overbury, S. H. *Journal of the American Chemical Society* **2012**, *134*, 18034.
- (73) Loffreda, D.; Jugnet, Y.; Delbecq, F.; Bertolini, J. C.; Sautet, P. *Journal of Physical Chemistry B* **2004**, *108*, 9085.
- (74) Liu, Z.-M.; Zhou, X.-L.; Buchanan, D. A.; Kiss, J.; White, J. M. *J. Am. Chem. Soc.* **1992**, *114*, 2031.
- (75) Liu, Z.-M.; Akhter, S.; Roop, B.; White, J. M. *J. Am. Chem. Soc.* **1988**, *110*, 8708.
- (76) Tjandra, S.; Zaera, F. *Journal of Vacuum Science & Technology a-Vacuum Surfaces and Films* **1992**, *10*, 404.
- (77) C.D., W.; W.M., R.; L.E., D.; J.F., M. *Handbook of X-ray Photoelectron Spectroscopy*; Perkin-Elmer: MN, 1979.
- (78) Zaera, F.; H, H.; P, G. *Vacuum* **1990**, *41*, 735.
- (79) Smith, A. L. *The Coblenz Society Desk Book of Infrared Spectra*; The Coblenz Society: Kirkwood, MO, 1982.
- (80) Douberly, G. E.; Ricks, A. M.; Ticknor, B. W.; Schleyer, P. v. R.; Duncan, M. A. *J. Am. Chem. Soc.* **2007**, *129*, 13782.
- (81) Rasul, G.; Chen, J. L.; Prakash, G. K. S.; Olah, G. A. *J. Phys. Chem. A* **2009**, *113*, 6795.
- (82) Sheppard, N.; Delacruz, C. *Advances in Catalysis, Vol 41* **1996**, *41*, 1.
- (83) Avery, N. R.; Sheppard, N. *Proceedings of the Royal Society of London Series a-Mathematical Physical and Engineering Sciences* **1986**, *405*, 1.
- (84) Lee, I.; Zaera, F. *Journal of Physical Chemistry C* **2007**, *111*, 10062.
- (85) Weaver, J. F.; Ikai, M.; Carlsson, A.; Madix, R. J. *Surface Science* **2001**, *470*, 226.

- (86) *CRC handbook of chemistry and physics*; 94 ed.; CRC Press: Cleveland, Ohio, 2013.
- (87) Stephenson, R. M.; Malanowski, S.; Elsevier: New York: *Handbook of the Thermodynamics of Organic Compounds*, 1987.
- (88) White, J. M.; Henderson, M. A. *Journal of Physical Chemistry B* **2005**, *109*, 14990.
- (89) Campbell, C. T.; Sellers, J. R. V. *J. Am. Chem. Soc.* **2012**, *134*, 18109.
- (90) Scott, D. W. *Chemical thermodynamic properties of hydrocarbons and related substances : properties of the alkane hydrocarbons, C₁ through C₁₀, in the ideal gas state from 0 to 1500 K*; Washington : U.S. Dept. of the Interior, Bureau of Mines : For sale by the Supt. of Docs., U.S. Govt. Print. Off.: Washington], 1974.
- (91) Benson, S. W.; Amano, A. *J. Chem. Phys.* **1962**, *37*, 197.
- (92) Stevens, W. R.; Walker, S. H.; Shuman, N. S.; Baer, T. *Journal of Physical Chemistry A* **2010**, *114*, 804.
- (93) Cox, J. D.; Wagman, D. D.; Medvedev, V. A. *CODATA key values for thermodynamics*; Hemisphere Publishing Corp.: New York, 1984.
- (94) Pedley, J. B. *Thermochemical data and structures of organic compounds*, Thermodynamics Research Center, Texas A&M University, 1994.
- (95) Tsang, W. In *Energetics of organic free radicals.*; Martino Simoes, J. A., Greenberg, A., Liebman, J. F., Eds.; Blackie Academic and Professional: London, 1996, p 22.
- (96) Tkatchenko, A.; Batina, N.; Cedillo, A.; Galvan, M. *Surface Science* **2005**, *581*, 58.
- (97) Ford, D. C.; Xu, Y.; Mavrikakis, M. *Surface Science* **2005**, *587*, 159.
- (98) Silbaugh, T. L.; Giorgi, J. B.; Xu, Y.; Tillekaratne, A.; Zaera, F.; Campbell, C. T. *Journal of Physical Chemistry C* **2014**, *118*, 427.
- (99) Poelsema, B.; Mechttersheimer, G.; Comsa, G. *Surface Science* **1981**, *111*, 519.
- (100) Borroni-Bird, C. E.; King, D. A. *Chem. Phys. Lett.* **1991**, *183*, 516.
- (101) Stuckless, J. T.; Frei, N. A.; Campbell, C. T. *Rev. Sci. Instrum.* **1998**, *69*, 2427.
- (102) Lew, W.; Lytken, O.; Farmer, J. A.; Crowe, M. C.; Campbell, C. T. *Rev. Sci. Instrum.* **2010**, *81*, 024102.
- (103) Schiesser, A.; Hartz, P.; Schafer, R. *Surface Science* **2010**, *604*, 2098.
- (104) Lew, W.; Crowe, M. C.; Karp, E.; Lytken, O.; Farmer, J. A.; Arnadottir, L.; Schoenbaum, C.; Campbell, C. T. *J. Phys. Chem. C* **2011**, *115*, 11586.
- (105) Lew, W.; Crowe, M. C.; Campbell, C. T.; Carrasco, J.; Michaelides, A. *J. Phys. Chem. C* **2011**, *115*, 23008.
- (106) Vattuone, L.; Yeo, Y. Y.; Kose, R.; King, D. A. *Surface Science* **2000**, *447*, 1.
- (107) Lytken, O.; Lew, W.; Harris, J. J. W.; Vestergaard, E. K.; Gottfried, J. M.; Campbell, C. T. *J. Am. Chem. Soc.* **2008**, *130*, 10247.
- (108) Ihm, H.; Ajo, H. M.; Gottfried, J. M.; Bera, P.; Campbell, C. T. *Journal of Physical Chemistry B* **2004**, *108*, 14627.
- (109) Gottfried, J. M.; Vestergaard, E. K.; Bera, P.; Campbell, C. T. *Journal of Physical Chemistry B* **2006**, *110*, 17539.
- (110) Klimes, J.; Michaelides, A. *Journal of Chemical Physics* **2012**, *137*, 12.
- (111) Stuck, A.; Wartnaby, C. E.; Yeo, Y. Y.; Stuckless, J. T.; AlSarraf, N.; King, D. A. *Surface Science* **1996**, *349*, 229.

- (112) Cox, J. D.; Pilcher, G. *Thermochemistry of organic and organometallic compounds*; Academic Press: London; New York, 1970.
- (113) Hugenschmidt, M. B.; Domagala, M. E.; Campbell, C. T. *Surface Science* **1992**, 275, 121.
- (114) Grabow, L. C.; Gokhale, A. A.; Evans, S. T.; Dumesic, J. A.; Mavrikakis, M. *Journal of Physical Chemistry C* **2008**, 112, 4608.
- (115) Flaherty, D. W.; Yu, W. Y.; Pozun, Z. D.; Henkelman, G.; Mullins, C. B. *Journal of Catalysis* **2011**, 282, 278.
- (116) Sawada, T.; Liu, Z. X.; Takagi, N.; Watanabe, K.; Matsumoto, Y. *Chemical Physics Letters* **2004**, 392, 334.
- (117) Endo, M.; Matsumoto, T.; Kubota, J.; Domen, K.; Hirose, C. *Surface Science* **1999**, 441, L931.
- (118) Endo, M.; Matsumoto, T.; Kubota, J.; Domen, K.; Hirose, C. *Journal of Physical Chemistry B* **2000**, 104, 4916.
- (119) Endo, M.; Matsumoto, T.; Kubota, J.; Domen, K.; Hirose, C. *Journal of Physical Chemistry B* **2001**, 105, 1573.
- (120) Miller, A. V.; Kaichev, V. V.; Prosvirin, I. P.; Bukhtiyarov, V. I. *Journal of Physical Chemistry C* **2013**, 117, 8189.
- (121) Barth, J. V.; Costantini, G.; Kern, K. *Nature* **2005**, 437, 671.
- (122) Sarikaya, M.; Tamerler, C.; Jen, A. K. Y.; Schulten, K.; Baneyx, F. *Nature Materials* **2003**, 2, 577.
- (123) Lynch, I.; Cedervall, T.; Lundqvist, M.; Cabaleiro-Lago, C.; Linse, S.; Dawson, K. A. *Advances in Colloid and Interface Science* **2007**, 134-35, 167.
- (124) Kasemo, B. *Surface Science* **2002**, 500, 656.
- (125) Grasemann, M.; Laurency, G. *Energy & Environmental Science* **2012**, 5, 8171.
- (126) Cuesta, A.; Cabello, G.; Osawa, M.; Gutierrez, C. *Acs Catalysis* **2012**, 2, 728.
- (127) Avery, N. R. *Applied Surface Science* **1983**, 14, 149.
- (128) Columbia, M. R.; Crabtree, A. M.; Thiel, P. A. *J. Electroanal. Chem.* **1993**, 351, 207.
- (129) Avery, N. R. *Applied Surface Science* **1982**, 11-2, 774.
- (130) Hodgson, A.; Haq, S. *Surface Science Reports* **2009**, 64, 381.
- (131) Yeo, Y. Y.; Vattuone, L.; King, D. A. *Journal of Chemical Physics* **1997**, 106, 392.
- (132) Coolidge, A. S. *Journal of the American Chemical Society* **1928**, 50, 2166.
- (133) Columbia, M. R.; Crabtree, A. M.; Thiel, P. A. *J. Am. Chem. Soc.* **1992**, 114, 1231.
- (134) McCarty, J. G.; Madix, R. J. *Surface Science* **1976**, 54, 210.
- (135) Campbell, C. T.; Sellers, J. R. V. *Chemical Reviews* **2013**, 113, 4106.
- (136) Millikan, R. C.; Pitzer, K. S. *Journal of Chemical Physics* **1957**, 27, 1305.
- (137) Ohtani, T.; Kubota, J.; Wada, A.; Kondo, J. N.; Domen, K.; Hirose, C. *Surf. Sci.* **1996**, 368, 270.
- (138) Chapman, D. *Journal of the Chemical Society* **1956**, 225.
- (139) Stephenson, R. M.; Malanowski, S.; Elsevier: New York: Handbook of the Thermodynamics of Organic Compounds, 1987.
- (140) Sexton, B. A. *Surface Science* **1981**, 102, 271.

- (141) Sexton, B. A.; Hughes, A. E.; Avery, N. R. *Surface Science* **1985**, *155*, 366.
- (142) Solymosi, F.; Kiss, J.; Kovacs, I. *Surface Science* **1987**, *192*, 47.
- (143) Barteau, M. A.; Bowker, M.; Madix, R. J. *Surface Science* **1980**, *94*, 303.
- (144) Lebedeva, N. D. **1964**, *38*, 1435.
- (145) Karp, E. M.; Campbell, C. T.; Studt, F.; Abild-Pedersen, F.; Nerskov, J. K. *Journal of Physical Chemistry C* **2012**, *116*, 25772.
- (146) Silbaugh, T. L.; Karp, E. M.; Campbell, C. T. *Journal of the American Chemical Society* **2014**, *136*, 3964.
- (147) Jarvi, T. D.; Sriramulu, S.; Stuve, E. M. *Journal of Physical Chemistry B* **1997**, *101*, 3649.
- (148) Sriramulu, S.; Jarvi, T. D.; Stuve, E. M. *Electrochimica Acta* **1998**, *44*, 1127.
- (149) Chen, Y. X.; Miki, A.; Ye, S.; Sakai, H.; Osawa, M. *Journal of the American Chemical Society* **2003**, *125*, 3680.
- (150) Neurock, M.; Janik, M.; Wieckowski, A. *Faraday Discussions* **2008**, *140*, 363.
- (151) Samjeske, G.; Osawa, M. *Angewandte Chemie-International Edition* **2005**, *44*, 5694.
- (152) Cuesta, A.; Cabello, G.; Gutierrez, C.; Osawa, M. *Physical Chemistry Chemical Physics* **2011**, *13*, 20091.
- (153) Osawa, M.; Komatsu, K.-i.; Samjeske, G.; Uchida, T.; Ikeshoji, T.; Cuesta, A.; Gutierrez, C. *Angewandte Chemie-International Edition* **2011**, *50*, 1159.
- (154) Chen, Y. X.; Heinen, M.; Jusys, Z.; Behm, R. J. *Langmuir* **2006**, *22*, 10399.
- (155) Chen, Y. X.; Heinen, M.; Jusys, Z.; Behm, R. J. *Angewandte Chemie-International Edition* **2006**, *45*, 981.
- (156) Gao, W.; Keith, J. A.; Anton, J.; Jacob, T. *Journal of the American Chemical Society* **2010**, *132*, 18377.
- (157) Joo, J.; Uchida, T.; Cuesta, A.; Koper, M. T. M.; Osawa, M. *Journal of the American Chemical Society* **2013**, *135*, 9991.
- (158) Gao, W.; Keith, J. A.; Anton, J.; Jacob, T. *Dalton Transactions* **2010**, *39*, 8450.
- (159) Akhter, S.; White, J. M. *Surface Science* **1986**, *167*, 101.
- (160) Greeley, J.; Mavrikakis, M. *J. Am. Chem. Soc.* **2002**, *124*, 7193.
- (161) Campbell, C. T.; Sun, Y. K.; Weinberg, W. H. *Chemical Physics Letters* **1991**, *179*, 53.
- (162) Yatsu, T.; Nishimura, H.; Fujitani, T.; Nakamura, J. *Journal of Catalysis* **2000**, *191*, 423.
- (163) Wang, G. C.; Morikawa, Y.; Matsumoto, T.; Nakamura, J. *Journal of Physical Chemistry B* **2006**, *110*, 9.
- (164) Nakamura, I.; Nakano, H.; Fujitani, T.; Uchijima, T.; Nakamura, J. *Journal of Vacuum Science & Technology a-Vacuum Surfaces and Films* **1999**, *17*, 1592.
- (165) Fischer-Wolfarth, J.-H.; Hartmann, J.; Farmer, J. A.; Flores-Camacho, J. M.; Campbell, C. T.; Schauermaun, S.; Freund, H.-J. *Rev. Sci. Instrum.* **2011**, *82*, 024102.
- (166) Ertl, G.; Neumann, M.; Streit, K. M. *Surface Science* **1977**, *64*, 393.
- (167) Campbell, C. T.; Ertl, G.; Kuipers, H.; Segner, J. *Surface Science* **1981**, *107*, 207.
- (168) Collins, D. M.; Spicer, W. E. *Surface Science* **1977**, *69*, 85.
- (169) McCabe, R. W.; Schmidt, L. D. *Surface Science* **1977**, *65*, 189.
- (170) Chao, J.; Rossini, F. D. *Journal of Chemical and Engineering Data* **1965**, *10*, 374.

- (171) Bryndza, H. E.; Fong, L. K.; Paciello, R. A.; Tam, W.; Bercaw, J. E. *J. Am. Chem. Soc.* **1987**, *109*, 1444.
- (172) Bryndza, H. E.; Domaille, P. J.; Tam, W.; Fong, L. K.; Paciello, R. A.; Bercaw, J. E. *Polyhedron* **1988**, *7*, 1441.
- (173) Bulls, A. R.; Bercaw, J. E.; Manriquez, J. M.; Thompson, M. E. *Polyhedron* **1988**, *7*, 1409.
- (174) Chase, M. W.; National Institute of Standards and, T. *NIST-JANAF thermochemical tables*; American Chemical Society ; American Institute of Physics for the National Institute of Standards and Technology: [Washington, D.C.]; Woodbury, N.Y., 1998.
- (175) Gross, H.; Campbell, C. T.; King, D. A. *Surf. Sci.* **2004**, *572*, 179.
- (176) Newton, M. A.; Campbell, C. T. *Catalysis Letts.* **1996**, *37*, 15.
- (177) Montemore, M. M.; Medlin, J. W. *J. Chem. Phys.* **2012**, *136*.
- (178) Montemore, M. M.; Medlin, J. W. *J. Phys. Chem. C* **2013**, *117*, 20078.
- (179) Karp, E. M.; Silbaugh, T. L.; Crowe, M. C.; Campbell, C. T. *J. Am. Chem. Soc.* **2012**, *134*, 20388.
- (180) Jacob, T. *Fuel Cells* **2006**, *6*, 159.
- (181) Luo, Y. R. *Comprehensive Handbook of Chemical Bond Energies*; Taylor & Francis: Boca Raton Fl., 2010.
- (182) Karp, E. M.; Studt, F.; Abild-Pedersen, F.; Nørskov, J. K.; Campbell, C. T. *J. Phys. Chem. C* **2012**, *116*, 25772.
- (183) Blanksby, S. J.; Ellison, G. B. *Accounts Chem. Res.* **2003**, *36*, 255.
- (184) Shustorovich, E.; Sellers, H. *Surf. Sci. Rep.* **1998**, *31*, 5.
- (185) Shustorovich, E. *Metal-surface reaction energetics: theory and applications to heterogeneous catalysis, chemisorption, and surface diffusion*; VCH: New York, NY, 1991.
- (186) Wiberg, K. B.; Hao, S. *J. Org. Chem.* **1991**, *56*, 5108.
- (187) Lide, D. R. *CRC Handbook of Chemistry and Physics: A Ready-reference Book of Chemical and Physical Data*; CRC Press: Boca Raton Fl., 2004.
- (188) MacNaughton, J. B.; Naslund, L. A.; Anniyev, T.; Ogasawara, H.; Nilsson, A. *Phys. Chem. Chem. Phys.* **2010**, *12*, 5712.
- (189) Keith, J. M.; Muller, R. P.; Kemp, R. A.; Goldberg, K. I.; Goddard, W. A.; Oxgaard, J. *Inorg Chem* **2006**, *45*, 9631.
- (190) Karp, E. M.; Silbaugh, T. L.; Campbell, C. T. *J. Phys. Chem. C* **2013**, *117*, 6325.
- (191) Karp, E. M.; Silbaugh, T. L.; Campbell, C. T. *J. Am. Chem. Soc.* **2013**, *135*, 5208.
- (192) Campbell, C. T.; Sharp, J. C.; Yao, Y.; Karp, E. M.; Silbaugh, T. L. *Faraday Discuss.* **2011**, *152*, 227.
- (193) Abild-Pedersen, F.; Greeley, J.; Studt, F.; Rossmeisl, J.; Munter, T. R.; Moses, P. G.; Skulason, E.; Bligaard, T.; Nørskov, J. K. *Phys. Rev. Lett.* **2007**, *99*.
- (194) Karp, E. M.; Silbaugh, T. L.; Campbell, C. T. *Journal of the American Chemical Society* **2014**, *136*, 4137.
- (195) Carter, E. A.; Koel, B. E. *Surface Science* **1990**, *226*, 339.
- (196) Carter, E. A. *Chemical Physics Letters* **1990**, *169*, 218.
- (197) Gross, H.; Campbell, C. T.; King, D. A. *Surface Science* **2004**, *572*, 179.
- (198) Weaver, J. H. *Physical Review B* **1975**, *11*, 1416.
- (199) Stuckless, J. T.; Alsarraf, N.; Wartnaby, C.; King, D. A. *Journal of Chemical Physics* **1993**, *99*, 2202.

- (200) Wartnaby, C. E.; Stuck, A.; Yeo, Y. Y.; King, D. A. *Journal of Chemical Physics* **1995**, *102*, 1855.
- (201) Yeo, Y. Y.; Vattuone, L.; King, D. A. *Journal of Chemical Physics* **1996**, *104*, 3810.
- (202) Yeo, Y. Y.; Vattuone, L.; King, D. A. *Journal of Chemical Physics* **1997**, *106*, 1990.
- (203) Vattuone, L.; Yeo, Y. Y.; King, D. A. *Journal of Chemical Physics* **1996**, *104*, 8096.
- (204) Parker, D. H.; Bartram, M. E.; Koel, B. E. *Surface Science* **1989**, *217*, 489.
- (205) Smith, R. S.; Huang, C.; Wong, E. K. L.; Kay, B. D. *Surface Science* **1996**, *367*, L13.
- (206) Smith, R. S.; Daschbach, J. L.; Zubkov, T.; Kay, B. D. *Abstracts of Papers of the American Chemical Society* **2006**, 232.
- (207) Lofgren, P.; Ahlstrom, P.; Chakarov, D. V.; Lausmaa, J.; Kasemo, B. *Surface Science* **1996**, *367*, L19.
- (208) Speedy, R. J.; Debenedetti, P. G.; Smith, R. S.; Huang, C.; Kay, B. D. *Journal of Chemical Physics* **1996**, *105*, 240.
- (209) Lawton, T. J.; Carrasco, J.; Baber, A. E.; Michaelides, A.; Sykes, E. C. H. *Physical Chemistry Chemical Physics* **2012**, *14*, 11846.
- (210) Baber, A. E.; Lawton, T. J.; Sykes, E. C. H. *Journal of Physical Chemistry C* **2011**, *115*, 9157.
- (211) Lawton, T. J.; Carrasco, J.; Baber, A. E.; Michaelides, A.; Sykes, E. C. H. *Physical Review Letters* **2011**, *107*.
- (212) Carlson, H. G.; Westrum, E. F. *Journal of Chemical Physics* **1971**, *54*, 1464.
- (213) Tauer, K. J.; Lipscomb, W. N. *Acta Crystallographica* **1952**, *5*, 606.
- (214) Green, S. D.; Bolina, A. S.; Chen, R.; Collings, M. P.; Brown, W. A.; McCoustra, M. R. S. *Monthly Notices of the Royal Astronomical Society* **2009**, *398*, 357.
- (215) Persson, B. N. J. *Surface Science* **1991**, *258*, 451.
- (216) Lehwald, S.; Ibach, H.; Demuth, J. E. *Surface Science* **1978**, *78*, 577.
- (217) Netzer, F. P.; Matthew, J. A. D. *Solid State Communications* **1979**, *29*, 209.
- (218) Rodriguez, J. A.; Campbell, C. T. *Journal of Catalysis* **1989**, *115*, 500.
- (219) Rodriguez, J. A.; Campbell, C. T. *Journal of Physical Chemistry* **1989**, *93*, 826.
- (220) Henn, F. C.; Diaz, A. L.; Bussell, M. E.; Hugenschmidt, M. B.; Domagala, M. E.; Campbell, C. T. *Journal of Physical Chemistry* **1992**, *96*, 5965.
- (221) Bussell, M. E.; Henn, F. C.; Campbell, C. T. *Abstracts of Papers of the American Chemical Society* **1992**, *203*, 276.
- (222) Land, D. P.; Pettiettehall, C. L.; McIver, R. T.; Hemminger, J. C. *Journal of the American Chemical Society* **1989**, *111*, 5970.
- (223) Pettiettehall, C. L.; Land, D. P.; McIver, R. T.; Hemminger, J. C. *Journal of the American Chemical Society* **1991**, *113*, 2755.
- (224) Land, D. P.; Erley, W.; Ibach, H. *Surface Science* **1993**, *289*, 237.
- (225) Henderson, M. A.; Mitchell, G. E.; White, J. M. *Surface Science* **1987**, *184*, L325.
- (226) Henderson, M. A.; Mitchell, G. E.; White, J. M. *Surface Science* **1991**, *248*, 279.
- (227) Brown, W. A.; Kose, R.; King, D. A. *Journal of Molecular Catalysis a-Chemical* **1999**, *141*, 21.

- (228) Kose, R.; Brown, W. A.; King, D. A. *Chemical Physics Letters* **1999**, *311*, 109.
- (229) Clay, C.; Haq, S.; Hodgson, A. *Physical Review Letters* **2004**, *92*, 4.
- (230) Held, G.; Clay, C.; Barrett, S. D.; Haq, S.; Hodgson, A. *Journal of Chemical Physics* **2005**, *123*.
- (231) Bedurftig, K.; Volkening, S.; Wang, Y.; Wintterlin, J.; Jacobi, K.; Ertl, G. *Journal of Chemical Physics* **1999**, *111*, 11147.
- (232) Marks, T. J.; Gagne, M. R.; Nolan, S. P.; Schock, L. E.; Seyam, A. M.; Stern, D. *Pure and Applied Chemistry* **1989**, *61*, 1665.
- (233) Schulze, M.; Reissner, R.; Bolwin, K.; Kuch, W. *Fresenius Journal of Analytical Chemistry* **1995**, *353*, 661.
- (234) Schennach, R.; Bechtold, E. *Surface Science* **1997**, *380*, 9.
- (235) Tait, S. L.; Dohnalek, Z.; Campbell, C. T.; Kay, B. D. *Journal of Chemical Physics* **2006**, *125*.
- (236) Lei, R. Z.; Gellman, A. J.; Koel, B. E. *Surface Science* **2004**, *554*, 125.
- (237) Xi, M.; Yang, M. X.; Jo, S. K.; Bent, B. E.; Stevens, P. *Journal of Chemical Physics* **1994**, *101*, 9122.
- (238) Zhou, X. L.; Castro, M. E.; White, J. M. *Surface Science* **1990**, *238*, 215.
- (239) Hertel, T.; Wolf, M.; Ertl, G. *Journal of Chemical Physics* **1995**, *102*, 3414.
- (240) Wu, K. J.; Kevan, S. D. *Journal of Chemical Physics* **1991**, *94*, 7494.
- (241) Grunze, M.; Bozso, F.; Ertl, G.; Weiss, M. *Applied Surface Science* **1978**, *1*, 241.
- (242) Weiss, M.; Ertl, G.; Nitschke, F. *Applied Surface Science* **1979**, *2*, 614.
- (243) Seabury, C. W.; Rhodin, T. N.; Purtell, R. J.; Merrill, R. P. *Surface Science* **1980**, *93*, 117.
- (244) Redondo, A.; Zeiri, Y.; Low, J. J.; Goddard, W. A. *Journal of Chemical Physics* **1983**, *79*, 6410.
- (245) Klauber, C.; Alvey, M. D.; Yates, J. T. *Surface Science* **1985**, *154*, 139.
- (246) Anger, G.; Winkler, A.; Rendulic, K. D. *Surface Science* **1989**, *220*, 1.
- (247) Campbell, J. M.; Campbell, C. T. *Surface Science* **1991**, *259*, 1.
- (248) Sandl, P.; Bischler, U.; Bertel, E. *Surface Science* **1993**, *291*, 29.
- (249) Osterlund, L.; Rasmussen, P. B.; Thostrup, P.; Laegsgaard, E.; Stensgaard, I.; Besenbacher, F. *Physical Review Letters* **2001**, *86*, 460.
- (250) Rasmussen, P. B.; Holmblad, P. M.; Christoffersen, H.; Taylor, P. A.; Chorkendorff, I. *Surface Science* **1993**, *287*, 79.
- (251) Foss, M.; Besenbacher, F.; Klink, C.; Stensgaard, I. *Chemical Physics Letters* **1993**, *215*, 535.
- (252) Chorkendorff, I.; Rasmussen, P. B. *Surface Science* **1991**, *248*, 35.
- (253) Bozso, F.; Ertl, G.; Grunze, M.; Weiss, M. *Applications of Surface Science* **1977**, *1*, 103.
- (254) Burke, M. L.; Madix, R. J. *Surface Science* **1990**, *237*, 20.
- (255) Merrill, P. B.; Madix, R. J. *Surface Science* **1996**, *347*, 249.
- (256) Christma.K; Schober, O.; Ertl, G.; Neumann, M. *Journal of Chemical Physics* **1974**, *60*, 4528.
- (257) Eg; G Services, N. E. T. L.; U.S. Dept. of Energy, Office of Fossil Energy, National Energy Technology Laboratory: Morgantown, WV, 2004.

- (258) Vielstich, W. L. A. G. H. A. Y. H. *Handbook of fuel cells : fundamentals, technology, and applications*; Wiley: Chichester, England; Hoboken, N.J., 2003.
- (259) Jarvi, T. D.; Stuve, E. M. In *Electrocatalysis*; Lipkowski, J., Ross, P. N., Eds.; Wiley-VCH: 1998.
- (260) Bryndza, H. E.; Fong, L. K.; Paciello, R. A.; Tam, W.; Bercaw, J. E. *Journal of the American Chemical Society* **1987**, *109*, 1444.
- (261) Barrio, L.; Liu, P.; Rodriguez, J. A.; Campos-Martin, J. M.; Fierro, J. L. G. *Journal of Physical Chemistry C* **2007**, *111*, 19001.
- (262) Liu, W.; Carrasco, J.; Santra, B.; Michaelides, A.; Scheffler, M.; Tkatchenko, A. *Physical Review B* **2012**, *86*.
- (263) Yang, M. L.; Zhu, Y. A.; Fan, C.; Sui, Z. J.; Chen, D.; Zhou, X. G. *Journal of Molecular Catalysis a-Chemical* **2010**, *321*, 42.
- (264) Vines, F.; Lykhach, Y.; Staudt, T.; Lorenz, M. P. A.; Papp, C.; Steinruck, H. P.; Libuda, J.; Neyman, K. M.; Gorling, A. *Chemistry-a European Journal* **2010**, *16*, 6530.
- (265) Zhang, R. G.; Song, L. Z.; Wang, Y. H. *Applied Surface Science* **2012**, *258*, 7154.
- (266) Nykanen, L.; Honkala, K. *Journal of Physical Chemistry C* **2011**, *115*, 9578.
- (267) Yang, M. L.; Zhu, Y. A.; Zhou, X. G.; Sui, Z. J.; Chen, D. *Acs Catalysis* **2012**, *2*, 1247.
- (268) Goda, A. M.; Neurock, M.; Barteau, M. A.; Chen, J. G. *Surface Science* **2008**, *602*, 2513.
- (269) Morin, C.; Simon, D.; Sautet, P. *Journal of Physical Chemistry B* **2004**, *108*, 12084.
- (270) Saeys, M.; Reyniers, M. F.; Marin, G. B.; Neurock, M. *Journal of Physical Chemistry B* **2002**, *106*, 7489.
- (271) Blonski, P.; Lopez, N. *Journal of Physical Chemistry C* **2012**, *116*, 15484.
- (272) Cahyanto, W. T.; Padama, A. A. B.; Escano, M. C. S.; Kasai, H. *Physica Scripta* **2012**, *85*, 6.
- (273) Skoplyak, O.; Menning, C. A.; Barteau, M. A.; Chen, J. G. G. *Topics in Catalysis* **2008**, *51*, 49.
- (274) Desai, S. K.; Neurock, M.; Kourtakis, K. *Journal of Physical Chemistry B* **2002**, *106*, 2559.
- (275) Michaelides, A.; Hu, P. *Journal of the American Chemical Society* **2001**, *123*, 4235.
- (276) Gajdos, M.; Eichler, A.; Hafner, J. *Journal of Physics-Condensed Matter* **2004**, *16*, 1141.
- (277) O'Brien, C. P.; Miller, J. B.; Morreale, B. D.; Gellman, A. J. *Journal of Physical Chemistry C* **2012**, *116*, 17657.
- (278) Fleutot, B.; Miller, J. B.; Gellman, A. J. *Journal of Vacuum Science & Technology A* **2012**, *30*, 10.
- (279) Brouard, M.; Halford, E.; Lauer, A.; Slater, C. S.; Winter, B.; Yuen, W. H.; John, J. J.; Hill, L.; Nomerotski, A.; Clark, A.; Crooks, J.; Sedgwick, I.; Turchetta, R.; Lee, J. W. L.; Vallance, C.; Wilman, E. *Review of Scientific Instruments* **2012**, *83*, 9.

Appendix A

In this section, two methods for analyzing the detector pulseshape are discussed. If we consider the slope method that is used to analyze experiments with instantaneously deposited heat, both molecular and laser pulses have the same shape, as shown by comparison of the intensity-normalized lineshapes in Figure A.1, and by extension the same rise-time. Here rise-time is defined as the amount of time, in ms, to go from 10% to 90% of the maximum signal intensity ($t_{0.9V_{\max}} - t_{0.1V_{\max}}$).

Figure A.2 shows how the laser calibration lineshape changes upon convolution with an exponential decay ($\tau = 350$ ms). The rise-time has increased and the peak height and slope have decreased as a consequence of the pulse broadening. Figure A.3 plots the rise-time and slope of the convoluted laser pulse as a function of τ over the range of 20-400 ms. Increasing τ (i.e. slower heat deposition) leads to an increase in the rise-time and decrease in the slope consistently over this range. Because each pulse shape will have a unique rise-time, this parameter is used as the matching criteria rather than the entire pulse shape.

By creating this database of rise-time and slope of the convoluted laser pulse as a function of τ (Figure A.3), we can easily analyze broadened molecular pulses in the following manner: (1) determine the rise-time of each molecular pulse, (2) use the rise-time to find the corresponding slope and τ for the matching convoluted laser pulse, (3) use the slope of S_{conv} in place of the slope of S_{laser} to calculate the total heat.

This rise-time slopes (slopes_{RT}) method allows for the quick calculation of the total heat deposited and the time constant for the heat deposition process during each pulse if all of the heat deposition is dictated by a pseudo first order reaction. The standard deviation of the rise-time for

a typical set of laser pulses is 2 ms. Averaging the response of 4 molecular pulses therefore results in a detection limit for the reaction time constant of ~ 10 ms.

We will now discuss the more general example of the two-step heat deposition process where q_1 and q_2 are of similar magnitudes. The rise-time will now be dependent on τ and the ratio of the heats in each step. The consequence of this multivariable dependence is that the $\text{slopes}_{\text{RT}}$ method discussed above only represents the true pulse shape if one of these two pieces of information is known. Knowledge of the step 1 heat can be obtained by performing experiments at a lower temperature where it is known that the reaction represented by step 2 occurs on a timescale >1000 ms. It can then be assumed that the heat from this low temperature experiment completely accounts for the step 1 heat in the higher temperature experiment. For example, one could use the heats obtained from SCAC studies performed at conditions (e.g. cryogenic temperatures) where it is already known that molecular adsorption is the dominant surface process and then assume that all heat deposition in step 1 at the elevated temperature is due to molecular adsorption. If we reconsider Equations 10 and 12 from Chapter ZZZZ and assume that we know the amount of heat deposited in the first step (i.e. $x_{S1} = x_{S1}'$), its signal contribution can be removed by subtracting an intensity-normalized laser calibration pulse scaled with x_{S1} :

$$S_{\text{mol},S2} = S_{\text{mol}} - (x_{S1}/x_{\text{laser}})S_{\text{laser}} = x_{S2}'(C * R) \quad (1)$$

$$S_{\text{sim},S2} = S_{\text{sim}} - (x_{S1}/x_{\text{laser}})S_{\text{laser}} = x_{S2}(C * D) * R. \quad (2)$$

This yields pulses whose lineshapes are dependent only on τ , and thus can be analyzed using the $\text{slopes}_{\text{RT}}$ method discussed above.

We will now discuss how well the $\text{slopes}_{\text{RT}}$ method works if the step 1 heat used is incorrect (i.e. $x_{S1} \neq x_{S1}'$). An example of this situation would be if x_{S1}' was assumed to be due

entirely to molecular adsorption, but in actuality the rate limiting step did not immediately follow this process. In this example, using a heat for step 1 (x_{S1}) based on lower temperature experiments would underestimate the actual value (x_{S1}'). Equation 1 would thus not be simplified as shown previously by subtracting off the step 1 heat using x_{S1} as a scaling factor. The resulting equation,

$$S_{mol,S2} = S_{mol} - x_{S1}/x_{laser} S_{laser} = (x_{S1}' - x_{S1})(C*R) + x_{S2}' (C'*R), \quad (3)$$

would still contain some portion of the instantaneous heat signal and consequently introduce error into the $slopes_{RT}$ method.

Our methodology for this portion of the study is as follows: First a pulse representing a two step heat deposition process with one slow step is created with a value of τ (τ_{actual}) and heat values x_{S1}' and x_{S2}' for the two steps. The step 1 heat contribution is then removed by subtracting a laser pulse that has been scaled with an incorrect value of x_{S1} ($x_{S1} \neq x_{S1}'$), resulting in a pulse represented by Equation 3. The $slopes_{RT}$ method is then applied to obtain calculated values for the step 2 heat (x_{S2}) and time constant (τ_{calc}).

First we will discuss how the magnitude of the discrepancy between x_{S1} and x_{S1}' affects the accuracy of the calculated time constant (τ_{calc}) when using the $slopes_{RT}$ method. Figure A.4 shows how the ratio of the calculated and actual time constants ($\tau_{calc}/\tau_{actual}$) changes as a function of τ_{actual} and x_{S1}/x_{S1}' while holding $x_{S1}' = x_{S2}'$ (i.e. the amount of heat deposited during each step is the same). Starting in the bottom right corner of Figure A.4 where the amount of heat in step 1 is correct ($x_{S1} = x_{S1}'$), we see not surprisingly that $\tau_{calc} = \tau_{actual}$. However, moving toward the top left corner where x_{S1}/x_{S1}' is decreasing (i.e. the guess of the step 1 heat becomes less accurate) and τ_{actual} is increasing (i.e. the chemical process becomes slower), the accuracy of τ_{calc} begins to decrease dramatically. However, Figure A.5 shows that if the rate limiting step has a τ below

~50 ms or the value of x_{S1}' is known to within 7%, the value of τ_{calc} obtained with this method is within 10% of the true value for cases where the heat in steps 1 and 2 are equal.

Figure A.5 shows how $\tau_{\text{calc}}/\tau_{\text{actual}}$ varies as a function of τ_{actual} and the ratio of the heat in steps 1 and 2 (x_{S2}'/x_{S1}'). In this case a constant 20% underestimate of x_{S1}' is used ($x_{S1} = 0.8 x_{S1}'$). As a larger proportion of the total heat is deposited slowly (i.e. x_{S2}'/x_{S1}' increases), the underestimate of x_{S1}' begins to have a lesser effect on the accuracy of τ_{calc} . This makes sense because the residual signal due to our incorrect guess of x_{S1}' becomes proportionally smaller as the amount of heat in step 1 becomes a smaller proportion of the total heat. It is apparent from Figure A.5 that the accuracy of the τ calculation is very sensitive to the ratio of the step 2 to step 1 heats, particularly for values of $x_{S2}'/x_{S1}' < 0.5$. Using the slopes_{RT} method in this regime can result in extremely large discrepancies in calculated time constants if x_{S1}' is not known accurately.

We will now discuss how the underestimate of x_{S1}' affects the accuracy of the total heat calculated using this method. Figure A.6 shows a contour plot of the percent error for the calculated total heat, defined here as

$$\text{PE} = ((x_{S1}+x_{S2})-(x_{S1}'+x_{S2}'))/(x_{S1}'+x_{S2}'), \quad (4)$$

versus τ_{actual} and the ratio of the guessed and true values of the step 1 heat (x_{S1}/x_{S1}'). Again we hold the ratio of the heats in the two steps constant at $x_{S2}'/x_{S1}'=1$. From this plot we see that the error in the total heat calculation follows the same general trend as seen for the time constant calculation (Figure A.5), with PE increasing with increasing τ_{actual} and decreasing x_{S1}/x_{S1}' . Note that for an underestimate of the initial heat step, the calculated total heat is always underestimated.

Figure A.7 shows PE versus τ_{actual} and the ratio of the heat in the two steps (x_{S2}'/x_{S1}') with x_{S1} again underestimated by 20% ($x_{S1} = 0.8 x_{S1}'$). We can see that if τ is lower than ~ 100 ms, the total heat calculation will be within 4%, or better, of the true value. As the proportion of heat in the slow step becomes small ($x_{S2}'/x_{S1}' < 0.25$), we see that the error in the total heat becomes much less sensitive to the kinetics of the rate limiting step. This makes sense because although we may be underestimating the step 2 heat by a large percentage, this step now makes up a very small fraction of the total heat.

These results are intuitive based on our earlier discussion. We know that the instantaneous heat signal results in a shorter rise-time and a larger slope than a heat signal arising from slower heat deposition (Figure A.3). This means that the pulse which still contains a fast heat deposition component will always have a shorter rise-time than if a correct value of fast heat deposition was known. This rise-time will match with a smaller time constant in the database, resulting in a calculated time constant that is always smaller than the true value. Likewise, this smaller calculated time constant will result in the use of a larger slope from the database for the step 2 heat calculation, yielding a calculated total heat ($x_{S1} + x_{S2}$) that always underestimates the true heat deposition.

After the slope_{RT} method has been applied to a data set, it is important to check the quality of the calculation. As we have shown, large errors in the calculated τ and total heat values can arise if discrepancies exist between the guessed and actual step 1 heat. The simplest check of accuracy is to use the calculated values for the heat steps and time constant to create a simulated pulse. The shape of this pulse can then be compared to the molecular pulse to determine the quality of fit. A noticeable difference in shape indicates that the τ and total heat

calculated using the $\text{slopes}_{\text{RT}}$ method are inaccurate. In this case, the best-fit method described below provides more accurate numbers.

It was also noticed that as the guess for the fast heat deposition step became too large, the peak resulting from subtracting this fast heat pulse had a noticeable negative dip initially. This negative dip leads to a decrease in the apparent slope and thus a lower heat in the $\text{slopes}_{\text{RT}}$ method. It may therefore be possible, if the noise level of the measured pulses is sufficiently low, to run an algorithm where the fast heat is increased stepwise and the $\text{slopes}_{\text{RT}}$ method is applied following each step to determine the total heat. The fast heat estimate that yields the maximum calculated total heat would correspond to the correct heat value for that pulse. Although this method has not yet been applied, it may provide a very fast method for fitting SCAC detector data.

Let us now consider the case where the calculated values from the $\text{slopes}_{\text{RT}}$ method produced poor fits to the molecular pulse shape or, more generally, where a good estimate of x_{S1}' is not available. The creation of an intensity-normalized simulated pulse with the correct shape requires correct values of τ and x_{S2}/x_{S1} (i.e. $x_{S2}/x_{S1} = x_{S2}'/x_{S1}'$). Rather than trying to remove the fast heat deposition step by assuming a step 1 heat, the best-fit method adjusts both the time constant and heat ratios until the residual between the intensity-normalized simulated and molecular pulses is minimized.

Implementation of this method uses the following methodology: (1) initially create a simulated pulse using arbitrary values for τ and x_{S2}/x_{S1} , (2) calculate the residual between the intensity-normalized simulated and molecular pulses, (3) adjust x_{S2}/x_{S1} while holding τ constant, (4) calculate residual, (5) repeat steps 3 and 4 over a wide range of values, (6) adjust τ , (7) repeat steps 3-5. Better estimates of the initial and possible range of values of τ and x_{S2}/x_{S1} can be

made as more iterations are performed, greatly speeding up this process. If we create a “molecular pulse” as we did for the simulations outlined in the previous section, it is clear that the accuracy of the best-fit method is dictated by the size of x_{S2}/x_{S1} and τ steps used, with perfect convergence possible when infinitely small steps are used. As real experimental data, such as that from methyl iodide adsorption on Pt(111) discussed in the following paragraphs, will contain noise, choosing a time constant step size on the order of the detection limit determined for the slopes_{RT} method (10 ms here) is reasonable.

To illustrate the utility of this method, we will now show the results of a best-fit analysis of data from a recent study of methyl iodide adsorption at 270 K on Pt(111). These results are compared to an analysis of the same data using the standard slopes and the new slopes_{RT} method. Details of the experimental methodology can be found elsewhere.^{10,32,102,107} Briefly, methyl iodide pulses of 102 ms duration contained 0.0046 ML and were repeated every 5 seconds. Here ML is defined as the surface density of Pt atoms in the (111) plane ($1.5 \times 10^{19}/\text{m}^2$). The sticking probability of methyl iodide is unity up to 0.11 ML coverage at this temperature. We can therefore convert the x_{S1} and x_{S2} from J/pulse to kJ/mol using the measured flux and sticking probabilities. To improve the signal to noise ratio, the detector signals from four pulses were summed together, so that each summed methyl iodide pulse effectively contains 0.0184 ML.

A representative heat signal from such a (summed) molecular pulse for this experiment is shown in Fig.A. 9, in the coverage range 0.037-0.055 ML at 270 K, along with the average heat signal from the laser calibration pulses. Broadening of the molecular pulse with respect to the laser pulse is clearly seen.

The application of the best-fit method was applied in the following manner. The initial guess for x_{S2}/x_{S1} was 0. The τ values were initially adjusted in 100 ms increments. This was then

followed by further refinement to 10 and 25 ms intervals at τ values below and above ~ 300 ms respectively. These intervals are consistent with the detection limit of the $\text{slopes}_{\text{RT}}$ method of ~ 10 ms at low τ and ~ 25 ms at high τ . For all pulses, calculated heat values for the two steps were rounded to the nearest kJ/mol.

Figure A.9 shows a comparison of the signal lineshape for this molecular pulse with a simulated pulse. The signal contributions from the two steps that make up the simulated pulse are also included. It is clear that the simulated pulse reproduces the experimental pulse extremely well, meaning that the differential heat deposited in each of the two steps ($x_{\text{S1}}' = 136$ kJ/mol and $x_{\text{S2}}' = 76$ kJ/mol) and the τ of the slow reaction step (240 ms) used in this simulation are accurate.

The heat of adsorption of methyl iodide (in kJ/mol) is shown in Figure A.10 as a function of the methyl iodide surface coverage. Each set of data points represent a different analysis method. The lowest calculated heats (red squares) were obtained using the standard slope comparison method generally applied to non-broadened pulses ($\text{slopes}_{\text{Laser}}$). The best-fit method (blue circles) provides the highest calculated total heats. The $\text{slopes}_{\text{RT}}$ method (black triangles) performed with an x_{S1} value of 88 kJ/mol (average molecular adsorption energy measured at 95 K²⁰) underestimates the total heat as compared to the best-fit method, but still provides more accurate values than the standard $\text{slopes}_{\text{Laser}}$ method. If we take the calculated total heats of the third pulse (Fig. from the $\text{slopes}_{\text{RT}}$ and best-fit methods (185 and 212 kJ/mol respectively), we see that the $\text{slopes}_{\text{RT}}$ method gives an underestimate of 13% in comparison to the best-fit method. The τ_{calc} values from the $\text{slopes}_{\text{RT}}$ and best-fit methods (78 and 240 ms respectively) provide a ratio of 0.35.

Let us consider the time constant and heat values obtained for the third pulse using the best-fit method (i.e. $\tau = 240$ ms, $x_{S1} = 136$ kJ/mol, and $x_{S2} = 76$ kJ/mol) as the true values. If we create a simulated pulse using these parameters and then apply the rise time method with our initial guess of x_{S1} as the average molecular adsorption energy of 88 kJ/mol measured at 95 K ($x_{S1}/x_{S1}' = 0.68$), we can perform similar calculations to those used to make Figure A.7 (where $x_{S1}/x_{S1}' = 0.8$). This results in a predicted error of -16% in the total heat. Using calculations similar to those used to make Figure A.5, we can also predict an underestimate of τ_{calc} of 77% (i.e. $\tau_{\text{calc}}/\tau_{\text{actual}} = 0.23$). The actual errors (-13% for the total heat PE and 0.35 for the time constant ratio) would not be expected to be in such good agreement with the predicted errors unless the best-fit analysis is providing heat and time constant values that are in very close agreement to the true values. The comparison of the two analysis methods can therefore be used as a check of the accuracy of the values obtained with the best-fit method. In a separate publication, the heats obtained from the best-fit analysis were in good agreement with data collected at 320 K where the reactions are fast and no peak broadening occurs, which further verifies the accuracy of this analysis.

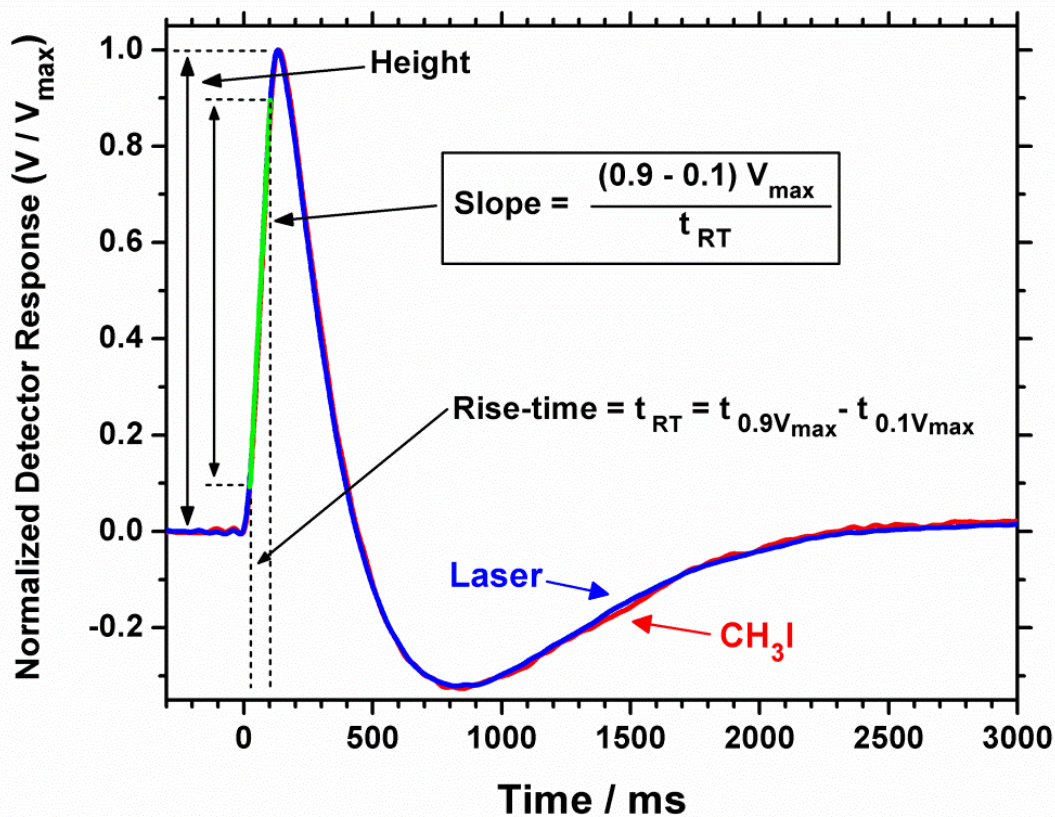


Figure A.1: Heat detector response for a pulse of methyl iodide adsorbing on Pt(111) at 100 K (red) and for a laser pulse used to calibrate the signal (blue). Each pulse was 102 ms long (FWHM) and repeated every 5 s (only the first 3 s are shown), and multiple pulses were averaged to improve signal to noise ratio. Also shown are demonstrations of measurements of the heat signal magnitude using either the peak height (from the initial baseline to the peak maximum, as shown) or the slope of the initial fast rise. The slope is obtained from a linear fit to the data between 10% and 90% of the peak maximum, as shown in green. The rise-time is defined as the time for the signal to rise through this 10% to 90% range, as shown.

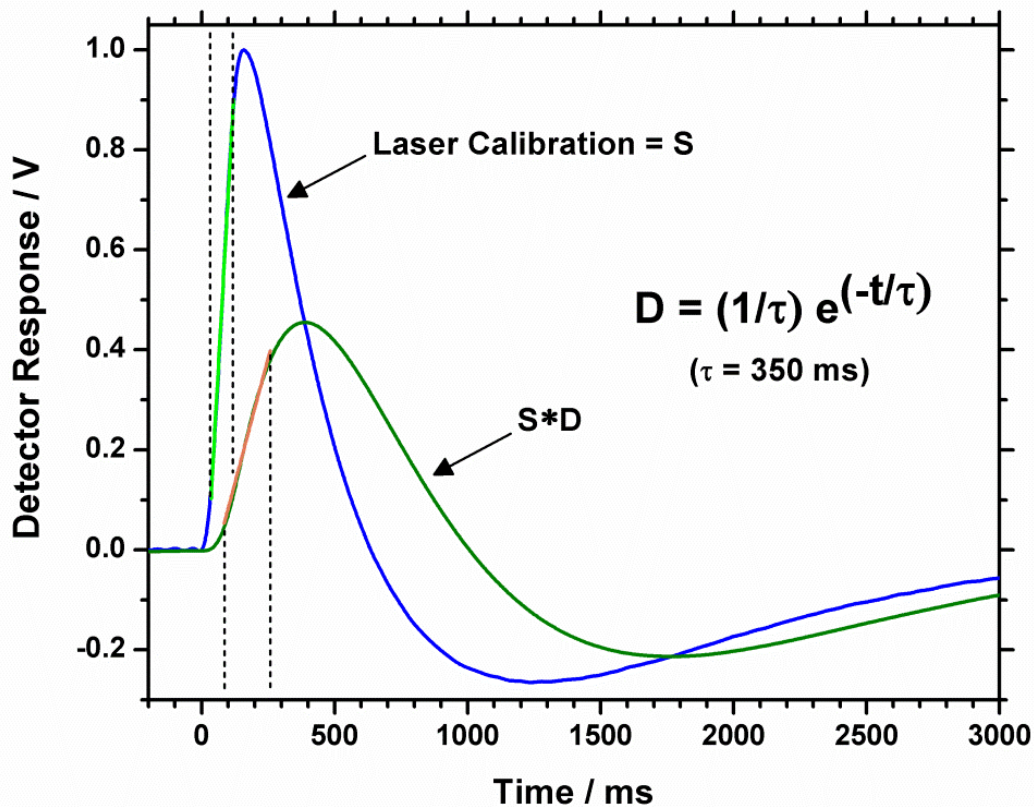


Figure A.2: Detector responses to single pulses of the laser used for calibration (blue) and of the laser convoluted with a first-order decay with a time constant of 350 ms (green). This latter corresponds to a 2-step kinetic model where the first step (physisorption) is instantaneous but has negligible heat, and the heat is all deposited in the second, slow step whose rate constant is $(350 \text{ ms})^{-1}$.

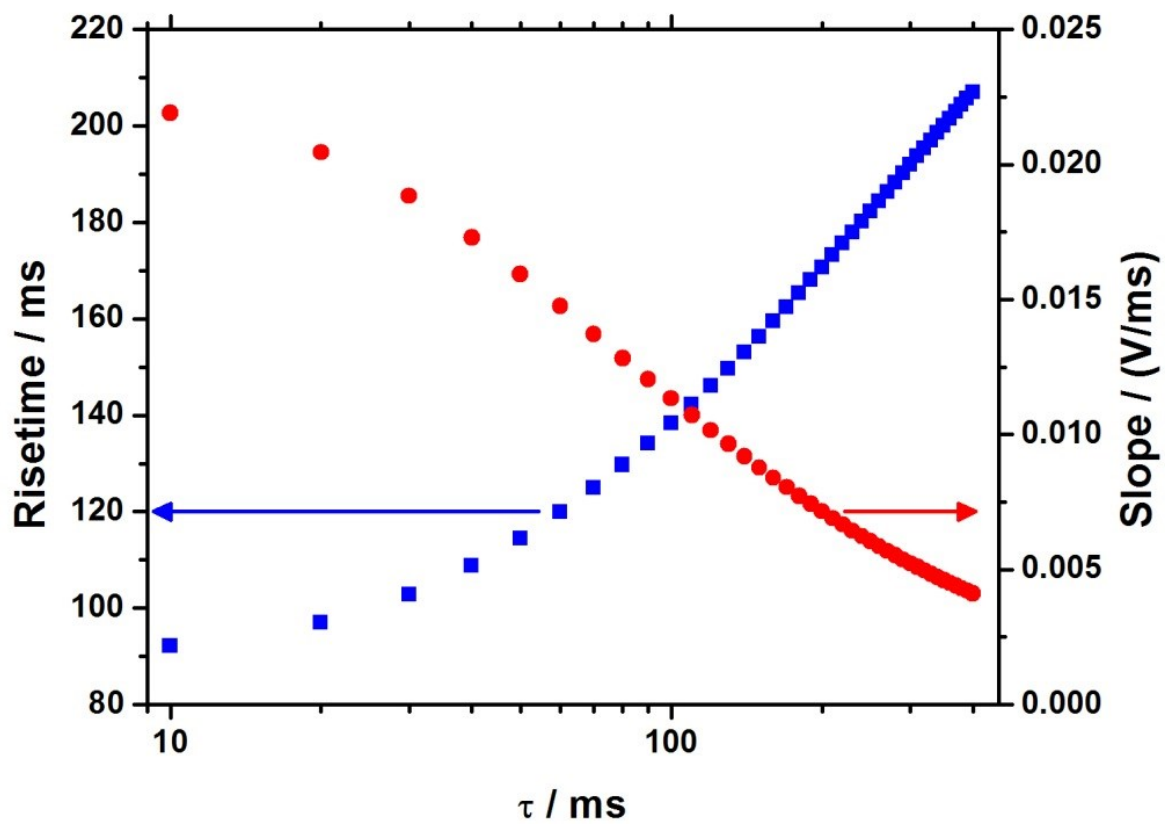


Figure A.3: Risetime and slope of the convoluted laser calibration signal as a function of the exponential decay time constant, τ , for a 2-step kinetic model where the first step (physisorption) is instantaneous but has negligible heat, and the heat is all deposited in the second, slow step whose rate constant is τ^{-1} .

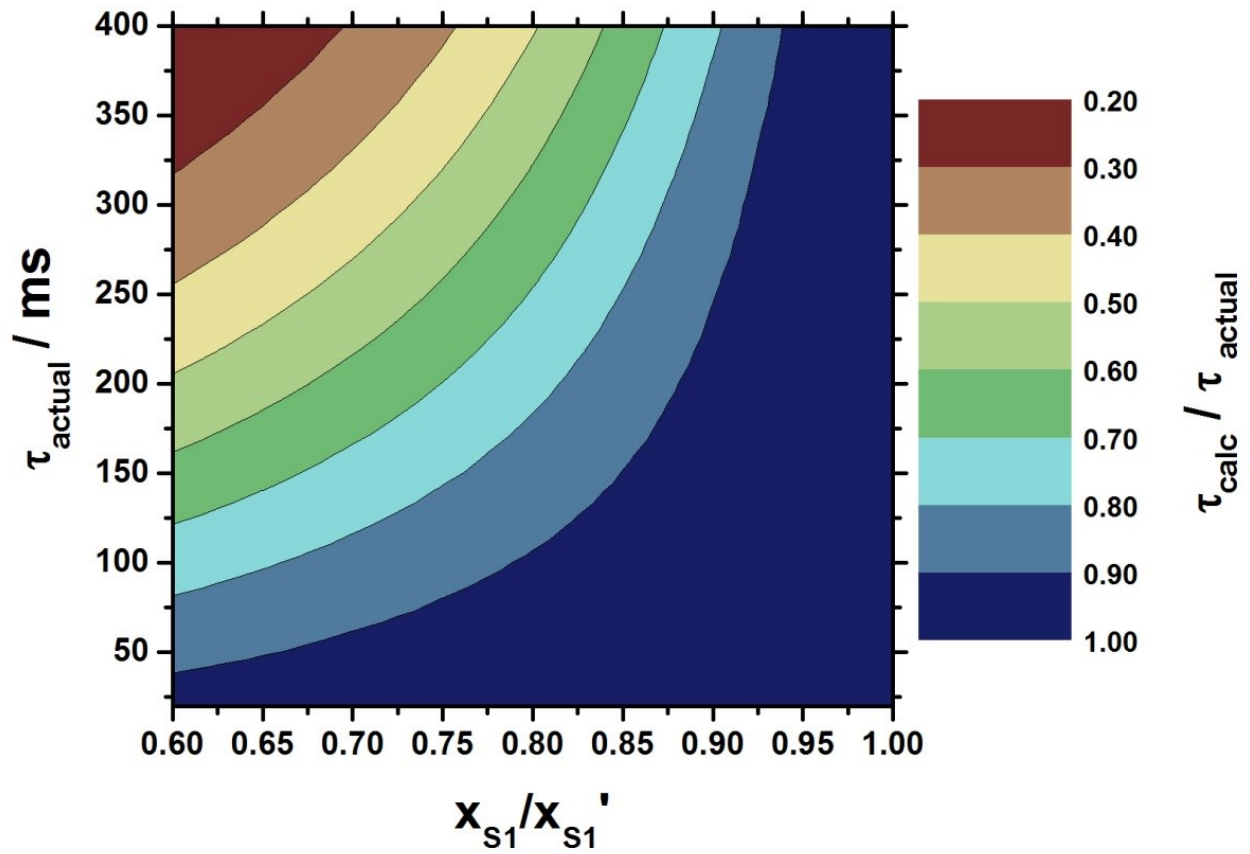


Figure A.4: Ratio of the time constant calculated using the slopes_{RT} method (τ_{calc}) and the actual time constant (τ_{actual}) (color bar) as a function of τ_{actual} and the accuracy of the guess of the step 1 heat (x_{S1}/x_{S1}').

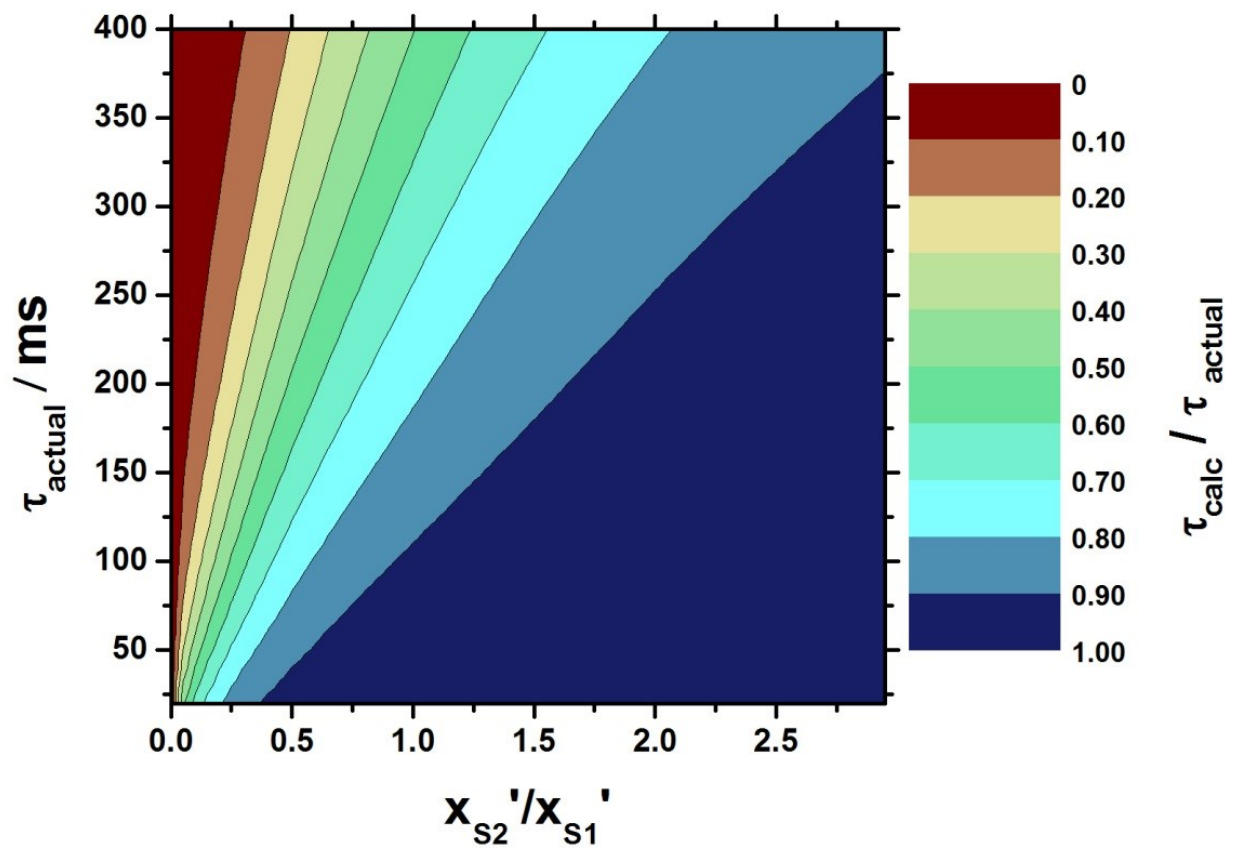
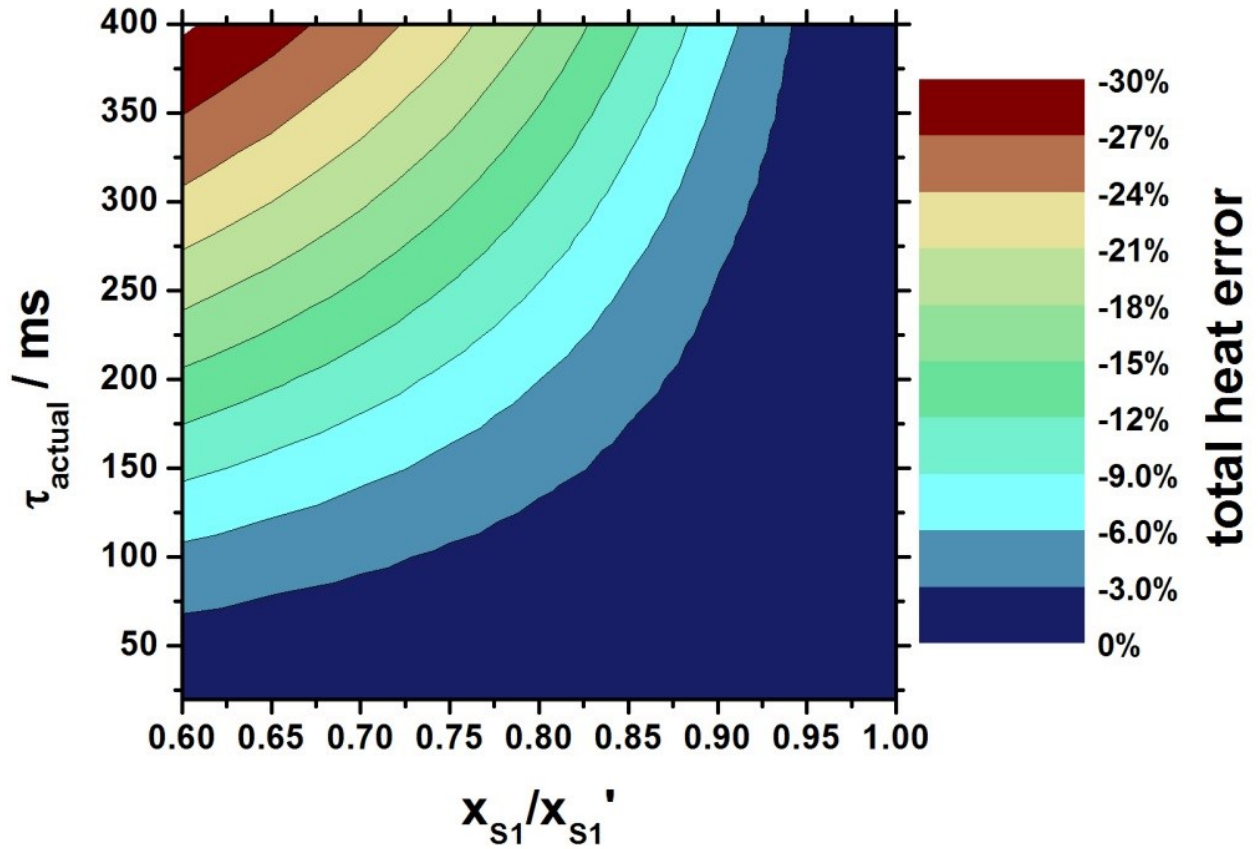


Figure A.5: Ratio of the time constant calculated using the slopes_{RT} method (τ_{calc}) and the actual time constant (τ_{actual}) (color bar) as a function of τ_{actual} and the ratio of step 2 to step 1 heat (x_{S2}'/x_{S1}').



FigureA.6: Percent error of the total heat (color bar) as a function of τ_{actual} and the accuracy of the guess of the step 1 heat (x_{s1}/x_{s1}'). Negative errors indicate an underestimate of the total heat when using the slopes_{RT} method.

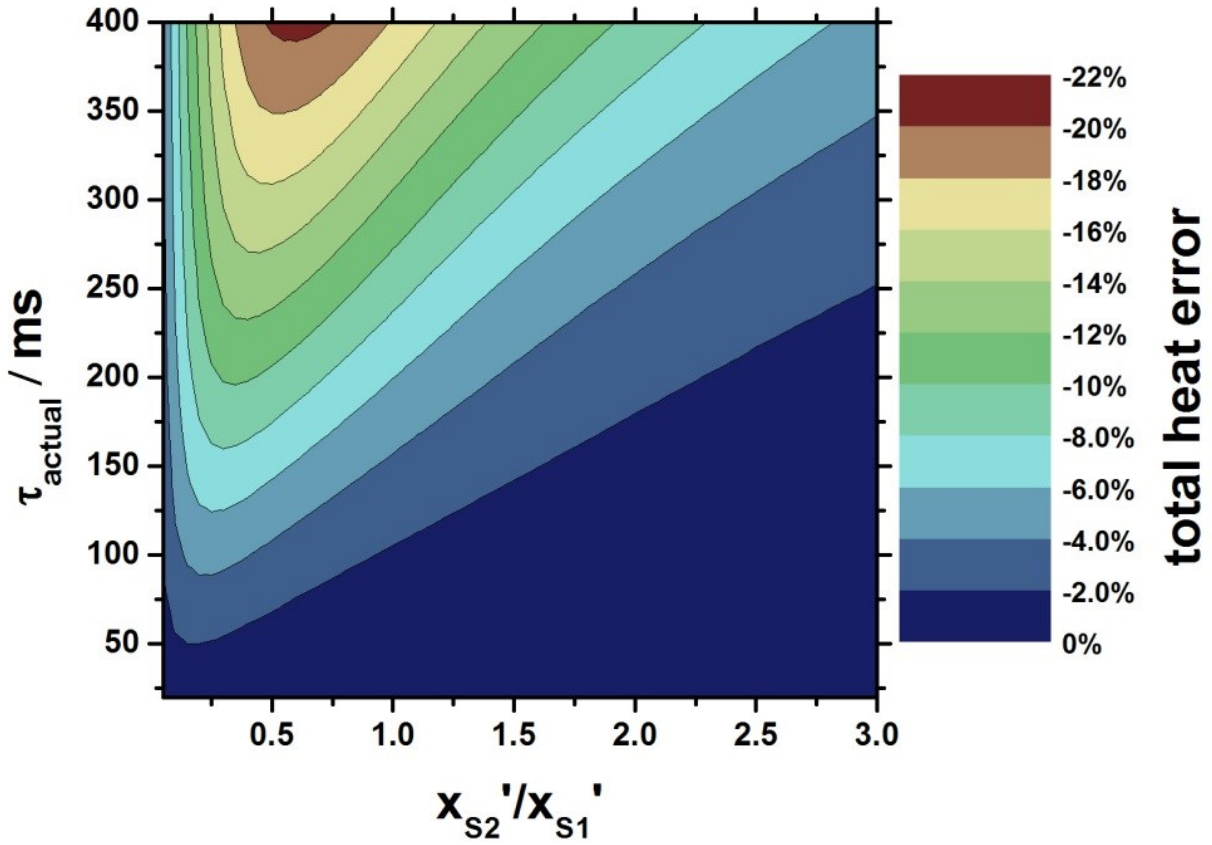


Figure A.7: Percent error of the total heat (color bar) as a function of τ_{actual} and the ratio of step 2 to step 1 heat (x_{S2}' / x_{S1}').

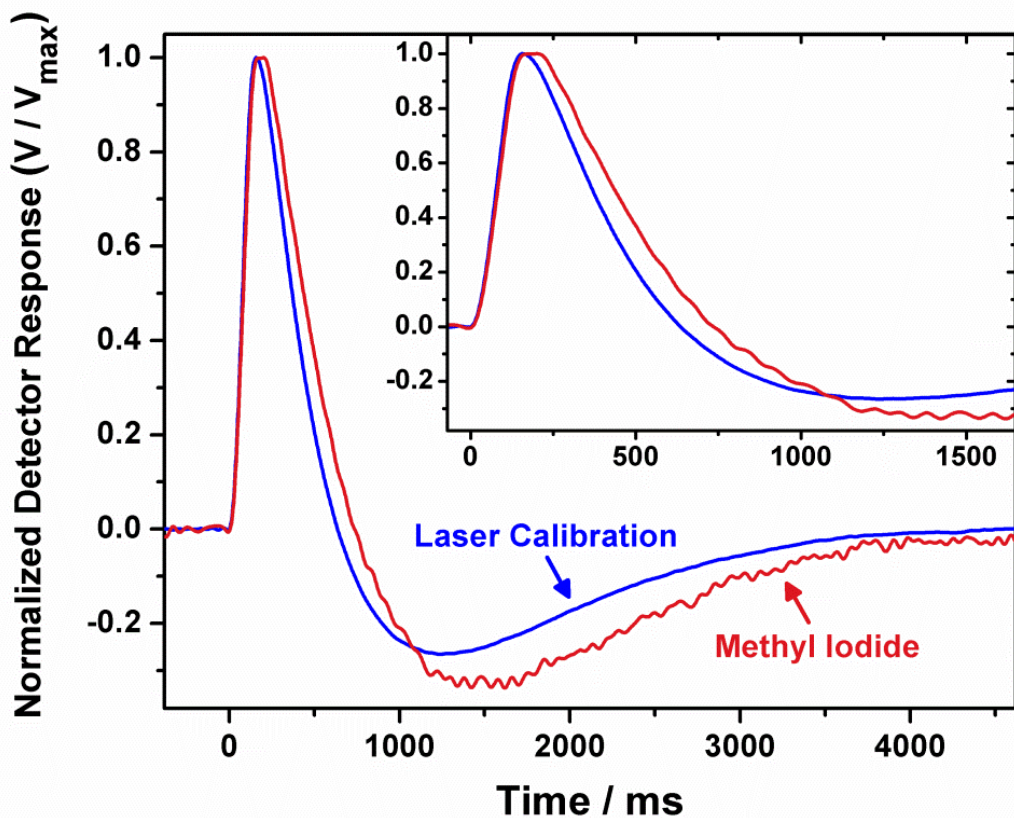


Figure A.8: Normalized detector responses for the laser calibration and molecular adsorption of methyl iodide on Pt(111) at 270 K. The response from molecular adsorption is broadened due to slow heat deposition. The inset shows the same pulses on a shorter timescale.

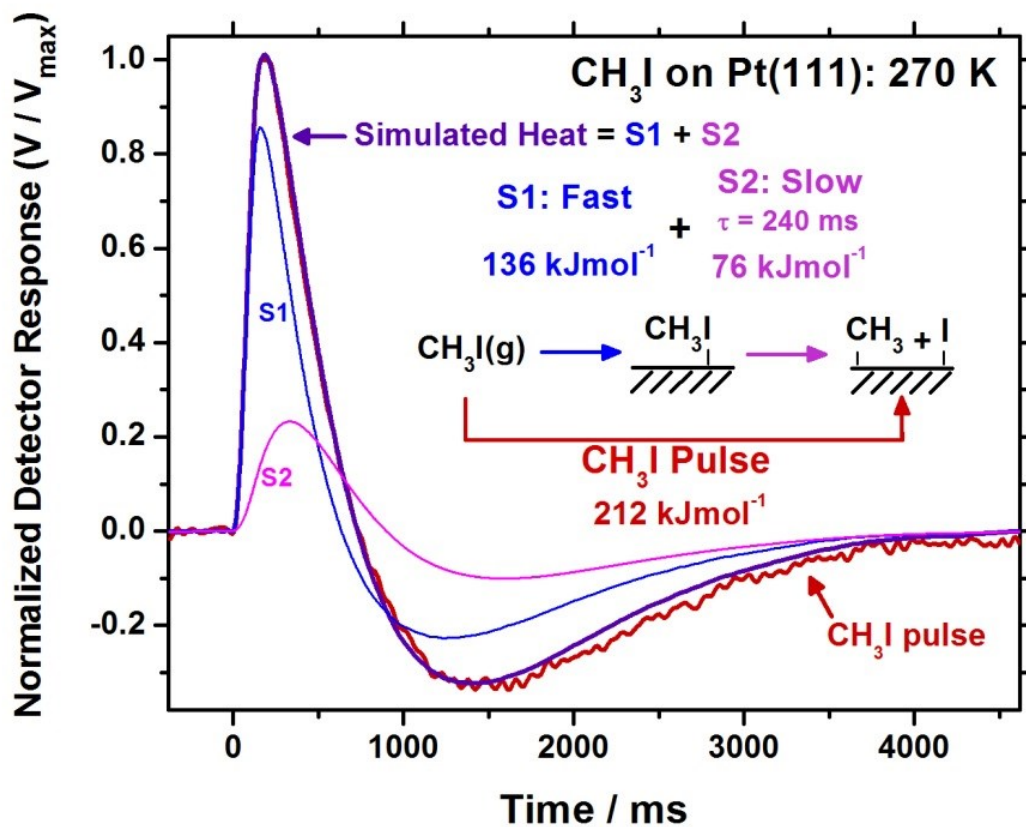


Figure A.9: Simulated heat pulse (purple) of 212 kJmol⁻¹ created using values obtained from the best fit method for the third average methyl iodide pulse (0.037-0.055 ML) on Pt(111) at 270 K (red). This simulated heat pulse is the sum of the fast step 1 heat (green) of 136 kJmol⁻¹ and slow step 2 heat (pink) of 76 kJmol⁻¹ that is deposited with a τ of 240 ms.

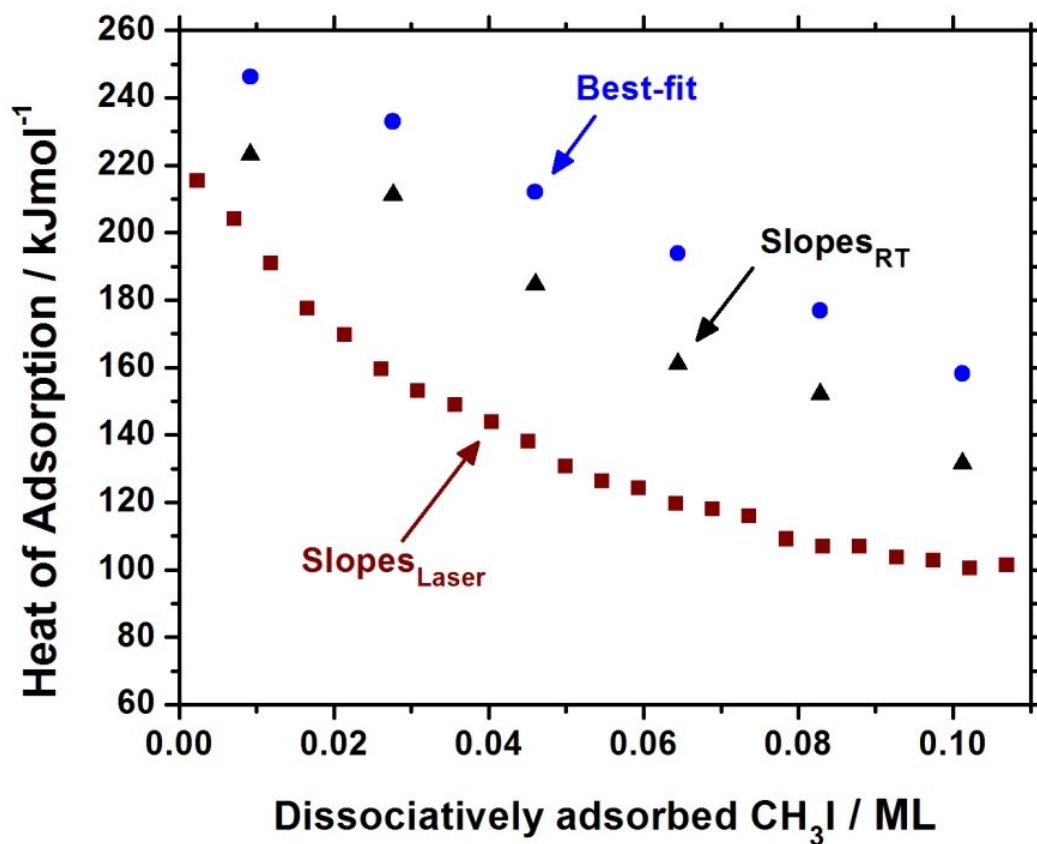


Figure A.10: Calculated total heat of adsorption obtained using laser slope (red squares), slopes_{RT} (black triangles) and best-fit (blue circles) methods for methyl iodide pulses on Pt(111) at 270 K as a function of dissociatively adsorbed methyl iodide coverage, θ , in ML.

Curriculum Vitae

TRENT L. SILBAUGH

DOB: 11/04/1986

U.S. citizen

4417 Evanston Ave. N Apt. 305, Seattle, WA 98103 | (480)332-7324 | tsilbaug@u.washington.edu

EDUCATION

University of Washington, Seattle, WA

PhD Chemical Engineering

Anticip. 2014

MS Chemical Engineering

2011

Arizona State University, Tempe, AZ

BSE Chemical Engineering

2009

GPA: 3.89 overall (3.97 in Major)

RESEARCH EXPERIENCE

Research Assistant

2009–Present

Charles T. Campbell PhD., University of Washington, Department of Chemical Engineering, Seattle, WA

- Purpose: The development of trends that relate thermodynamic properties of adsorbed molecules on metal surfaces to their catalytic performance. Provide experimental benchmarks for the improvement of state-of-the-art computational methods used for catalyst discovery.
- To date:
 - Studies have led to the determination of the heats of formation of important intermediates derived from oxygenates (adsorbed methoxy and formate) and small hydrocarbons (methyl, methylidyne, and *t*-butyl) on well-defined platinum samples which has led to the development of a trend that allows for the prediction of bond strengths of adsorbed molecular fragments from widely available gas phase data.
 - Developed a data analysis method that allows for the first time the determination of kinetic information from SCAC data.
 - Worked with a team to improve and maintain the world's most sensitive and versatile calorimeter for ultrahigh vacuum measurements of the energies of surface reactions on single-crystal surfaces under the clean conditions of ultrahigh vacuum, supported by a powerful array of surface analysis techniques

Undergraduate Research Assistant

1/2008–5/2009

Robert Pfeffer PhD. and Jerry Y.S. Lin PhD., Department of Chemical Engineering, Tempe, AZ

- Separation of organic contaminants from wastewater using hydrophobic silica aerogels in an inverse fluidized bed.

AWARDS

Graduate School Fund for Excellence and Innovation Travel Award	2012
Jane and Joseph McCarthy Outstanding Teaching Assistant	2010–2011
Department of Chemical Engineering Travel Award	2011
Top Scholar Fellowship (UW Graduate School)	2009
Early Bird Graduate Award (UW Center for Nanotechnology)	2009
Dean's List (Arizona State University): All semesters	2005–2009
President's Scholarship (Arizona State University)	2005–2009

PUBLICATIONS

1. **T.L. Silbaugh**, C.T. Campbell, F. Studt, J.K. Norskov, Experimental Benchmarks for Density Functional Theory Calculations of Surface Reactions, (*In Preparation*)
2. **T.L. Silbaugh**, C.T. Campbell, A comprehensive review of experimental adsorption energies measured by single crystal adsorption calorimetry, (*In Preparation*)
3. C.A. Wolcott, I.X. Green, **T.L. Silbaugh**, C.T. Campbell, Energetics of Adsorbed CH₂ and CH on Pt(111) Studied by Single Crystal Adsorption Calorimetry, (*In Preparation*)
4. **T.L. Silbaugh**, E.M. Karp, C.T. Campbell, Energetics of Methanol and Formic Acid Oxidation on Pt(111): Mechanistic Insights from Single Crystal Adsorption Calorimetry, (*In Preparation*)
5. S. Schauermann, **T.L. Silbaugh**, C.T. Campbell, Single Crystal Adsorption Calorimetry on Well-Defined Surfaces: from Single Crystals to supported Nanoparticles, (*Submitted*)
6. E.M. Karp, **T.L. Silbaugh**, C.T. Campbell, Bond energies of molecular fragments to metal surfaces track their bond energies to H atoms, *J. Amer. Chem. Soc.*, 136 (2014) 4137-4140
Featured in: C&EN
7. **T.L. Silbaugh**, E.M. Karp, C.T. Campbell, Energetics of formic acid conversion to adsorbed formates on Pt(111) by transient calorimetry, *J. Amer. Chem. Soc.*, 136 (2014) 3964-3971
Featured in: Spotlight on Recent JACS publications, C&EN
8. **T.L. Silbaugh**, J.B. Giorgi, Y. Xu, K.A. Tillekaratne, F. Zaera, C.T. Campbell, Adsorption Energy of tert-Butyl on Pt(111) by Dissociation of tert-Butyl Iodide: Calorimetry and DFT, *J. Phys. Chem. C*, 118 (2014) 427-438
9. **T.L. Silbaugh**, E.M. Karp, C.T. Campbell, Surface Kinetics and Energetics from Single Crystal Adsorption Calorimetry Lineshape Analysis: Methyl from Methyl Iodide on Pt(111), *J. Catal.*, 308 (2013) 114-121.
10. E.M. Karp, **T.L. Silbaugh**, C.T. Campbell, Energetics of Adsorbed CH₃ on Pt(111) by Calorimetry, *J. Amer. Chem. Soc.*, 135 (2013) 5208-5211.
11. E.M. Karp, **T.L. Silbaugh**, C.T. Campbell, Energetics of Adsorbed CH₃ and CH on Pt(111) by Calorimetry: Dissociative Adsorption of CH₃I, *J. Phys. Chem. C*, 117 (2013) 6325-6336.

12. E. M. Karp, **T. L. Silbaugh**, M.C. Crowe, C.T. Campbell, Energetics of Adsorbed Methanol and Methoxy on Pt(111) by Microcalorimetry, *J. Amer. Chem. Soc.*, 134 (2012) 20388-20395.
13. C.T. Campbell, J.C. Sharp, Y.X. Yao, E.M. Karp, **T.L. Silbaugh**, Insights into Catalysis by Gold Nanoparticles and their Support Effects through Surface Science Studies of Model Catalysts, *Faraday Discussions* 152 (2011) 227-239.
14. D. Wang, **T. Silbaugh**, R. Pfeffer, Y.S. Lin, Removal of emulsified oil from water by inverse fluidization of hydrophobic aerogels, *Powder Technology* 203 (2010) 298-309.

PRESENTATIONS

UW Dept. of Chem. Engineering Graduate Student Symposium, Seattle, WA (Oral)	10/2013
AVS 59 th Annual International Symposium, Tampa Bay, FL (Oral)	10/2012
UW Dept. of Chem. Engineering Graduate Student Symposium, Seattle, WA (Oral)	10/2012
AVS 58 th Annual International Symposium, Nashville, TN (Oral)	10/2011
Chemical Reactions at Surfaces Gordon Research Conference, Ventura, CA (Poster)	10/2010
FURI Undergraduate Research Symposium, Tempe, AZ (Poster)	4/2009
Deans reception for permanent Chem. Engineering Dept. Chair, Tempe, AZ (Poster)	5/2008

TEACHING AND MENTORSHIP

Teaching Aide, ChemE 460 Process Control Laboratory and Lecture	2014
Teaching Aide, ChemE 460 Process Control Laboratory	2013
Teaching Aide, ChemE 460 Process Control Laboratory	2012
Teaching Aide, ChemE 436 Units Operations Laboratory I	2011
Mentored four undergraduate students	2010–2013

LEADERSHIP

Chapter Secretary, AVS University of Washington Student Chapter	2010–2012
Chapter President, Tau Beta Pi Engineering Honors Society: AZ Beta	2008–2009

OUTREACH

Science EXPO Day	6/2013
University of Washington DYSSS Selection Committee	2012, 2013
MESA outreach program at the University of Washington	2011
Science is Fun Internship (ASU)	2008–5/2008
<ul style="list-style-type: none"> o Performed science experiments at elementary schools in Phoenix, AZ in order to increase interest in science. Communication of complex ideas in a manner that could be understood by the target audience. 	

ORGANIZATIONS

AVS UW Student Chapter Member	2010–Present
AVS National Chapter Member	2010–Present
Tau Beta Pi Engineering Honors Society	2007–Present